Dissertation
submitted to the
Combined Faculties of the Natural Sciences and Mathematics
of the Ruperto-Carola-University of Heidelberg, Germany
for the degree of
Doctor of Natural Sciences

Put forward by
Justus Zorn
Born in Waldkirch
Oral examination: 18.12.2019

# Cherenkov Camera and Analysis Development for Highest-Energy Gamma-Ray Astronomy

Referees:
Prof. Dr. Jim Hinton
Prof. Dr. Stefan Wagner

*Für meine Frau*
*Weil du die Beste bist!*

# Zusammenfassung

Atmosphärische Cherenkov Teleskope werden zur Detektion von Gammastrahlen mit den höchsten Energien verwendet. Die vorliegende Arbeit beschäftigt sich mit zwei Experimenten dieser Art: Das sich in Betrieb befindende High Energy Stereoscopic System (H.E.S.S.) und das für die Zukunft geplante Cherenkov Telescope Array (CTA). Bei vier der fünf H.E.S.S. Kameras wurde vor einigen Jahren die Elektronik ausgetauscht, wodurch die Datenauslese und Analysetechniken, insbesondere bei den höchsten Energien, verbessert wurden. Die Compact High-Energy Camera (CHEC) ist ein Design für die sogenannten kleinen Teleskope von CTA, welche die Detektion von Gammastrahlen mit Energien oberhalb von 1 TeV ermöglichen.

Der erste Teil der Arbeit widmet sich der Charakterisierung zweier CHEC Prototypen, welche nacheinander entwickelt wurden: CHEC-M und CHEC-S. Hierzu präsentiere ich Ergebnisse, welche sowohl bei Messungen im Labor als auch bei Teleskop-Messkampagnen erzielt wurden. Bei den Ergebnissen von CHEC-S konzentriere ich mich insbesondere auf Parameter, welche bei den Tests mit CHEC-M leistungslimitierende Probleme aufgezeigt hatten, und deshalb bei der Überarbeitung des Designs für CHEC-S berücksichtigt wurden.

Der zweite Teil beschäftigt sich mit den aufgerüsteten H.E.S.S. Kameras. Hierbei zeige ich Studien zu Monte-Carlo Simulationen, welche die Übereinstimmung zwischen Messung und Simulation insgesamt verbesserten, sowie die neu entwickelte Analysekette im Zusammenhang mit der Auslese der vollständigen Wellenformen der Cherenkov-Lichtsignale, wodurch verbesserte Ergebnisse insbesondere bei den höchsten Energien erwartet werden.

Im letzten Teil präsentiere ich eine neue Analyse der galaktischen Gammastrahlenquelle HESS J1646–458, welche mit Westerlund 1, dem massereichsten Sternenhaufen in unserer Galaxie, assoziiert wird.

# Abstract

Imaging atmospheric Cherenkov telescopes are used for the detection of highest-energy $\gamma$-rays. This thesis focuses on two experiments equipped with such telescopes: The operating High Energy Stereoscopic System (H.E.S.S.) and the future Cherenkov Telescope Array (CTA). Four of the five H.E.S.S. cameras saw a major electronics upgrade a few years ago enabling improved readout and analysis techniques mainly at the highest energies. The Compact High-Energy Camera (CHEC) is a design for the Small-Sized Telescopes of CTA focusing on the detection of $\gamma$-rays with energies exceeding 1 TeV.

The first part of the thesis is dedicated to the characterisation of two CHEC prototype cameras developed successively: CHEC-M and CHEC-S. I present results of laboratory and on-telescope measurements for both cameras. In the case of CHEC-S, I focus on those parameters that had been shown to be performance-limiting in CHEC-M and which were therefore addressed in the design iteration for CHEC-S.

The second part is devoted to the upgraded H.E.S.S. cameras. I present results of Monte-Carlo simulation studies, analysis developments, and performance measurements using full-waveform readout. In the former case I demonstrate a general consistency between simulations and measurements, in the latter case I show that the use of full-sampled waveform readout improves the performance, especially at the highest energies.

In the last part, I present a new analysis of the Galactic $\gamma$-ray source HESS J1646–458 which is associated with Westerlund 1, the most massive stellar cluster in our Galaxy.

# Contents

# List of Figures

# List of Tables

# List of Acronyms

**AC** alternating current.

**ADC** analog-to-digital converter.

**AGN** active galactic nucleus.

**AR** adaptive ring.

**ASIC** application-specific integrated circuits.

**ASTRI** Astrofisica con Specchi a Tecnologia Replicante Italiana.

**BDT** boosted decision tree.

**BEE** back-end electronics.

**BP** backplane.

**CE** collection efficiency.

**CHEC** Compact High-Energy Camera.

**CM** charge mode.

**CMB** cosmic microwave background.

**CR** cosmic ray.

**CTA** Cherenkov Telescope Array.

**DAC** digital-to-analog converter.

**DACQ** data acquisition.

**DC** direct current.

**DCR** dark count rate.

**DESY** Deutsches Elektronen Synchrotron.

**DL1** data level 1.

**DST** data summary tape.

**EAS** extensive air shower.

**ECAP** Erlangen Centre for Astroparticle Physics.

**ENF** excess noise factor.

**FADC** flash-ADC.

**FEE** front-end electronics.

**FF** flat-field.

**FIR** far infrared.

**FITS** flexible image transport system.

**FoV** field of view.

**FPGA** field programmable gate array.

**FS** fast signal.

**FWHM** full width at half maximum.

**GCR** Galactic cosmic ray.

**GCT** Gamma-ray Cherenkov Telescope.

**GMC** giant molecular cloud.

**H.E.S.S.** High Energy Stereoscopic System.

**H.E.S.S. IU** upgraded H.E.S.S. I camera.

**HAWC** High-Altitude Water Cherenkov Gamma-Ray Observatory.

**HD** Heidelberg.

**HE** high energy.

**HGPS** H.E.S.S. Galactic plane survey.

**HKFPGA** house-keeping FPGA.

**HO** hold-off.

**HV** high voltage.

**IACT** imaging atmospheric Cherenkov telescope.

**IC** inverse Compton.

**ICRC** International Cosmic-Ray Conference.

**IFR** infrared background.

**IQRM** interquartile range method.

**IRF** instrument response function.

**ISM** interstellar medium.

**LED** light-emitting diode.

**LHC** Large Hadron Collider.

**LMC** Large Magellanic Cloud.

**LST** large-sized telescope.

**MAGIC** Major Atmospheric Gamma-Ray Imaging Cherenkov Telescopes.

**MAPM** multi-anode photomultiplier.

**MC** Monte-Carlo.

**MPIK** Max-Planck Institut für Kernphysik Heidelberg.

**MST** medium-sized telescope.

**ND** neutral density.

**NIR** near infrared.

**NIST** National Institute of Standards and Technology.

**NN** next neighbour.

**NS** neutron star.

**NSB** night sky background.

**OPCT** optical crosstalk.

**PA** Paris.

**PB** power board.

**PCB** printed circuit board.

**PDE** photon detection efficiency.

**PMT** photomultiplier tube.

**PoI** pixel of interest.

**PPG** periodic pulse generator.

**PSF** point spread function.

**PSU** power supply unit.

**PWN** pulsar wind nebula.

**QE** quantum efficiency.

**RPG** random pulse generator.

**RSG** red supergiant.

**SB** slow-control board.

**SC** stellar cluster.

**SD** sending data.

**SED** spectral energy distribution.

**SiPM** Silicon photomultiplier.

**SL** star light.

**SM** sample mode.

**SN** supernova.

**SNMP** simple network management protocol.

**SNR** supernova remnant.

**SP** superpixel.

**SpB** superbubble.

**SPE** single photoelectron.

**SPI** serial peripheral interface.

**SS** slow signal.

**SSC** Synchrotron self-Compton.

**SST** small-sized telescope.

**TARGET** TeV array readout with GSa/s sampling and event trigger.

**TEC** thermoelectric cooler.

**TF** transfer function.

**TFPGA** trigger FPGA.

**TM** TARGET module.

**UDP** user datagram protocol.

**UHE** ultra high energy.

**UV** ultra-violet.

**VERITAS** Very Energetic Radiation Imaging Telescope Array System.

**VHE** very high energy.

**Wd1** Westerlund 1.

# Introduction

> "What we observe is not nature itself, but nature exposed to our method of questioning."
>
> Werner Heisenberg

The origin of our interest in the Universe dates back to antiquity when astronomical objects and phenomena were mostly linked to religious and mythological beliefs. A more scientific view on astronomy started around 1800 BC when the Babylonians were the first to recognise astronomical phenomena as being periodic and to apply mathematics to their predictions. While for a long time, astronomy was restricted to observations in the optical where the radiation is mostly of thermal origin, technical developments in the $20^{\text{th}}$ century allowed the detection of radiation in other wavelengths such as the radio and $\gamma$-ray regimes with the first $\gamma$-ray observations performed with instruments on board of satellites in the 1960s. $\gamma$-ray astronomy is a comparatively very young field observing radiation of non-thermal origin resulting from the most extreme and energetic processes in the Universe. With further understanding of the physics of extensive air showers (EASs) and technological development, the use of ground-based $\gamma$-ray detectors, such as EAS arrays and imaging atmospheric Cherenkov telescopes (IACTs), increased the maximum detectable $\gamma$-ray energy by about three orders of magnitude from a few tens and hundreds of GeV (for space-based experiments) to tens and hundreds of TeV. This opened another astronomical, the so-called very high energy (VHE) $\gamma$-ray window with improved observation capabilities that shed light on the most energetic $\gamma$-ray bursts and the mysteries of cosmic ray (CR) acceleration. At least some sources in our Galaxy, the so-called PeVatrons, are expected to accelerate hadronic CRs up to PeV energies which in turn should result in $\gamma$-ray energies of the order of 100 TeV. The VHE $\gamma$-ray regime is the highest-energy regime in which electromagnetic radiation has been detected so far.

In this thesis, I will cover several aspects of highest-energy $\gamma$-ray astronomy. After an introduction to CRs and $\gamma$-rays in Ch. 2, I will present the physics of EASs and atmospheric Cherenkov radiation, and the resulting concept of IACTs in Ch. 3. Additionally, I will give examples of two IACT experiments in this chapter: the operational High Energy Stereoscopic System (H.E.S.S.) and the future Cherenkov Telescope Array (CTA). I will further set a

special focus on the upgraded H.E.S.S. I cameras (H.E.S.S. IU) and the Compact High-Energy Camera (CHEC) as they both promise to improve the detection of highest-energy $\gamma$-rays and since hardware and analysis development of both cover the main part of the thesis. In Ch. 4, I will introduce the CHEC design and the data taking procedures which will be followed by Ch. 5 & 6, in which I will present characterisation tests and results of two CHEC camera prototypes: CHEC-M and CHEC-S. Due to the upgrade of the H.E.S.S. I cameras, in which all electronic parts were replaced, a verification of the new Monte-Carlo (MC) simulation chain is required which I performed in the scope of this work and which I will present in Ch. 7. In Ch. 8, I will introduce the full-waveform processing enabled by the H.E.S.S. I camera upgrade and I will show the resulting performance improvements especially for the detection of highest-energy $\gamma$-rays. In Ch. 9, I will present new analyses of the PeVatron candidate HESS J1646–458, an extended VHE $\gamma$-ray source associated with the stellar cluster (SC) Westerlund 1 (Wd1). Finally, in Ch. 10, I will give a conclusion putting the different chapters in a global context.

# Cosmic and gamma rays

> "We are made of stellar ash. Our origin and evolution have been tied to distant cosmic events. The exploration of the cosmos is a voyage of self-discovery."
>
> Carl Sagan

Cosmic rays (CRs) are charged, massive particles, mainly ionised atomic nuclei and electrons (and their anti-particles), reaching Earth from outside the Solar System, i.e. from Galactic or extragalactic sources. They are observed up to energies of $10^{20}$ eV, and their abundances varies over 19 magnitudes, from about 1 particle/m$^2$/s at 1 GeV to less than 1 particle/km$^2$/century at $10^{20}$ eV (cf. Fig. 2.1). While CRs are sensitive to magnetic fields, thus loosing their direction information when travelling through the Universe, $\gamma$-rays, produced in secondary processes and not affected by magnetic fields, point back to their production site. Thus, their detection helps to understand the CR acceleration processes and to locate their sources.

One of the main scientific questions in the observation of CRs and $\gamma$-rays is the morphology of the energy spectrum since it can provide valuable information about source characteristics such as acceleration mechanism and underlying CR particle population. Typically one distinguishes between the integrated energy spectrum/flux given by the number of particles $N_x$ ($x$ being the particle type) per area $A$, time $t$, and solid angle $\Omega$ as function of the particle energy $E_x$, and the differential energy spectrum/flux $\Phi_x$, being the integrated energy spectrum per energy unit d$E_x$ [1], thus defined as

$$\Phi_x(E_x) := \frac{\mathrm{dN_x}}{\mathrm{dAdtd\Omega dE_x}}.$$ 

(2.1)

The all-particle CR spectrum measured on Earth (cf. Fig. 2.1) shows several features, such as the so called "knee" at an energy of a few PeV. Above that energy, the spectrum steepens, i.e. the spectral index $\alpha$ increases from ∼2.7 to ∼3.0, and the chemical composition changes from manly proton-dominated to heavier elements [2, 3]. Up to the knee, the spectrum can

---

[1]Throughout the thesis, the expression "spectrum" is always referred to the differential energy spectrum if not stated differently.
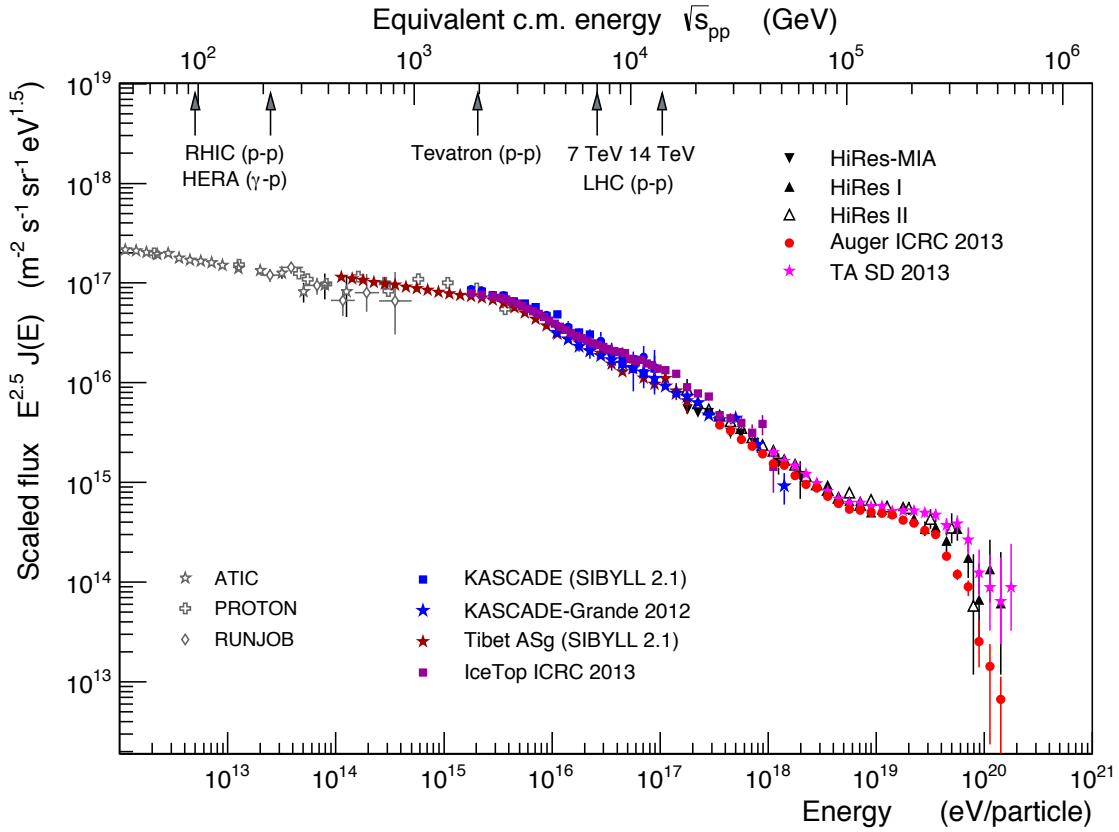
**Figure 2.1** All-particle CR spectrum at Earth measured by the indicated experiments. As a comparison, the centre of mass energy $\sqrt{s_{\mathrm{pp}}}$ for proton-proton collision at the Large Hadron Collider (LHC) is indicated. Adapted from [1].

be parameterised by [4]

$$\Phi_{\mathrm{CR}} = 0.18 \left( \frac{E}{1~\mathrm{TeV}} \right)^{-2.7} \mathrm{m}^{-2}\,\mathrm{s}^{-1}\,\mathrm{TeV}^{-1}\,\mathrm{sr}^{-1}, \tag{2.2}$$

with $E$ being the energy of the primary CR.

Another expression often used is the spectral energy distribution (SED) of photons, defined as the differential photon energy spectrum multiplied with $E_\gamma^2$, i.e. $E_\gamma^2 \Phi_\gamma(E_\gamma)$. Typically, when talking about the SED, one refers to the SED over many orders of photon energies including measurements with different instruments in different wavelength bands.

In the following sections, I will first explain CR and $\gamma$-ray production mechanisms (cf. Sec. 2.1). Then, I will discuss source candidates for CRs and $\gamma$-rays, their required characteristics, and examples such as supernova remnants (SNRs), SCs, and molecular clouds (cf. Sec. 2.2). Finally, I will present general procedures for the interpretation of $\gamma$-ray observations including multi-wavelength analyses (cf. Sec. 2.3).

## 2.1 Production of cosmic and gamma rays

### 2.1.1 Cosmic ray acceleration and propagation

A well-established theory to explain the acceleration of CRs is the diffusive shock acceleration, also referred to as first-order Fermi acceleration in the presence of strong shock waves [5]. In this mechanism, a particle $x$ crosses a shock front several times by interacting with the magnetic fields on both sides of the shock front yielding an overall (constant) energy gain per crossing of

$$\left\langle \frac{\Delta E_x}{E_{0,x}} \right\rangle = \frac{v_{\mathrm{s}}}{c} =: \xi, \tag{2.3}$$

where $E_{0,x}$ is the energy of the particle when entering the shock front system, $v_{\mathrm{s}}$ the velocity of the shock front in the laboratory system, i.e. in the system where the interstellar medium (ISM) is in rest, and $c$ the velocity of light in vacuum. Taking into account the probability of the particle to escape from the acceleration site for one crossing cycle $P_{\mathrm{esc,x}}$ (being independent from the initial particle energy), this results in a power-law source spectrum of the particle, given by

$$\Phi_x(E_x) \propto \left( \frac{E_x}{E_{0,x}} \right)^{-\beta_x}, \tag{2.4}$$

with the exponent

$$\beta_x = p_x + 1 \tag{2.5}$$

and

$$p_x = -\frac{\ln(1 - P_{\mathrm{esc,x}})}{\ln(1 + \xi)} \simeq \frac{P_{\mathrm{esc,x}}}{\xi} \tag{2.6}$$

for $P_{\mathrm{esc}}$ and $\xi$ much smaller than 1. $p_x$ is calculated to typically lie in the range between 1 and 1.5, depending on the characteristics of the shock front such as orientation of the magnetic field lines relative to it. In many cases, $\gamma$-ray observations revealed cutoffs in the corresponding spectra what may be related to a maximum energy that sources of CRs and $\gamma$-rays can provide. As such a cutoff is often parameterised by an exponential function with a characteristic cutoff energy $E_{\mathrm{c,x}}$ [6], Eq. 2.4 evolves into

$$\Phi_x(E_x) \propto \left( \frac{E_x}{E_{0,x}} \right)^{-\beta_x} \exp\left( -\frac{E_x}{E_{\mathrm{c,x}}} \right). \tag{2.7}$$

After the CRs have left their acceleration sites, they are expected to propagate through the ISM. To fully model this propagation, several effects have to be taken into account, including the diffusion of particles in the randomly orientated magnetic fields of the Galaxy, convection effects by Galactic winds as well as the possible streaming of particles by the structured magnetic field component. In most models, the effects of diffusion are assumed to be the most dominant ones with effects of convection only being important for energies $E < 5$ GeV. Hence, for $E > 5$ GeV, the CR propagation can be treated as a random walk through the ISM. The typical distance $d$ the particle travelled in the time $\tau$ is then given by [7]

$$d = 2\sqrt{D(E)\,\tau}. \tag{2.8}$$

$D(E)$ is the energy-dependent diffusion coefficient of the ISM, typically parameterised by [7]

$$D(E) = D_0 \left( \frac{E}{E_0} \right)^{\delta}, \tag{2.9}$$

**Table 2.1** Classification of $\gamma$-rays into different bands according to their energy [9].

| Energy band name | Abbreviation | Energy range |
|---|---|---|
| Low/medium energy | LE/ME | 0.1 – 30 MeV |
| High energy | HE | 30 MeV – 100 GeV |
| Very-high energy | VHE | 100 GeV – 100 TeV |
| Ultra-high energy | UHE | >100 TeV |

with $D_0 \simeq 3 \times 10^{28}\,\mathrm{cm}^2/\mathrm{s}$, $E_0 = 10$ GeV, and $\delta = 0.3$–$0.6$ for the Galactic plane, determined via a fit to the observed primary to secondary CR ratios (cf. [8] for details). As a consequence, in this model, the CR spectrum observed on Earth (with spectral index $\alpha$) would be given by the source spectrum modulated by diffusion of CRs in the Galaxy, hence

$$\alpha = \beta + \delta. \tag{2.10}$$

Combining the model of first-order Fermi acceleration in shock fronts and diffusion in randomly orientated Galactic magnetic fields results in a theory for CR acceleration and propagation. This theory is well-established in the CR community since

- shock fronts are observed in many astrophysical processes,

- it may explain the origin of the observed power-law CR spectrum (cf. Fig. 2.1) and the value of the spectral index ($\alpha = 2.7$) of the all-particle CR spectrum observed on Earth, e.g. with values for $\beta$ and $\delta$ of $\beta = p + 1 = 1.2 + 1 = 2.2$ and $\delta = 0.5$, and

- it may be applicable in a wide range of scenarios.

### 2.1.2 Gamma ray production

As the accelerated CR particles propagate through the region local to the source and beyond, they should not only diffuse but also undergo energy losses through a variety of mechanisms. Several of those may lead to the production of $\gamma$-rays. In astronomy, $\gamma$-rays are typically classified by their energy into different energy bands (cf. Tab. 2.1). This classification will also be used throughout the thesis.

The processes converting energy from CRs into $\gamma$-rays are typically characterised based on the physical origin of the CR being either leptonic or hadronic and are described in the following sections.

#### 2.1.2.1 Leptonic processes

CR leptons loose their energy via three main processes: bremsstrahlung, synchrotron radiation, and inverse Compton (IC) scattering.

**Bremsstrahlung**  When interacting with matter, electrons and positrons[2] loose energy according to the Bethe-Bloch-formula [10, 11]. While below a critical energy of $\sim$350 MeV (for hydrogen, cf. [7]), the energy loss is dominated by ionisation processes, this is different

---

[2]The term "electrons" refers to both, electrons and positrons, hereafter if not stated differently.

for energies above the critical energy where bremsstrahlung is the dominating process. The energy loss of a relativistic electron of energy $E_e$ due to bremsstrahlung is given by [12]

$$P_{\text{brems}} = -\left(\frac{dE_e}{dt}\right) = \frac{Z(Z+1.3)e^6 n}{8\pi^2 \epsilon_0^3 m_e^2 c^4 h}\left[\ln\left(\frac{183}{Z^{1/3}}\right) + \frac{1}{8}\right] E_e \propto E_e, \qquad (2.11)$$

where $n$ is the number density of nuclei with proton number $Z$, $e$ the elementary charge, $\epsilon_0$ the electric constant, $m_e$ the electron mass and $h$ the Planck constant. The resulting spectral index is [7]

$$\alpha_\gamma = \alpha_e, \qquad (2.12)$$

meaning that the observed $\gamma$-ray spectrum should directly reflect the underlying spectrum of the electron population. The cooling time, defined as the characteristic time scale over which a particle looses its energy due to a given process, is for bremsstrahlung given by [7]

$$\tau_{\text{brems}} = \frac{E_e}{P_{\text{brems}}} \simeq 4 \times 10^7 \left(\frac{n}{1\,\text{cm}^3}\right) \text{yr}. \qquad (2.13)$$

Due to the dependence on the particle density, bremsstrahlung contributes to the production of cosmic $\gamma$-rays especially in dense gaseous regions. However, in most of the cases, it is less dominant than the other mechanisms explained in the following paragraphs.

**Synchrotron radiation**  When deflected by magnetic fields, all charged particles loose energy while emitting synchrotron radiation, a polarised radiation boosted (in the laboratory frame) into the direction of motion of the particle with an opening angle of $1/\Gamma$ ($\Gamma$ being the Lorentz factor). Considering the case of the charged particle being an electron (with energy $E_e$, mass $m_e$ and velocity $\beta$ in units of $c$), the power of this radiation, and equal to the energy loss of the electron, is given by [13]

$$P_{\text{sync}} = -\left(\frac{dE_e}{dt}\right) = \frac{4}{3}c\,\sigma_T\left(\frac{E_e}{m_e c^2}\right)^2 \beta^2\,u_B. \qquad (2.14)$$

$\sigma_T = 8\pi/3\,[e^2/(m_e c^2)]^2$ is the so-called Thomson cross-section, $u_B = B^2/(2\mu_0)$ the magnetic energy density of the magnetic field $B$, and $\mu_0$ the magnetic permeability in vacuum. For any charged particle with mass $m$, it holds that $P_{\text{sync}} \propto 1/m^4$ (since $\sigma_T \propto 1/m^2$). Thus, higher energy loss resulting in stronger synchrotron emission is expected for lighter particles. Comparing electrons and protons with same energy and $\beta \simeq 1$, the loss due to synchrotron radiation is by a factor of $\sim 10^{13}$ times higher for electrons. This is why synchrotron radiation is expected to be mainly observed for CR electrons. The synchrotron radiation emitted by a single electron of energy $E_e$ is described by a continuous energy spectrum peaking at a characteristic energy of [6]

$$E_{\text{sync}} \simeq 0.2\left(\frac{E_e}{1\,\text{TeV}}\right)^2\left(\frac{B}{10\,\mu\text{G}}\right) \text{eV} \qquad (2.15)$$

as shown by Fig. 2.2a. For a non-mono-energetic electron population following a power-law spectrum with spectral index $\alpha_e$, the total synchrotron spectrum is a convolution of the mono-energetic synchrotron and the electron spectrum (cf. Fig. 2.2b). The resulting photon spectrum then follows again a power law with spectral index [16]

$$\alpha_\gamma = \frac{\alpha_e + 1}{2}. \qquad (2.16)$$
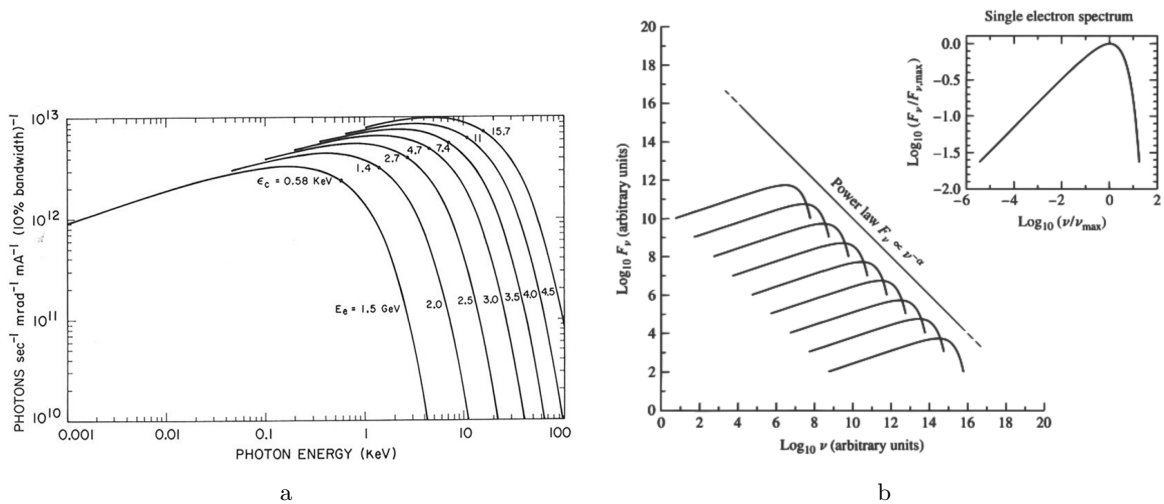
**Figure 2.2** Synchrotron spectrum (a) calculated for single electrons with certain energies $E_e$ resulting in different characteristic peak energies of $E_{sync} \equiv \epsilon_c$ (adapted from [14]) and (b) shown as a superposition of single electron spectra where the single electrons are part of an electron population following a power-law spectrum (adapted from [15]).

The cooling time of synchrotron radiation, given by [7]

$$\tau_{sync} = \frac{E_e}{P_{sync}} \simeq 1.2 \times 10^3 \left(\frac{B}{10\,\mu G}\right)^{-2} \left(\frac{E_e}{100\,\text{TeV}}\right)^{-1} \text{yr}, \qquad (2.17)$$

decreases for high-energy electrons in strong magnetic fields.

**Inverse Compton scattering**   The scattering of a photon with a wavelength much less than the size of an atom by a (loosely bound) electron is called Compton scattering, typically resulting in an energy loss of the photon and an energy gain of the electron. IC scattering refers to the opposite process, i.e. when a high-energy electron is scattered off a low-energy photon, resulting in an energy gain of the photon and an energy loss of the incident electron. In such a way, CR electrons interacting with ambient photon fields like the cosmic microwave background (CMB), star light (SL), or the infrared background (IFR) can scatter up those photons to much higher ($\gamma$-ray) energies. Depending on the photon energy of the ambient radiation field $E_{ph}$ and the incoming electron energy, one distinguishes between two different regimes: the Thomson regime for $\epsilon = E_{ph}\, E_e/(m_e\, c^2)^2 \ll 1$ with a cross section of [7]

$$\sigma_{IC,T} \simeq \sigma_T\,(1 - 2\,\epsilon) \simeq \sigma_T = \text{const} \qquad (2.18)$$

and the Klein-Nishina regime for $\epsilon \gg 1$ where relativistic effects make the cross section dropping according to [7]

$$\sigma_{IC,KN} \simeq \frac{3\,\sigma_T\,\ln(4\,\epsilon)}{8\,\epsilon}. \qquad (2.19)$$

Fig. 2.3 illustrates the ratio between the overall IC and the Thomson cross section as function of the energy of the incoming electron for three different ambient photon fields: CMB, diffuse Galactic dust (i.e. IFR), and SL. It can be observed that IC scattering is strongly suppressed for very high incoming electron energies ($>100$ TeV) and that for smaller electron energies and scattering off the CMB, the Thomson cross section is a good approximation. Hence,
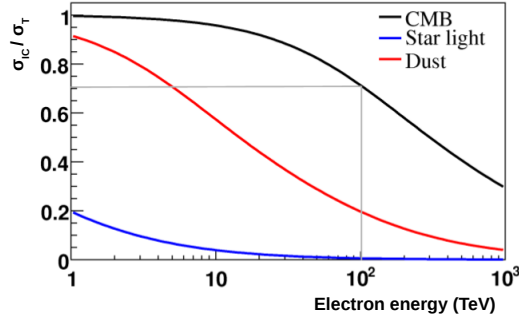
**Figure 2.3** Ratio between the full IC cross section $\sigma_{\mathrm{IC}}$ and the Thomson cross section $\sigma_{\mathrm{T}}$ as function of the energy of the incoming electron for three different ambient photon target fields: CMB, diffuse Galactic dust background, and SL photons. Adapted from [17].

the energy loss of a CR electron due to IC scattering can be approximately described in the Thomson regime. It is given by [16]

$$P_{\mathrm{IC,T}} = -\left(\frac{\mathrm{d}E_{\mathrm{e}}}{\mathrm{d}t}\right) = \frac{4}{3}\, c\, \sigma_{\mathrm{T}} \left(\frac{E_{\mathrm{e}}}{m_{\mathrm{e}}c^2}\right)^2 \beta^2 u_{\mathrm{R}}, \tag{2.20}$$

where $u_{\mathrm{R}}$ is the energy density of the ambient radiation field. The energy of the up-scattered photon can then be calculated as [18]

$$E_{\mathrm{IC}} \simeq 33 \left(\frac{E_{\mathrm{e}}}{1\,\mathrm{TeV}}\right)^2 \left(\frac{E_{\mathrm{ph}}}{1\,\mathrm{eV}}\right) \mathrm{TeV}. \tag{2.21}$$

Inserting an electron energy of $E_{\mathrm{e}} = 100$ TeV and the energy of the CMB ($E_{\mathrm{ph}} \sim 6 \times 10^{-4}$ eV) as photon energy results in an energy of the resulting $\gamma$-ray of $\sim 10$ TeV. Hence, 100 TeV electrons are expected to produce 10 TeV $\gamma$-rays in environments where the CMB dominates over other ambient radiation fields.

A comparison of Eq. 2.14 with Eq. 2.20 reveals similarities between the synchrotron emission process (scattering on virtual photons of the $B$-field) and the IC process (scattering on a real photon field):

$$\frac{P_{\mathrm{IC,T}}}{P_{\mathrm{sync}}} = \frac{u_{\mathrm{R}}}{u_{\mathrm{B}}}. \tag{2.22}$$

As a consequence, also the cooling time for IC scattering looks similar [7]

$$\tau_{\mathrm{IC}} = \frac{E_{\mathrm{e}}}{P_{\mathrm{IC}}} \simeq 3 \times 10^5 \left(\frac{u_{\mathrm{R}}}{1\,\mathrm{eV/cm^3}}\right)^{-1} \left(\frac{E_{\mathrm{e}}}{1\,\mathrm{TeV}}\right)^{-1} \mathrm{yr} \tag{2.23}$$

and both spectra exhibit the same shape, i.e. also for IC scattering it holds that

$$\alpha_\gamma = \frac{\alpha_{\mathrm{e}} + 1}{2}. \tag{2.24}$$

Furthermore, following the same argument as above for synchrotron radiation, due to the $m^{-4}$ dependence of $P_{\mathrm{IC,T}}$, the energy loss-rate of protons due to IC scattering is suppressed by a factor of $\sim 10^{13}$ compared to electrons, making this process less important for hadrons.

a          b          c
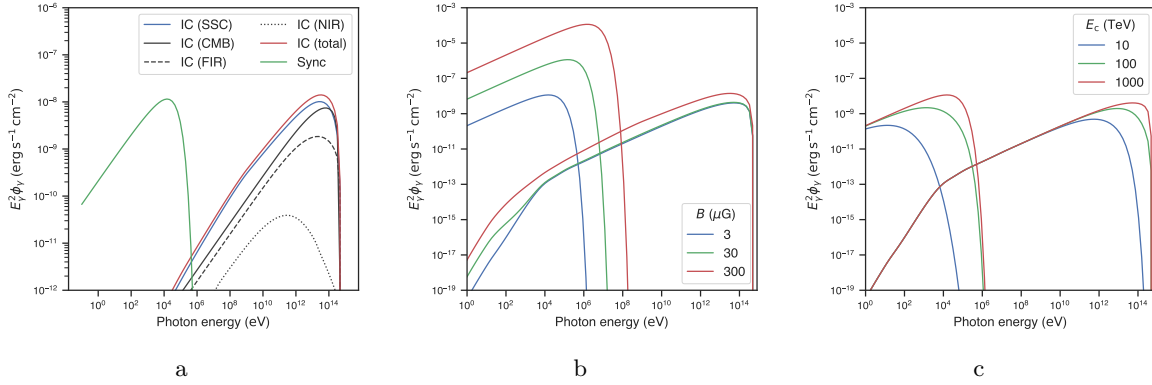
**Figure 2.4** Modelling of SEDs using the Python package `naima` [19] for an electron population with a spectrum of $\Phi_{\mathrm{e}}(E_{\mathrm{e}}) = \Phi_0 \left(\frac{E_{\mathrm{e}}}{1\,\mathrm{TeV}}\right)^{-2} \exp\left(-\frac{E_{\mathrm{e}}}{E_{\mathrm{c,e}}}\right)$ (a) with $E_{\mathrm{c,e}} = 1$ PeV, a magnetic field strength of 3 $\mu$G and showing the different components contributing to the IC emission being ambient radiation fields, such as CMB ($T = 2.72$ K, $u_{\mathrm{R}} = 0.261$ eV/cm$^3$), near infrared (NIR) ($T = 30$ K, $u_{\mathrm{R}} = 0.5$ eV/cm$^3$), and far infrared (FIR) ($T = 3000$ K, $u_{\mathrm{R}} = 1$ eV/cm$^3$), as well as SSC, (b) with $E_{\mathrm{c,e}} = 1$ PeV showing the influence of different magnetic field values, and (c) with different $E_{\mathrm{c,e}}$ at a typical Galactic magnetic field value of 3 $\mu$G.

**Synchrotron self-Compton scattering**   Synchrotron self-Compton (SSC) scattering happens when not the ambient radiation field like CMB, IFR, or SL but the emitted photons from synchrotron radiation act as the seed radiation field for IC scattering. In general, the SSC additionally contributes to the IC scattering off the ambient (thermal) radiation fields. The strength of this contribution depends on the characteristic of the source region ($B$-field, cutoff energy of the underlying electron population, energy density of the ambient radiation fields, etc.). Fig. 2.4a shows a modelled SED where the SSC contributes the most to the overall IC emission.

**Relation between synchrotron radiation and IC scattering**   If both, synchrotron and IC radiation are emitted by the same population of electrons, their spectra are expected to be strongly correlated. If considering the CMB as the dominant ambient radiation field with $E_{\mathrm{CMB}} \simeq 6 \times 10^{-4}$ eV, combining Eq. 2.15 and 2.21 results in

$$E_{\mathrm{syn}} \simeq 0.07 \left(\frac{E_{\mathrm{IC}}}{1\,\mathrm{TeV}}\right) \left(\frac{B}{10\,\mu\mathrm{G}}\right)\,\mathrm{keV}. \tag{2.25}$$

Furthermore, from Eq. 2.22 it follows that the ratio of the corresponding energy fluxes $f(E)$ is given by

$$\frac{f_{\mathrm{IC}}(E)}{f_{\mathrm{sync}}(E)} = \frac{u_{\mathrm{R,CMB}}}{u_B} \simeq 0.1 \left(\frac{B}{10\,\mu\mathrm{G}}\right)^{-2}. \tag{2.26}$$

This means that (1) the peak of the synchrotron radiation typically lies at lower photon energies than the peak of the IC radiation and (2) the synchrotron radiation exhibits a larger flux than the IC radiation for all magnetic field strengths above the average ISM value of $B \simeq (2-5)\,\mu$G. Fig. 2.4b and 2.4c illustrate the interplay of synchrotron and IC radiation for different $B$-field values and cutoff energies $E_{\mathrm{c,e}}$ of the electron spectrum. The latter one just shifts the synchrotron and IC peak to higher photon energies since higher energy electrons also emit higher energy photons.
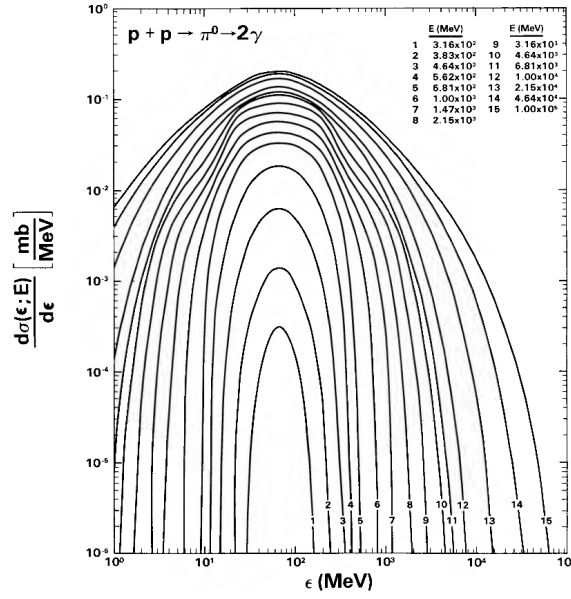
**Figure 2.5** Differential cross section for the $\gamma$-ray production from the decay of $\pi^0$ particles produced in collisions of isotropic, mono-energetic protons with protons at rest. Shown are scenarios with a variety of proton kinetic energies. Reproduced from [20].

### 2.1.2.2 Hadronic processes

Inelastic hadronic interactions, such as collisions of a CR proton with a proton or nucleus of the ISM often results – amongst others – in the production of both, charged and neutral pions, roughly produced in the same quantities. The minimum kinetic energy of the CR proton required for the production of neutral pions, resulting from energy and momentum conservation, is given by

$$E_{\mathrm{kin,m}} = \frac{(2m_{\mathrm{p}}c^2 + m_{\pi}c^2)^2 - 2m_{\mathrm{p}}^2 c^4}{2m_{\mathrm{p}}c^2} = 2m_{\pi}c^2 + \frac{m_{\pi}^2}{2m_{\mathrm{p}}}c^2 = 280\,\mathrm{MeV}, \qquad (2.27)$$

with the proton mass $m_{\mathrm{p}} = 938$ MeV/c$^2$ and the pion mass $m_{\pi} = 135$ MeV/c$^2$. The charged pions decay into muons and neutrinos via weak interaction and then further into electrons and neutrinos

$$\begin{aligned}
\pi^+ &\to \mu^+ + \nu_\mu \to e^+ + \overline{\nu_\mu} + \nu_e + \nu_\mu \\
\pi^- &\to \mu^- + \overline{\nu_\mu} \to e^- + \nu_\mu + \overline{\nu_e} + \overline{\nu_\mu}.
\end{aligned} \qquad (2.28)$$

Hence, detection of neutrinos from a certain source provide a smoking gun for identification of hadronic interactions and thus for the underlying CR population to be of hadronic origin. The neutral pions undergo an electromagnetic decay into photons

$$\pi^0 \to \gamma + \gamma. \qquad (2.29)$$

In the rest frame of the neutral pion, both photons are emitted with the same energy of $m_{\pi}c^2/2 = 67.5$ MeV and in exactly opposite direction. Due to the transferred kinetic energy from the proton on the pion, a Lorentz transformation of this decay results in a photon energy spectrum with a distinct bell-type feature, referred to as "$\pi^0$-decay-bump", symmetrically distributed around $m_{\pi}c^2/2$ (cf. Fig. 2.5). Due to the convolution with the underlying hadronic CR spectrum, the exact shape of the $\pi^0$-decay-bump and its position vary, typically

lying between 100 MeV and a few GeV [21]. The observed photons resulting from $\pi^0$-decay can have energies in the VHE $\gamma$-ray regime especially in regions of dense gas and ambient material, i.e. high abundance of ISM hadrons, and relativistically moving protons.

## 2.2 Sources of cosmic and gamma rays

A variety of source candidates for CRs and $\gamma$-rays exists. Sec. 2.2.1 gives an overview including basic constraints. Astronomic objects, CR acceleration and/or $\gamma$-ray emission has been observed for or is expected from, are presented in Sec. 2.2.2.

### 2.2.1 Overview and basic constraints

A very basic but essential constraint for CR acceleration was given by A.M. Hillas in 1984. It relates the velocity of the shock front $\beta_s$ (in units of $c$), in which vicinity the particles with charge $Z\,e$ are accelerated, with the maximum achievable particle energy $E_{max}$, the object size $R_s$, and the magnetic field strength $B$ [22]. This is the so-called Hillas condition, given by

$$E_{max} = 3\,e\,Z\,B\,\beta_s\,R_s. \tag{2.30}$$

Fig. 2.6a shows a visualisation of this condition overplotted with typical sizes and magnetic fields of several astronomical objects. According to that, CR hadrons with $E \simeq 10^{20}$ eV can only be accelerated by a very efficient mechanism (with $\beta_s \sim 1$) in very extreme objects such as neutron stars (NSs), active galactic nuclei (AGNs), and jets of radio galaxies. CR hadrons with those energies and energies down to $10^{17} - 10^{18}$ eV are expected to be mostly of extragalactic origin [25] while CRs with energies below the knee are expected to origin from sources in our Galaxy.

A bunch of theories exist explaining the origin of the knee. It could for example reflect the the fact that most cosmic accelerators in the Galaxy have reached their maximum energy while effects of propagation and confinement in the Galaxy [26] also need to be considered[3]. To be able to prove or disprove the different scenarios for the knee, finding the sources accelerating hadronic CRs to PeV energies – so-called PeVatrons – is crucial. Fig. 2.6a suggests a handful PeVatron candidates, such as SNRs. They are very prominent PeVatron candidates since their characteristics, such as provided power and resulting CR spectrum as well as lifetime, match expectations from theoretical considerations (cf. Sec. 2.2.2.1).

The identification of sources in general and of PeVatrons in particular is impossible using CR detection experiments only since CRs loose their direction information due to deflection in interstellar magnetic fields when propagating to Earth. This is where VHE $\gamma$-ray detection can help. The higher the CR energy, the higher also the expected energy of $\gamma$-rays emitted from a certain source. However, when propagating through the universe, $\gamma$-rays interact with diffuse background radiation via pair production ($\gamma + \gamma_{background} \longrightarrow e^+ + e^-$) strongly decreasing their horizon. Fig. 2.6b shows the mean free path $\lambda$ for $\gamma$-rays as function of their primary energy. It can be inferred that the detection of $\gamma$-rays from extragalactic sources (typical distances > 1–10 MPc) is only possible either in the low VHE or in the high UHE band (with energies > $10^{20}$ eV [4]). This also means that the predominant majority of $\gamma$-rays detected in the mid and high VHE band, i.e. at TeV energies, are expected to originate

---

[3]A discussion of a variety of models for the knee can be found in [27].

[4]Observation of photons of those energies are neither expected from theoretical models nor accessible by current instruments. However, the most stringent limits so far for the detection of $\gamma$-rays at $\sim 10^{18}$ eV have been set by measurements with the Pierre Auger Observatory, cf. [28] for further details.
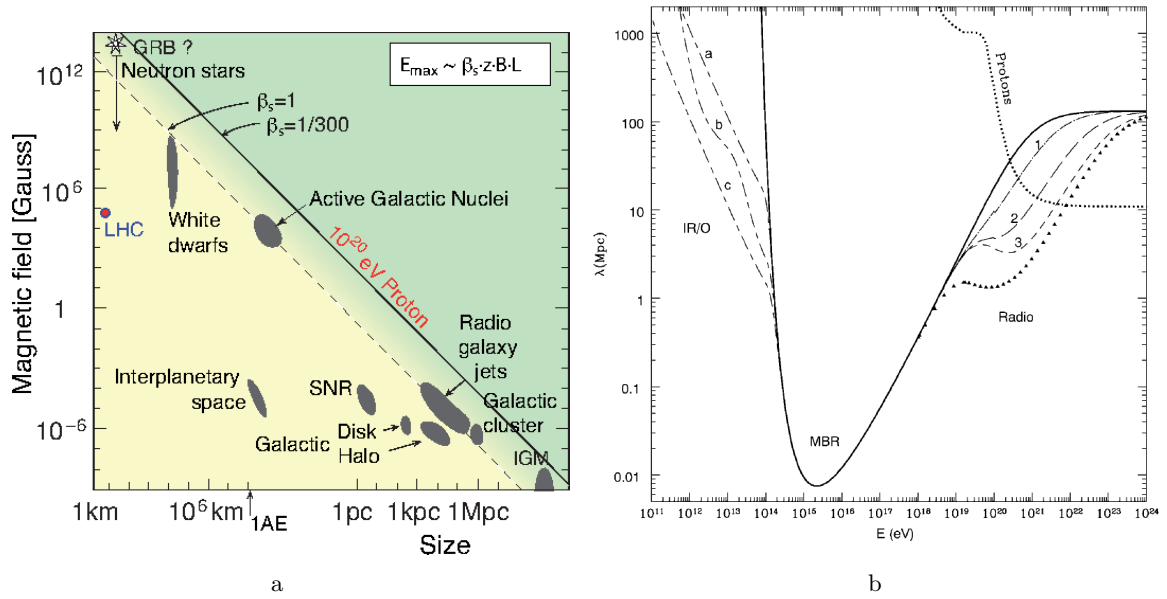
**Figure 2.6** (a) Visualisation of the Hillas condition showing the size and magnetic field strength of astronomical objects acting as possible sites for particle acceleration. Objects below diagonal lines cannot accelerate protons up to $10^{20}$ eV for $\beta_s = 1$ (dashed line) and $\beta_s = 1/300$ (solid line). Furthermore, the position of the LHC is also indicated (adapted from [23], originally from [22]). (b) Local pair-production mean free path $\lambda$ for VHE photons of energy $E$ at redshift $z = 0$ (no cosmological effects included). Below $10^{14}$ eV, VHE photons interact primarily with infrared and optical (IR/O) photons, above $10^{19}$ eV, they interact with radio photons, between $10^{14}$ and $10^{19}$ eV, they interact with CMB ($\equiv$MBR) photons. Curves a, b, and c show $\lambda$ for the IR/O backgrounds for different galaxy formation scenarios. Curves 1, 2, and 3 show $\lambda$ for the extragalactic radio background estimate with a low-frequency cutoff at 5, 2, and 1 MHz. The triangles give the lower limit on $\lambda$ obtained assuming the total observed radio background is extragalactic. The heavy dotted line shows the energy-loss mean free path for energetic protons. Further details are given in [24] where this graphic is adapted from.

from our Galaxy. At those energies, a number of Galactic sources (mostly SNRs) are well-established $\gamma$-ray emitters [29] but current observations do not allow (yet) to clearly identify whether only hadronic or leptonic CRs or even a combination of both are responsible for the $\gamma$-ray signals from them. However, since $\sim$PeV protons expect to produce $\sim$100 TeV photons [3] and since the leptonic emission is strongly suppressed at $\gamma$-ray energies $> 10$ TeV due to reduced IC losses in the Klein-Nishina regime (cf. Sec. 2.1.2.1), detection of $\gamma$-rays at energies exceeding 10 TeV could give rise to the identification of PeVatrons[5].

## 2.2.2 Examples

As shown by Fig. 2.6a, several source candidates for Galactic PeVatron exist. The most famous candidates are remnants of supernova (SN) explosions, presented in Sec. 2.2.2.1. However, over the last decade, the space- and ground-based $\gamma$-ray telescopes have revealed many classes of Galactic $\gamma$-ray source populations. Some of them may be considered as com-

---

[5]However, $\gamma$-rays with energies of the order of 100 TeV have already been observed from pulsar wind nebulae (PWNe), known to be leptonic accelerators (cf. Sec. 2.2.2.2), such as Geminga [30]. Hence, detection of $\gamma$-rays with energies exceeding 10 TeV can only provide an indication and not a proof for a source to be a PeVatron.
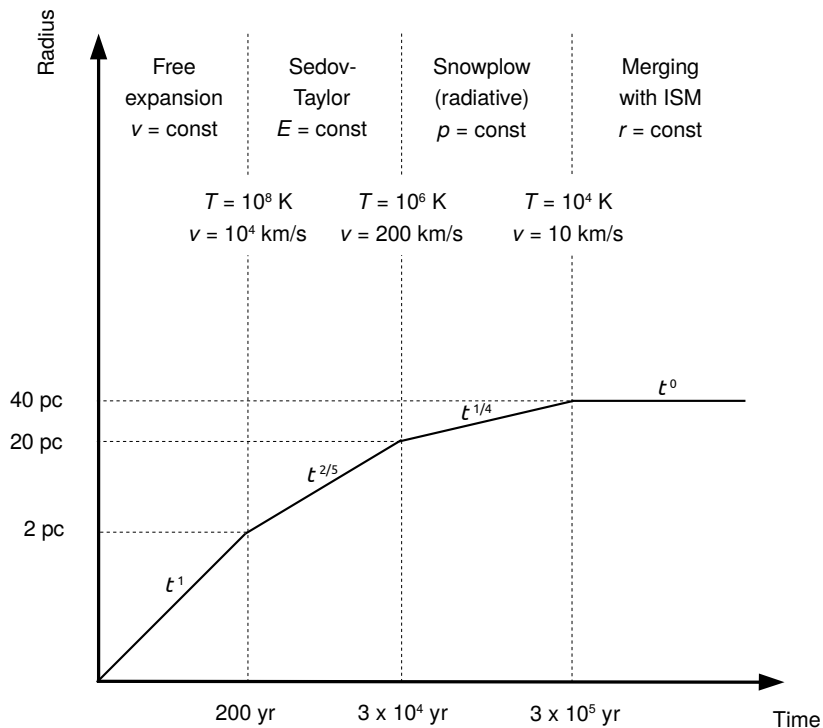
**Figure 2.7** An illustration of the four different phases in the SNR dynamics. Typical timescales and sizes as well as rough estimates for the temperature and velocity at the end of each phase are given. Reproduced from [32].

plementary or alternative hadronic CR factories. Of particular interest are SCs introduced in Sec. 2.2.2.3. $\gamma$-ray emission is also expected from molecular clouds (cf. Sec. 2.2.2.4), especially if there are in the vicinity of hadronic CR acceleration sites. They typically contain a lot of interstellar material able to serve as seeds for $\gamma$-ray production due to the inelastic scattering of CR hadrons off it.

However, as $\gamma$-rays can also be produced by leptonic processes, the identification of a $\gamma$-ray source as a CR PeVatron is often hindered by the compatibility of the observation with scenarios of leptonic production processes. Known sources with leptonic $\gamma$-ray origin and accounting for the largest proportion of Galactic objects in the TeV sky, are PWNe (cf. Sec. 2.2.2.2), with the Crab Nebula being their most prominent representative.

### 2.2.2.1 Supernova remnants

The life of a star with $M_* > 8\,M_\odot$ is expected to typically end with an SN, releasing about 10% of the rest mass of the star (typically $\sim 3 \times 10^{53}$ erg [31]), with most of it ($\sim 99\%$) carried away by the neutrinos produced during the SN. The remaining $\sim 1\%$ is believed to be transferred onto the ejected material expanding into the ISM with typical velocities of a few 1000 km/s. The combination of this material, swept up ambient gas, shock fronts, and turbulent magnetic fields constitute the so-called SNR. SNRs are expected to run through different evolutionary states with according characteristics (cf. Fig. 2.7). Those sates and characteristics are presented as they are expected by the well-established SNR evolution theory:

1. The *free-expansion* or *ejecta-dominated phase* begins with the SN explosion. In this phase, the SNR shell expands at constant, supersonic velocity [31]

$$v_{\text{shell}} \simeq 1 \times 10^4 \left( \frac{M_\odot}{M_{\text{ejecta}}} \right)^{1/2} \text{km/s} \tag{2.31}$$

($M_{\text{ejecta}}$ being the mass of the ejecta) and sweeps up the surrounding ISM. Given the constant velocity, the radius of the shell is given by

$$R_{\text{shell}} = v_{\text{shell}} \, t \propto t. \tag{2.32}$$

Due to the supersonic expansion of the shell, a discontinuity in pressure and density occurs resulting in a shock front preceding the ejecta. The ambient ISM with mass $M_{\text{ISM,shocked}}$ gets accelerated, compressed, and heated by this shock. Since $M_{\text{ISM,shocked}} \ll M_{\text{ejecta}}$, the shock is not influenced by the ISM which is why $v_{\text{shell}}$ is constant.

2. During the further expansion of the ejecta, more and more ISM material is swept up. After a characteristic time, of [31]

$$t_{\text{ST}} \simeq 220 \left( \frac{M_{\text{ejecta}}}{M_\odot} \right)^{5/6} \left( \frac{n_{\text{ISM}}}{1\,\text{cm}^{-3}} \right)^{-1/3} \left( \frac{E_{\text{ejecta}}}{10^{51}\,\text{erg}} \right)^{-1/2} \text{yr}, \tag{2.33}$$

with $n_{\text{ISM}}$ being the number density of the surrounding ISM and $E_{\text{ejecta}}$ the initial energy of the ejected mass, the mass of the swept-up material becomes comparable to the ejected mass, i.e. $M_{\text{ISM,shocked}} \simeq M_{\text{ejecta}}$. This ushers in the so-called *adiabatic* or *Sedov-Taylor phase* (with $t_{\text{ST}} \simeq \mathcal{O}(100\,\text{yr})$) and causes the SNR to slows down, resulting in a reverse shock travelling backwards into the ejecta. The velocity of the shell in this phase is given by [31, 33]

$$v_{\text{shell}} \simeq 1950 \left( \frac{n_{\text{ISM}}}{1\,\text{cm}^{-3}} \right)^{-1/5} \left( \frac{E_{\text{ejecta}}}{10^{51}\,\text{erg}} \right)^{1/5} \left( \frac{t}{10^3\,\text{yr}} \right)^{-3/5} \text{km/s} \tag{2.34}$$

and the radius by

$$R_{\text{shell}} \simeq 1.54 \times 10^{19} \left( \frac{n_{\text{ISM}}}{1\,\text{cm}^{-3}} \right)^{-1/5} \left( \frac{E_{\text{ejecta}}}{10^{51}\,\text{erg}} \right)^{1/5} \left( \frac{t}{10^3\,\text{yr}} \right)^{2/5} \text{cm}. \tag{2.35}$$

3. The *radiative phase* begins when the temperature in the region behind the shock front (referred to as downstream) begins to drop below $10^6$ K. In this phase, radiative cooling by line emission of heavy ions becomes important resulting in a further decrease of the expansion speed with $R_{\text{shell}}(t) \propto t^{1/4}$.

4. After a typical timescale of $10^5$ yr, the expansion becomes subsonic resulting in the remnant merging with the surrounding ISM.

Beside the fact that SNRs have been observed to contain shock fronts, believed to be very efficient particle accelerators and in combination with diffusion theory able to reproduce the observed CR spectrum on Earth (cf. Sec. 2.1.1), another main argument for SNRs to be source candidates for Galactic cosmic rays (GCRs) results from global energetic considerations. Star formation and evolution theory as well as observations predict approximately three SNe per decade in our Galaxy, i.e. $\Delta t_{\text{SN}} \simeq 33$ yr. As mentioned above, the typical energy expected

to be transferred from an SN onto the SNR is $E_{\mathrm{SNR}} \simeq 10^{51}$ erg. This results in an expected power of all Galactic SNRs of

$$P_{\mathrm{SNR}} = \frac{E_{\mathrm{SNR}}}{\Delta t_{\mathrm{SNR}}} \simeq 10^{42}\,\mathrm{erg/s}. \tag{2.36}$$

On the other hand, the measured mean energy density in GCRs is $\omega_{\mathrm{GCR}} \simeq 0.5$ eV/cm$^3$ [31]. With the typical time CRs are believed to remain in our Galaxy of $\tau_{\mathrm{GCR}} \simeq 2 \times 10^7$ yr (determined for example from ratio observations of $^{10}$Be/$^9$Be) and the volume of our Galaxy $V_{\mathrm{gal}} \simeq 5 \times 10^{67}$ cm$^3$, the required power to reproduce the observed GCR energy density is calculated to be

$$P_{\mathrm{GCR}} = \frac{\omega_{\mathrm{GCR}}\, V_{\mathrm{gal}}}{\tau_{\mathrm{GCR}}} \simeq 10^{41}\,\mathrm{erg/s}. \tag{2.37}$$

Hence, SNRs are expected to be able to power GCRs in case at least about 10% of their energy is transferred to CRs.

Observations conducted in HE and VHE $\gamma$-ray bands in the last decade generally confirm the effective acceleration of CRs in SNRs. However, no SNR has been confidentially confirmed as a PeVatron yet due to the compatibility of the observations with leptonic scenarios (such as PWNe, cf. next subsection) or due to observed cutoffs in the SED at energies below 10 TeV.

### 2.2.2.2  Pulsars, magnetars, and pulsar wind nebulae

Depending on the mass of the stellar core that remains after an SN, either an NS (for masses smaller than the Oppenheimer-Volkov limit [34] of $\sim$3 $M_\odot$) or a stellar black hole is expected to form.

**Neutron stars, magnetars, and pulsars**  NSs are very compact objects with masses $m \simeq M_\odot$, radii of some tens of kilometres, and densities of $\sim$10$^{14}$ g/cm$^3$, being the typical density of atomic nuclei. Furthermore, they are observed to have magnetic fields $B$ in the order of 10$^8$–10$^{15}$ G with their origin not yet being fully understood (cf. e.g. [35]). Due to angular momentum conservation between the progenitor star and the NS, NSs rotate very fast with typical periods $P$ between 0.01 and 1 s. Near the magnetic poles, particles are believed to be accelerated resulting in electromagnetic radiation. In case the magnetic and rotational axes are not aligned, this radiation is emitted as pulses which can be detected at a frequency corresponding to the NS rotation period whenever the magnetic axis points towards the Earth[6]. An NS showing such as pulsed emission is therefore also referred to as pulsar. Due to the energy transferred into radiation, NSs slow down over time with the so-called spin-down rate $\dot{P}$ being the decrease in period per period, typically given in units of s/s. $\dot{P}$ can be used to estimate the characteristic age[7] [37]

$$\tau \equiv \frac{P}{2\dot{P}}, \tag{2.38}$$

the spin-down power

$$\dot{E} \equiv 4\pi I \frac{\dot{P}}{P^3} \tag{2.39}$$

---

[6]This is how NSs were detected in the first place in 1967 [36].

[7]The characteristic age gives an estimate for the true age of a pulsar. However, this formula is only valid under a few assumptions such as that the initial spin period was very much smaller than the one observed today. Since this is not the case for young pulsars, $\tau$ is somewhat larger than the true age for those pulsars.

(with $I$ being the moment of inertia), and the magnetic field

$$B = 3.2 \times 10^{19} \sqrt{\frac{P}{1\,\mathrm{s}} \dot{P}}\,\mathrm{G}. \tag{2.40}$$

With the values for $\dot{E}$ and $\tau$, the total energy released in the life time of a pulsar, given by

$$E_{\mathrm{rel}} = \dot{E}\,\tau, \tag{2.41}$$

can be estimated. For most pulsars, $\dot{E}$ is comparable to the measured electromagnetic luminosity $L$ which is why it is believed that the radiation is powered by the rotational kinetic energy of the NS.

However, a class of NSs exists showing $B$-fields exceeding $10^{13}$ G and luminosities exceeding the spin-down power by a factor of $\sim 100$. Their emission is therefore believed to be mainly powered by the decay of enormous internal magnetic fields, which is why they were named "magnetars" [38]. Up to now, 29 astronomical sources have been identified as magnetars. In general, they are proposed to form from NSs rotating with a period of $\sim 1$ ms at birth, which assists a fast dynamo [38]. In this picture, an NS with $B > 10^{14}$ G and spinning at 1 ms would very quickly loose most of its rotational energy. This would result in an energy release in the order of $10^{52}$ erg [37], greater than the SN energy itself. Hence, magnetars would very likely be associated with either anomalously large shell SNRs or no SNR at all, in case it expanded fast enough to dissipate on a few hundred year time scale. Eight of the 23 confirmed magnetars are reliably associated with SNR shells. The shells do not show unusual properties what challenges the dynamo model and triggered discussions about new theories for the formation of the strong $B$-fields of magnetars (e.g. [39] about the magnetars' $B$-field resulting from strong fossil fields from the progenitor star).

**Pulsar wind nebulae** Particles escaping from the vicinity of the pulsar as part of the supersonic pulsar wind may form a wind termination shock in the surrounding region, where medium is less dense, having been effectively evacuated due to the SN forward shock. In this termination shock, they can undergo diffusive shock acceleration, gaining energy on each shock crossing (cf. Sec. 2.1.1), and resulting in a so-called PWN with highly energetic particles (mostly electrons) gradually growing. After a certain time, the reverse shock from the SNR will meet the PWN, leading to a crushing effect. This is accompanied by a corresponding increase in the magnetic field, causing an increase in the synchrotron energy losses of the electrons. The crushing also causes an increased pressure in the region which may result in an increase of the expansion speed of the PWN (when the pressure surpasses that of the reverse shock). PWNe typically undergo several reverberations before the shock strength fades. As the SNR dissipates, the PWN continues to form whereas at this stage, due to the pulsar's net drift velocity at its birth and asymmetric crushing effects, the nebula may be significantly distorted and offset from the current pulsar position and the original site of the supernova explosion.

The upper limit for the total electron energy in a PWN is given by the total energy released by the pulsar (cf. Eq. 2.41). This value may be compared to the total electron energy observed in the vicinity of a PWN

$$W_{\mathrm{e}} = L_\gamma\,\tau_{\mathrm{cool}}, \tag{2.42}$$

deduced from the observed $\gamma$-ray luminosity $L_\gamma$ and cooling time of the electrons $\tau_{\mathrm{cool}}$. The latter is given by the reciprocal sum of the dominant electron cooling processes in a given

scenario. For a PWN, these are typically synchrotron radiation and IC, hence

$$\frac{1}{\tau_{\text{cool}}} = \frac{1}{\tau_{\text{sync}}} + \frac{1}{\tau_{\text{IC}}}. \tag{2.43}$$

From $\tau \propto E_{\text{e}}^{-1}$ (cf. Eq. 2.17 & 2.23), $d \propto \sqrt{D(E)\,\tau}$ (cf. Eq. 2.8), and $D(E_{\text{e}}) \propto E_{\text{e}}^{\delta}$ (cf. Eq. 2.9), it follows that

$$d(E_{\text{e}}) \propto E_{\text{e}}^{(\delta-1)/2}, \tag{2.44}$$

where $d$ is the distance electrons travel within the cooling time. Since $\delta < 1$, the typical distances electrons can travel before they have lost a significant amount of their energies decreases with energy. This is why PWNe typically decrease in their size with increasing energy.

### 2.2.2.3 Massive stellar clusters

Massive stars are believed to form in groups inside giant molecular clouds (GMCs) often ending as dense gravitationally bound SCs [40]. Interactions between the stars resulting in colliding wind binaries – $\sim$70% of massive stars are found to be bound within binary systems [41] – and collective stellar winds as well as SN explosions inside SCs are expected to give rise to the formation of acceleration sites for CRs.

**Stellar winds**   The total stellar wind energy, integrated over a massive star's lifetime, amounts typically to $10^{51}$ erg and is therefore comparable to the final SN explosion energy itself [42]. Furthermore, the total stellar wind luminosity of all massive stars in the Galaxy is estimated to be $\sim$1.1 $\times 10^{41}$ erg/s [43] which is about 1/10–1/4 of the power of all Galactic SNRs. Assuming that 1–10% of the wind luminosity may be converted to GCRs through collisionless shocks such as termination shocks in superbubbles (SpBs), colliding-wind shocks in binaries, and bow-shocks of massive runaway stars, stellar winds may contribute significantly to the production of GCRs.

   In a SC, each massive star blows a steady wind with a typical average power of

$$L_{*,\text{wind}} \simeq 3 \times 10^{36}\ \text{erg/s} \tag{2.45}$$

into a homogeneous medium of density $n \simeq 10^2\ \text{cm}^{-3}$ which is the typical average density for the parent GMC. According to standard wind bubble theory [44], the radius of the external shock in the semi-adiabatic phase resulting from the wind is given by [42]

$$R_{\text{ext}} \simeq 13 \left(\frac{t}{10^6\,\text{yr}}\right)^{3/5} \left(\frac{L_{\text{wind}}}{3 \times 10^{36}\,\text{erg/s}}\right)^{1/5} \left(\frac{n}{10^2\,\text{cm}^{-3}}\right)^{-1/5}\ \text{pc}. \tag{2.46}$$

This is significantly larger than the typical mean half-distance between massive stars in an SC given by [42]

$$R_* \simeq 6 \left(\frac{R_{\text{SC}}}{35\,\text{pc}}\right) \left(\frac{N_{\text{SC}}}{100}\right)^{-1/3}\ \text{pc}, \tag{2.47}$$

with $R_{\text{SC}}$ being the SC radius and $N_{\text{SC}}$ the number of stars in the SC. Hence, the individual wind bubbles are not only expected to collide but also to merge. In this way a large, collective bubble, a so-called SpB, expanding almost spherically around the whole SC should form during the first million year of stellar activity in the SC.

   The energy release inside an SpB is not continuous and experiences strong peaks, e.g. in case of a transformation of an OB into a Wolf-Rayet star or in case of an SN inside the SC.

However, for sufficiently evolved SCs (after a few Myr) such variations of the driving power are expected to be smoothed out since the shells of the individual SNe or stellar wind shocks typically become subsonic before they reach the so-called supershell, being the shell of the SpB. Hence, the released energy in an SN or by a stellar wind is transferred into internal energy of the SpB before it can have direct influence on the supershell dynamic [42]. The SpB interior thus acts as a buffer which absorbs the rapid variations of the input power. The whole SpB can therefore be treated as a very large wind bubble with a superwind power of

$$L_{\mathrm{SC,wind}} = \sum L_{*,\mathrm{wind}}.$$ (2.48)

The radius $R_{\mathrm{SpB}}$ of the SpB is given by [45]

$$R_{\mathrm{SpB}} = 267 \left( \frac{L_{\mathrm{SC,wind}}}{10^{38}\,\mathrm{erg/s}} \right)^{1/5} \left( \frac{n_0}{1\,\mathrm{cm}^{-3}} \right)^{-1/5} \left( \frac{t}{10^7\,\mathrm{yr}} \right)^{3/5},$$ (2.49)

with $n_0$ being the external ISM density. The density inside the SpB is typically much lower and can be described by a simplified model given by [42]

$$n_{\mathrm{SpB}}(r) \simeq 4.0 \times 10^{-3} \left( \frac{L_{\mathrm{SC,wind}}}{10^{38}\,\mathrm{erg/s}} \right)^{6/35} \left( \frac{n_0}{1\,\mathrm{cm}^{-3}} \right)^{19/35} \left( \frac{t}{10^7\,\mathrm{yr}} \right)^{-22/35} \left( 1 - \frac{r}{R_{\mathrm{SpB}}} \right)^{-2/5} \mathrm{cm}^{-3}$$ (2.50)

with $r$ being the radial distance to the SpB centre. Hence, a void is expected to be observed in the gas distribution inside the bubble.

Due to the steadiness of the stellar winds, CRs are expected to be continuously injected at the SC position and then to diffuse away in the ISM. Hence, a $1/r$-dependence of the radial CR distribution is expected.

**Supernovae in stellar clusters**  Since massive stars with masses $M \geq 8\,M_\odot$ undergo SN explosions after a few Myr, such explosions are also expected in SCs with an age of a few Myr or more. Contrary to the case of isolated SNRs, SpB environments offer a unique opportunity to use not only the SN explosion energy, but also the energy of the strong stellar winds. Due to the lower density in the SpB than in the ISM, the SNR shell is not only expected to grow quicker than the shell of isolated SNRs but also to become subsonic and to merge with the surrounding ISM before becoming radiative (different to isolated SNRs, cf. Sec. 2.2.2.1). Hence, a higher fraction of the SNR energy may be turned into the internal energy of the SpB and be available for acceleration of particles to very high energies.

Inside an SpB with an age $t_{\mathrm{SpB}}$, the SNR enters the Sedov-Taylor phase after a typical time of [42]

$$t_{\mathrm{ST}} \simeq 13 \left( \frac{M_{\mathrm{ejecta}}}{10\,M_\odot} \right)^{5/6} \left( \frac{t_{\mathrm{SpB}}}{10^7\,\mathrm{yr}} \right)^{0.21} \left( \frac{E_{\mathrm{ejecta}}}{10^{51}\,\mathrm{erg}} \right)^{-1/2} \mathrm{kyr}.$$ (2.51)

The radius of the SNR with an age $t_{\mathrm{SNR}}$ is then given by [42]

$$R_{\mathrm{SNR}} \simeq 38 \left( \frac{t_{\mathrm{SNR}}}{10^4\,\mathrm{yr}} \right)^{2/5} \left( \frac{t_{\mathrm{SpB}}}{10^7\,\mathrm{yr}} \right)^{0.126} \mathrm{pc}.$$ (2.52)

**Summary and implications**  SCs are suggested to be sources of GCRs. Determinations of their basic properties may indicate what fraction of kinetic energy of the stellar winds may be transferred to non-thermal particles and therefore what VHE $\gamma$-ray luminosity to expect. An obvious property is the total SC mass determining the number of massive stars and hence

the total available mechanical energy in stellar winds and expanding SNR shells, if present. The SC age further implies the expected number of massive stars that already evolved into SNe. Finally the fraction of massive stars bound in binary systems defines the contribution from colliding wind binaries.

Due to the available power from stellar winds and SNRs, SCs (and their corresponding SpBs) may be able to accelerate CRs up to PeV energies making them potential PeVatron candidates. VHE $\gamma$-ray observations with H.E.S.S. from the direction of Wd1, which is the most massive SC in our Galaxy, may constrain such a scenario (cf. Ch. 9).

### 2.2.2.4 Molecular clouds

As explained in Sec. 2.1.2.2, inelastic scattering of hadronic CRs off gas of the ISM, mainly consisting of atomic and molecular hydrogen, results in $\gamma$-ray emission. While the atomic hydrogen (HI) is quite uniformly distributed in the Galaxy with a higher abundance in the Galactic plain, molecular hydrogen ($H_2$) is typically aggregated in dense clouds. Hence, a particularly intense and localised $\gamma$-ray emission is estimated from such clouds in case hadronic CRs are present. Thanks to its dipole moment, HI can be directly observed by radio telescopes through the characteristic 21 cm line ($\sim 1.4$ GHz)[8]. In contrast to that, the symmetric $H_2$ molecule does not radiate in the radio range. However, the asymmetric $^{12}CO$ molecule, being the second-most abundant molecule in the ISM after $H_2$, is excited to the first rotational level by collisions with $H_2$ molecules [46]. Hence, the $H_2$ abundance is estimated from the measured $^{12}CO$ abundance via the $^{12}CO$ (1-0) emission line[9]. Expressions for quantitative estimations of HI and $H_2$ column densities are given in Sec. 2.3.2.

## 2.3 Interpretation of multi-wavelength observations

To conclude on CR source characteristics, such as the underlying CR population (hadronic or leptonic), density, and spatial distribution, a multi-wavelength analysis including observations at other wavelength in addition to VHE $\gamma$-ray observations is required.

### 2.3.1 Cosmic ray population

The morphology of the SED of a source can be used to derive the underlying CR population (leptonic or hadronic) as well as the magnetic field strength. As mentioned in Sec. 2.1.2.1 (especially Eq. 2.25 & 2.26) and shown by Fig. 2.4, the location and height of the synchrotron and IC peak in the SED are related to each other in case they result from the same underlying electron population. If the underlying CRs are of hadronic origin, a $\pi^0$-decay-bump should be observed being independent of the magnetic field strength but instead dependent on the gas distribution within the source. Hence, fitting the observed multi-wavelength data with a leptonic, a hadronic, or a combined model may help to identify the underlying CR population.

### 2.3.2 Hadronic cosmic ray density

The density $\omega_{CR}(\geq 10\,E_\gamma)$ of hadronic CRs with energies $\geq 10\,E_\gamma$ in a certain source region can be calculated from the observed luminosity $L_\gamma(\geq E_\gamma)$ of $\gamma$-rays with energies $\geq E_\gamma$ and

---

[8]Photons are emitted at this wavelength and frequency due to the atomic transition of an electron between the two hyperfine levels of the hydrogen 1s ground state.

[9]For simplicity, $^{12}CO$ (1-0) is referred to as CO throughout the thesis.

the total mass of hydrogen $M_H$ present in the interstellar matter in the region of interest [47]:

$$\omega_{CR}(\geq 10\,E_\gamma) = 1.8 \times 10^{-2} \left(\frac{\eta}{1.5}\right)^{-1} \left(\frac{L_\gamma(\geq E_\gamma)}{10^{34}\,\mathrm{erg\,s^{-1}}}\right) \left(\frac{M_H}{10^6\,M_\odot}\right)^{-1} \mathrm{eV\,cm^{-3}}. \qquad (2.53)$$

$\eta$ is a factor accounting for the presence of nuclei heavier than hydrogen in both CRs and interstellar matter typically lying between 1.5 and 2. $L_\gamma(\geq E_\gamma)$ can be calculated from the observed $\gamma$-ray spectrum on Earth $\Phi_\gamma(E)$ and the distance $d$ to the source via

$$L_\gamma(\geq E_\gamma) = 4\,\pi\,d^2 \int_{E_\gamma}^\infty \mathrm{d}E\,E\,\Phi_\gamma(E). \qquad (2.54)$$

$\omega_{CR}(\geq 10\,E_\gamma)$ can then be compared to the average GCR density of $\sim$0.5 eV/cm$^3$ for $E_{CR} > 1$ GeV or $\sim$0.01 eV/cm$^3$ for $E_{CR} > 1$ TeV [31]. The ratio between measured and average GCR density is the so-called CR enhancement factor $k$ and can be calculated (for all $\gamma$-ray energies $\geq E_\gamma$) from [48]

$$k = \left(\frac{F(\geq E_\gamma)}{1.45 \times 10^{-13}\,\mathrm{cm^{-2}\,s^{-1}}}\right) \left(\frac{M_H}{10^5\,M_\odot}\right)^{-1} \left(\frac{d}{1\,\mathrm{kpc}}\right)^2 \left(\frac{E_\gamma}{1\,\mathrm{TeV}}\right)^{1.75} \qquad (2.55)$$

with $F(\geq E_\gamma)$ being the integrated $\gamma$-ray flux given by

$$F(\geq E_\gamma) = \int_{E_\gamma}^\infty \mathrm{d}E\,\Phi_\gamma(E). \qquad (2.56)$$

The total mass of hydrogen in the region of interest (and used in Eq. 2.53 and 2.55), being the sum of the HI ($M_{HI}$) and H$_2$ ($M_{H_2}$) masses, can be deduced from the observed column density $N_H$, composed of the HI ($N_{HI}$) and H$_2$ ($N_{H_2}$) column densities, and from the solid angle $\Omega$ of the region of interest confined by a range of Galactic latitudes $b$ and longitudes $l$. Hence, the total hydrogen mass in the region of interest is given by

$$M_H = M_{HI} + M_{H_2} = m_H \int \mathrm{d}\Omega\,N_H(\Omega) = m_H \left(\frac{\pi}{180}\right)^2 d^2 \int\int \mathrm{d}l\,\mathrm{d}b\,(N_{HI}(l,b) + 2\,N_{H_2}(l,b)), \qquad (2.57)$$

where $m_H \simeq 1.67 \times 10^{-27}$ kg is the mass of the hydrogen atom. As mentioned in Sec. 2.2.2.4, $N_{HI}(l,b)$ and $N_{H_2}(l,b)$ can be determined from radio observations, where the conversion from measured brightness temperature $T_B(l,b,v)$ (in K) to column density (in cm$^{-2}$) is given

- for HI by [49]

$$N_{HI}(l,b) = 1.823 \times 10^{18}(\mathrm{cm^{-2}\,K^{-1}\,km^{-1}\,s}) \int \mathrm{d}v\,T_B(l,b,v), \qquad (2.58)$$

- for H$_2$ by

$$N_{H_2}(l,b) = X_{CO} \int \mathrm{d}v\,T_B(l,b,v), \qquad (2.59)$$

where $X_{CO}$ is the conversion factor from the actual measured CO brightness temperature to H$_2$ column density being highly dependent on the region of interest. For the Wd1 vicinity, a value of $X_{CO} \simeq 1.5 \times 10^{20}$ s/(cm$^2$ K km) was determined [50].

The velocity band in which to integrate the HI and CO data is typically determined by the expected radial velocity of the region of interest and by features observed in the data itself as function of velocity. In practice, the integrals over velocity as well as Galactic latitude

and longitude are summations determined by the velocity and angular resolution of the given telescope or survey. Furthermore, the brightness temperatures typically have to be corrected for (divided by) an oversampling factor

$$f = \frac{A_{\text{beam}}}{A_{\text{pixel}}},$$

(2.60)

where $A_{\text{beam}}$ is the beam and $A_{\text{pixel}}$ the pixel area, both being characteristics of the radio telescope or survey. The HI and CO data is typically provided in a well-defined data format, called flexible image transport system (FITS) format [51] widely used in the astronomy community. With the information about the telescope or survey characteristics stored in the FITS header, given as keywords (e.g. `BMAJ`), $A_{\text{beam}}$ and $A_{\text{pixel}}$ can be determined from

$$A_{\text{beam}} = 1.333 \, (\texttt{BMAJ}) \, (\texttt{BMIN}) \, \text{deg}^2$$

(2.61)

and

$$A_{\text{pixel}} = (\texttt{CDELT1}) \, (\texttt{CDELT2}) \, \text{deg}^2.$$

(2.62)

# The imaging atmospheric Cherenkov technique

*"The soul without imagination is what an observatory would be without a telescope."*

Henry W. Beecher

The Earth's atmosphere is only transparent for electromagnetic radiation in two specific windows of the spectrum: in the visible (optical) and in the radio regime (cf. Fig. 3.1). While the absorption of $\gamma$- and X-rays by the atmosphere was crucial for the development of life on Earth, it precludes the possibility for direct detection of cosmic $\gamma$-rays using ground-based experiments. However, by going up in the atmosphere using balloons or even to outer space using satellites or spacecrafts, it is possible to directly detect $\gamma$-rays. A variety of experiments were and are still using this approach (e.g. the Vela satellite in the 70s [53] and Fermi-LAT today [54]). However, due to the power-law decrease of the $\gamma$-ray flux with energy and the limited collection area in space (mainly because of costs and technical feasibility), their current upper energy limit is of the order of $\sim$300 GeV. Hence, the VHE $\gamma$-ray regime can only be explored using indirect detection mechanisms based on EAS characteristics and secondary effects such as atmospheric Cherenkov radiation emission. I will explain both, the theory and physics of EASs and atmospheric Cherenkov radiation in detail in Sec. 3.1. Imaging
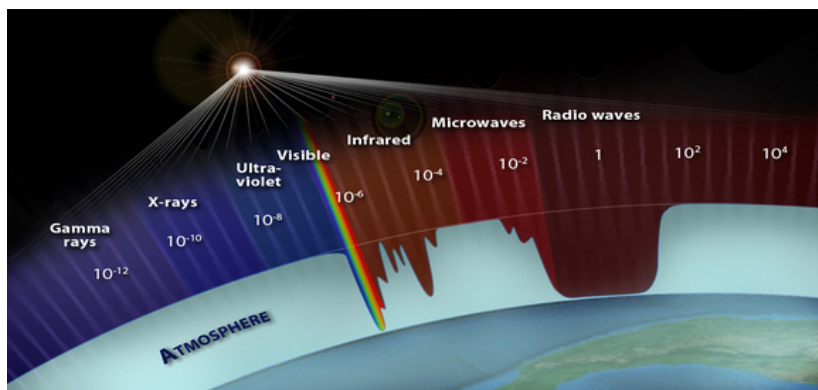


**Figure 3.1** Transmission of the atmosphere for different wavelengths. Adapted from [52].

atmospheric Cherenkov telescopes (IACTs) are used to detect the atmospheric Cherenkov radiation. In Sec. 3.2, I will present their working principle and give examples of two instruments, being H.E.S.S., operating since 2004, and the future CTA observatory. When introducing those experiments, I will focus on the parts that I worked on in the scope of the thesis, i.e. in case of H.E.S.S., the upgraded cameras, referred to as H.E.S.S. IU, and the CHEC camera in case of CTA. Furthermore, I will discuss commonalities between both camera types.

## 3.1 Extensive air showers and atmospheric Cherenkov radiation

A CR or $\gamma$-ray entering the Earth's atmosphere interacts with particles in the air, mainly nitrogen and oxygen nuclei due to their high abundance in comparison to other elements. In those interactions, a variety of other, secondary particles are produced. They travel through the atmosphere towards the Earth's surface, also interacting with other air nuclei producing further particles. Consequently, a cascade with millions of particles is formed, a so-called EAS.

### 3.1.1 Characteristics and physics of extensive air showers

Depending on the primary particle type (hadron or lepton) initiating an EAS, the shower development is different. A lepton-initiated EAS produces electrons and photons by bremsstrahlung and pair production in presence of the Coulomb field of the air nuclei and also (to a lesser content) by ionisation. A hadron-initiated EAS is initiated by the spallation of the initial air nucleus and typically consists of several sub-showers with different components (cf. Fig. 3.2). Those are classified by the particles inside them and the physical processes their production is based on. The muons, forming the muonic shower component, are mostly produced via the decay of charged pions and kaons. The electromagnetic component is formed by the decay of neutral pions and muons and then follows the same processes as a lepton-initiated EAS, i.e. pair production and bremsstrahlung. It contains a couple of hundred times more particles than the hadronic and muonic component.

Several EAS properties can be approximately calculated using the Heitler model for an electromagnetic shower or an extension of this model, the Heitler-Matthews model [56], for a hadron induced shower. In both, the assumption is used that (1) in each interaction the same type and number of particles are produced and (2) the energy is distributed evenly among all secondary particles in each step. For a hadronic shower (cf. Fig. 3.3b), those are neutral ($\pi^0$) and charged pions ($\pi^{+/-}$) with the ratio 1:2. The neutral pions then instantly decay into two photons and are therefore "lost" into the electromagnetic shower component while the charged pions undergo the next interaction (after a typical interaction length of 120 g/cm$^2$) forming again charged and neutral pions. In the model of an electromagnetic shower (cf. Fig. 3.3a), in each interaction either a photon converts into an electron-positron pair via pair production or an electron looses energy via bremsstrahlung producing an additional photon. Furthermore, it is assumed that the typical interaction length $\lambda_{em}$ is the same for bremsstrahlung and pair-production and of the order of the radiation length $X_0$ of an electron in air ($X_{0,air} \sim$ 37–38 g/cm$^2$).

Since two particles are produced in each interaction of an electromagnetic shower, the particle number $N_i$, energy of each particle $E_i$, and atmospheric depth $X_i$ at the $i$-th interaction
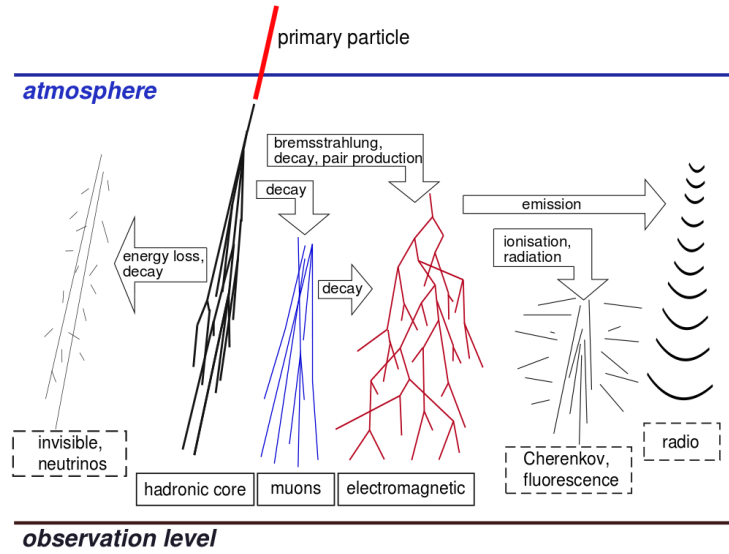
**Figure 3.2** A primary hadronic CR hitting the atmosphere initiates a cascade of particles travelling as an EAS towards the Earth's surface. This schematic illustartes the different physical processes and components associated with a hadronic-initiated EAS. Adapted from [55].

are

$$N_i = 2^i, \tag{3.1}$$

$$E_i = E_0/2^i, \tag{3.2}$$

$$X_i = i\,\lambda_{\mathrm{em}}, \tag{3.3}$$

where $E_0$ is the energy of the primary leptonic particle when initiating the electromagnetic (sub-)shower. The electromagnetic shower reaches its maximum, i.e. contains the maximum number of particles, when the ionisation losses start to dominate the losses due to bremsstrahlung, i.e. when $E_i = E_\mathrm{c} \simeq 80$ MeV. Thus, the maximum number of particles is (combining
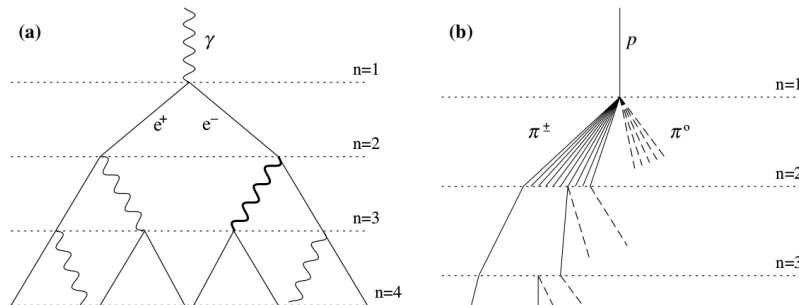


**Figure 3.3** Schematic views of (a) an electromagnetic cascade and (b) a hadronic shower. In the hadron shower, dashed lines indicate neutral pions which do not re-interact, but quickly decay, yielding electromagnetic subshowers (not shown). Not all pion lines are shown after the n=2 level. Adapted from [56].
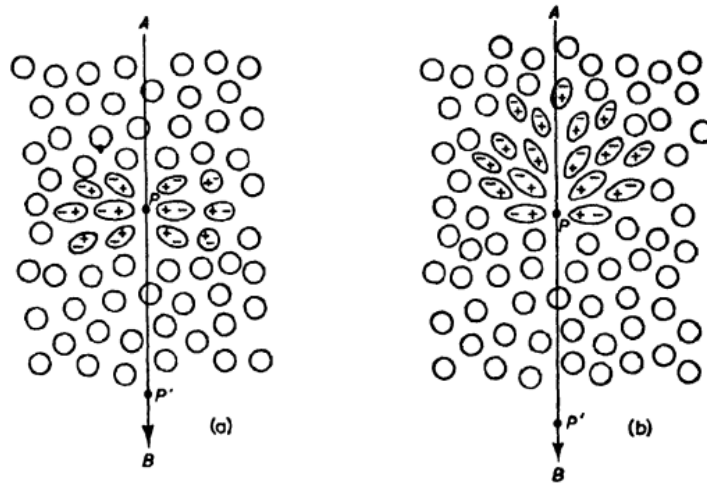
**Figure 3.4** The polarisation set-up in atmosphere (or any dielectric medium) by the passage of a charged particle (here negatively charged) in case the velocity of the particle is (a) smaller and (b) higher than the phase velocity of light in the medium. Adapted from [57].

Eq. 3.1 & 3.2) given by

$$N_{\text{max}} = \frac{E_0}{E_{\text{c}}} \tag{3.4}$$

and the atmospheric depth of the electromagnetic shower maximum is (combining Eq. 3.1, 3.3 & 3.4) given by

$$X_{\text{max}} = \lambda_{\text{em}} \log_2 \left( \frac{E_0}{E_{\text{c}}} \right). \tag{3.5}$$

As will be explained in the next section, Cherenkov radiation is emitted by the charged particles in the EAS. Since most of them are part of the electromagnetic shower (component), the properties of all other components of a hadron-initiated EAS are not examined here in detail. For further explanations see for example [1, 56].

### 3.1.2 Characteristics and physics of atmospheric Cherenkov radiation

When the charged particles of the EAS move through the atmosphere, the surrounding atoms and molecules move to compensate the presence of the charge and behaving like elementary dipoles. In case the velocity of the charged particle $v = \beta c_0$ ($c_0$ being the velocity of light in vacuum) is smaller than the phase velocity of light in the medium (here the atmosphere), given by $c_0/n$ ($n$ being the refractive index of the medium) the polarisation field is completely symmetric which is why there is no resultant field at large distances and thus no radiation (cf. Fig 3.4a). However, if the particle velocity is higher than the phase velocity of light in the medium, i.e.

$$\beta c_0 > c_0/n, \tag{3.6}$$

the polarisation field is no longer symmetric (cf. Fig 3.4b) resulting in a dipole field even at large distances from the particle track and thus in an emission of radiation. This radiation is only observable in case the emission is coherent and forming a plane wave front. From Fig. 3.5a it can be inferred that this only is possible if the particle travels the distance AB in the same time as the emitted photon travels the distance AC, i.e.

$$\beta c_0 \Delta t = \frac{c_0}{n} \Delta t. \tag{3.7}$$
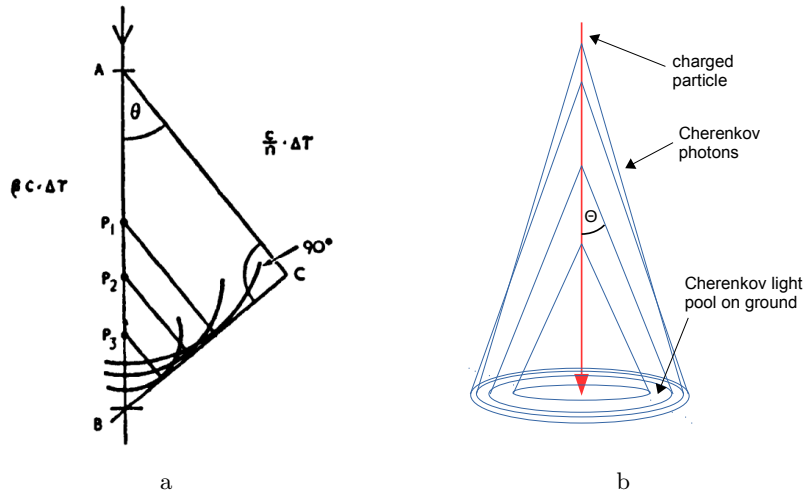
**Figure 3.5** Drawings showing (a) the formation of coherent plane wave fronts in the Cherenkov emission process (adapted from [57]) and (b) the atmospheric Cherenkov emission and increasing emission angle $\Theta$ with decrease in height from a downward-moving single charged particle.

Using geometry, this results in

$$\cos \Theta = \frac{1}{\beta \, n},\tag{3.8}$$

with $\Theta$ being the emission angle of the Cherenkov radiation w.r.t. the individual trajectory of each charged particle in the EAS fulfilling the condition given by Eq. 3.6. This condition can also be translated into a minimum (threshold) energy $E_\mathrm{thr}$ of a charged particle of rest mass $m_0$ for which it can emit Cherenkov light (inserting $E = \gamma m_0 c^2$ with $\gamma = 1/\sqrt{1 - \beta^2}$ in Eq. 3.6):

$$E_\mathrm{thr} = \frac{m_0 \, c^2}{\sqrt{1 - n^{-2}}}.\tag{3.9}$$

Due to the height dependence of the atmospheric refractive index, $\Theta$ and $E_\mathrm{thr}$ change with height lying in between $\sim 0.8°$ and $\sim 40$ MeV for an electron at a height of 10 km and $\sim 1.4°$ and $\sim 20$ MeV at sea level. This causes Cherenkov radiation to occur in a cone along the shower axis, illuminating an area on the ground (typically called Cherenkov light pool) for a few nanoseconds, illustrated by Fig. 3.5b. The edge of the pool with a typical diameter of 250 m on ground at $\sim 2$ km a.s.l. is defined by the overall cone formed around the shower axis from the sum of individual contributions. The "edge-fuzziness" and the filling of the pool centre results from shower particles being scattered around the shower axis and thus emitting Cherenkov light at a slightly different angle w.r.t. the shower axis.

The number of emitted Cherenkov photons $N$ per unit wavelength $\lambda$ and as function of the travelled distance $x$ is given by the Frank-Tamm formula [58]

$$\frac{d^2 N}{dx d\lambda} = 2\pi \alpha z^2 \lambda^{-2} \left( 1 - \frac{1}{\beta^2 n^2(\lambda)} \right),\tag{3.10}$$

where $\alpha$ is the fine-structure constant and $z$ the charge number of the charged particle. Due to the absorption of UV radiation by the atmosphere, the (differential) emission spectrum shows a sharp cutoff at around 300 nm before it follows the $\lambda^{-2}$ dependence for higher wavelength as given by Eq. 3.10 and shown in Fig. 3.6a. In total, this results in a very fast and faint

a

b
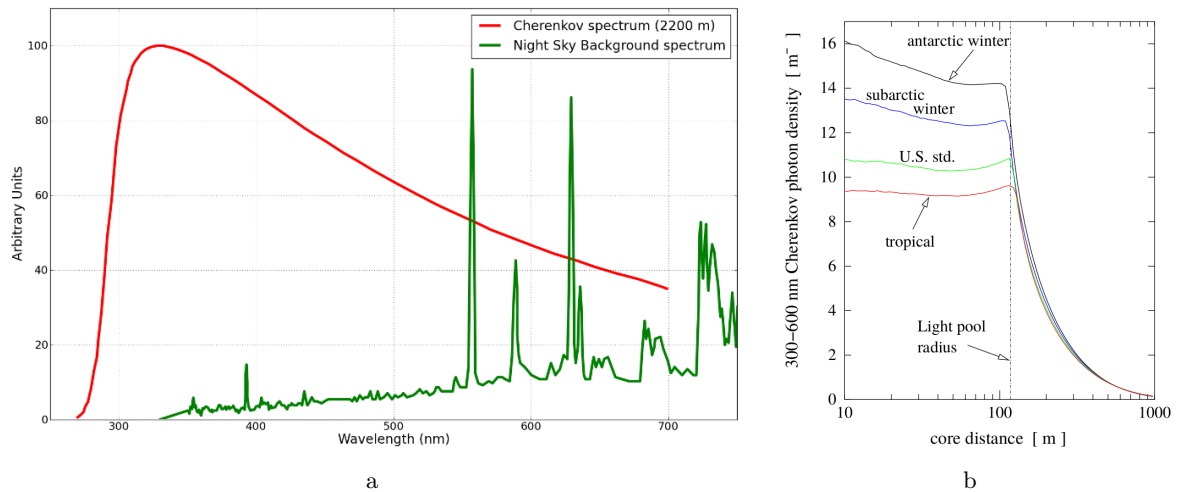
**Figure 3.6** (a) Differential emission spectrum $dN/d\lambda$ of Cherenkov photons from EASs at an altitude of 2200 m and of the night sky, measured in La Palma (adapted from [59]). (b) Lateral distribution per unit area of the optical Cherenkov emission from a $\gamma$-ray-induced shower with primary energy of 100 GeV for various atmospheric profiles (adapted from [60]).

signal on ground, lasting only a few nanoseconds and containing only a few tens of photons as shown by Fig. 3.6b.

The overwhelming majority of EASs are initiated by hadronic CRs rather than VHE $\gamma$-rays. Since, as mentioned above (cf. Sec. 3.1.1), even in a hadron-initiated EAS the electromagnetic particles are by far the most abundant species, experiments measuring $\gamma$-ray-initiated EASs will have a huge background resulting from the electromagnetic component of the hadron-initiated EAS. However, reduction of this hadronic background can be achieved by exploiting the intrinsic differences in the properties of lepton and hadron-initiated EASs. In case of the latter one, the early EAS development is dominated by strong interactions between the primary CR and the air nuclei. The transversal momentum transfer to the produced (secondary) particles in those interactions is much higher than in electromagnetic interactions (dominated by Coulomb scattering). Furthermore, the presence of hadronic particles in the hadron-initiated EAS leads to the formation of several subshower with higher fluctuations. As a consequence, a hadron-initiated EAS shows a much higher lateral spread (compare Fig. 3.7a & 3.7d) which is also reflected in the characteristics of the Cherenkov light signal on ground such as the arrival time and lateral distribution. While the Cherenkov photons of a VHE $\gamma$-ray-initiated EAS arrive within a few nanoseconds at a given radial distance from the shower core, the arrival of Cherenkov photons of a hadron-initiated EAS can be much more irregular due to the presence of sub-showers (compare Fig. 3.7b & 3.7e). The formation of sub-showers also causes the lateral distribution of the Cherenkov light on ground looking much more irregular for a hadron-initiated EAS showing several Cherenkov light pools while only one regular light pool is visible for a VHE $\gamma$-ray-initiated shower (compare Fig. 3.7c & 3.7f). This difference can be used in the discrimination of VHE $\gamma$-ray events from hadronic events, often referred to as "$\gamma$-hadron-separation".
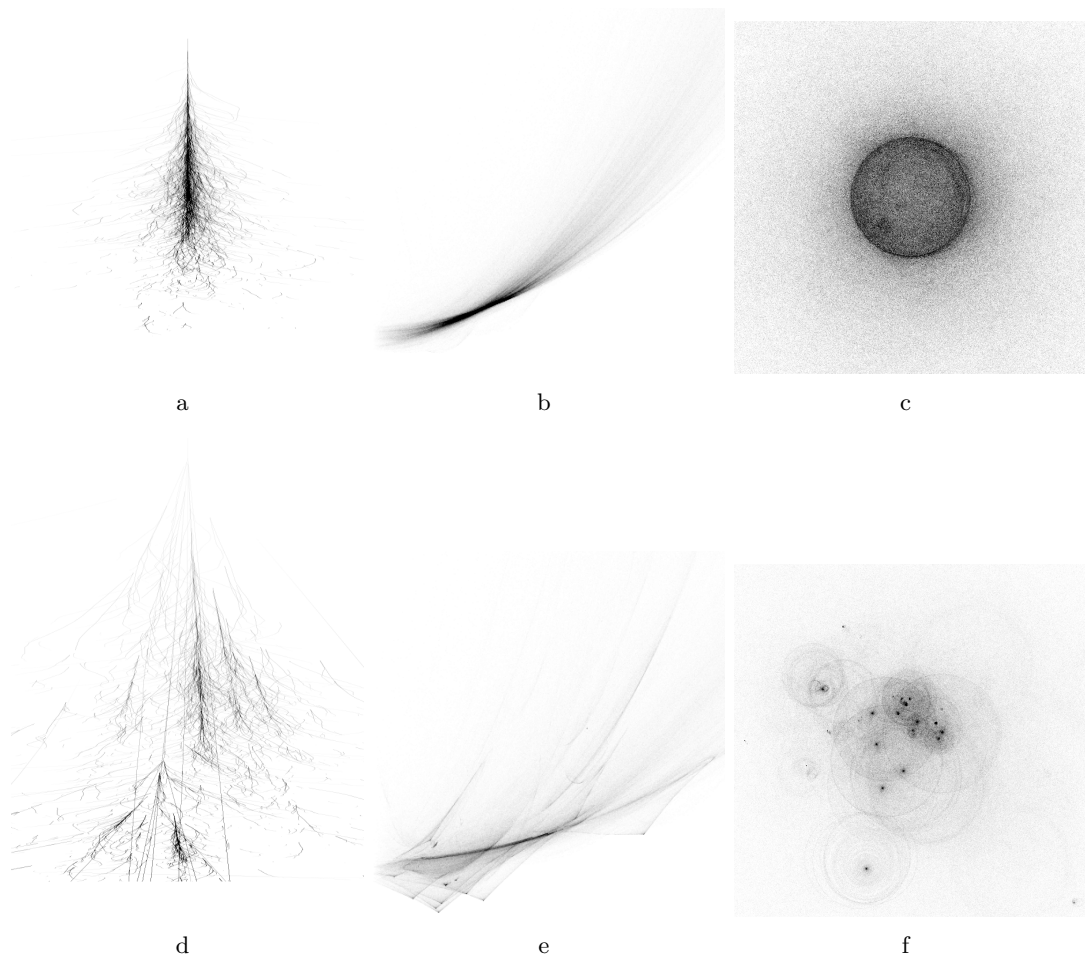
**Figure 3.7** Simulation of a 300-GeV photon (a-c) and a 1-TeV proton (d-f) initiated EAS: a & d: longitudinal view in x-z plane showing the tracks of Cherenkov emitting particles; b & e: time of Cherenkov light arrival on ground versus core distance; c & f: lateral view of Cherenkov light on the ground. Adapted from [61].

## 3.2 Imaging atmospheric Cherenkov telescopes

In general, one distinguishes between two kinds of ground-level $\gamma$-ray detectors: (1) EAS detectors such as HAWC [62] and (2) IACTs such as the operating experiments H.E.S.S. [63], VERITAS [64], and MAGIC [65]. The latter ones are also called 3rd-generation IACT experiments consisting of five, four, and two telescopes, respectively. The future 4th-generation IACT experiments are arrays of many more telescopes. An example of such a future array is CTA [66] consisting of two arrays (one in the Northern and one in the Southern hemisphere) with $\sim$100 telescopes in total.

Ground-level EAS detectors have to be located at rather high altitudes ($\geq$4 km) for the particles of a $\gamma$-ray-initiated EAS to reach the detector. They typically have a wide field of view (FoV) close to half of the sky with an angular resolution of $\sim$0.1°, a high sensitivity outperforming the one of current IACT experiments for $\gamma$-ray energies exceeding a few TeV,

and a duty cycle of nearly 100%. In contrast to that, IACTs measure the Cherenkov light emitted by an EAS to determine the primary particle characteristics. In order to do so, they have to be optimised to account for the Cherenkov signal features explained in the previous section. (1) Since the signal is very faint (only ∼100 photons/m$^2$ at 2 km a.s.l. for a primary 1-TeV $\gamma$-ray), reflective optics (mirrors) are used. They catch and concentrate enough light on a camera equipped with very sensitive photosensors able to detect single photons. However, due the weakness of the signal and the sensitivity of the sensors, data taking is typically restricted to periods of low background light conditions, i.e. hours of dark night (sun 18° below the horizon) and low moon levels. This results in a theoretical duty cycle of ∼17% which may decrease down to ∼11% (∼1000 h/year) including observation time loss due to bad weather (rain or high cloud coverage) and technical issues. (2) To account for the fast Cherenkov signal lasting only a couple of nanoseconds, the photosensors and electronics have to be fast, i.e. being able to trigger on ns-pulses and to digitise them with a ns-resolution. (3) To account for the Cherenkov radiation wavelength dependence, photosensors with an intrinsic high photon detection efficiency (PDE), in particular around the maximum emission wavelength of ∼320 nm, should be used. Furthermore, they should have a low PDE in the red or use special coating or filters to minimise the number of night sky background (NSB) photons being converted into a signal and thus contributing to the background in the signal.

Transferring those considerations into technical solutions is the main challenge when designing and building an IACT. However, in the last 20 years IACTs have already proven to be the most sensitive instruments for $\gamma$-ray detection in the VHE range with an angular resolution lower than 0.1° and a typical FoV of 5 to 10°. How this can be realised from a technical point of view will be explained in the following section.

### 3.2.1 Working principle

A dish (consisting of a single mirror or a mirror system) reflects the Cherenkov photons onto a camera which is installed in the focal plane. The size of the dish should ideally be as big as possible to capture enough Cherenkov photons. However, the choice of the size typically is a compromise between scientific goal and costs. Since the atmospheric Cherenkov light yield strongly depends on the energy of the primary $\gamma$-ray (∼2 photons/m$^2$ in the shower core for an EAS initiated by a 100-GeV $\gamma$-ray compared to ∼600 photons/m$^2$ for a 10-TeV $\gamma$-ray), larger dishes are used for lower VHE $\gamma$-ray observations with energies of tens to hundreds of GeV (mostly extragalactic sources). For VHE $\gamma$-ray observations in the TeV-regime (mostly Galactic sources), the use of smaller dishes is sufficient. The angular resolution of IACTs is limited by the intrinsic EAS fluctuations, typically being of the order of 0.1°. Thus the mirror quality and purity is by far not as critical as for observations in the optical band where angular resolutions close to the diffraction limit are achieved (∼arcsec). This is also why IACTs typically are not covered by a dome and mirror cleaning happens in the order of every half a year. However, continuous monitoring of the optical efficiency is done using atmospheric Cherenkov light of muons (cf. e.g. [67, 68]).

Since Cherenkov photons from different parts (heights) of an EAS are emitted at different angles, they hit the mirror under different incident angles and also the camera at different positions/pixels (cf. Fig. 3.8). The image recorded by the Cherenkov camera reflects the EAS characteristics. A VHE $\gamma$-ray-initiated EAS typically generates a characteristically elliptical image in the camera while a hadron-initiated EAS generates a rather irregular image (cf. Fig. 3.9) due to the presence of subshowers (cf. Sec. 3.1.2). The length of the ellipse depends on both the inclination of the EAS w.r.t. the telescope pointing and the distance of the shower core to the telescope (also referred to as impact distance). The latter
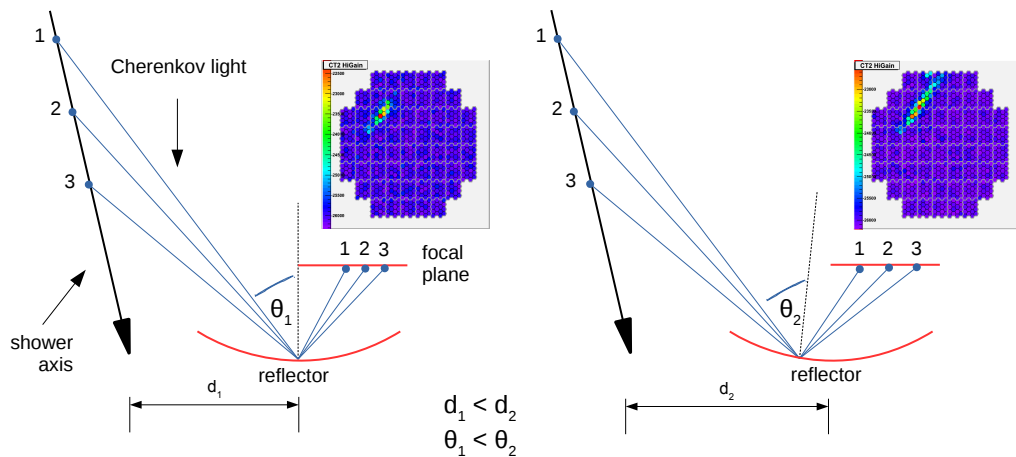
**Figure 3.8** Drawing showing the reflection of Cherenkov photons emitted in an EAS at three positions (1, 2, and 3) by a mirror onto a camera (focal plane) for two different distances $d_1$ and $d_2$ between shower axis and telescope position. Adapted from (Zorn, 2019) [69].

one is illustrated in Fig. 3.8 where the shower at distance $d_2$ produces a longer image in the camera than the shower at distance $d_1$ since the incident angle increases with distance. The ellipse characteristics can be used not only for the direction reconstruction of the primary $\gamma$-ray but also for further analyses. Those are for example $\gamma$-hadron-separation or energy estimation of the primary $\gamma$-ray using the the integrated intensity of the shower image in the camera (referred to as image size). Such an analysis based on the ellipse characteristics was first introduced by M. A. Hillas in 1985 [70] and is therefore often referred to as "Hillas analysis". Over the years more sophisticated analysis techniques were developed, such as the `ImPACT` analysis [71] using likelihood fitting of camera pixel amplitudes.

Stereoscopic observations, i.e. using several (at least two) telescopes observing the same EAS in coincidence, allow a more precise determination of the shower direction by projecting the images in all triggered telescope cameras into one camera (cf. Fig. 3.10). Then the intersection point of the image major axes yields the shower direction. Thus, compared to observations with a single telescope, the angular resolution, the energy resolution, the background rejection, and the sensitivity are improved. In addition, this method allows the 3-dimensional reconstruction of the EAS, including the height of the shower maximum.

A Cherenkov telescope is a self-triggering unit. This means it uses an internal threshold defined for example in units of photoelectrons (p.e.) or signal amplitude (measured in mV) above which it triggers the readout chain. The operation point is defined based on the so-called trigger bias scan, being a measurement of the trigger rate as function of the threshold. The bias curve consists of two parts (cf. Fig. 3.11): the so-called "NSB wall" where the trigger is dominated by accidental (un-correlated) NSB photons and the CR part where the trigger is dominated by CRs and $\gamma$-rays. The exact shape of the bias curve depends on the electronics and trigger logic of the camera and on the CR-flux $\Phi_{CR}$ (cf. Eq. 2.2). The operation point and the corresponding threshold is typically set around the transition point where the trigger migrates from being NSB-dominated to being CR-dominated. The trigger rate $f$ at any point of the bias curve in the CR-dominated part is then given by

$$f = A_{\text{eff,trig}} \int \int \Phi_{CR} \mathrm{d}E \, \mathrm{d}\Omega, \tag{3.11}$$
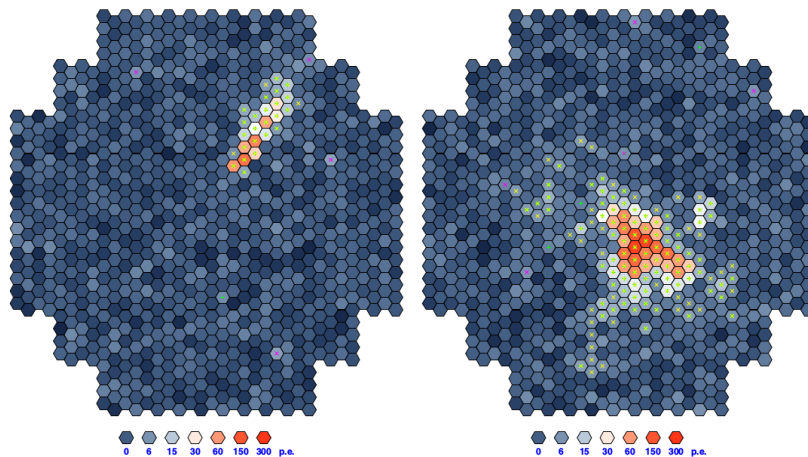
**Figure 3.9** Simulations showing Cherenkov events detected by the H.E.S.S. cameras and generated by a 1 TeV-$\gamma$-ray-induced EAS (left) and a 2.6 TeV-proton-induced EAS (right). The charge in each pixel in units of p.e. is given by the colour scale. Adapted from [60].
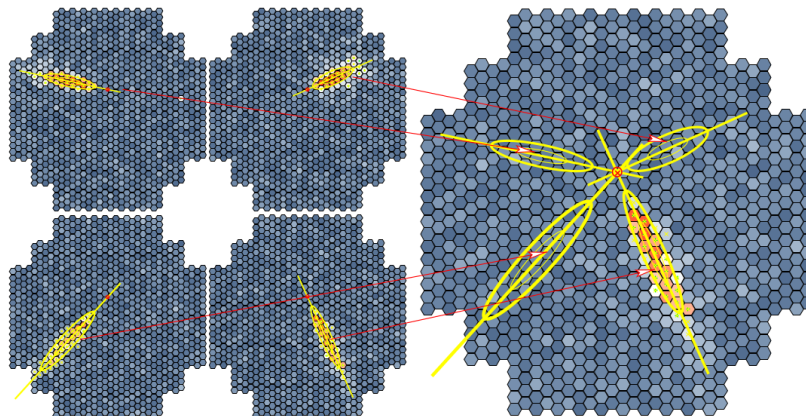


**Figure 3.10** Projection of coincidentally detected (simulated) Cherenkov images from the four H.E.S.S. I telescopes into one camera plane. Also shown are the signal intensity of each pixel (indicated by different colours) and the Hillas ellipses used for the direction reconstruction in each camera. Adapted from [60].

with $A_{\text{eff,trig}}$ being the trigger effective area.

The effective area of an IACT results from MC simulations. One distinguishes between the trigger effective area $A_{\text{eff,trig}}$ and the true effective area $A_{\text{eff,true}}$ (often just referred to as effective area $A_{\text{eff}}$). They are defined as

$$A_{\text{eff,trig}} = \frac{n_{\text{trig}}}{n_{\text{sim}}} A_{\text{sim}} \tag{3.12}$$

and

$$A_{\text{eff}} \equiv A_{\text{eff,true}} = \frac{n_{\text{anal}}}{n_{\text{sim}}} A_{\text{sim}}. \tag{3.13}$$

$n_{\text{trig}}$, $n_{\text{anal}}$, and $n_{\text{sim}}$ are the number of Cherenkov events that triggered the IACT camera, that survived selection/analysis cuts, and that were simulated, respectively. $A_{\text{sim}}$ is the area on the ground around the IACT for which EASs were simulated. The effective area of an IACT typically is significantly larger than the physical size of the detector and increases with
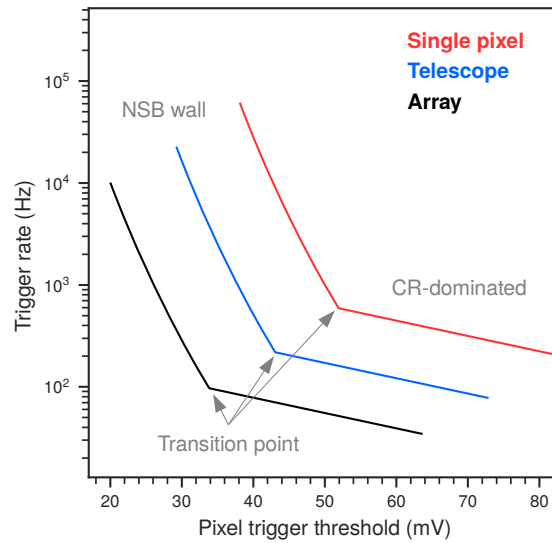
**Figure 3.11** Sketch showing examples of trigger bias curves for different scenarios with the trigger being based on a single pixel threshold, a coincidence of pixels (telescope trigger), or a coincidence of telescopes (array trigger). The two different parts of the bias curve (NSB wall and CR-dominated part) as well as the transition point are indicated.

energy (since high-energy EAS produce more Cherenkov photons, hence can be detected at higher impact distances what increases the effective area). Convolving it with a source energy spectrum gives the sensitivity, being the expected number of $\gamma$-rays detectable by the IACT as function of energy.

Fig. 3.11 shows trigger bias curves for different scenarios with the trigger being based on a single pixel, a coincidence of pixels to form a telescope trigger, or a coincidence of telescopes to form an array trigger. The required coincidence (between pixels or telescopes) helps to reduce the number of accidental (un-correlated) NSB triggers for a given threshold. At the same time – however – also the rate of CR triggers for a given threshold may be reduced in case the Cherenkov event does not cover the required number of pixels to form a telescope trigger or is not visible by all telescopes required to form the array trigger.

### 3.2.2  The High Energy Stereoscopic System and the H.E.S.S. IU cameras

#### 3.2.2.1  Overview

The High Energy Stereoscopic System (H.E.S.S.) is an array of five IACTs (cf. Fig.3.12) and is named in honour of Victor Hess (for his discovery of CRs [72] awarded with the Nobel Prize in 1936). It first started observations in 2003 and is situated in the Khomas Highlands of Namibia at 1800 m a.s.l. at a geographic latitude of 23°16'18" S and a longitude of 16°30'00" E. The location was chosen for its dry climate, its lighting conditions (isolation from population), the low geomagnetic field strength of ∼28000 nT [74][1], and its geographic latitude offering a good view of the Milky Way in the Southern hemisphere. Since the other

---

[1]The intensity of the geomagnetic field, typically measured in nT, lies between 25000 and 65000 nT. It tends to decrease from the poles to the equator. A minimum intensity occurs in the South Atlantic Anomaly over South America while there are maxima over northern Canada, Siberia, and the coast of Antarctica south of Australia [75]. Namibia is strongly influenced by the South Atlantic Anomaly which is why the geomagnetic field is rather low compared to e.g. Australia being located at a similar geographic latitude.

**Figure 3.12** Picture showing the H.E.S.S. experiment with CT1–4 in the corners of the $(120 \times 120)$ m$^2$ array and CT5 in the middle. Picture adapted from [73].

main operational $\gamma$-ray experiments (VERITAS, MAGIC, and HAWC) are all located in the Northern hemisphere, the contribution of H.E.S.S. is considerable, with many of the currently known TeV $\gamma$-ray sources being discovered by H.E.S.S..

The four smaller telescopes of the H.E.S.S. array, called CT1–4 and also often referred to as H.E.S.S.-I telescopes, have a reflector dish diameter of 12 m and form a square with 120 m edge length. It was chosen based on the expected Cherenkov light pool radius of about 120–130 m at 1800 m a.s.l. for $\gamma$-rays originating from zenith to allow stereoscopic observations with the whole array. The bigger telescope, called CT5, has a reflector dish diameter of 28 m, was added in 2012 and placed in the middle of the array. Its inauguration initiated the H.E.S.S. phase II with the aim to extend the sensitivity of H.E.S.S. towards lower energies (from 100 GeV to several tens of GeV) to close the gap between space- and ground-based observations. All H.E.S.S. telescopes consist of a large single reflector dish compromised of many individual mirror facets focusing the light onto a fast-imaging camera. While the optics of CT1–4 are based on Davies-Cotton design [76] (all mirror facets having the same focal length $f$ and being arranged on a sphere of radius $f$), the CT5 dish is designed with a parabolic shape (mirror facets being arranged on a paraboloid $z = r^2/(4f)$ and having different focal lengths depending on the distance from the optical axis). The use of different dish sizes and optical designs results from the particular science goals tackled by the individual telescope types (for more details cf. e.g. [77]):

- One of the major science goals of H.E.S.S., as the only IACT on the Southern hemisphere with the best view on the Galactic centre, is to observe Galactic sources. As mentioned in Sec. 2.2.1, $\gamma$-rays exceeding energies of 500 GeV (and producing hundreds of Cherenkov photons per m$^2$, cf. Sec. 3.2.1) are expected to be observed from such sources. In addition, due to their close distance, the source region can appear rather extended (>1°). Thus, CT1–4 use smaller dishes with Davies-Cotton optics, being favourable for off-axis imaging.

- The major motivation to add a fifth telescope to the H.E.S.S. array was to improve the sensitivity for extragalactic observations. This can mainly be achieved by lowering the energy threshold since $\gamma$-rays from extragalactic sources are expected to have energies in the HE and low VHE range (cf. Sec. 2.2.1) resulting in much lower amount of Cherenkov photons than for $\gamma$-rays with TeV energies (cf. Sec. 3.2.1). Hence, CT5 uses a bigger dish with parabolic shape to realise a lower energy threshold.

a b
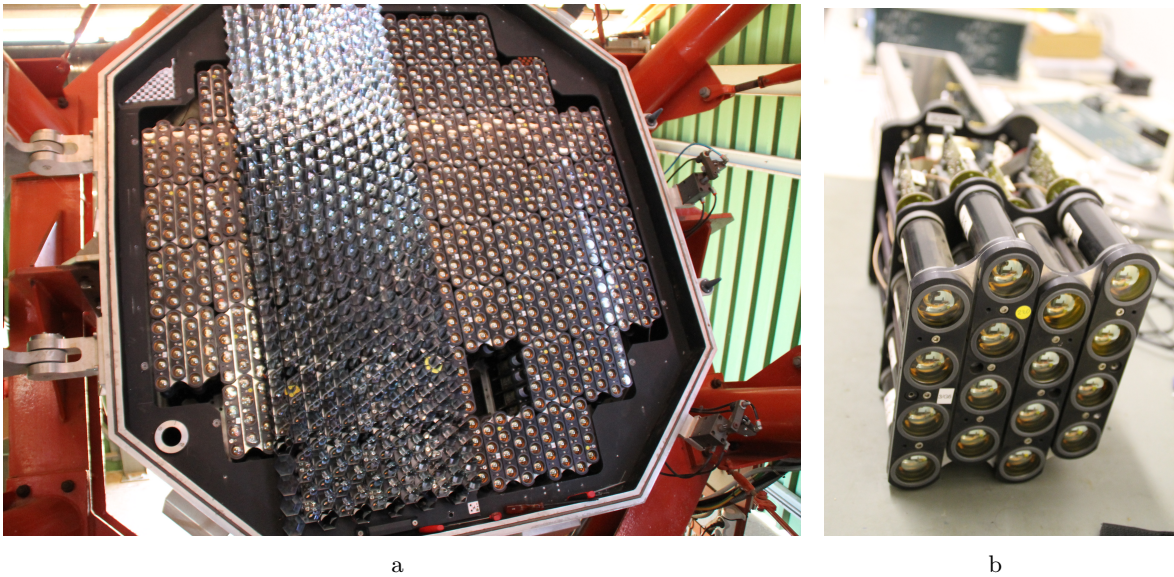
**Figure 3.13** (a) Picture of the H.E.S.S. IU focal plane showing the 9×8 rectangular matrix of drawers with one drawer removed from the second to bottom row. To be able to remove the drawer, the light cones needed to be untightened and moved. (b) Picture of a drawer when outside of the camera, equipped with 16 PMTs.

Both, CT1–4 and CT5 are equipped with 960 and 2048 Photonis XP2960 photomultiplier tubes (PMTs) with a diameter of 42 mm, equivalent to a FoV of 0.16° (CT1–4) and 0.067° (CT5), and resulting in a total camera FoV of 5.0° and 3.2°, respectively. A sampling frequency of 1 GHz and two gain channels for each pixel are used to obtain a large dynamic range. The 960 PMTs of CT1–4 are organised into 60 modules, called drawer. In the camera, the drawers are arranged in a 9×8 rectangular matrix, with each corner of the matrix devoid of 3 drawers (cf. Fig. 3.13a). A drawer (cf. Fig. 3.13b) consists of 16 PMTs, two 8-channel analogue boards (responsible for the amplification, discrimination and digitisation of the PMT signals), and a slow control board (hosting drawer and power control units). To account for the non-sensitive space between PMTs and to increase the light collection efficiency, light cones are installed in front of each PMT.

The trigger of the H.E.S.S. IU cameras is two-fold [78]. The lowest trigger layer (L0) is on the pixel level. A comparator discriminates the analogue signal of each pixel against a certain pixel threshold $t$. For the camera-wide (L1) trigger, the camera is subdivided into 38 sectors, which overlap horizontally by one half drawer and vertically by one full drawer. An L1 trigger is issued in case of an $N$-fold time coincidence within a trigger sector, i.e. whenever at least $N$ pixels in any sector are triggering simultaneously (majority logic). $N$ is usually set to 3.

### 3.2.2.2 H.E.S.S. IU

In 2015/16, the H.E.S.S.-I camera electronics (PMTs excluded) saw a major upgrade for several reasons [79]:

1. The dead time of ∼450 $\mu$s, which led to negligible losses in case of typical H.E.S.S. phase I trigger rates of 200–300 Hz, became significant when operating in coincidence with CT5, triggering at rates higher than 1.5 kHz due to the lower energy threshold. In

such cases, a significant fraction of events lost their stereoscopic quality because CT1–4 could be in readout state while CT5 saw a new trigger.

2. After >10 years of operation in the harsh conditions in Namibia the ageing of the electronics became significant causing an increasing number of failures.

3. Using new electronics in the H.E.S.S. IU cameras offered to include new technical developments and to use new tailored software to improve the overall performance of the camera.

The latter aspect included a design change in the trigger chain while keeping the general trigger architecture to be the same [80]. Inspired by the digital camera trigger design for CTA [81], the L0 comparator of H.E.S.S. IU outputs an 800 MHz sampled signal which is different from the asynchronous logic in the old cameras. An advantage of using a synchronous logic is that the L0 signal can be delayed and stretched, another is the possibility to implement alternative L1 trigger logic architectures. Two such new logics were implemented, being the compact next-neighbour logic [82], and a pseudo-analogue sum trigger logic [83] resulting in a lower trigger threshold.

Using new electronics and tailored software also improved the data transfer rate. A higher data transfer rate enabled the possibility of full-waveform readout, referred to as sample mode (SM), in addition to the nominal readout mode, referred to as charge mode (CM). In CM, the Cherenkov signal is integrated over a fixed window of 16 ns in case trigger conditions are met. The position of the integration window is anchored to the trigger time and is the same for all camera pixels. In SM, the full 1 GHz-sampled, 40 ns-long waveforms are read out in parallel to CM. This allows a higher flexibility in data analysis such as signal integration along the signal time gradient and is expected to increase the performance of the experiment in many aspects. In the scope of this work, the SM data taking was implemented and investigated. Details about the readout scheme, charge extraction, integration into the analysis framework, data integrity investigations, and performance studies are presented in Ch. 8.

Due to the use of new camera hardware and trigger logics, also the MC simulation chain (introduced in Sec. 3.2.5) needed to be updated and verified. This was done in the scope of this work and is presented in Ch. 7.

### 3.2.3 The Cherenkov Telescope Array and the CHEC camera

#### 3.2.3.1 Overview

The Cherenkov Telescope Array (CTA) [66, 84] is a future multi-km$^2$ IACT array consisting of a large number (>100) of closely spaced telescopes (distance of 100–200 m) with single-telescope FoVs similar to operating IACTs such as the H.E.S.S. telescopes (5°–10°). To cover a wide energy range (from 20 GeV to 300 TeV) it uses three telescope classes: small, medium, and large-sized (abbreviated with SST, MST and LST). Their dish diameters range from 4 to 23 m (cf. Fig. 3.14) and different quantities of telescopes for each class will be used. Furthermore, CTA will consist of a northern and a southern hemisphere site to cover the whole sky. Following the same argumentation as in the previous section, telescopes covering the lower part of the energy range require bigger dishes to capture enough Cherenkov photons. However, due to the higher $\gamma$-ray flux in this energy range, a fewer number of LSTs is required compared to a much higher number of SSTs covering the TeV energy range. Furthermore, since $\gamma$-rays at TeV energies are expected to mostly origin from Galactic sources (cf. Sec. 2.2.1), which can be better observed (at higher elevation) from the southern hemisphere, SSTs are planed to be built on the southern hemisphere site only. The complete array
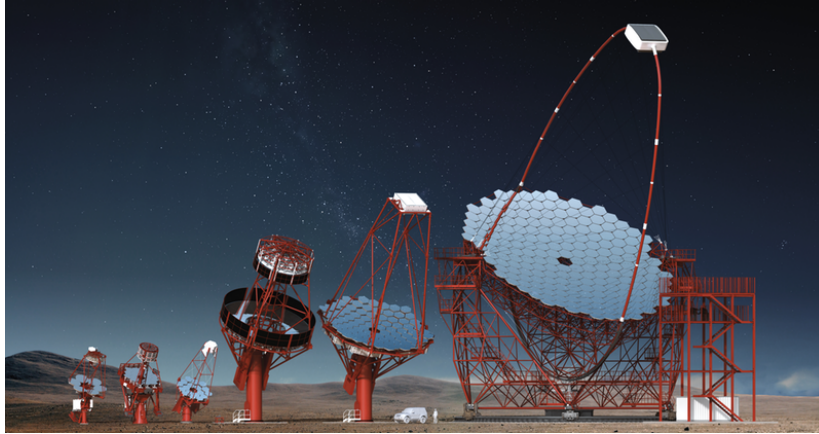
**Figure 3.14** Artist's impression showing the prototypes for the different telescope types of CTA. From Left: The three SST prototype designs (4 m dish diameter), the two MST prototype designs (12 m) and the LST (23 m) prototype design. Adapted from [85].

**Table 3.1** CTA northern and southern site array specifications [85].

|  | Northern hemisphere | Southern hemisphere |
|---|---|---|
| Location | La Palma (Spain) | Atacama Desert (Chile) |
| - Latitude | 28° 45' 43.7904" North | 24° 41' 0.34" South |
| - Longitude | 17° 53' 31.218" West | 70° 18' 58.84" West |
| Array area coverage (km$^2$) | 0.7 | 4 |
| Telescope number | 19 | 99 |
| - LST | 4 | 4 |
| - MST | 15 | 25 |
| - SST | 0 | 70 |
| Energy range | 20 GeV–20 TeV | 20 GeV–300 TeV |

specifications of both, the northern and southern hemisphere site, are given in Tab. 3.1 and the final array layouts are shown in Fig. 3.15. Thanks to those characteristics (array size, use of different telescope types, and technology improvements), CTA will outperform operational IACTs and other VHE $\gamma$-ray experiments by a factor of $\sim$10 in sensitivity (cf. Fig. 3.16) and improve VHE $\gamma$-ray observations in many other aspects such as in angular resolution (factor $\sim$1.5 improvement) etc. .

### 3.2.3.2 Small-sized telescopes and the CHEC camera

As mentioned above, the SSTs of CTA should provide sensitivity in an energy range from about 1 to more than 300 TeV, being the upper end of CTA's energy reach. At those energies, the expected CR background and the $\gamma$-ray flux is such that the expected mean trigger rate of an SST is $\sim$300 Hz. Hence, an SST camera is required to handle mean event rates of that order. The Cherenkov light of EASs initiated by $\gamma$-rays with energies above a few TeV can also be detected outside the light pool of fairly uniform illumination of about 200–250 m diameter. Hence, a possible realisation to achieve a threshold of 1 TeV is using an array with a telescope spacing of $\sim$250 m with each telescope having a diameter $D$ of 4 m and an FoV
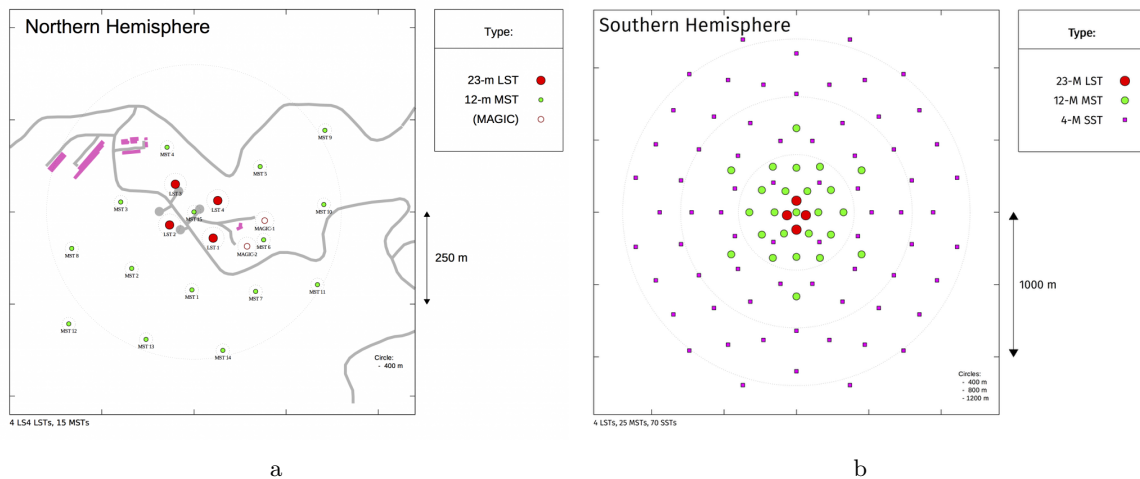
**Figure 3.15** CTA array layouts of the (a) northern and (b) southern hemisphere site. Adapted from [85].

of 8°–9°. For a conventional IACT design with such a diameter, using a single-mirror dish with a parabolic reflector or Davies-Cotton design, the cost of the camera dominates that of the telescope. The use of a secondary reflector and aspherical Schwarzschild–Couder [87, 88] optics instead (cf. Fig. 3.17), enables a reduction in the plate scale of a 9°-FoV telescope by a factor of ∼3 [89]. An angular size of a camera pixel of ∼0.2° is required to be less than the full width at half maximum (FWHM) of a typical 1 TeV-$\gamma$-ray image [66, 86]. This can be achieved by low-cost photosensors with pixel diameters of ∼6 mm (cf. Fig. 3.17), setting the telescope focal length $f$ to ∼2 m. The resulting $f/D$ ratio of ∼0.5 can be realised with the dual-mirror Schwarzschild–Couder design. In this configuration, a 9° FoV can then be realised by a camera with a diameter of only ∼35 cm, equipped with ∼2000 pixels in a focal plane with a curved surface (being in contrast to conventional one-mirror designs using cameras with a plane focal plane).

The reduced plate scale of the telescope and the required compact nature of the camera enables the use of rather novel options for the camera photosensor technology and electronics. Those include commercially available multi-pixel photon-counting photosensors, such as multi-anode photomultipliers (MAPMs) and Silicon photomultipliers (SiPMs), and custom application-specific integrated circuitss (ASICs), such as TARGET (TeV array readout with GSa/s sampling and event trigger) ASICs [91], providing a high-performance low-cost solution for the trigger and readout electronics. As mentioned above, the camera is typically the cost-driving factor of a telescope. Hence, when using small cameras in a dual-mirror telescope design, the overall telescope costs are expected to be considerably reduced compared to bigger cameras equipped with conventional PMTs in a single-mirror SST design. Thus, a larger array of SSTs, and therefore an increased area coverage at fixed cost and telescope spacing is possible when using a dual-mirror design for the SSTs.

Two such designs are currently being prototyped for the SSTs of CTA: The Gamma-ray Cherenkov Telescope (GCT) [92, 93] situated at the Observatory of Paris in Meudon (France) and the Astrofisica con Specchi a Tecnologia Replicante Italiana (ASTRI)-Horn telescope [94] located at the Italian National Institute for Astrophysics on Mount Etna in Sicily (Italy).

CHEC is a proposed camera for the dual-mirror SST design. It is suitable to be used with both design, as has been verified by dedicated on-sky observation campaigns with CHEC
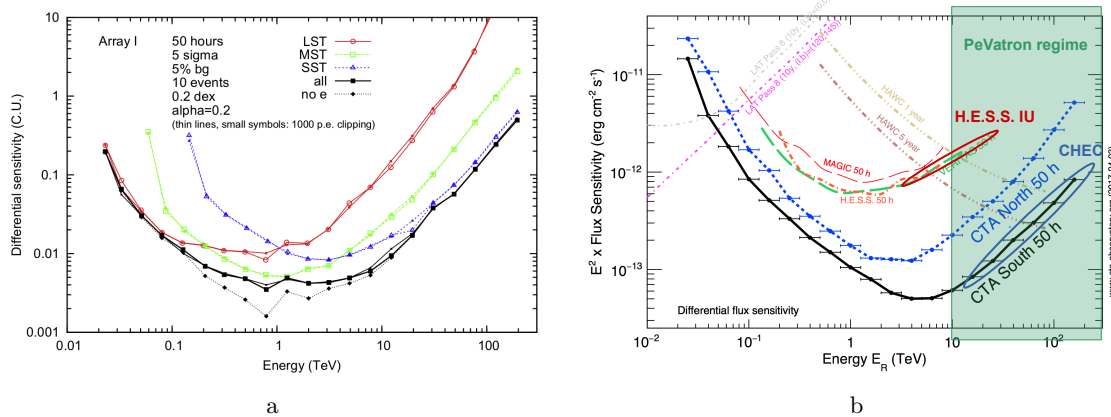
**Figure 3.16** Point source differential sensitivity of CTA: (a) Contribution of the individual telescope types. For this study, an array consisting of three LSTs (red, open circles), 18 MSTs (green, open squares), and 56 SSTs (blue, open triangles) were assumed. Thin lines with small symbols illustrate the limited impact of a reduced dynamic range of PMT readout electronics. The relevance of the electron background on the combined sensitivity is shown by the dashed black line with diamonds, where this background is ignored. More details given in [86] where this figure is adapted from. (b) In comparison with other experiments (note that the curves shown allow only a rough comparison due to different methods of calculations, cf. [85] for more details). Furthermore, the expected sensitivity improvement of H.E.S.S. (thanks to the use of SM with H.E.S.S. IU), the part of the CTA sensitivity covered by the CHEC camera, as well as the PeVatron regime (energy range in which VHE $\gamma$-ray detection indicates the observed source to be a PeVatron candidate) is indicated. Reproduced from [85].

being installed on either of the telescope prototypes (cf. Fig. 3.18 and Sec. 5.11 & 6.5). Under the main lead of the Max-Planck Institut für Kernphysik Heidelberg (MPIK), research and development for CHEC is progressing via the development of two prototype cameras: CHEC-M, based on MAPMs, and CHEC-S, based on SiPMs. Details about the technical design of both prototypes will be presented in Ch. 4. Furthermore, the technical work on the hardware and software as well as performance and characterisation tests with both prototypes were major topics explored in the scope of the thesis and will be presented in Ch. 5 & 6.

Recently, the final SST design was chosen to be based on the ASTRI-Horn telescope structure equipped with a CHEC-like camera. Possible design iteration are currently under investigation for both, the telescope structure and camera, while the work presented in this thesis is used as a valuable input for the design iteration of CHEC.

### 3.2.4  Commonalities between CHEC and H.E.S.S. IU

Even though the technology (such as electronics and photosensors) of CHEC and H.E.S.S. IU is different, they show several commonalities in the data format and science goals. As mentioned previously, H.E.S.S. IU provides full-waveform readout as does CHEC. This improves the performance especially at the upper energy limit, but also the reconstruction of lower VHE events.

**Improvements at high-energies**   Events with a large time gradient are very often truncated in CM since the signal in each pixel is integrated in a fixed time window after the camera trigger (16 ns in H.E.S.S.). In SM however, more sophisticated methods to extract
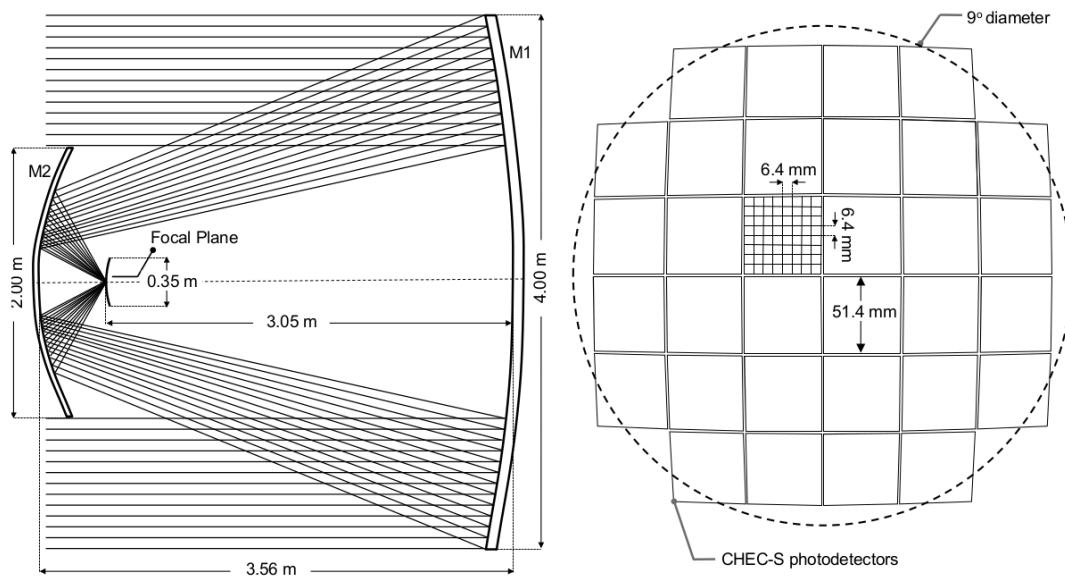
**Figure 3.17** A schematic showing an overview of the Schwarzschild-Couder dual-mirror SST geometry (left), and SST-camera geometry (showing the exact dimensions in case of CHEC-S) as viewed towards the camera face (right). Adapted from [90].

the pixel charge exist, such as the integration in smaller time windows along the Cherenkov image time gradient to avoid truncation (cf. Ch 8 for further details). Fig. 3.19 illustrates this effect. It shows a Cherenkov event observed with H.E.S.S. IU, read out in SM, and the waveform of four pixels along the time gradient of the Cherenkov signal with the CM integration window indicated. In the latter case the Cherenkov signal is detected only by half of the pixels since for pixels with peak times >16 ns the signal lies outside of the integration window. Due to geometry (cf. Fig. 3.8), Cherenkov images of EASs with high impact distances typically show a long time gradient (often >16 ns). At the same time, since the lateral Cherenkov photon density in an EAS increases with the primary $\gamma$-ray energy, Cherenkov events detected at high impact distances are typically high-energy events. Thus, SM readout is expected to improve the performance especially at the upper end of the energy range of an IACT (cf. Fig. 3.16b for expected improvement of the H.E.S.S. sensitivity thanks to SM readout with H.E.S.S. IU). This is of particular interest for the search for PeVatrons as the detection of $\gamma$-rays with $E_\gamma > 10$ TeV is a basic requrienment for a source to be classified as a PeVatron candidate. Even though CTA promises a much higher sensitivity at this energy than H.E.S.S., the H.E.S.S. IU SM readout can bridge this gap until CTA is fully operational and, at the same time, serve as a playground for the development of analysis methods for SM data.

**Improvements at low energies** Integrating smaller time windows reduces the number of integrated NSB photons and thus increases the signal-to-noise ratio. This is of special interest for faint (typically low-energy) events where SM data can help to lower the energy threshold.

a                                                          b

**Figure 3.18** Pictures, taken during on-telescope campaigns with different CHEC prototypes (CHEC-M and CHEC-S) being installed on the prototypes of GCT and of the ASTRI-Horn telescope: (a) CHEC-M on GCT and (b) CHEC-S on ASTRI-Horn. The red arrow in each picture indicates the mounting position of CHEC.

### 3.2.5 Data reconstruction and analysis procedure

The analysis of VHE $\gamma$-ray observations consists of different data processing steps to go from raw data (measured charges in individual camera pixels) via camera images (characterised by e.g. the Hillas length, width, and amplitude) to final event lists, spectra, and morphological images of sources (so-called maps). For this purpose,

1. the instrument, i.e. details of the camera electronics and optical system, must be well understood and calibrated,

2. an algorithm to clean (preselect) and parameterise the calibrated data and to perform $\gamma$-hadron-separation must exist,

3. deep MC simulations must exist reflecting both the EAS and camera behaviour as close as possible to reality to produce the so-called instrument response functions (IRFs),

4. the IRFs have to be applied on the data for direction and energy reconstruction, and

5. a source analysis scheme taking into account observation methods and background subtraction must be in place.

The different steps of this procedure will be explained in the following paragraphs in general but also with a special emphasis on the tools used in H.E.S.S. (Heidelberg (HD) chain[2]) and/or CTA.

---

[2]Two calibration and analysis chains exist in H.E.S.S., referred to as Paris (PA) and HD chain. The way the data is processed and analysed in both chains is fundamentally different (e.g. different MC simulation softwares are used). Those fundamental differences are used to independently cross check results. This is why in general, a cross-check by the other analysis chain is always required by the H.E.S.S. collaboration before a result is approved to be publishable. In the scope of this thesis, only the HD chain was used.
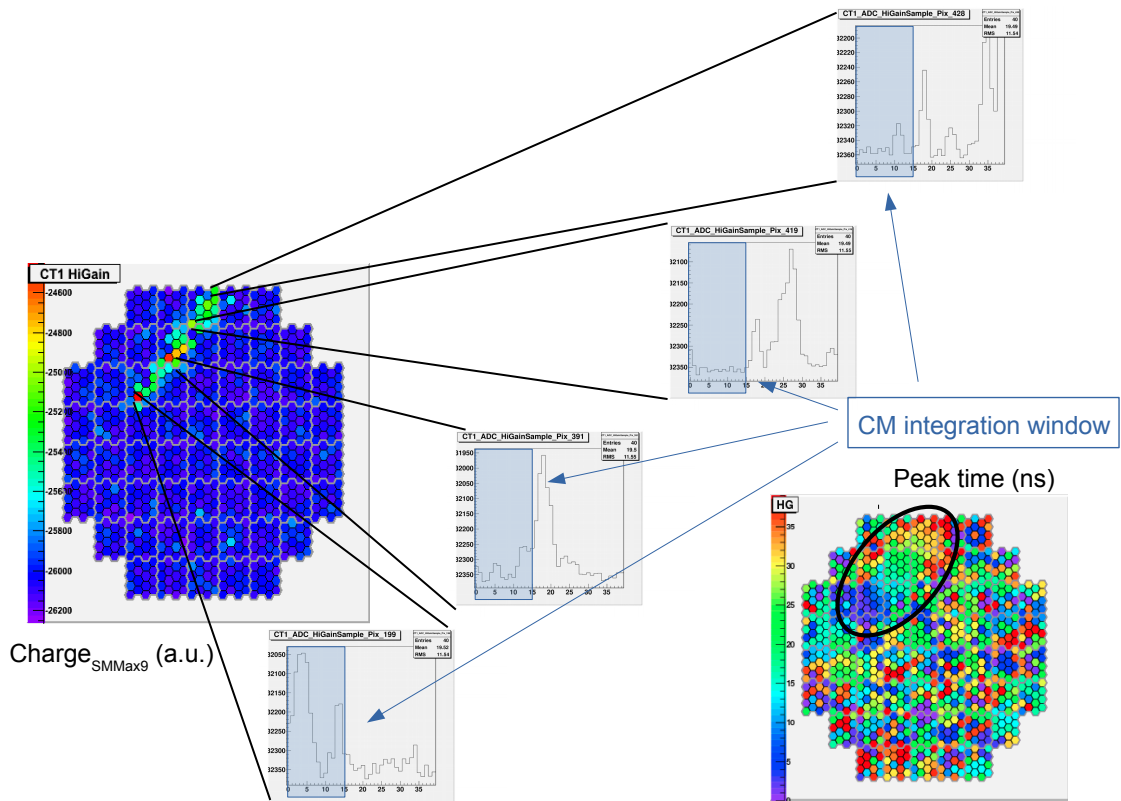
**Figure 3.19** Cherenkov event observed with H.E.S.S. IU and read out in SM. For details see text. Adapted from (Zorn, 2019) [69].

**Calibration**  The calibration procedure is used to remove any artefacts to be known to result from camera electronics including pedestal estimation and subtraction as well as to convert the charge (typically in ADC counts or any quantity proportional to the number of detected photons) of each pixel into a number of p.e. and then into a number of photons (taking into account the PDE of the photosensor and the optical efficiency of the optical system). In H.E.S.S., the resulting files of this process are called data data summary tapes (DSTs), in CTA, they are called data level 1 (DL1) files.

**Image cleaning and parameterisation**  Classical image processing proceeds first with cleaning the image, i.e. removing pixels not containing Cherenkov but NSB signal only. In H.E.S.S., for this purpose a so-called tail cut algorithm is applied, only keeping pixels which contain more then y (x) p.e. and having a neighbouring pixel with at least x (y) p.e. where x (y) is set to 5 (10) in nominal CM analyses. The next step typically consist of the determination of the so-called Hillas parameters, usually parameterising the image ellipse with a width and length parameter, which are then scaled per telescope and, in stereoscopic systems, the mean over all triggered telescopes is found [70]. Hillas parameters, including the centroid position of the ellipse and its distance from the camera centre, as well as the ellipse width and length, are calculated for each camera image. These parameters along with the image amplitude (total charge of all pixels passing the tail cuts) are used to characterise the image. Next, two further cuts are typically applied: A local-distance cut removing images with a centroid too far from the camera centre as they could be truncated, biasing the elliptical fit,

and a cut on the image amplitude (removing very faint images to increase the signal-to-noise ratio). The values used for the cuts depend on the individual analysis (cf. [95] for details).

**MC simulations and IRFs**   Unlike the direction reconstruction, which could be performed on the basis of the shower images only, the energy reconstruction needs further input from MC simulations. Look-up tables (also referred to as IRFs), generated from $\gamma$-ray-induced EAS and IACT MC simulations, are used to determine the primary particle energy according to the integrated image amplitude and the reconstructed impact parameter. The state-of-the-art tool for EAS simulation is `CORSIKA` [96], the simulation tool for the IACT description used in H.E.S.S. (HD chain) and CTA is `sim_telarray` [97]. For the latter one, hardware measurements (such as pulse shapes, response functions, gain settings, etc.) are required as input for the correct description of the camera behaviour in the simulation. In a next step, a validation of the simulation chain is needed – a process which was examined in detail in the scope of this work for the H.E.S.S. IU cameras (cf. Ch. 7).

**IRF application and $\gamma$-hadron separation**   As the numerically dominant hadron-induced EASs produce less elliptical images than $\gamma$-ray induced EAS, their difference in shape (cf. Fig. 3.9) can be exploited to suppress the hadronic background. Beside a very simple approach (just rejecting every non-ellipsoidal image as background), a more advanced algorithm using the produced IRFs is typically applied. It consists of comparing the extracted width $w_i$ and length $l_i$ of the shower image of telescope $i$ to the mean values ($<w_i>$ and $<l_i>$, respectively) expected from $\gamma$-ray MC simulations, given their image amplitude, impact distance, zenith angle, and offset from the system pointing direction. The difference is then scaled by the spread of the simulated distribution ($\sigma_{w,i}$ and $\sigma_{l,i}$, respectively) and averaged over all participating telescopes to yield the mean reduced scaled width ($MRSW$) and length ($MRSL$), given by

$$MRSW = \frac{1}{N_{\text{tel}}} \sum_i^{N_{\text{tel}}} \frac{w_i - <w_i>}{\sigma_{w,i}} \tag{3.14}$$

and similar for $MRSL$. Applying cuts on those parameters are very discriminating variables which can be used for $\gamma$-hadron separation, especially as it combines information from each telescope that views the same EAS from a different angle. Furthermore, as the hadronic background is isotropic, a restriction on the angular distance $\theta$ between reconstructed shower direction and the source position (in case no "blind" source searching is done) can be used to further suppress the residual hadronic background.

A more advanced algorithm for $\gamma$-hadron separation, increasing the sensitivity compared to the – robust but less sensitive – Hillas approach explained above, is based on multivariate analysis techniques. These techniques combine several EAS parameters into one number giving the likeness of an event with a $\gamma$-ray or CR. In H.E.S.S. a so-called boosted decision tree (BDT) method [98], provided by the TMVA package [99], is used to determine such a single parameter $\zeta_{\text{BDT}}$. In decision trees, at each branching, a binary split criterion (passed or failed) on one of the characterising input parameters is applied. In such a way, they classify events of unknown type as signal-like or background-like. The determination of these criteria is also referred to as training of a decision tree and is performed with a training set with events of known type.

In addition to the Hillas and BDT methods, the analysis tool `ImPACT`, based on likelihood fitting templates, provides another method for $\gamma$-hadron separation and is used in H.E.S.S. .

**Source analysis scheme**   The events passing the $\gamma$-hadron separation are so-called $\gamma$-like events meaning that the events look like $\gamma$-rays in terms of the parameters used for cuts. Since under certain circumstances depending on EAS geometry, observation angle, impact distance, etc., CR events look like $\gamma$-ray events, there always is a certain fraction of them among the $\gamma$-like events. To remove them from the "real" $\gamma$-ray events, the isotropic arrival direction characteristic of CRs is used. CRs can therefore be treated as a $\gamma$-like background present in all pixels of the FoV of a certain observation run which needs to be subtracted from the signal in each pixel. For the estimation of the $\gamma$-like background, different models exist which are summarised in [100]. For the scope of the thesis, two of them are of special interest and introduced below.

In the *ring background* approach, the background is estimated from a ring around the source position with a specified inner radius and thickness. The regions corresponding to that ring are referred to as OFF regions. The ON region is the region where $\gamma$-like events are detected from, typically the whole region of the FoV. In case of isolated point-like (typically extragalactic) sources, this approach is straight forward. In case of complex regions with multiple sources and/or in case of extended sources (as in case of Wd1, cf. Ch. 9) the size of the ring may be adapted across the FoV, either by varying the inner radius and keeping the ring thickness fixed, or vice versa. The method is then referred to as adaptive ring (AR) method. In this way, it is ensured that background estimates are taken from parts of the sky which are large enough and well beyond exclusion regions. The latter ones are masks which exclude regions of expected significant emission, such as the region around the source of interest and other known $\gamma$-ray sources in the FoV. In the estimation of the number of excess events $N_{\mathrm{excess}}$, being the number of events that remain after background subtraction, the dependence of the $\gamma$-ray acceptance on the camera pixel position (see below for further explanations), the differences in covered area as well as in exposure time of the ON and OFF regions have to be taken into account. The normalisation parameter $\alpha$ accounts for all those aspects and $N_{\mathrm{excess}}$ is therefore given by

$$N_{\mathrm{excess}} = N_{\mathrm{on}} - \alpha\, N_{\mathrm{off}}, \tag{3.15}$$

where $N_{\mathrm{on}}$ ($N_{\mathrm{off}}$) are the number of $\gamma$-like events detected in the ON (OFF) region.

In the *FoV background* approach, the $\gamma$-ray acceptance is used to estimate the background. To derive the acceptance for a given source region, the observation of an "empty" region of the sky, i.e. without known VHE $\gamma$-ray sources, performed at similar zenith angles as the observations of the source region, is used. Fig. 3.20 shows an example of the measured H.E.S.S. $\gamma$-ray acceptance map in an "empty" region (top left panel) and the model deduced from it (bottom left panel). Assuming radial symmetry, a radial profile can be computed for different energy and zenith angle ranges (right panel in Fig. 3.20). In the background estimation procedure, the $\gamma$-ray acceptance of each image pixel (given by the acceptance model) is then normalised to the total number of events detected outside the exclusion regions of the source region. In this way, a background estimate for all image pixels is deduced. The FoV background model is especially well suited for very extended sources that cover a large fraction of the FoV. Furthermore, since in this model $\alpha \to 0$, it yields the maximum possible signal significance $S$ [100]. The general formula for $S$ is given by Eq. 17 in [102], but simplifies for $\alpha \to 0$ to [103]

$$S = \sqrt{2 \left[ N_{\mathrm{on}} \ln\left( \frac{N_{\mathrm{on}}}{\alpha\, N_{\mathrm{off}}} \right) - N_{\mathrm{on}} + \alpha\, N_{\mathrm{off}} \right]}. \tag{3.16}$$

The caveat of this method is that it uses a model, i.e. it does not use an instantaneous measurement and therefore does not take into account the status of the instrument at the
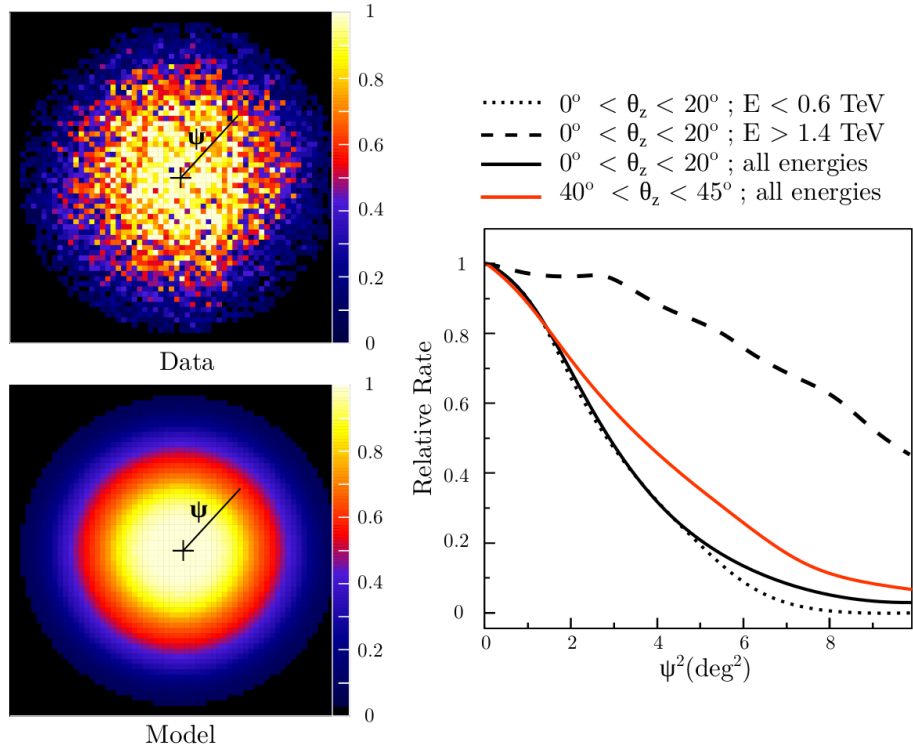
**Figure 3.20** (Top left) 2D image showing the measured H.E.S.S. $\gamma$-ray acceptance (normalised to central camera pixel) for a certain energy and zenith angle range. (Bottom left) Model deduced from the measurement. (Right) Radial profile of the H.E.S.S. $\gamma$-ray acceptance for different energy and zenith angle ranges, deduced from the model. Adapted from [101].

time of observation. Hence it is quite sensitive on deviations of the model from the true system acceptance. This is why the acceptance needs regular updating and best to be deduced from data.

Once the background has been estimated, the excess (cf. Eq. 3.15) and significance (cf. Eq. 3.16) can be calculated and so-called excess and significance maps can be produced. Furthermore, histograms showing the significance distribution for the source region and for regions used for the background estimation are typically used to evaluate the goodness of the background estimation and the significance of a detection. In case of a perfect background estimation, the background histogram is expected to be describable by a Gaussian distribution with $\mu = 0$ and $\sigma = 1$.

For better visualisation and identification of structures in the morphology of a region, the excess is often smoothed with a correlation radius $r_c$. In H.E.S.S., a correlation radius of 0.1° is typically used for point source analyses and a radius of 0.22° for the analysis of extended sources.

# Technical design of CHEC and data taking procedures

"My life is shaped by the urgent need to wander and observe, and my camera is my passport."

Steve McCurry

The prototype CHEC camera contains 2048 pixels instrumented as 32 Hamamatsu H109-66B MAPMs (CHEC-M) and 32 Hamamatsu S12642-1616PA-50 SiPMs (CHEC-S), respectively, each comprising 64 pixels of $\sim$6$\times$6 mm$^2$ and arranged in the curved focal plane to approximate the required radius of curvature of 1 m. Front-end electronics (FEE) modules connect to each photosensor providing full-waveform digitisation for every pixel channel and the first level (L1) of camera trigger. A backplane (BP) forms a (second-level, L2) camera trigger decision based on the trigger signals from all FEE modules. Data is read out from all FEE modules via data acquisition (DACQ) board(s) routed off-camera via fibre-optic links. A slow-control board (SB) intelligently controls power to camera components based on monitored environmental conditions. LED flashers, located in each corner of the focal plane, provide a calibration source. An internal network switch provides control connections to the SB, LED flashers, and DACQ board(s). A camera server PC, installed off-camera, runs software to collect data, control, and monitor the camera.

The general design and architecture of both prototypes are the same (cf. Fig. 4.1 for a comparison of both camera architectures). The major changes in the transition from CHEC-M to CHEC-S are the use of different photosensors, the splitting of the triggering and digitisation process from one ASIC per 16 pixels into two, and the upgrade from four 1 Gbps data links to one 10 Gbps one. Other system components were adapted to support this.

Fig 4.2 shows an annotated schematics of the internal structure with the individual components of CHEC-S. This is similar for CHEC-M. In the following sections, I will describe the individual components in detail: Camera mechanics and thermal control in Sec. 4.1, photosensors in Sec. 4.2, FEE in Sec. 4.3, back-end electronics (BEE) in Sec. 4.4, LED calibration flashers in Sec. 4.5, and power- and slow control in Sec. 4.6. In each case, I will point out commonalities and differences between both prototypes. Furthermore, I will present the control software (cf. Sec. 4.7) of which I have written and developed the main fraction in the scope of this work. Finally, I will introduce the data calibration and processing scheme of CHEC (cf. Sec. 4.8) and will give a short summary (cf. Sec. 4.9).
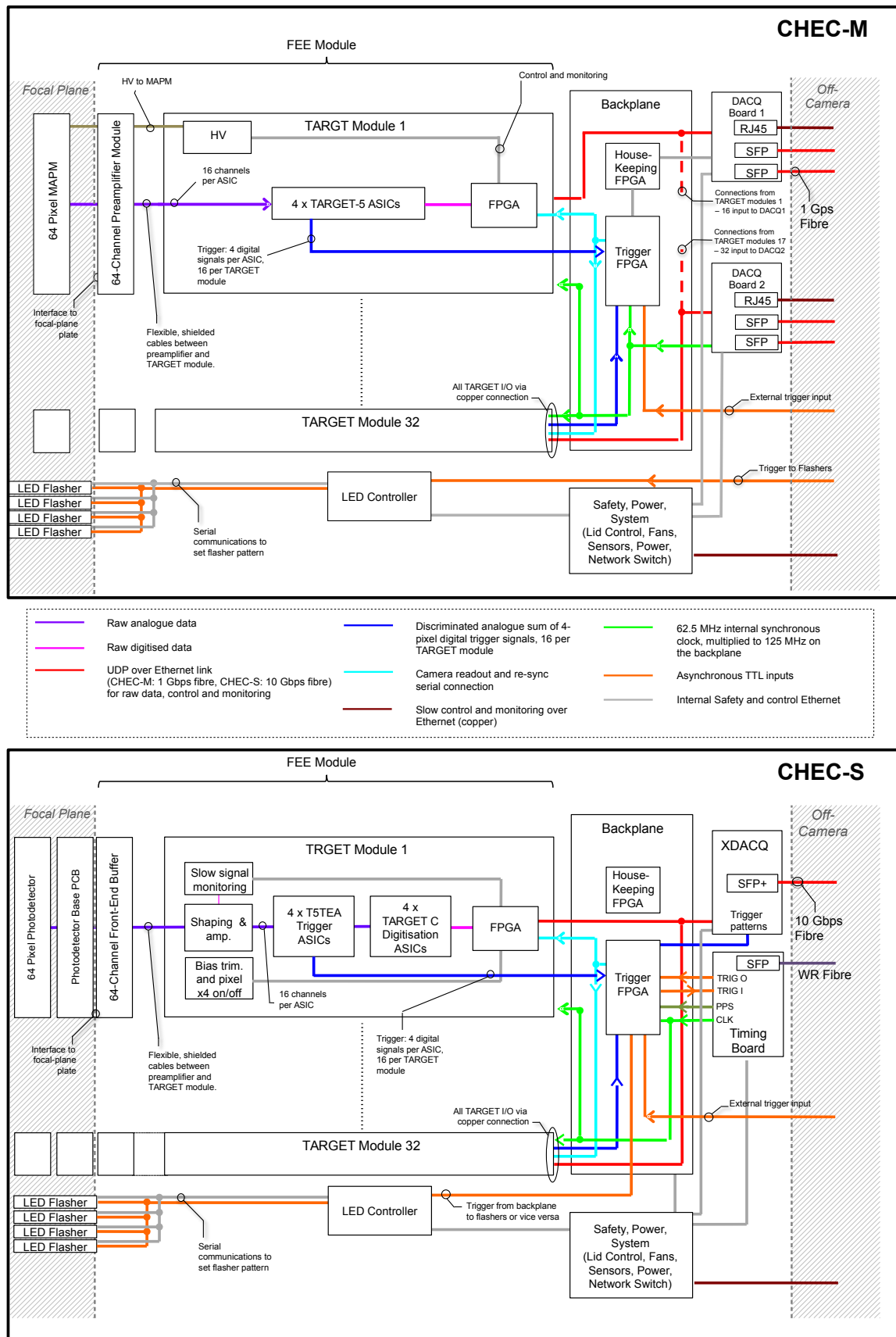
**Figure 4.1** Schematic showing the logical elements of CHEC-M and CHEC-S. The CHEC-M schematic was reproduced from [104].
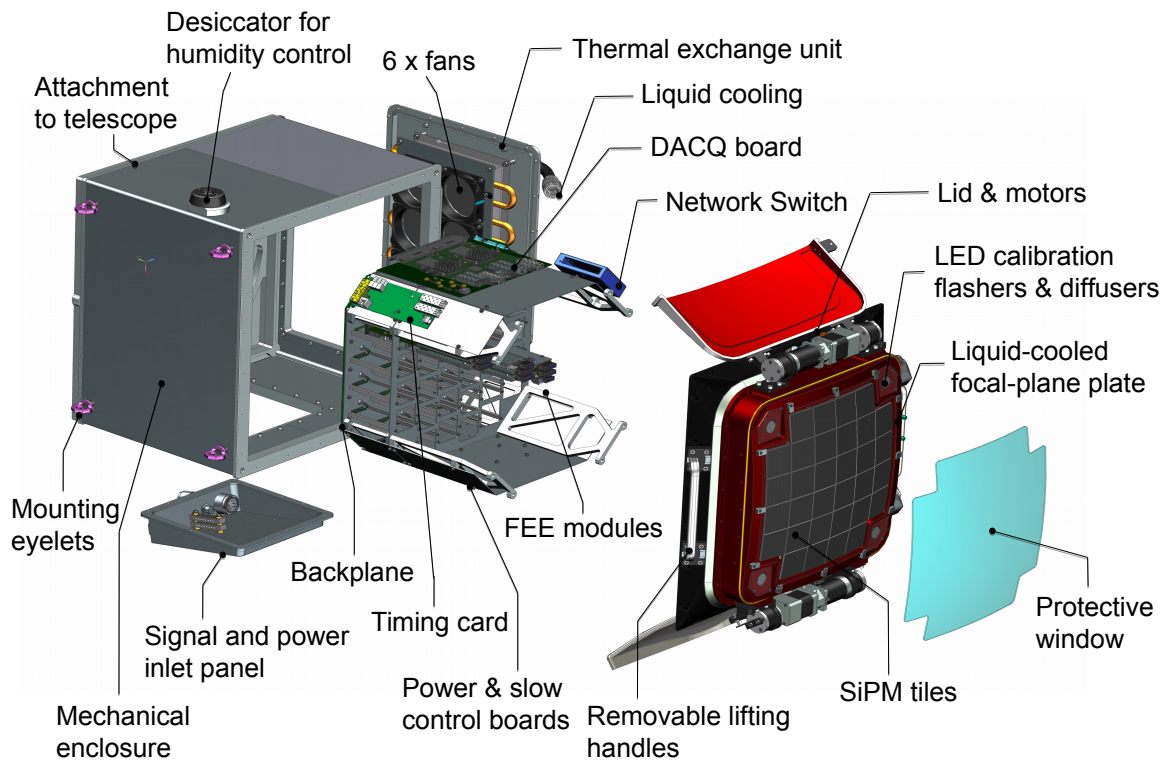
**Figure 4.2** Annotated CHEC-S schematics showing different hardware components. Adapted from (Zorn, 2018)[105].

Most of the information I will present in this chapter about CHEC-M has already been published and is therefore adapted from (Zorn et al., 2018) [106].

## 4.1 Camera mechanics and thermal control

### 4.1.1 Camera mechanics

The mechanical structure of CHEC is manufactured entirely from aluminium and consists of an external enclosure with focal-plane plate, an internal rack, a thermal exchange unit, a window (only in case of CHEC-S), and a lid. Fig. 4.3 shows annotated pictures taken from the front of both prototypes with the major mechanical elements highlighted.

The focal-plane plate located at the front of the camera is responsible for the accurate positioning of the photodetectors. As shown in Fig. 4.9a, the FEE modules are slotted through this plate and into the internal rack (same for both prototypes) with alternating orientation in a column (cf. Fig. 4.4). On the rear of the internal rack is an aluminium plate with through-holes and screws for securing the FEE modules and for electrical connectors. Once all FEE modules are secured, the internal rack is installed in the enclosure (cf. Fig. 4.9b) and the photodetector units are attached. The interface backplate at the rear of the camera provides a stable mounting point for attachment to the telescope structure.

There are two access panels in the enclosure sides, into which machined, removable aluminium panels are fastened. One access panel contains the feed-through for power cables and optical fibres via bulk-head connectors, whilst the other houses the thermal-control assembly. Both prototypes include a lid to protect against dust and liquid ingress. While in
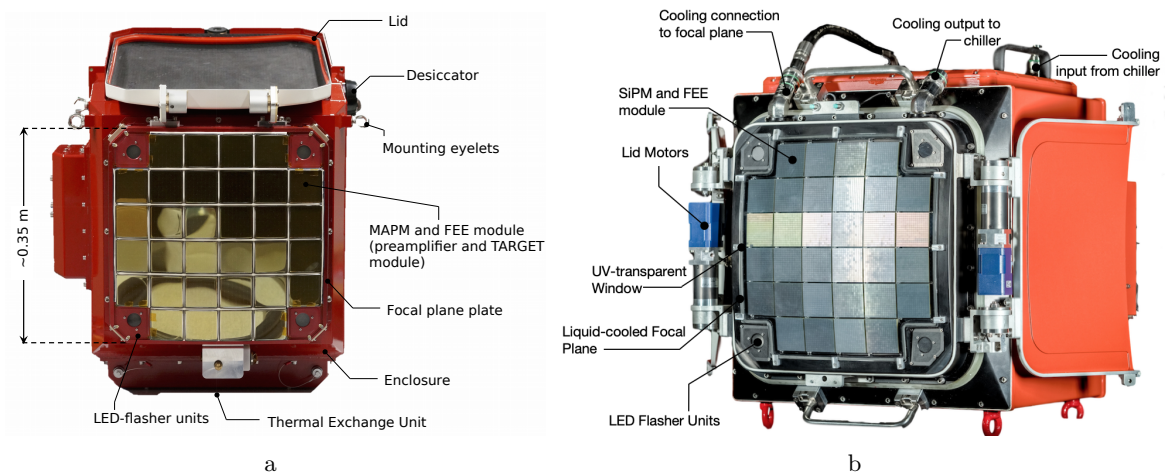
**Figure 4.3** Pictures of (a) CHEC-M and (b) CHEC-S with major elements indicated. (a) is adapted from (Zorn et al., 2018) [106], (b) from [107].

CHEC-M, the lid is operated manually, CHEC-S contains a motor for automatic closing and opening. In contrast to MAPMs, SiPMs are not covered by a protective glass. This is why CHEC-S contains an additional window to properly seal the camera enclosure and to protect the SiPM surface from dust and moisture. For the prototype, the window comprises a curved, ~3 mm thick piece of PMMA[1]. Both prototypes are painted with corrosion-resistant automotive paint.

### 4.1.2 Thermal control

The total power dissipation of CHEC-M / CHEC-S during normal operation is ~450 W / ~900 W (cf. investigations in Sec. 6.1). The thermal control system is designed to keep the camera temperature stable over a wide range of ambient temperatures up to the maximum required 25°C during normal operation and to protect the camera electronics up to an ambient temperature of 45°C. A breather desiccator removes humidity from the camera interior.

The thermal control system consists of four (CHEC-M) / six (CHEC-S) fans coupled to a liquid-cooled heat sink. The fans, together with a system of baffles, provide a recirculating airflow within the sealed camera enclosure. Since SiPMs show higher temperature dependence in their performances, in CHEC-S also the focal plane plate is liquid-cooled and attaches to the SiPM tiles via copper heat sinks which are bonded to the tiles. A temperature sensor is attached to each SiPM for temperature monitoring. A commercially available chilling unit (Rittal SK 3336.209) provides a flowing liquid (R134a: water glycol mixture) of controllable temperature. It delivers a cooling power of ~1.5 kW, and can operate over an ambient temperature range from −20 to 45°C. The unit weighs 97 kg (without liquid) and measures 485 mm × 965 mm × 650 mm. It is installed at the azimuth axis of the telescope and is connected by 3/4" pipes to the thermal exchange unit inside the camera. Quick-release non-leak couplings allow the chiller and the camera to be disconnected quickly from the telescope structure whilst preventing fluid loss or spillage.

---

[1]The final material is being explored for future iterations.
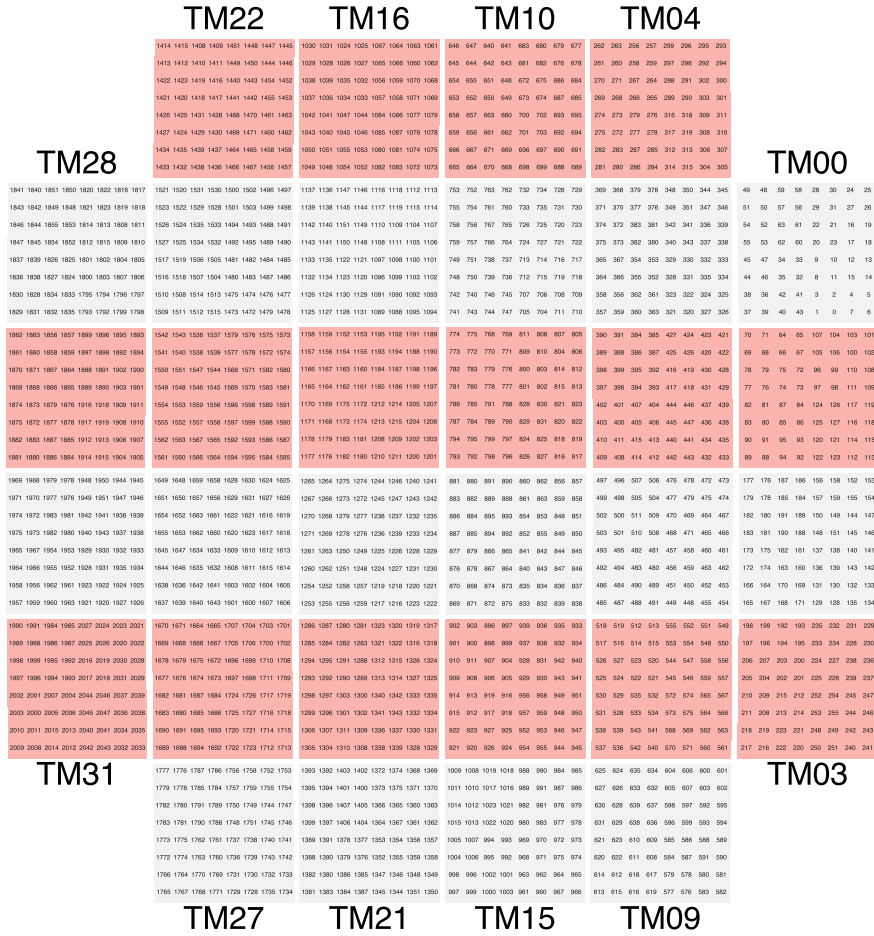
**Figure 4.4** Camera drawings showing the FEE module orientation when installed in the camera and on telescope, i.e. the top is towards the sky and the bottom towards the ground. Red background colour: orientation as shown in Fig. 4.8b, i.e. TARGET module (TM) power board on top, referred to as orientation A. White background colour: FEE rotated by 180°, i.e. TM primary board on top, referred to as orientation B. The pixel indexing is overlayed.

## 4.2  Photosensors

### 4.2.1  MAPM

A PMT is a very sensitive photon detector, typically providing a high dynamic range in photon detection from single up to thousands of photons. The detection mechanism is based on the photoelectric effect: photons hitting the photocathode are converted to photoelectrons. The probability for this conversion is given by the PDE $q$. The produced photoelectrons are then amplified by high electric fields in a multi-stage dynode system resulting in a measurable current at the anode. The gain $G$, describing the amplification factor of a PMT, is given by

$$G = \frac{n_{\text{p.e.,K}}}{n_{\text{e,A}}} \propto U^{\alpha}, \tag{4.1}$$

where $n_{\text{p.e.,K}}$ and $n_{\text{e,A}}$ are the number of photoelectrons produced at the photocathode and the number of electrons reaching the anode, respectively. It depends on the overall HV $U$ (internally divided and distributed to the individual dynode stages), typically ranging between
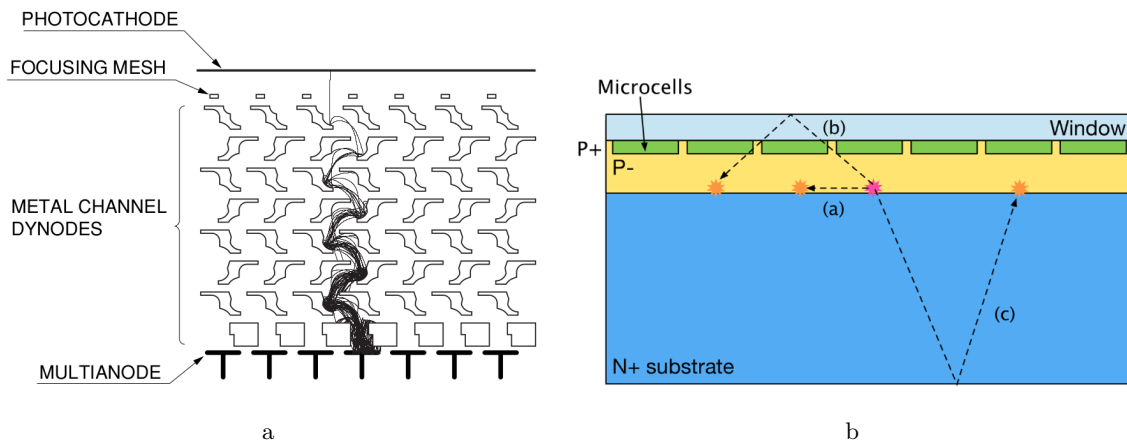
**Figure 4.5** (a) Annotated schematic drawing of an MAPM illustrating the electrode structure and electron trajectories (adapted from [108]). (b) Schematic drawing of a part of an SiPM pixel showing the PN junction and the different microcells. It also illustrates various ways in which secondary photons can travel to neighbouring microcells to cause optical crosstalk (adapted from [109]).

a few hundred to a few thousand volts, and an individual PMT-dependent parameter $\alpha$. The achievable gains typically lie in the order of $10^3$ to $10^6$. Fluctuations in the gain, resulting from multiplicative fluctuations in the amplification process of a PMT (e.g. fluctuations in the number of emitted electrons at each dynode), are expressed by the excess noise factor (ENF). As those fluctuations get reflected in the measured anode charge, single photoelectron (SPE) spectra (cf. Sec. 5.3 for SPE spectra of CHEC-M) can be used to determine the ENF value ($\sigma_{\mathrm{ENF}}$) for a given PMT via

$$\sigma_{\mathrm{ENF}} = \frac{\sqrt{\sigma_{\mathrm{Noise}}^2 - \sigma_{\mathrm{SPE}}^2}}{\gamma_e}, \tag{4.2}$$

with $\sigma_{\mathrm{Noise}}$ being the width of the noise and $\sigma_{\mathrm{SPE}}$ the width of the SPE peak of an SPE distribution, and $\gamma_e$ the SPE value, all resulting from an appropriate fit to the given SPE spectrum (as explained in detail in Sec. 5.3).

While a conventional PMT is a zero-dimensional detector, in which the spatial information of the intensity along the $x$- and $y$-axes is lost and summed by one large anode that intercepts all the secondary electrons, an MAPM provides a one or even two-dimensional spatial information of the intensity depending on its type (linear or matrix). The Hamamatsu H10966B MAPM used in CHEC-M is of matrix-type consisting of $8 \times 8$ pixels. Even though all pixels are assembled in the same housing consisting of only one photocathode, each has its own dynode system connecting to a single anode channel. Thus each pixel effectively functions as a single PMT (cf. Fig. 4.5a) with the caveat of a common HV for all pixels and therefore no control over pixel-wise gain adjustments.

The PDE $q$ of a PMT is the product of the wavelength-dependent quantum efficiency (QE) $\eta(\lambda)$ of the photocathode and the collection efficiency (CE) $\alpha$ of the first dynode, thus given by

$$q(\lambda) = \eta(\lambda)\,\alpha. \tag{4.3}$$

The Hamamatsu H10966B MAPM has a super-bialkali photocathode with a spectral response between $\sim$280 nm and $\sim$680 nm, peaking at $\sim$370 nm (cf. Fig. 4.6). The measured peak PDE is $\sim$31% with a peak QE of $\sim$36% and a peak CE of $\sim$85%. The high efficiency
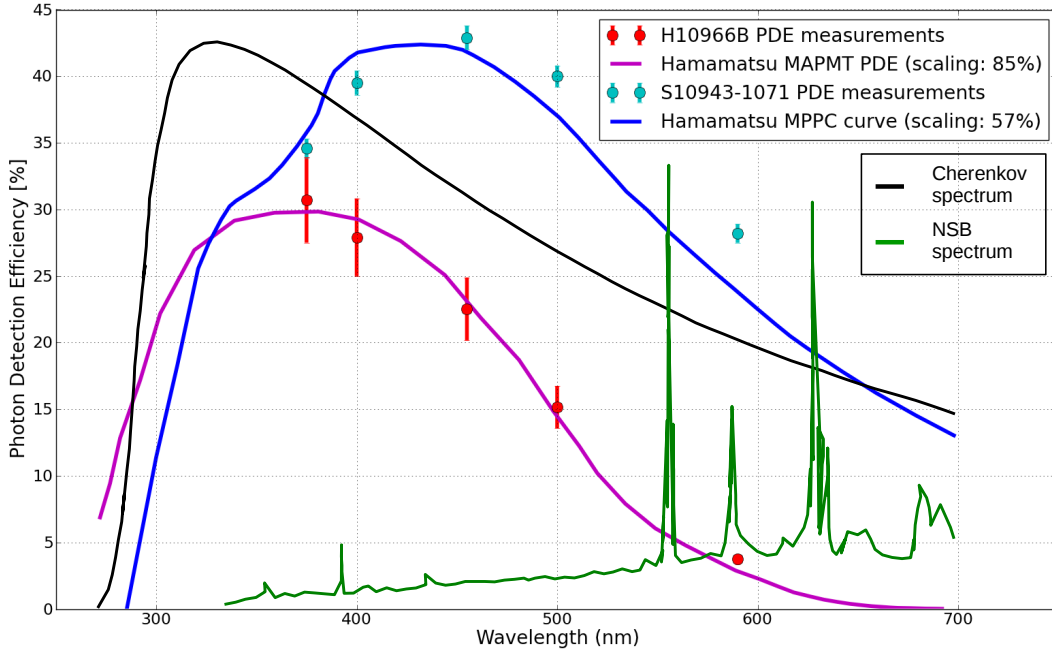
**Figure 4.6** PDE of the Hamamatsu H10966B MAPM (used in CHEC-M) and of Hamamatsu S10943-1071 SiPM (similar to the one used in CHEC-S) as function of the wavelength of the incident photon. Solid curves give an approximate fit to the data using a scaled version of the QE curves (provided by Hamamatsu for these devices) to account for the CE. Overplotted are the Cherenkov and NSB spectra in arbitrary units, extracted from Fig. 3.6a. Reproduced from [59].

in the blue and the low efficiency in the red makes it a suitable device for the detection of atmospheric Cherenkov photons (with their spectrum peaking at ∼320 nm) with a complementary suppression of most of the NSB signal (showing significant emission lines for wavelengths >550 nm, cf. Fig. 4.6).

The drawback of the achieved spatial information by using a dense packing of "individual PMTs" is crosstalk between different pixels mainly caused by

- the broadening of the electron flow when light is converted into electrons and those electrons are multiplied by multiple dynode sections [108] or

- by electrical crosstalk in the readout chain of the anode due to the marginal spatial distance between the channels making effective shielding difficult.

Crosstalk measurements have been carried out for the MAPM-preamplifier-chain of CHEC-M; results are presented in Sec. 5.6. Another drawback is that an MAPM takes only one HV source resulting in gain variation between pixels in the order of 10–30% depending on the HV. This is caused by small differences in the dynode system of each pixel resulting in different values for $\alpha$ in Eq. 4.1 and therefore causing the individual *G-U* curves to spread out. The gain spread has been measured for CHEC-M; results are presented in Sec. 5.3. For nominal operation, the MAPM gain is set to $8 \times 10^4$ resulting in a dynamic range extending from a single p.e./pixel to thousands of p.e./pixel (cf. investigations in Sec. 5.7). Furthermore, the MAPM produces output pulses with an FWHM of about 1 ns.

An MAPM pixel corresponds to a camera pixel. Its size is 6 mm × 6 mm corresponding to an average angular size of 0.15° when installed on the GCT telescope structure. The value

of $D_{80}$ (the diameter which contains 80% of the light resulting from a point source) for the telescope design is smaller than 6 mm over the full camera FoV once the telescope mirrors have been aligned. Due to the arrangement in a curved focal plane, a gap of $\sim$2 mm between the front of the MAPMs is required to accommodate their depth of 25.8$\pm$0.26 mm. When combined with the dead space at the edges of each MAPM, a total maximum dead space of $\sim$5 mm (corresponding to the gap between the corners of two MAPMs) is achieved.

## 4.2.2 SiPM

In contrast to a conventional PMT or MAPM, the photon detection with an SiPM is based on a different physical principle. SiPMs are semiconductors consisting of an array of avalanche photodiodes. Depending on the pixel size, one pixel contains several thousands of diodes referred to as microcells with a size of few tens of $\mu$m. Each microcell is a PN junction (cf. Fig. 4.5b) supplied with a reverse bias voltage above breakdown. This operation mode is called Geiger mode, in analogy to the Geiger counter. In this mode, a photon or thermal excitation may produce an electron-hole pair in the depleted region. Those charge carriers may in turn trigger an avalanche in a microcell ("fire the microcell") resulting in a high amplification of the incoming photon signal. A quench resistor is used to limit the current in the substrate and to reset the microcell to a quiet state for it to be photosensitive again. Thus, one avalanche is proportional to one electron-hole pair (also referred to as p.e. in analogy to PMTs) producing a highly uniform and quantised amount of charge. The signal of one SiPM pixel is the sum of the signal of all microcells, read out over their quenching resistor via a common output. The maximum number of microcells sets the upper limit of the dynamic range of a pixel, i.e. the maximum signal or maximum number of p.e. detectable synchronously.

The gain $G$ of a single SiPM microcell (and hence of an SiPM pixel) is defined as charge of a fired microcell divided by the elementary charge $e$, depending on both, the microcell capacitance $C$ and the applied over voltage $V_{OV}$. Hence,

$$G = \frac{C\,V_{OV}}{e}. \tag{4.4}$$

The achievable gains are of similar orders of magnitude as for PMTs and MAPMs.

The PDE $q$, being the probability that an incoming photon results in an avalanche, is not only a function of the likelihood of converting a photon into a photoelectron (being the QE $\eta$) but also depends on the avalanche initiation probability $\epsilon$ and the fill factor $F$. In case of a semiconductor, the QE is given by the probability that an electron moves from the valence band into the conduction band. This depends on the band gap and is therefore a function of the wavelength of the incoming photon only. $\epsilon$ takes into account the fact that not all charge carriers in the active volume will initiate an avalanche. The likelihood of an avalanche increases with increasing $\vec{E}$-field in the depletion region and therefore depends on $V_{OV}$. $F$ is the ratio of active to inactive area on the SiPM and results from the dead space between the microcells and therefore depends on the microcell size. In total it follows that

$$q(\lambda, V_{OV}) = \eta(\lambda)\,\epsilon(V_{OV})\,F. \tag{4.5}$$

Hence, the resulting PDE of an SiPM does not only depend on the wavelength of the incoming light, but also on the over voltage the SiPM is supplied with, a fundamental difference compared to MAPMs. An exemplary wavelength dependence of the PDE at a fixed over voltage of 1.65 V for the Hamamatsu S10943-1071 SiPM is shown in Fig. 4.6.
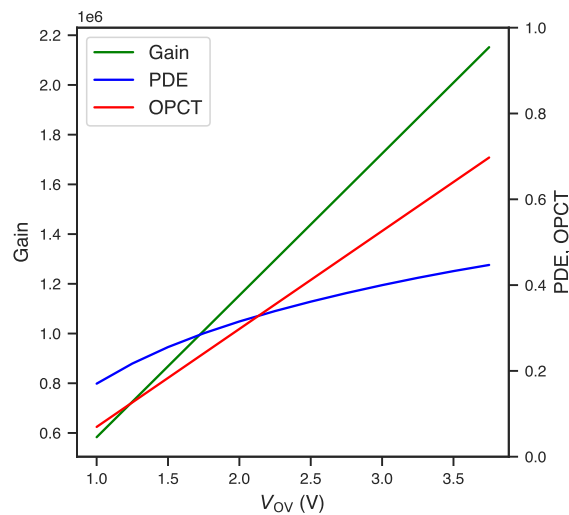
**Figure 4.7** Gain, PDE, and OPCT dependence on the over voltage for the Hamamatsu S12642-1616PA-50 SiPM tile. Adapted from [110].

The SiPM used in CHEC-S is a Hamamatsu S12642-1616PA-50 SiPM tile consisting of a surface-mount-type multi-pixel photon counter array using through-silicon via. It contains 16 × 16 pixels with a 3 mm × 3 mm effective photosensitive area each. Each pixel has a pitch of 50 $\mu$m and consists of 3584 cells. $F$ is 62%. The photosensitive area is covered by a thin-film coating ($\sim$20 $\mu$m-thick) with a refractive index of 1.55. Four SiPM pixels are combined to one camera pixel of same size as in CHEC-M so that the same number of readout channels can be used. One bias voltage is supplied to four neighbouring camera pixels, referred to as SP. The bias voltage is controlled by a digital-to-analog converter (DAC) with an 8-bit resolution and a calibrated step size of $-40$ mV per DAC count. Fig. 4.7 shows the dependence of the gain, PDE, and optical crosstalk (OPCT, cf. definition below) on the over voltage for the Hamamatsu S12642-1616PA-50 SiPM tile, measured at a wavelength of 408 nm.

Compared to PMTs/MAPMs, there a few (main) technical challenges to be tackled when using SiPMs:

- Temperature dependence:
  Many SiPM characteristics are subject to much stronger temperature dependencies than it is the case for PMTs. For example, the main source of noise is the dark count rate (DCR) primarily due to thermal electrons generated in the active volume. It can be suppressed by operating the SiPM at reasonably low temperatures like $\sim$20°C. The gain also shows a rather strong temperature dependence, changing by 3.7%/°C in case of the Hamamatsu S12642-1616PA-50 SiPM used in CHEC-S [110]. As a consequence, temperature stabilisation of the SiPMs is desirable (to avoid a significant reduction of the performance due to DCR) and precise monitoring of their temperature is crucial to be able to perform online and/or offline temperature correction of the SiPM parameters.

- Optical crosstalk:
  During avalanche, accelerated carriers in the high-field region will emit photons. These secondary photons tend to have wavelengths in the near infrared region and can travel substantial distances through the silicon. As shown in Fig. 4.5b, there are a number of different ways how these secondary photons may reach neighbouring microcells: (a) directly to a neighbouring microcell, (b) reflected from the window material on the top

of the sensor (usually epoxy or glass), or (c) reflected from the bottom of the silicon substrate. OPCT is defined as the probability that those secondary photons are not only emitted but also initiate a secondary avalanche in a neighbouring microcell. The process happens instantaneously and as a consequence, single incident photons may occasionally generate signals equivalent to two or three photons, or even higher. In the picture of a conventional PMT, this is what is expressed by the ENF. Hence, the ENF of an SiPM can be parameterised by [111]

$$\sigma_{\text{ENF}} \simeq 1 + P_{\text{OPCT}} \tag{4.6}$$

or

$$\sigma_{\text{ENF}} \simeq 1 + P_{\text{OPCT}} + 1.5 \, P_{\text{OPCT}}^2, \tag{4.7}$$

depending on whether a geometrical chain model of the OPCT behaviour (each single electron response is capable of only producing 1 or 0 further electron responses) or a branching Poisson model (each single electron response produces a Poisson distributed random number of further electron responses) is used. The number of p.e. produced in a microcell is therefore the convolution of the incident number of photons hitting this microcell (multiplied with the PDE) and the OPCT. Due to the increased number of carriers crossing the junction with increasing over voltage, the optical crosstalk also increases. A high OPCT worsens several performance parameters including charge resolution and trigger performance. Thus, in terms of OPCT, a low over voltage is desired. However, since a lower over voltage also results in a lower PDE and gain, a trade-off between OPCT and PDE/gain must been made.

- Sensitivity in the red:
  Even though the higher peak sensitivity achievable with SiPMs compared to PMTs and MAPMs in the atmospheric Cherenkov emission wavelength regime (cf. Fig. 4.6) is an advantage, the disadvantage is the SiPM sensitivity ranging also to higher wavelengths (in the red). This means SiPMs are by design also more sensitive to NSB photons resulting in a higher NSB level[2]. In case this is not acceptable performance-wise, a filter or coated window may be used.

Despite the technical challenges the advantages in using SiPMs in CHEC outweigh the disadvantages. Those are among other things

- higher peak-PDE,

- magnetic-field independence,

- use of moderate voltages (70 V compared to 1000 V),

- robustness against high-background illuminations, especially desirable for atmospheric Cherenkov observations under moonlight or when crossing the moon during a source position change (no HV reduction or switch off necessary),

- smaller depth of an SiPM compared to an MAPM tile allowing a smaller gap between the front of the SiPMs in the curved focal plane and thus increasing the active area,

- better angular response since no protective glass as in case of MAPMs is needed,

---

[2]Throughout the thesis, the NSB level is defined as a p.e. rate, i.e. number of p.e. induced by NSB photons per pixel and second.

**Table 4.1** ASIC parameters relevant in the scope of this work and their functionalities.

| Parameter name | Functionality |
|---|---|
| `Pmtref4` | sets the reference voltage for the summing amplifier, used to set the L1 trigger threshold |
| `Thresh` | sets the reference voltage for the comparators, used to set the L1 trigger threshold |
| `Wbias` | sets the length of the digital L1 trigger output signal |
| `Vped` | sets the pedestal voltage of each pixel, used for common-mode noise rejection and as a reference to fix the L1 trigger threshold |
| `Isel` | sets the control current to ramp the slope circuit, used to maximise the range in which the transfer function is linear |

- possibility of setting the voltage SP-wise instead of for the full tile (as in case of MAPMs) reducing the gain spread and thus improving the trigger uniformity,

- simple gain determination using SPE spectra from dark counts,

- manufacture of SiPMs being simpler and at a lower cost than MAPMs with the price per mm$^2$ continuously decreasing so that in near future it will be less than for any other photomultiplier technology, and

- active development of SiPMs, being a rather new technology and used in many other areas such as medical devices while PMTs and MAPMs have been on the market for more than 50 yr with very little active development going on at present.

## 4.3 Front-end electronics

The FEE modules developed for CHEC-M and CHEC-S, shown in Fig. 4.8, consist of a preamplifier module (CHEC-M) / buffer board (CHEC-S) connected to a TM based around TARGET ASICs, 16-channel devices for digitisation, and trigger functionalities [91, 112, 113]. The ASICs are configured via hundreds of parameters. An overview of the ones being relevant and investigated in the scope of this thesis is given in Tab. 4.1.

In case of CHEC-M, four TARGET-5 ASICs are used where each provides digitisation and trigger functionalities for 16 camera pixels. Due to noise effects observed during the commissioning of CHEC-M (cf. Sec. 4.4.1), digitisation and trigger functionalities are split into two different ASICs in case of CHEC-S and an improved electrical shielding mechanism for all switching components is used. This is why each CHEC-S FEE-module contains eight ASICs: four T5TEA ASICs providing trigger functionalities and four TARGET-C ASICs for signal digitisation (in both cases one ASIC is connected to 16 camera pixels).

The photodetectors produce narrow pulses that must be shaped to optimise the camera trigger performance. Simulations show that the optimal pulse FWHM for triggering is around 5 to 10 ns with a 10-90% risetime of 2 to 6 ns. If the pulses are faster, the time gradient of Cherenkov images across neighbouring pixels forming the analogue sum prevents pile-up to reach the trigger threshold. If they are slower, NSB photons limit the performance of the camera trigger.

Samtec 40 pin connector to the backplane carrying raw data, trigger and sync signals and power

Xilinx Spartan 6 FPGA *(on reverse of PCB)*

Samtec individually shielded coaxial ribbon cables for analogue signals and preamplifier power

Preamplifier module consisting of 4 x 16 channel preamplifier boards

Front-most FEE PCB forming the interface to the focal plane plate

Mechanical standoff with threaded hole for securing the *TARGET* module to the backplane

High Voltage supply *(12 V in, 0 – 1200 V out, 12 bit resolution)*

*TARGET* ASIC providing 16 channels of digitisation and triggering

Individual amplifier circuit

High Voltage connection to the MAPM *(cable secured and pins insulated during normal operation)*

MAPM *(Hamamatsu H10966B)*

a

Samtec 40 pin connector to the backplane carrying raw data, trigger, clock signals, electronics power (12 V) and SiPM bias voltage (~70 V)

Power board provides low voltages, SiPM bias voltage trimming and monitoring

Shielding for all switching components and ASICs

SiPM bias voltage

Low-voltage power on separate cable to buffer

Front-most front-end buffer PCB forming the interface to the focal plane plate

Copper heat-sink arrangement to focal plane plate

Primary board and auxiliary boards each contain 32 channels of readout

TARGET C and T5TEA ASICs provide 16 channels of digitisation and triggering. Slow ADCs provide a parallel readout stream for monitoring of DC signal component

Amplifier and shaper circuits for optimal signal-to-noise

Cables used to remove radius of curvature in focal plane

Samtec individually shielded coaxial ribbon cables for analogue signals

Temperature sensor

Buffer circuits for noise immunity

SiPM Tile

~50 mm

b

**Figure 4.8** Annotated pictures of (a) an MAPM attached to a CHEC-M FEE module consisting of preamplifier-amplifier module, ribbon cables, and TM based around four TARGET 5 ASICs (adapted from (Zorn et al., 2018) [106]) and (b) an SiPM attached to a CHEC-S FEE module consisting of a buffer PCB, ribbon cables, and TM based around four TARGET C and four T5TEA ASICs (adapted from (Zorn, 2018) [105]).

In CHEC-M, the signals are preamplified and shaped by a preamplifier module connecting

directly to the photosensor to provide noise immunity for signal transport to the TM. The signal is then routed to the TM via individually shielded ribbon cables. Their use minimises the influence of noise and provides the flexible connection to the curved focal plane, allowing the use of a planar internal rack to house the modules. In CHEC-S, a thin buffer board connects to the photosensor from where the signal is routed to the TM via Ribbon cables. The signal amplification and shaping is done on the TM itself.

Each TM provides 64 channels of digitisation and first-level triggering. For this purpose, both the signal and a reference signal (set via `Vped`) are input to each ASIC and simultaneously processed for sampling (data path) and triggering (trigger path). The TARGET-5 / TARGET-C ASIC is an analogue sampling chip and capable of digitising signals with 12-bit resolution. It provides an effective dynamic range of 1 to ∼500 p.e./pixel (with the recovery of larger signals offline possible due to the full-waveform digitisation). The sampling rate is tunable, set to 1 GSa/s for the use in CHEC. Two capacitor arrays are used – a 64 ns deep analogue sampling array followed by a storage array with a maximum depth of 16384 ns – to simultaneously achieve a large analogue bandwidth and a deep buffer. Acquisition occurs in one group of 32 cells in the sampling array while the charge of the cells of the other group is transferred to the storage array cells. Such a ping-pong approach provides continuous sampling (cf. [91] for further details). The position of the readout window digitised from storage array is settable in 32 ns blocks, nominally set to 128 ns for CHEC (chosen to capture high-energy, off-axis events and/or events with a high impact parameter as they transit through the FoV).

A field programmable gate array (FPGA) – a Xilinx Spartan-6 in CHEC-M and an ARTIX-7 in CHEC-S – on board each TM is used to configure the ASICs and other module components, to read out raw data from the ASICs, and to package and buffer raw data for output from the module. Module control and raw data output are managed via user datagram protocol (UDP) over a 1 Gbps Ethernet link at the rear of the modules. The data size $S$ per event is given by

$$S = t\,p\,s_p \tag{4.8}$$

where $t$ is the number of TMs and $p$ is the number of packets per event and TM. $s_p$ is the size per packet and is given by

$$s_p = x\,s\,b + h_{\text{Ethernet}} + h_{\text{TM}} + h_{\text{pix}}\,x, \tag{4.9}$$

where $x$ is the number of pixels per packet, $s$ the number of samples per pixel, $b = 0.002$ kB the data size per sample, $h_{\text{Ethernet}} = 0.028$ kB the Ethernet header size, $h_{\text{TM}} = 0.026$ kB the TM header size, and $h_{\text{pix}} = 0.002$ kB the header size per pixel. With the settings as they are implemented in CHEC ($s = 128$, $p = 2$, and $x = 32$), this adds up to

$$s_p = 8.310\,\text{kB}, \tag{4.10}$$

and hence to a total event size of

$$S = 32 \times 2 \times 8.310\,\text{kB} \simeq 532\,\text{kB}, \tag{4.11}$$

The TARGET-5 / TARGET-C ASIC is continuously sampling and dead time free, i.e. sampling continues while data is being digitised.

In case of CHEC-M, the TARGET-5 ASICs also provide the L1 trigger of the camera; in CHEC-S this is provided by the T5TEA ASIC. In both cases, the trigger is based on the analogue sum of a square of four neighbouring pixels (forming an SP), which is then discriminated. The threshold for discrimination is set individually for each SP by the combination

of the two ASIC parameters `Pmtref4` and `Thresh`. There is a certain range of combinations of those parameters for which the trigger functions properly and different combinations can lead to the same trigger threshold but with a slightly different trigger noise levels (cf. [112] for detailed information and test results). A full camera trigger threshold setting consists of 512 (32 × 16) possibly different pairs of `Pmtref4` and `Thresh`. Each ASIC outputs four digital trigger signals of settable length via the ASIC parameter `Wbias` (cf. Fig. 29 in [114] for calibration), which are routed through the module to the BP, resulting in 16 differential LVDS trigger signals per module and 512 (32 × 16) in total for the whole camera.

In case of CHEC-M, the HV required by the MAPMs is generated on board of the TMs, i.e. the outside of the camera is isolated from any HV source. In case of CHEC-S, the 70 V (less human safety critical) to set the bias voltage of the SiPMs is provided by the power supply and routed – similar as the main 12 V power – to the camera and internally via the BP to the TMs (cf. Sec. 4.6.2). Each TM consists of 16 regulators with output voltage control via a digital potentiometer with 8-bit resolution to en-/disable and to set the bias voltage for each SP individually improving the gain uniformity.

Furthermore, the CHEC-S TMs feature the continuous digitisation and readout of the slow SiPM signal of each camera pixel in a data stream in parallel to the nominal data stream. The slow signal provides information about the NSB level in each pixel and hence about stars in the camera FoV. This is not only useful for internal real-time camera feedback (e.g. whether a bright SP should be masked or switched off to avoid it dominating the camera trigger) but also for telescope tracking purposes. When using the slow signal no additional telescope tracking camera is needed.

Each FEE module accepts a 12 V input for all electronics use and consumes ∼8 W (CHEC-M) / ∼18 W (CHEC-S) of power during full operation.

## 4.4 Back-end electronics

The back-end electronics (BEE) consist of a BP and two DACQ boards (CHEC-M) / one DACQ board (CHEC-S). Fig. 4.9 shows pictures of CHEC-M and CHEC-S taken from the back with and without the camera installed in the external enclosure. In Fig. 4.9a the main BEE elements are annotated.

### 4.4.1 Backplane

The BP provides the power, clock, trigger, and data interface to the FEE modules. Data links to the FEE modules are routed via the BP to the DACQ board(s). CHEC-M and CHEC-S contain different BP versions (version 1 and 2). While many features and implementations are the same in both versions – also the optical appearance is similar (cf. Fig. 4.9) –, there are a few major differences or additional features in version 2. They will be mentioned separately.

The BP triggering scheme is implemented in a single Xilinx Virtex-6 FPGA, referred to herein as the trigger FPGA (TFPGA). It accepts all 512 L1 trigger lines from the FEE modules and implements a flexible L2 trigger algorithm based on time coincidence of L1 triggers. In general, the accidental trigger rate $f$, i.e. a trigger fired due to accidental (uncorrelated) signals, of a trigger algorithm based on coincidence is given by

$$f = \sum_{i=1}^{N_{\text{comb}}} \left( \prod_{n=0}^{N} f_{\text{in}} \, t_{\text{coinc}}^{N-1} \right), \tag{4.12}$$

a                                                                          b
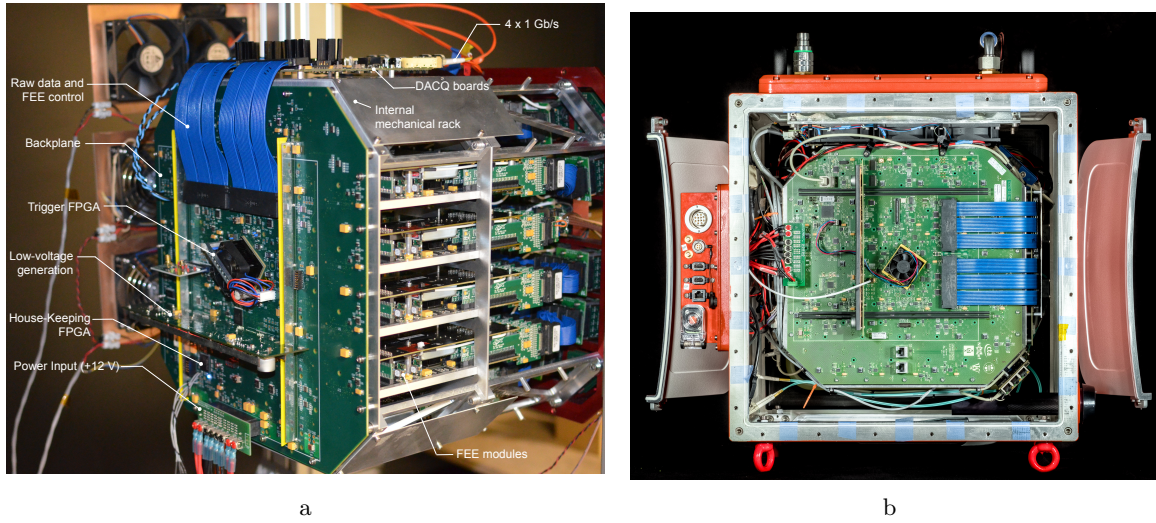
**Figure 4.9** (a) Annotated picture of CHEC-M without the external enclosure in place, taken from the back to highlight the BP. The TMs can be seen inserted into the internal rack mechanics, whilst the DACQ boards can be seen at the top of the rack, attached to the BP via two large Samtec ribbon cables. Adapted from (Zorn et al., 2018) [106]. (b) A picture of CHEC-S taken from the back to highlight the upgraded BP (version 2) and to illustrate how the internal rack is installed in the camera enclosure.

with $N_{\mathrm{comb}}$ being the number of combinations able to fire a trigger, $N$ the number of individual members in such a combination, $f_{\mathrm{in}}$ the individual trigger rate of each individual member, and $t_{\mathrm{coinc}}$ the coincidence time window. Optimised for atmospheric Cherenkov measurements with CHEC, the algorithm is set to a next neighbour (NN) logic with a coincidence window of 8 ns, i.e. an L2-trigger is formed in case at least two L1 triggers of neighbouring SPs ($N = 2$) occur within 8 ns (cf. Fig. 4.10). Thus, Eq. 4.12 is simplified to

$$f_{\mathrm{j}}^{\mathrm{L2}} = \sum_{\mathrm{i}=1}^{N_{\mathrm{comb}}} f_{\mathrm{a,ji}}^{\mathrm{L1}} f_{\mathrm{b,ji}}^{\mathrm{L1}} t_{\mathrm{coinc}}, \tag{4.13}$$

with $f_{\mathrm{j}}^{\mathrm{L2}}$ being the L2 trigger rate at threshold $j$ and $f_{\mathrm{a,ji}}^{\mathrm{L1}}$ and $f_{\mathrm{b,ji}}^{\mathrm{L1}}$ are the L1 trigger rates of the SPs that are NNs for the given combination i. The coincidence window is defined by the length of the logical L1 trigger output signals (cf. Sec. 4.3). An L2 trigger is formed on the falling edge of the logical sum of two or more L1 triggers overlaying in the coincidence window. This means, in case of a theoretical accidental L2 trigger rate of $>1/(2\,t_{\mathrm{coinc}})$, the logical sum never falls back to 0 which is why the measured L2 trigger rate will be 0.

Given the camera geometry and the number of 512 SPs, the maximum number of valid NN-SP combinations that may form an L2 trigger can be calculated to

$$
\begin{aligned}
N_{\mathrm{comb}} = (8 \times 512 \quad &\text{start with assumption of 512 SPs with eight neighbours} \\
- 72 \times 3 \quad &\text{72 SPs with only 5 neighbours} \\
- 8 \times 5 \quad &\text{8 SPs with only 3 neighbours} \\
- 8 \times 2 \quad &\text{8 SPs with only 6 neighbours} \\
- 4 \times 1) \quad &\text{4 SPs with only 7 neighbours} \\
\times 0.5 \quad &\text{count each SP only once} \\
= 1910
\end{aligned}
\tag{4.14}
$$
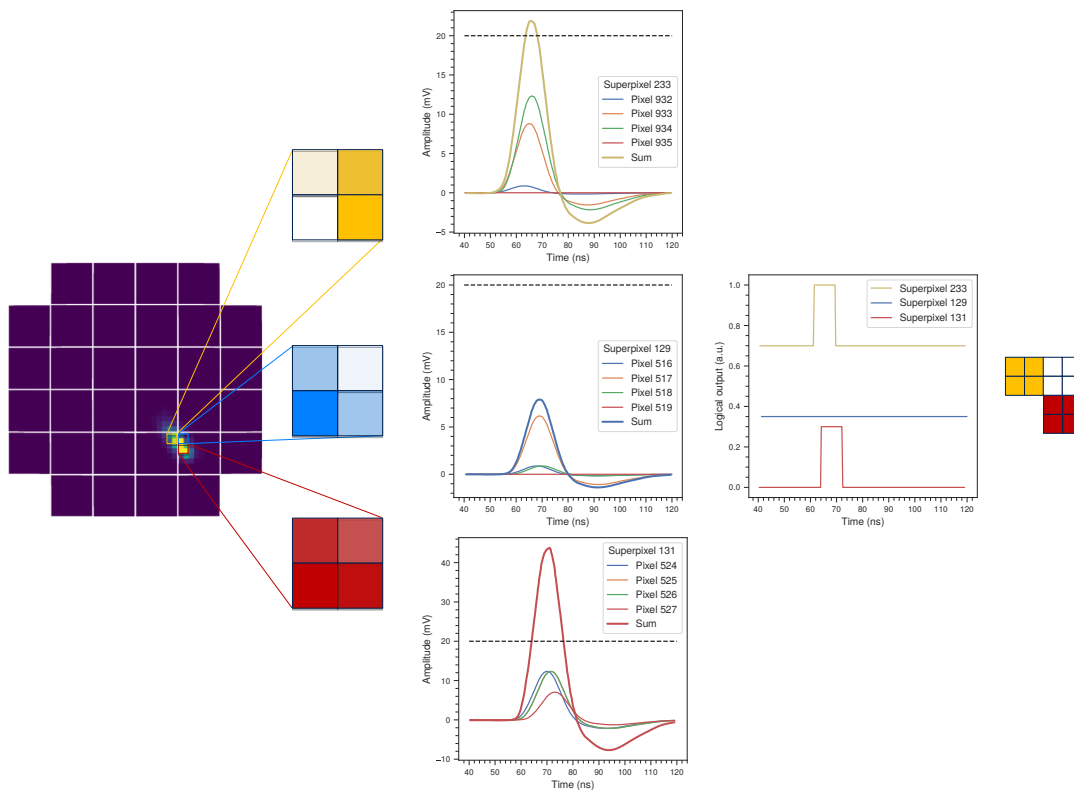
**Figure 4.10** Drawing illustrating the two-level trigger logic implemented in CHEC. It shows a Cherenkov image covering ~20 pixels. 12 pixels grouped into 3 neighbouring SPs (yellow, blue and red) are highlighted with their colour intensity reflecting their signal amplitude. In case of the yellow and red SP, the analogue sum of the four pixels forming an SP exceeds the predefined threshold (middle panel plots) resulting in an L1 trigger, a logic signal with a width of 8 ns (left panel-plot). This is not the case for the blue SP since the analogue sum stays below the threshold. Since the L1 trigger signals of the yellow and red SP are both non-zero within the time coincidence window of 8 ns, an L2 trigger is formed.

The TFPGA provides functionality to individually disable any of the 512 FEE module trigger inputs from the L2 trigger decision to prevent noisy trigger patches from dominating the event rate. In such a case the number of valid NN-SP combinations is reduced.

Following a successful L2 trigger, a readout request consisting of a serial message with a 64-bit nanosecond counter (known as a TACK message) is sent to the FEE modules to initiate a full camera readout. On the FEE modules the TACK is compared to a local counter to determine a look-back time in the ASIC buffers.

Rate control is implemented via a settable minimal time between consecutive L2 triggers (trigger hold-off (HO) time). During commissioning of CHEC-M, it was observed that the TARGET-5 ASIC produces noise whilst digitising previously sampled and stored analogue data. This noise corrupts any new data sampled and stored in the ASIC whilst this digitisation is ongoing. This is why in CHEC-M digitising is only enabled when a readout is requested and all data sampled within the time of the digitising process has to be discarded from the analysis. Furthermore, it was observed that triggering with the TARGET-5 ASICs based on signal discrimination leads to additional, false triggers due to pick-up by the trigger circuitry of the serial data signals from the FPGA used to read out the ASICs. Thus, a trigger

HO time between triggers of 80 $\mu$s (being slightly longer than the time required to readout the TARGET-5 ASICs) is used in CHEC-M to allow stable operation. This problem is solved by design in CHEC-S by using two independent ASICs for triggering and digitisation. Thus, in CHEC-S the BP HO time could in general be set to 0 ns. However, in case of two triggers occurring within 10 $\mu$s, "old" data (marked as "stale") is read out from the storage array cells since the ASICs are still being read out and blocked from the first trigger. Hence, the expected dead time for CHEC-S is 10 $\mu$s instead of 80 $\mu$s as in CHEC-M.

A second, smaller house-keeping FPGA (HKFPGA), Actel A3P400, provides access to status and monitoring registers on the TFPGA and monitors the current and voltage supplied to the FEE modules. In CHEC-M, control and monitoring of both FPGAs is provided via a serial peripheral interface (SPI) link routed to one of the DACQ boards. The upgraded BP version 2 consists of a separate Ethernet link for control and monitoring in addition to the SPI link via the DACQ board. Hence, a communication to the BP is possible without the DACQ board being switched on and connected.

The camera may be externally triggered via external pulses input to an SMA connector on the BP and routed to a bulk-head connector on the camera enclosure where a pulse generator can be connected to.

Clocks between the BP and the FEE modules are kept in-sync through a low-skew fan-out network and signals between the BP and the FEE modules are used to synchronise local time counters. While absolute time synchronisation is not present in CHEC-M, it is in CHEC-S. A prototype version of the so-called timing board is installed in CHEC-S acting as an interface between the camera and the CTA timing system. It is based on White Rabbit technology [115]. Furthermore, this board has the capability to trigger the BP and LED calibration flashers (synchronised with the internal clock), thus replacing the need of an external trigger device.

For power, the BP accepts a single 12 V input and generates all required voltages on a daughter board mounted perpendicular to the main printed circuit board (PCB).

### 4.4.2 DACQ board(s)

The DACQ board(s) form a link for raw data and communications between the FEE modules and the camera server PC. CHEC-M contains two DACQ boards, each connecting 16 FEE modules via wired 1 Gbps Ethernet links to two 1 Gbps fibre-optic links to the PC. CHEC-S consists of a single so-called X-DACQ board since it connects all 32 FEE modules via wired 1 Gbps Ethernet links to two 10 Gbps fibre-optic links (only one of them is used) to the PC. Network interface cards, capable to handle either 1 or 10 Gbps, are used on the PC to connect the fibres. Data is sent to and from the FEE modules via a custom format over UDP. Due to the limited buffer capabilities (RX buffer of 9.198 kB and main buffer of 262.144 kB) and bandwidth of the DACQ boards in CHEC-M, a combination of Jumbo frames [116] and delays between packet sending is used to prevent the 1 Gbps (up-)links to the PC from being saturated by the traffic from the 32 1 Gbps links to the FEE modules. With this method, a maximum readout rate of ∼900 Hz can be achieved with CHEC-M (cf. Sec. 5.1). The situation is more relaxed with the increased bandwidth of the X-DACQ board in CHEC-S achieving a maximum readout rate of ∼1.25 kHz.

Each DACQ board in CHEC-M is based around a Xilinx Virtex-6 FPGA providing 18 GTX serial transceivers and an ARM Atmel microprocessor running an entire light-weight Linux system for managing purposes. An Ethernet connection to each DACQ board enables controlling and monitoring using a UDP server which runs on the microprocessor. The SPI control of the BP is provided through another UDP server running only on one of the two

DACQ boards. The X-DACQ board design is similar. It is based around two Xilinx Virtex-6 FPGAs and also consists of an ARM Atmel microprocessor to run the necessary services and UDP server for managing purposes and SPI communication to the BP.

Both, the DACQ boards used in CHEC-M and the X-DACQ board used in CHEC-S, are custom-made revisions of network switches based on White Rabbit technology [115] which are also commercially available from the company Seven Solutions [117].

## 4.5 LED calibration flashers

The CHEC design contains four flasher units, each consisting of ten LEDs of different brightnesses placed in the corners of the focal plane to illuminate the photodetectors via reflection from the telescope secondary mirror (cf. [118]). A Thorlabs ED1-C20 one-inch circle-pattern engineered diffuser is mounted in front of the flashing LEDs. The LED flasher units are based around fast gated TTL drive pulses and 3 mm, low self-capacitance, Bivar UV3TZ-400-15 LEDs , with a peak wavelength of 400 nm. The Bivar LEDs are enabled/disabled by an on-board microcontroller and triggered via an external TTL pulse. An LED controller based on an Arduino Leonardo ETH board connects all flasher units and provides an interface to set the LED pattern and to fan out a trigger signal. The TTL trigger signal is in-turn input to the LED controller from an SMA connector mounted on the camera chassis. In CHEC-S, an upgraded version of the LED controller is used. It can generate trigger pulses with a settable frequency by itself so that no external pulse generator is needed. Those trigger pulses can not only be used to trigger the LED flasher units but also to externally trigger the camera via the trigger input to the BP TFPGA. Communication with the LED controller is via a network switch installed on the internal camera rack and based on the same UDP scheme as used for the communication with the TMs and for several other devices in CHEC-M (cf. Sec. 4.7).

The LED flasher units are designed to flatfield the camera across a wide dynamic range, providing optical pulses of width ∼4.5 ns (FWHM) at 400 nm from 0.1 p.e./pixel, for absolute SPE calibration measurements, to over 1000 p.e./pixel, to characterise the camera up to and at saturation (cf. Sec. 5.9 for results of characterisation measurement). Since the time distribution of the flasher signals in the camera pixels can be calibrated, absolute single p.e. calibration using the flasher units is expected to be possible even under the presence of NSB with an expected nominal rate of about 15–25 MHz on the CTA site.

## 4.6 Power- and slow control

### 4.6.1 Slow control system

The camera slow control system provides the capability to remotely control power to camera components, control and monitor fan speeds, monitor component supply voltage and current draw as well as internal camera temperature and humidity. Furthermore, it monitors the status of the camera subsystems to prevent or reject actions taken by the user that would endanger the camera. It also issues alerts when certain conditions are met (e.g. temperature limits exceeded or communication lost), and automatically takes actions to minimise the risk of damage if the situation persists (e.g. switch off camera), i.e. if the user or software has not taken any action first to change the situation within a defined time window (alert-action-feedback).

The slow control system consists of a power board (PB) and SB mounted internally in the camera on the side of the FEE rack. The PB distributes 12 V to camera components

via relays controlled from the SB and provides analogue monitoring of camera component voltage supply and current draw to the SB. The SB contains a microprocessor controlling the PB relays, the digitisation of current and voltage readings from the PB, the reading of sensors, and the alert-action-feedback. An external high-current relay mounted on the internal camera chassis controls power to the BP and FEE. Communication with the SB is based on the same UDP interface as used for the LED controller.

### 4.6.2 Power supply

A single power supply unit (PSU) from the company ARTESYN (iMP series) provides CHEC with 12 V at up to 60 A for all electronics. The PSU contains two individually controllable 12 V units. One unit provides power to the camera slow control system for fans, SB, and PB. The PB then distributes 12 V to the camera internal network switch, DACQ boards, and LED controller via relays controlled from the SB. The second 12 V unit of the PSU provides power to the BP and FEE via a high-current relay, also controlled from the SB. The division of power distribution in this way allows safety-critical systems to be controlled independently from high-current components. The PSU used for CHEC-S consists of two additional 35 V units to provide the 70 V input for the SiPMs.

The PSU weighs ∼1 kg and measures only 60 mm × 120 mm × 250 mm. As such it can easily be housed at the rear of the secondary mirror of the telescope. A "sense" feed-back input from the camera ensures the desired voltage at the camera. The PSU can be externally controlled and monitored using basic SMBus protocols built on top of I$^2$C. An Ethernet-SMBus interface board has been implemented, based on an Arduino Leonardo ETH board, to allow easy Ethernet control using the same user-defined protocol based on UDP as for the LED controller and SB.

## 4.7 Control software

The camera control and readout software, called `CHECInterface`, has been developed in the scope of this work. It is designed to be maintainable, simple, and robust, and to fulfil the following requirements:

1. The number of dependencies on external software is at a minimum.

2. Only minimal code changes are necessary when a camera hardware component is upgraded.

3. The code is written in C++.

4. Scripts and programs written in other programming languages are only allowed for user interface, test programs, and other executables, but not for core-functionality.

5. Continuously buffering and writing of events without loss is ensured up to a rate of 600 Hz (corresponding to 2.5 Gbps) or even higher.

6. The software is easy to adapt as soon as a final data format or pipeline for CTA is in place.

Two external libraries (CFITSIO [119] and simple network management protocol (SNMP) [120]) and three self-developed libraries are used within the software: TargetDriver (for control and readout of TMs), TargetCalib (for applying TM calibration), and TargetIO (for reading
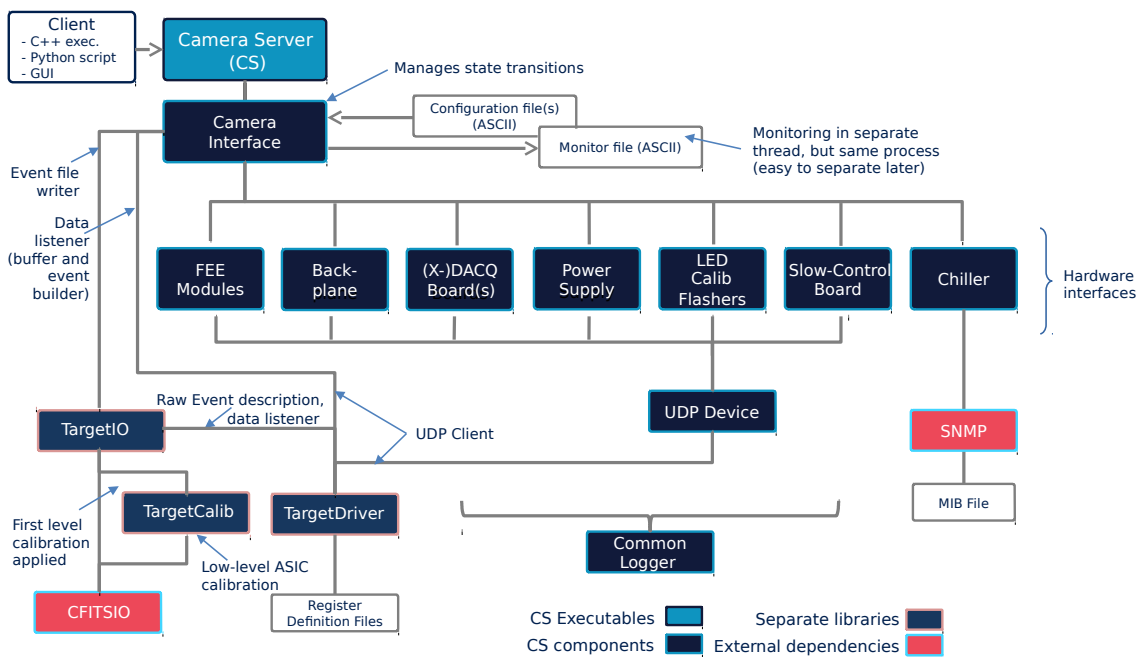
**Figure 4.11** Diagram showing different classes, their dependencies, and network protocols used in the camera control software `CHECInterface`.

and writing data from TMs). The software is structured so that each hardware component inside (e.g. TMs) and outside (e.g. chiller) the camera is represented by its own lower level class. The main class CameraInterface serves as interface to all lower level classes. Fig. 4.11 illustrates the software architecture with dependencies and libraries used. The user/client, which can be represented by a C++ executable, a Python script, or a GUI, can connect to the Camera Server (running on the camera server PC physically connected to the camera) via Ethernet. The server is implemented as a state machine, linking the client commands to functions and state transitions defined in the main interface class. The states are

1. Off
2. Safe
3. StandBy
4. Ready
5. Observing
6. Maintenance

and serve as preliminary placeholders for final camera states to be defined by CTA. Several safety features are implemented in the software, such as timeouts as well as temperature and current measurements, guaranteeing – in addition to the SB control system – that the camera is operated in safe conditions.

The hardware components are configured through ASCII files following a custom, but simple and human-readable, format. Communication with all hardware components except the chiller (which uses SNMP) is via a simple custom protocol based on UDP.

The camera readout and event building based on the 2048 full waveforms is implemented in and managed by the TargetDriver and TargetIO libraries. Events arrive at the camera server PC in asynchronous sets of 64 UDP packets (2 packets per event per module). They are first buffered and then assembled into associated events based on the TACK in each packet header which serves as a unique event identifier. A timeout is used to prevent the PC buffer filling up if (in an unexpected case) events with missing packets arrive or if the event building takes longer than expected. Missing packets are not requested again and incomplete
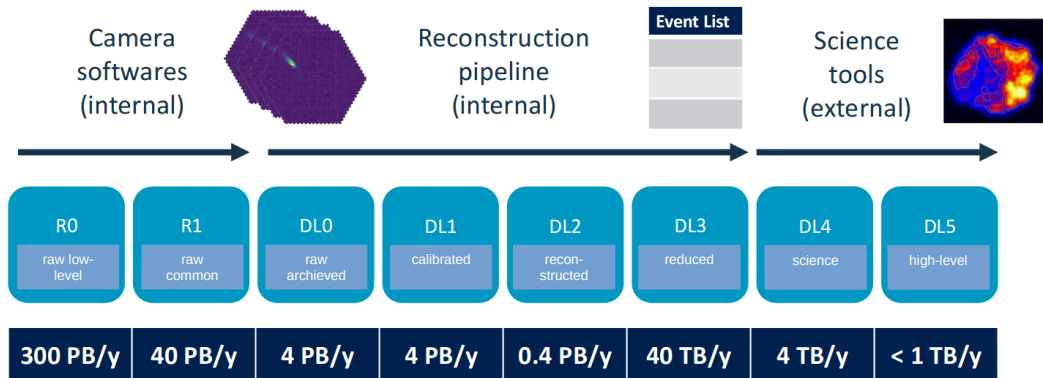
**Figure 4.12** Diagram showing the different data levels defined in CTA, at which stage they are produced, and what storage size they correspond to. Adapted from [122].

events are discarded. In a subsequent step, the events are written to disk as FITS files. Once CTA is operating and a final CTA data framework exists, the data will instead be further processed in a pipeline. However, even then it is planned to continue developing and using TargetDriver and TargetIO for stand-alone test purposes.

Due to the modest event rate per SST in CTA (600 Hz, cf. Sec. 3.2.3.2), no inter-telescope hardware array trigger is required. When a telescope triggers, all data is read out and transferred from the camera to be processed by the software array trigger system. Decisions on whether to proceed with the "array event building" in software including other camera events from neighbouring telescopes will then be based on the different camera event timestamps.

## 4.8 Data calibration and processing scheme

Within CTA different data processing levels are defined (cf. Fig. 4.12) [121]. The 2048 raw data waveforms (R0 data level) are calibrated and processed in different steps. These consist of (1) applying ASIC-specific calibration (transfer to R1 data level), (2) signal charge extraction and conversion to p.e. and photons, and (3) image cleaning and data reduction (transfer to DL1 data level). Fig. 4.13 shows camera images and waveforms of CHEC-M for the different steps in the data calibration and processing. It impressively illustrates the need for calibration.

### 4.8.1 ASIC-specific calibration

The ASIC-specific calibration consists of two steps, (1) pedestal subtraction and (2) transfer function (TF) application.

**(1) Pedestal subtraction** Since the response of each of the 16384 ASIC *storage* array cells (one storage array per pixel, cf. Sec. 4.3) to the reference voltage `Vped` is different, the pedestal of each cell has to be measured and then subtracted from the raw data. A run with at least 20000 asynchronously externally triggered events provides enough hits per cell to calculate the mean pedestal of each storage array cell.
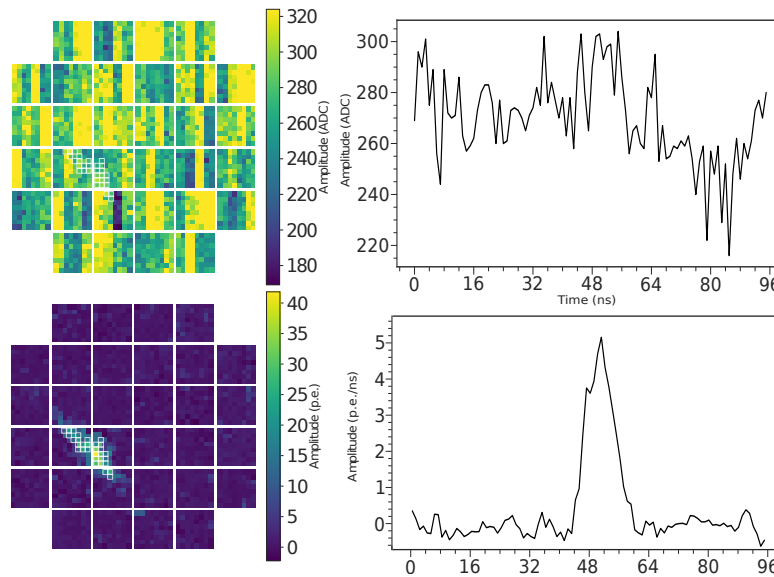
**Figure 4.13** Camera image and waveform for different steps in the data calibration and processing for the same Cherenkov event. Uncalibrated camera image at $t = 48$ ns (top left) and uncalibrated (raw data) waveform (top right) of pixel 1162. Calibrated camera image after charge extraction (bottom left) and calibrated waveform (bottom right) with pedestal subtraction, transfer function correction (cf. Sec. 4.8.1), and signal-to-p.e. conversion (cf. Sec. 4.8.2) applied for pixel 1162. The procedure of calibration and charge extraction is explained in the text. To get the y-unit of p.e./ns, the samples (in units of V) are divided by the SPE value (in units of V ns/p.e.), determined in SPE measurements (cf. Sec. 5.3). In both camera images, white squares indicate pixels which survive image cleaning (cf. Sec. 4.8.3). Adapted from (Zorn et al., 2018) [106].

**(2) TF application**   In addition to that, a look-up table to convert from sample amplitude that is read out from the ASIC (in ADC counts) to sample amplitude that is input into the ASIC (in mV) has to be generated. This look-up table, known as TF, is different for each of the 64 ASIC *sampling* array cells (one sampling array per pixel, cf. Sec. 4.3). Two forms of TF have been considered for CHEC, distinguished by the type of input used to generate them:

- A DC TF, created by applying a constant DC input of known voltage to each *sampling* array cell and iterating over the full dynamic range by varying the voltage, or

- an AC TF, generated by inputting a pulse of a known amplitude with a shape similar to that expected from the photosensor, and iterating as with the DC approach.

In case of CHEC-M, the DC TF was used and measured by recording the sampling array cell pedestal (in ADC counts) as function of the supplied cell voltage (given by `Vped`) in runs with 1000 externally triggered events for each `Vped` setting providing enough hits per cell to calculate its mean. The resulting TF of such a measurement is shown in Fig. 5.3. The slope of the TF depends on the ASIC parameter `Isel` [112] which is adjusted to maximise the range in which the TF is linear. Once determined, the values of `Vped` and `Isel` were set to default values and did not need to be adjusted for different measurement purposes. During further TARGET developments, a dependence of the TF on the signal frequency and input amplitude was observed [91, 112]. It was therefore decided to use AC TFs for the calibration in CHEC-S, generated by injecting pulses with different amplitudes. In contrast to CHEC-M, the TF measurement is part of the calibration process of each individual TM

(performed at the Erlangen Centre for Astroparticle Physics, ECAP). Since electrical pulses have to be injected from a pulse generator, the TF cannot repeatedly be generated once the TMs are installed in the camera (different to CHEC-M where fresh DC TF could be created every now and then).

### 4.8.2 Signal charge extraction and conversion to photoelectrons and photons

After pedestal subtraction and TF application resulting in 2048 waveforms with sample signal amplitudes in units of mV, the charge is extracted. For this step, several algorithms are currently under investigation in the scope of CTA. In case of CHEC-M, an algorithm integrating the waveform of each pixel in a fixed window around the sample containing the maximum signal was used. This sample is found using the "next-neighbour peak finding" algorithm which averages the waveforms in the pixels neighbouring the pixel of interest (PoI) and then takes the time of the maximum value in that averaged waveform as peak time for the PoI. The default size of the integration window was chosen to be 7 ns, with a shift to the left of the peak time of 3 ns. A correction using a single reference pulse shape for all pixels was used to determine the percentage of the pulse outside of the integration window thus reducing the dependence on the choice of the integration window size. The unit of the resulting charge per pixel is mV ns. In case of CHEC-S, in addition of using the same algorithm as in CHEC-M (but with an integration window size of 6 ns with a shift to the left of the peak time of 3 ns), another approach is investigated. It is based on a cross-correlation of each pixel waveform with a reference pulse shape and consists of the following steps: (1) cross-correlating the waveform in each pixel with the reference pulse shape, (2) averaging the cross-correlated waveforms across the pixels neighbouring to the PoI, and (3) selecting the maximum, which is then the bin that the cross-correlated-waveform value is taken from for the PoI. This value is used as the charge of the PoI in "cross-correlated units" (referred to as cc).

To convert the extracted charge in mV ns (CHEC-M) or cc (CHEC-S) to number of p.e., the charge resulting from one SPE needs to be known. This can be obtained via SPE measurements, described in detail for CHEC-M in Sec. 5.3. While in the lab a laser is used for those measurements, the LED calibration flashers (cf. Sec. 4.5) can be used on telescope in case a re-calibration is desired.

To further convert the extracted charge into number of photons, it has to be divided by the PDE of the MAPM/SiPM (cf. Sec. 4.2).

### 4.8.3 Image cleaning and data reduction

Similarly to the charge extraction methods, several algorithms for image cleaning and data reduction are under investigation. A possible procedure is the tail cut algorithm (cf. Sec. 3.2.5) with the cuts being optimised using Monte Carlo simulations. For CHEC-M on-sky data analysis, tail cuts of (17,8) have been used, for CHEC-S the optimisation is on-going. Currently (and for the studies presented in this thesis), tail cuts of (10,5) including a neighbour-time cleaning are used.

The results of calibration and waveform processing are waveforms and camera images as shown in the lower panels of Fig. 4.13. The software developed and used for calibration and charge extraction is part of the low-level data processing pipeline software `ctapipe` [123], currently under development for CTA. Further details on all steps concerning data calibration and processing are given in [107].

## 4.9 Summary

The technical design of CHEC, presented in this chapter, was realised in two camera prototypes (CHEC-M and CHEC-S). Their testing and characterisation was one of the major topics in the scope of the thesis and will be presented in the following two chapters. For this purpose, the control software `CHECInterface` as well as the data calibration and processing scheme, that have both been presented in this chapter, were written and implemented to control and readout both prototypes in laboratory tests and during on-telescope campaigns and to calibrate and process the data taken with them.

The laboratory set-up used for the testing of both prototypes was also assembled and characterised in the scope of this work. Details are given in App. A.

## CHEC-M characterisation and testing

"Research is what I'm doing when I don't know what I'm doing."

Wernher von Braun

In this chapter, I will present performance measurements and results of CHEC-M. In detail, those tests and results include

- data rate investigations (cf. Sec. 5.1),

- TF (cf. Sec. 5.2) and SPE/gain (cf. Sec. 5.3) measurements,

- determination of trigger thresholds (cf. Sec. 5.4),

- investigations of pulse shape characteristics (cf. Sec. 5.5), crosstalk (cf. Sec. 5.6), dynamic range (cf. Sec. 5.7), and timing characteristics (cf. Sec. 5.8),

- calibration of the LED calibration flashers (cf. Sec. 5.9), and

- investigation of warm-up, thermal distribution, and stability (cf. Sec. 5.10).

In addition, I will present results from an on-telescope campaign with CHEC-M installed on the GCT prototype in Sec. 5.11 and finally summarise the results in Sec. 5.12. A lot of the content of this chapter has already been published and is therefore adapted from (Zorn et al., 2018) [106]. Since several analyses presented in this paper and in the following sections are based on a collaborative work, I will accurately mention the corresponding authors of each analysis. Furthermore, as mentioned in Sec. 4.2.1, an MAPM gain of $8\times10^4$, corresponding to a high voltage (HV) of $\sim$800 V, is expected to be used for nominal data runs at the CTA site. However, due to the intrinsic performance of MAPMs, SPE can only be resolved when operating at a gain higher than nominal, corresponding to 1100 V. Hence, most of the characterisation and performance tests were done at this HV[1]. The effect of lowering the gain is discussed for each performance parameter separately if relevant.

An overview about the laboratory set-up used for the measurements presented in the following sections is given in App. A.

---

[1]Such an approach of increasing the HV, especially for SPE measurements, is a common procedure also used by operating IACTs like VERITAS, cf. e.g. [124].

**Figure 5.1** Schematic showing the data sending of 16 TMs connected to one DACQ board (eight modules at a time connected to one White Rabbit (wr) link). A configuration of two packets per TM and event and a delay of $\sim$530 $\mu$s between those packets is used.

## 5.1  Packet sending configuration and data rate measurements

As mentioned previously in Sec. 4.4.2, a combination of Jumbo frames and delays between packet sending is used to prevent the 1-Gbps links to the PC from being saturated by the traffic from the 32 1-Gbps links to the FEE modules (cf. Fig. 5.1). The speed to transfer data from a TM to the DACQ board is 1 Gbps which corresponds to 0.125 kB/$\mu$s. With a packet size of 8.310 kB (cf. Eq. 4.10), this results in an upload time per link of 66.480 $\mu$s. To allow the DACQ board to serialise the packets for sending them to the PC via the 1 Gbps link without the need of buffering, a time delay of $8 \times 66.480\,\mu\text{s} \simeq 530\,\mu\text{s}$ is used before the second packet from the same event and TM is sent. This means, the total time required by the DACQ boards to process one event is 1060 $\mu$s which fulfils the requirement of a mean goal data rate of 600 Hz. However, the camera must also be able to handle short trigger bursts, i.e. two or three triggers arriving within a few hundreds of microseconds. In such a case the DACQ board buffer (capable to buffer $\sim$1 event) and the TM buffer (capable to buffer 10 events) are used.

Using this packet sending configuration, the ability of the camera to read out waveforms from all 2048 pixels and send them in UDPs packets to the camera server as function of the trigger rate was assessed. To measure the data packet efficiency (number of arrived data packets divided by number of expected data packets[2]) as a function of the trigger rate, the camera was externally triggered by pulses randomly distributed in time. Cases with two different BP HO times (cf. Sec. 4.4.1) of 80 $\mu$s and 200 ns were investigated. Since the camera is triggered externally, no additional triggers due to sampling are expected in the latter one. Fig. 5.2 shows the result of such rate measurements. It can be observed that

- in case of no (or a very low) artificial BP HO time (of 200 ns), the camera readout efficiency is 1 ($\pm$0.1%) for L2 trigger rates smaller than $\sim$900 Hz. The uncertainty of 0.1% is due to the (in)accuracy of counting the pulse generator triggers in a given time window,

---

[2]The number of expected data packets is the product of the number of external triggers and the number of packets per event being 64 (2 packets for each module).
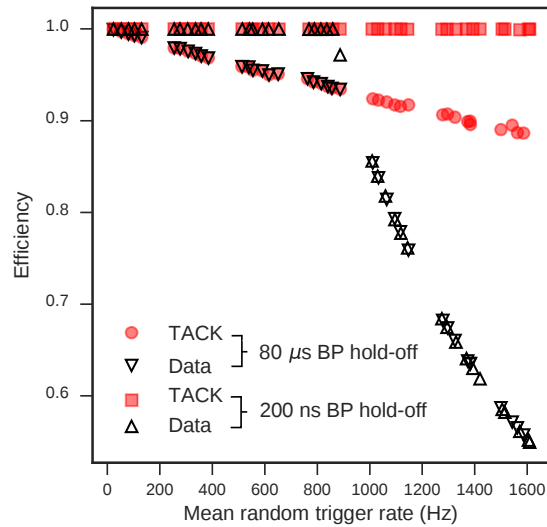
**Figure 5.2** TACK efficiency (number of readout requests divided by number of external triggers) and data packet efficiency (number of data packets divided by product of data packets per event (64) and number of external triggers) as a function of mean random trigger rate for two different BP HO times (see legend). Adapted from (Zorn et al., 2018) [106].

- in case of an artificial BP HO time of $80\,\mu$s, there is a chance of two or more (random) triggers arriving within that time. This chance increases with increasing mean trigger rate causing the packet efficiency being less than 1 at rates below $900\,$Hz and decreasing consistently with the fraction of readout requests, and

- the packet efficiency data points of both cases lie above each other at rates higher than $\sim$900 Hz. At this rate, the efficiency decreases (while the readout request fraction continues with the same slope) because the maximum transfer rate of the DACQ boards is reached causing packet loss being independent of any BP HO time.

To conclude, due to the artificial HO time of $80\ \mu$s implemented on the BP to avoid additional triggering on the trigger circuitry, the camera suffers a 5% data packet loss at the requested mean random rate of 600 Hz in normal operation mode. However, it is also shown that with a HO time of 200 ns, close to the theoretical HO time of 0 ns that could in general be used in CHEC-S, no losses occur at the requested rate of 600 Hz.

## 5.2  Transfer function measurements

As mentioned in Sec. 4.8.1, the TF provides a look-up table to relate ADC counts to signal amplitude in volts. Fig. 5.3 illustrates the range of TFs of all ASIC sampling cells of all pixels in the camera for the ASIC parameters `Vped` $= 1050$ (corresponding to 650 mV) and `Isel` $= 2816$. The chosen `Vped` value minimises the spread at low signal amplitudes while the selected `Isel` value ensures a high dynamic range of $\sim$3800 ADC counts with a reasonable linear shape of the TF.

The TF analysis to produce Fig. 5.3 was done by J. J. Watson [107] while the camera data needed for this analysis was taken by myself.
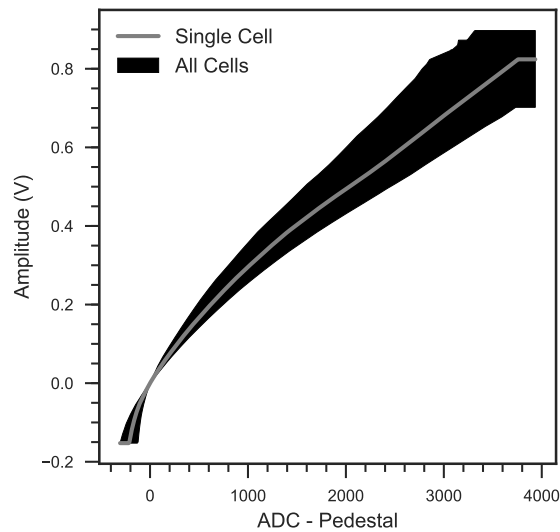
**Figure 5.3** Measured TF of all ASIC sampling cells of all pixels of CHEC-M and an example of a single cell are shown. Adapted from (Zorn et al., 2018) [106].

## 5.3 Single photoelectron measurements and charge extraction

Measuring the pulse area spectrum on the SPE level is a fundamental step in the calibration to determine the conversion factor between pulse area (in V ns) and p.e. (referred to as SPE value). This factor is different for each pixel and depends on the HV the MAPM is supplied with. Due to the intrinsic performance of the MAPM, the most reliable SPE resolution can be obtained at the highest possible MAPM gain, corresponding to an HV of 1100 V. This is why the SPE measurement was done at that HV illuminating the whole camera with a medium light level of ~0.35 p.e./pixel using the laser (cf. App. A). Fitting the spectrum of each pixel with a Poisson distribution convolved with a Gaussian for both, the noise and SPE peak (example for one pixel shown in Fig. 5.4a) leads to different fit parameters for all 2048 pixels such as mean illumination level, noise peak[3], SPE value (distance between first (noise) and second (1 p.e.) peak), and relative SPE width. The latter one is proportional to the ENF (cf. Eq. 4.2). Distributions of fit parameters including all 2048 pixels are shown in Fig. 5.4b (SPE value, rightmost blue distribution) and Fig. 5.5 (illumination, noise peak, and relative SPE width).

To measure SPE values at HVs less than 1100 V, in the first step the camera was illuminated at a higher illumination of ~100 p.e./pixel at 1100 V. The charge in p.e. was determined by calculating the pulse area and using the previously determined SPE value. In the second step, the HV was reduced keeping the illumination at the same level and thus the number of p.e. constant. However, since the gain $G$ decreases with decreasing HV, the pulse area also does so. This results in a lower SPE value, determined by measuring the pulse area at this lower HV and using the known number of p.e.. The blue distributions in Fig. 5.4b show the SPE values of all pixels when all MAPMs are set to the same HV (indicated on the x-axis). The spread can be reduced by "gain matching" the camera, i.e. by supplying each MAPM with a different HV. Three mean HV values (800 V, 900 V, and 1000 V), each of them consisting of 32 different HVs providing the same mean gain for all MAPMs, were determined

---

[3]The noise peak is centred around 0 since the pedestal was subtracted for each ASIC storage cell during calibration of the data (as explained in Sec. 4.8.1).

a                                                b
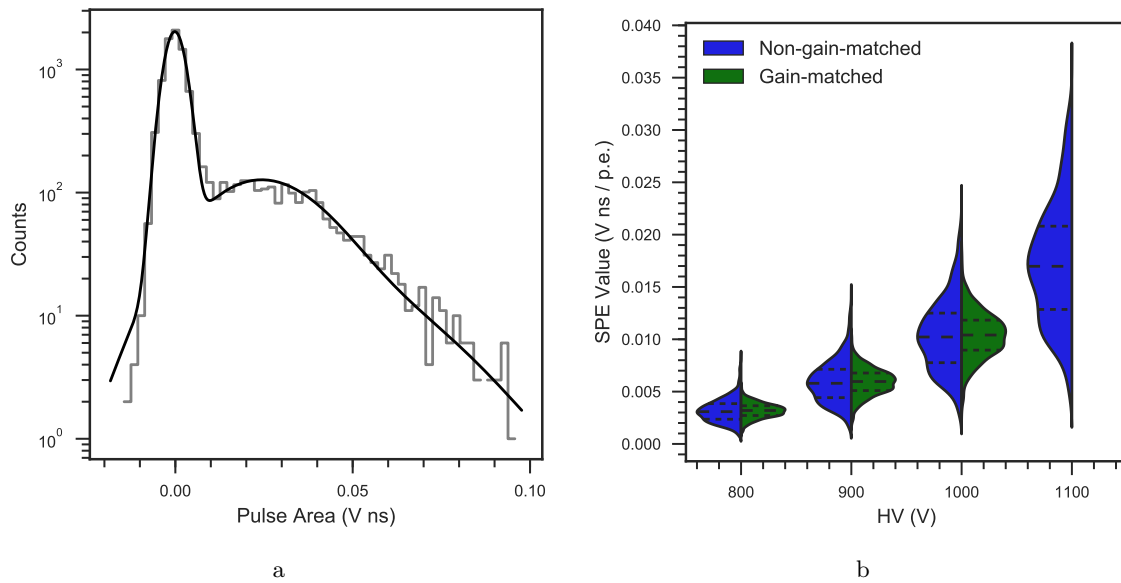
**Figure 5.4** (a) SPE spectrum and fit for pixel 1559 at 1100 V. (b) Distribution of SPE value across
the camera for a non-gain-matched camera (all MAPMs set to the same HV indicated on x-axis,
blue) and for a gain-matched camera (MAPMs set to different HVs, where mean HV is indicated
on x-axis, green). Lines show the median and the interquartile ranges. Adapted from (Zorn et al.,
2018) [106].

in specific laser measurements where the laser amplitude was kept fixed at a medium illumi-
nation level while the HV was altered. The gain spread over the camera after gain matching
is reduced, but still around 30% (cf. green distributions in Fig. 5.4b). This is due to the fact
that the HV can only be set individually for each MAPM, not for each pixel (a fundamental
feature of the MAPM design). However, since the camera was illuminated with the uniform
light source, the remaining gain differences between the pixels could be used to define pixel
dependent flat field coefficients, which are included in the SPE conversion factors.

The camera data used for the analyses shown in this section were taken by myself. The
analyses were a collaborative work between J. J. Watson and myself.

## 5.4 Trigger threshold determination

As described in Sec. 4.3, the TARGET-5 ASICs provide the L1 trigger of CHEC-M by discrim-
inating the analogue sum of four neighbouring pixels (referred to as SP) against a threshold
defined by the combination of the two ASIC parameters `Pmtref4` and `Thresh`. To identify
these values, the camera was uniformly illuminated at different laser amplitudes while count-
ing (with the BP TFPGAs) the L1 triggers for a given light/HV level and (`Pmtref4`/`Thresh`)
pair individually. The final (`Pmtref4`/`Thresh`) pair was chosen so that the L1 trigger ef-
ficiency[4] is about 50% for the given laser amplitude in each SP. In this way, five different
threshold settings (each with 512 pairs of `Pmtref4` and `Thresh`) at mean illumination levels
of around 2, 5, 11, 29, and 78 p.e./pixel at each of the three previously defined gain-matched
HV settings were defined. Fig. 5.6a shows the resulting mean L1 trigger rate as a function

---

[4]In general, the trigger efficiency is defined as the ratio of number of measured triggers and number of
expected triggers determined by the laser rate.
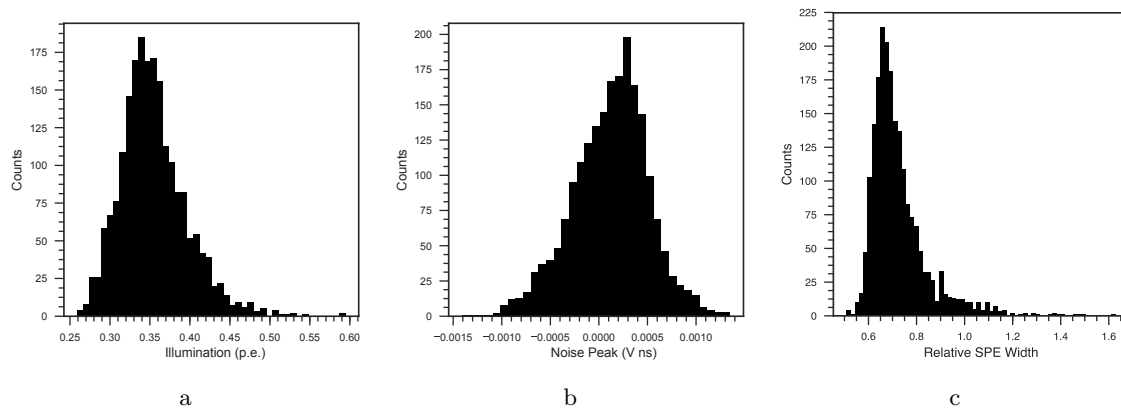
**Figure 5.5** Distributions of SPE fit results for all 2048 pixels: (a) mean illumination, (b) noise peak, and (c) relative SPE width. Adapted from (Zorn et al., 2018) [106].

of the laser illumination for the five threshold settings (at a mean HV of 800 V).

In the next step, an L2 trigger bias scan was performed. To understand the influence not only of the NSB but also of the TARGET-5 module sampling and data sending on the L2 trigger rate, three different scenarios were investigated in the lab (results shown in Fig. 5.6b):

1. BP HO time set to 80 $\mu$s as used in CHEC-M for nominal operation (BP HO on) and all TMs configured to not sample and not send data (sending data (SD) off) – blue data points in Fig. 5.6b,

2. BP HO on and all TMs configured to sample and send data (SD on) – green data points in Fig. 5.6b, and

3. BP HO off and SD off, with the DC ultra-violet (UV) LED (cf. App. A) emulating an NSB level of ∼50 MHz and the laser (cf. App. A) with a constant rate of 600 Hz (shown as grey line in Fig. 5.6b) emulating Cherenkov light of about 200 p.e./pixel – black data points in Fig. 5.6b.

It was observed that SD produces additional triggers causing the trigger rate to increase by ∼4 orders of magnitude at a camera trigger threshold of 5 p.e./pixel compared to the scenario where SD is disabled. This implies that the trigger circuitry picks up noise not only from the FPGA serial data signals used to read out the ASICs (already fixed by using a BP HO time of 80 $\mu$s, cf. Sec. 5.1) but also from the sampling and data sending process itself. As mentioned previously, both issues are solved by design in TARGET-C used in CHEC-S (cf. Sec. 6.4.4). This is why the third measurement in Fig. 5.6b (black curve) shows how the rate curve is expected to look like with CHEC-S under the influence of NSB and Cherenkov showers. In this example, the L2 trigger rate first decreases from ∼50 MHz at 2 p.e./pixel, where the trigger is completely dominated by the emulated NSB, down to 600 Hz at a camera trigger threshold of 29 p.e./pixel. From this point on, the L2 trigger is dominated by the laser, emulating a Cherenkov light signal.

For an SST with a CHEC-M-like camera, the NSB level on the CTA site is expected to lie between 15 and 25 MHz (lower than in the lab measurements shown in Fig. 5.6b). Thus, the rate curve is expected to flatten at lower trigger threshold compared to Fig. 5.6b, which means that a range of trigger threshold settings between 2 and 100 p.e./pixel should be sufficient. It is useful to determine additional intermediate trigger threshold settings. This can be done

a                                                  b
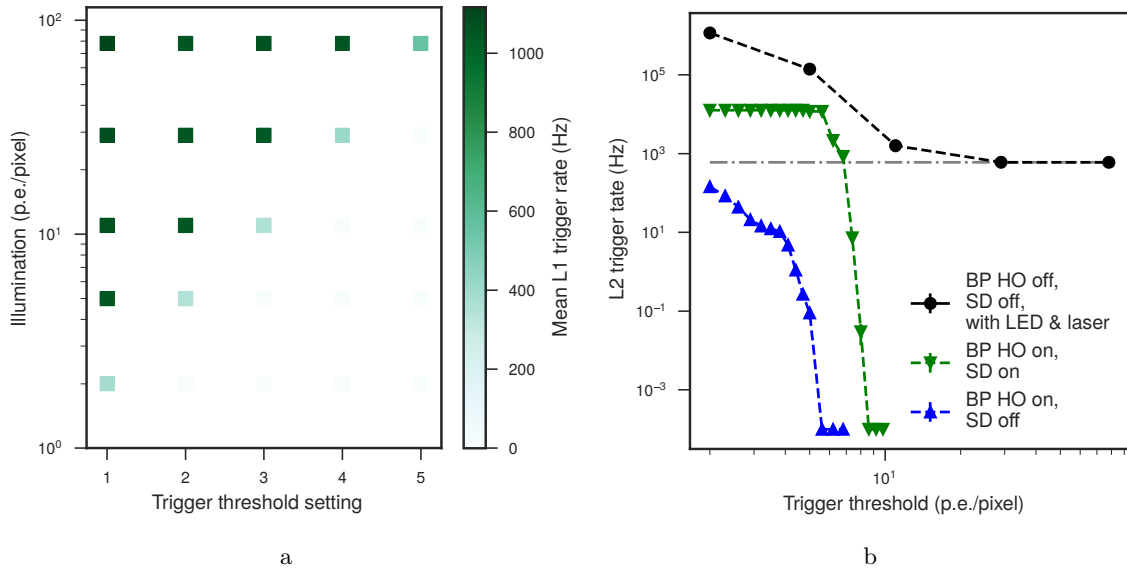
**Figure 5.6** (a) Mean L1 trigger rate as function of the trigger setting and illumination (in p.e./pixel) for a mean HV of 800 V, laser triggering at 1 kHz. The absolute illumination levels were deduced from the reconstructed mean pixel charges. (b) L2 trigger bias curves for three different scenarios all at a mean HV of 800 V: (1) BP HO on and SD off, (2) BP HO on and SD on, and (3) BP HO off, SD off, with DC UV LED of 50 MHz and the laser (cf. App. A) with a constant rate of 600 Hz and an illumination level of about 200 p.e./pixel – further explanation given in the text. Adapted from (Zorn et al., 2018) [106].

either by performing a finer and thus more time-consuming (`Pmtref4`/`Thresh`) scan or by interpolating the (`Pmtref4`/`Thresh`) values between two settings. The latter method was used in two of the three trigger rate measurements presented above (blue and green data points in Fig. 5.6b, intermediate steps between the previously determined five trigger threshold settings).

This procedure for trigger threshold determination was used to produce fine-grained steps of approximately 20 per decade in threshold for the use of on-sky measurements. Excessively noisy trigger pixels were disabled at each threshold setting until the L2 trigger rate stabilised.

## 5.5  Investigation of pulse shape characteristics

As explained in Sec. 4.3, to optimise the trigger performance, the signal pulse FWHM and 10–90% pulse risetime should lie between 5 and 10 ns and between 2 and 6 ns, respectively, over the whole SST energy range. Fig. 5.7 illustrates the FWHM and risetime for two pixels[5] as function of the illumination level for laser data taken at different laser illuminations all at 1100 V. It shows that the pulse shape requirements for optimal triggering are met at low illumination levels and that the pulse shape is stable up to an illumination of 200–400 p.e./pixel depending on the camera pixel. At these illuminations, saturation effects can be observed, i.e. while the pulse peak height stops to increase the FWHM continues to increase with increasing laser amplitude. The amplitude at which saturation occurs is different for

---

[5]These two pixels were chosen on a semi-random basis as qualitative representatives of all camera pixels. They show neither particularly good nor poor characteristics and are geometrically well separated (one is near the edge of the camera and one at the centre), rather than e.g. being of the same FEE module.
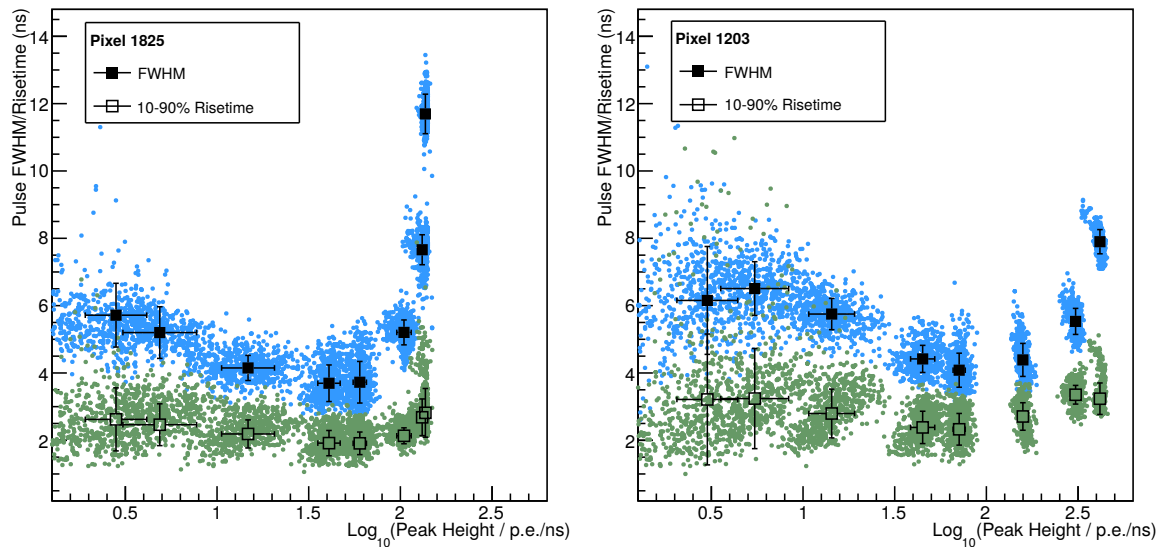
**Figure 5.7** Pulse FWHM (blue points) and 10–90% risetime (green points) as function of measured peak height for camera pixel 1825 (left) and 1203 (right). The peak height (in units of p.e./ns) was extracted from the data using the procedure explained in Sec. 4.8. The squares indicate different laser illumination levels, their y-position the mean pulse FWHM/risetime, and the bars the standard deviation in measured FWHM/risetime and peak height at each laser brightness. Adapted from (Zorn et al., 2018) [106].

each pixel due to different gains at 1100 V and/or different QE or CE. Since no QE or CE spread between different MAPMs and pixels are reported by the manufacturer, the influence of the latter aspect is expected to be small and much lower than the gain spread at 1100 V.

The influence of saturation can also be observed in Fig. 5.8 showing the FWHM and 10–90% risetime distribution for all 2048 pixels at different illumination levels (same dataset as used for the sample pixels in Fig. 5.7). As explained above, due to the gain spread at 1100 V, saturation occurs at a different illumination level for each pixel, resulting in a wide spread in FWHM, especially at the highest illumination levels when all pixels are affected by saturation effects. However, for all pixels, both the FWHM and 10–90% risetime fulfil the requirements for optimal triggering.

The intrinsic MAPM pulses are significantly shorter (FWHM of ∼1 ns, cf. Sec. 4.2.1) than the pulses measured with the whole chain (FWHM between 5 and 10 ns) being dominated by the preamplifier pulse shape characteristics. Thus, the effect of the HV (i.e. also of a lower HV and gain) on the pulse shape characteristics – measured at a given signal amplitude in V – is expected to be negligible[6].

The camera data used for the analyses shown in this section were taken by myself. The analyses were a collaborative work between J. J. Watson, J. A. Hinton, and myself.

---

[6]Of course, since a higher HV/gain results in higher SPE values and saturation effects affect the pulse shape characteristics (as shown in this section), a lower/higher HV affects the pulse shape characteristics, if measured as a function of illumination level, shifting the data points in Fig. 5.7 & 5.8 to higher/lower illumination levels.
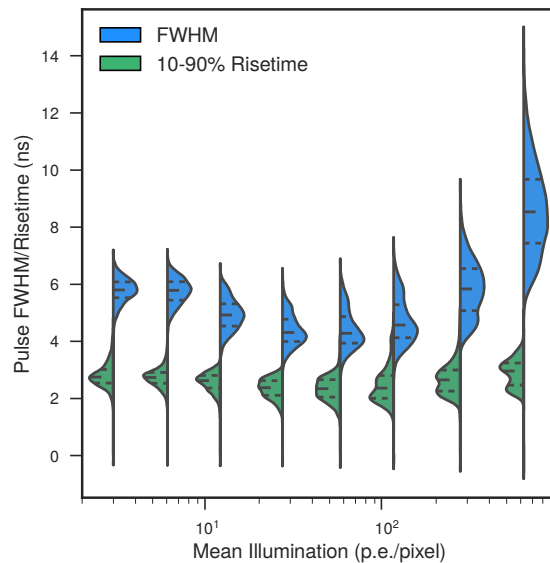
**Figure 5.8** Pixel distributions (mean for each pixel) for pulse FWHM (blue) and 10–90% rise-time (green) for different illumination levels. Lines show the median and the interquartile ranges. Adapted from (Zorn et al., 2018) [106].

## 5.6 Crosstalk measurements

The crosstalk measurement was performed at 1100 V with an MAPM connected to a CHEC-M preamplifier module which was in-turn probed with an oscilloscope while only one pixel was illuminated with the laser (cf. App. A), all other pixels physically masked. The peak-to-peak voltage of the average pulses from both the signal and candidate pixel were then measured and the ratio taken as an indication of the crosstalk. The 64 pixels of a single MAPM are mapped in groups of 16 to preamplifier boards, and then one-to-one to ASICs. Clear average pulses were seen in all pixels connected to the same board as the signal pixel, resulting in an average crosstalk of 4–5% and reaching a maximum of 6% in neighbouring pixels (cf. Fig. 5.9). No discernible pulses were measured in pixels of the other three preamplifier boards and the values shown for boards 0–2 in Fig. 5.9 represent the limit of the measurement technique and should be taken as an indication that no significant crosstalk has been measured. This measurement strongly indicates that the preamplifier PCBs rather than the MAPM are the dominant source of crosstalk in the system. A lower HV/gain is therefore not expected to have a significant impact on the crosstalk. Furthermore, this result is not entirely unexpected since in a compact, high-density system it is inevitable that signals must be routed in close proximity on any given PCB. However, the preamplifier board routing has been optimised in CHEC-S to minimise crosstalk.

The results of the crosstalk measurements have to be taken into account in the uncertainty evaluation. A maximum crosstalk of 6% between neighbouring pixels does not only degrade the charge resolution by the same amount, but also the SPE calibration, both affecting the image reconstruction: Taking into account a possible gain spread of about 30% between neighbouring pixels, high-gain pixels can bias the SPE calibration of neighbouring low-gain pixels by about 8% due to crosstalk. In addition, the crosstalk also affects other camera performance aspects like the trigger efficiency.

The measurements used for the analyses shown in this section were taken by R. White.
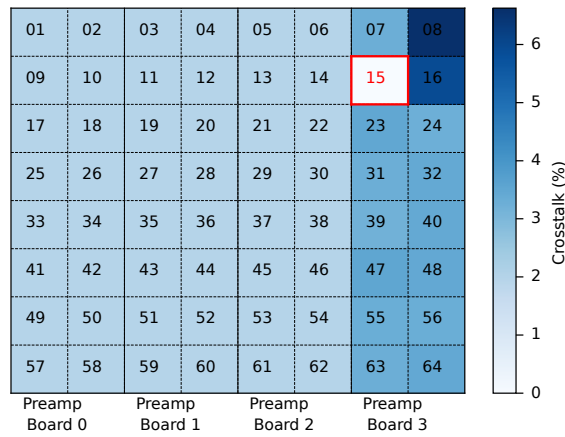
**Figure 5.9** Crosstalk (in %, indicated by colour bar) for different pixels of one MAPM at 1100 V routed to different preamplifier (preamp) boards when only pixel 15 (indicated by red square) was illuminated with the laser (cf. App. A), all other pixels were physically masked. For more details see text. Adapted from (Zorn et al., 2018) [106].

The analyses were a collaborative work between him and myself.

## 5.7 Dynamic range investigation

The dynamic range of the signal recording chain (MAPM and FEE module) was assessed by illuminating the entire camera with a uniform light level ranging from below 1 p.e./pixel to several hundreds of p.e./pixel in calibrated steps. The measurements were done supplying all MAPMs with the maximum voltage of 1100 V to be able to resolve SPE at low illumination. Results for two camera pixels (same as used for the FWHM and risetime investigation, cf. Sec. 5.5) and of an MAPM-only measurement for comparison are shown in Fig. 5.10a. For the camera pixel data points, the charge (y-axis) was reconstructed following the procedure explained in Sec. 4.8.2. Its value at ∼50 p.e./pixel was used as anchor for the illumination level on the x-axis to absolute calibrate the laser (cf. App. A). Other points on the x-axis were then inferred from the relative calibration of the filter wheel (cf. App. A) used to adjust the laser intensity, resulting in an illumination in units of p.e./pixel. The MAPM data points were inferred from measurements where the MAPM signal was directly measured with an oscilloscope.

According to Fig. 5.10a, clear deviation from a linear correlation between illumination level and reconstructed charge starts to occur at an illumination of ∼250 p.e./pixel for camera pixel 1825 while it is not observed in pixel 1203 over the range of laser illuminations used in these measurements. This can again (as in Sec. 5.5) be explained by saturation effects occurring at different illumination levels due to different gains at 1100 V and due to different QE and CE between the two pixels (less substantial). Furthermore, the full signal recording chain (MAPM and FEE module) has a similar response as the MAPM itself, showing non-linearity effects of about 20% at 1000 p.e./pixel. Consistent results are obtained when looking at the dynamic range of all pixels in the camera (cf. Fig. 5.10b).

As can be suggested from the waveforms of the two pixels at different illumination levels, shown in Fig. 5.11, as well as from the FWHM dependence on the illumination level (cf. Fig. 5.7), the pulse width increases with illumination. Thus, the relationship between pulse width at fixed amplitude (e.g. at 20 p.e./pixel) and input illumination level can be

a                                                      b
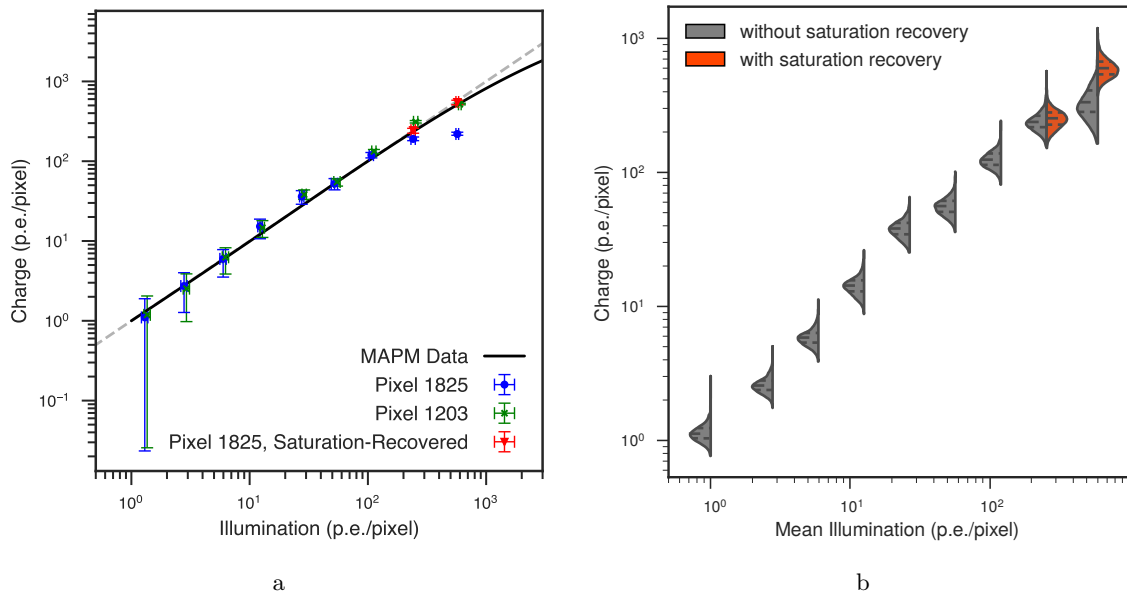
**Figure 5.10** (a) Reconstructed charge as function of the camera illumination for two camera pixels
with the full chain of MAPM and FEE module, and for the MAPM only. Points show the mean,
bars the $25^{th}$ and $75^{th}$ percentile of the charge distribution for the given pixel and illumination. A
first attempt for saturation recovery using the pulse width at a fixed peak amplitude is shown for
pixel 1825 (see text for details). The grey dashed line shows a 1:1 relation between the axes. (b)
Pixel distributions (mean for each pixel) for extracted charge at a given mean illumination level
with and without attempts to recover from saturation at the highest illumination levels using the
pulse width. Lines show the median and the interquartile ranges. Adapted from (Zorn et al., 2018)
[106].

used as a first attempt for recovery in saturation as shown in Fig. 5.10a for pixel 1825 and
Fig. 5.10b for all pixels.

The overall dynamic range can be shifted to higher illumination levels by reducing the
gain. Operating the camera at a mean HV of 800 V instead of 1100 V reduces the gain by a
factor of ∼6 shifting the upper end of the dynamic range to ∼6000 p.e./pixel, resulting in an
overall dynamic range of ∼4 orders of magnitude.

The camera data used for the analyses shown in this section were taken by myself. The
analyses were a collaborative work between J. J. Watson and myself.

## 5.8 Investigation of timing characteristics

To investigate time differences between digitised signals of different pixels hit by the same
light flash simultaneously, the camera was externally triggered while illuminated by the laser
(cf. App. A) at 1100 V. For each illumination level and pixel, the pulse peak time distribution
was determined out of 500 events, where the individual peak time of each pixel and event
was shifted by the camera mean of the given event to overlap different events. The time
resolution, defined as standard deviation of the peak time distribution, was measured for
different illumination levels (cf. Fig. 5.12 for two sample pixels and for the distribution of
all pixels, respectively). It improves with increasing illumination due to increasing signal-to-
noise ratio and is (for most of the pixels) better than 1 ns for illumination levels >6 p.e./pixel.
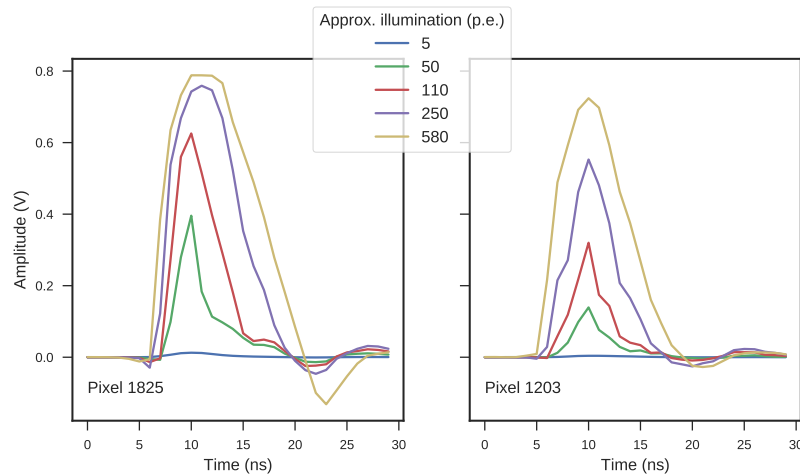
**Figure 5.11** Calibrated waveforms of camera pixel 1825 (left) and 1203 (right) at different illumination levels. At an illumination of 580 p.e./pixel, the pulse in pixel 1825 shows obvious saturation effects (plateau at the top). Adapted from (Zorn et al., 2018) [106].

Deterioration for illumination levels higher than 110 p.e./pixel is observed in the mean of the all-pixel distribution and for the sample pixel 1825, again due to saturation effects occurring at different illumination levels.

The timing and time resolution could be affected by a dependency of the pulse shape. This could explain the degradation of the time resolution at high illumination levels in the saturation regime. However as explained previously in Sec. 5.5, the impact of a lower HV/gain at a given signal amplitude in V is expected to be insignificant on the pulse shape, thus the same holds for the time resolution.

The analyses shown in this section were a collaborative work between J. J. Watson and myself while the camera data was taken by myself.

## 5.9 Calibration of LED calibration flashers

The four flasher units were tested for stability and temperature dependence, as well as on their dynamic range. They were operated in the temperature chamber while their brightness was measured with one of the SensL-SiPMs (cf. App. A). The overall dynamic range of one flasher consisting of ten LEDs is about four orders of magnitude with the illumination level at the camera ranging from sub-p.e./pixel up to a few thousands of p.e./pixel. The flasher brightness dependence on temperature is different for each combination of the ten LEDs (pattern). It shows an increase with temperature of <1%/°C for the brightest pattern up to 5%/°C for the dimmest (cf. Fig. 5.13a). Fitting this dependence with a polynomial of second order gives different fit results for each combination which can be used to correct for temperature effects in other datasets (cf. Fig. 5.13b). The spread after applying the temperature correction is about 3–8% for the eight dimmest LED combinations decreasing to about 1% for all other combinations. Whilst this resulting spread results in sufficient stability to utilise the LED flashers over the expected operating range of CHEC-M, some correlation with temperature clearly remains in Fig. 5.13b. The resulting residuals from a perfectly stable response are larger whilst the temperature decreases – implying a hysteresis in the temperature response that is not considered here (either in the derivation or application of temperature coefficients). The long-term stability (measured over the time-scale of several
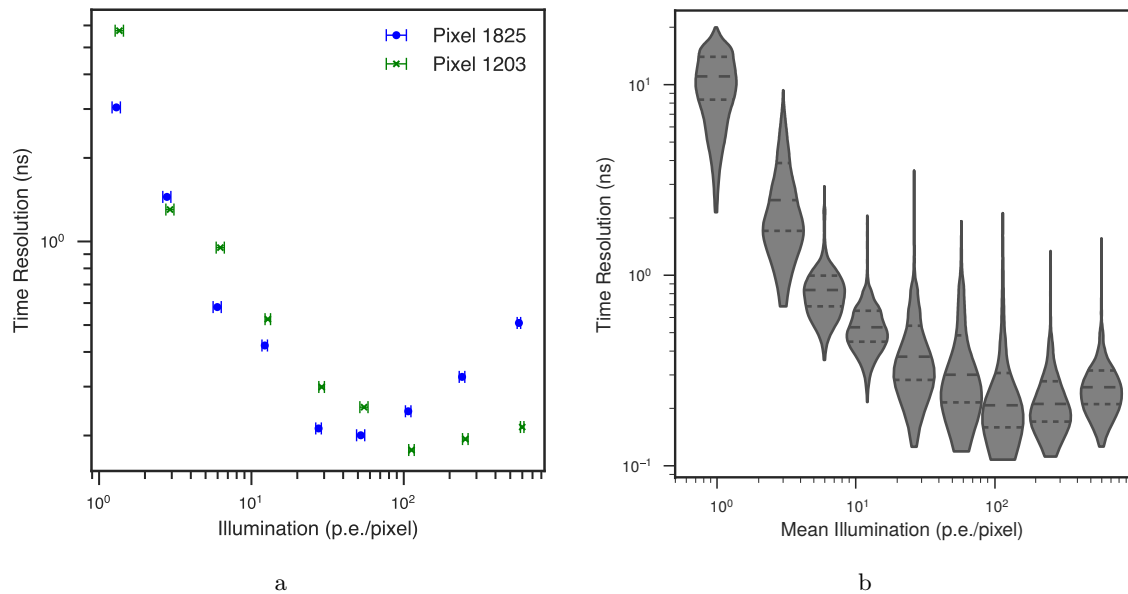
**Figure 5.12** Time resolution as function of the camera illumination (a) for camera pixels 1825 and 1203 and (b) for all pixels (distributions) with lines showing the median and the interquartile ranges. Adapted from (Zorn et al., 2018) [106].

days) shows a decrease in brightness ranging from 0.25%/hour and ∼1%/hour depending on the LED combination, recovering completely after a power down of one hour.

The measurements showed the flashers being appropriate devices for regular camera calibration with the possibility of absolute gain determination using the dimmest LEDs for SPE measurements and for monitoring changes in dynamic range and linearity of the full signal recording chain (MAPMs and FEE modules). Furthermore, the analytic description of the temperature dependence can be used to correct for changes in illumination in case temperature drifts occur. More detailed measurements including ray tracing simulations to predict the light intensity in each camera pixel when reflected off from the secondary mirror are currently on-going in the MPIK-CHEC-group.

Both, the analyses and measurements of this section, were a collaborative work between R. White and myself.

## 5.10 Warm-up, thermal distribution, and stability investigation

Several outdoor camera power cycle and temperature stability measurements were done to test the camera reliability and its behaviour with temperature.

Fig. 5.14a shows four power cycle measurements at a fixed chiller temperature of 5°C starting with the first power cycle at sunrise on a spring day at an ambient temperature of ∼5°C. It can be deduced that the maximum temperature difference between the TMs in the camera at a certain time is about 6°C and that the modules with the lowest temperature are those located at the top and bottom of the camera. This is expected since all auxiliary boards like safety, power, and DACQ boards are attached on the sides, while no boards are located at the top and bottom, and the fans are installed at the bottom. Furthermore, it was observed

a



b
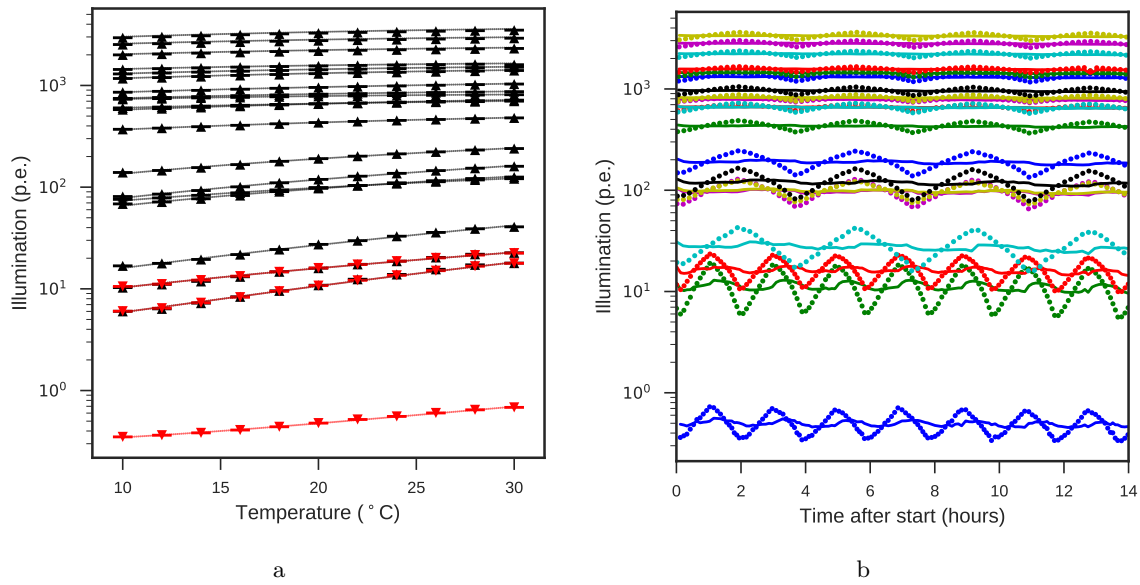
**Figure 5.13** (a) Flasher brightness, measured with one of the SensL-SiPM (cf. App. A), and converted into an illumination level per camera pixel as function of ambient temperature for 20 different LED patterns. Each line shows an individual polynomial fit of second order ($f(x) = a\,x^2 + b\,x + c$, a, b, c being fit parameters) to the data of each pattern. Black (upper) points: brightness measured with a neutral density (ND) filter of $\sim$10% transmission in front of the SiPM; red (lower) points: brightness measured without ND filter but additional amplifier to amplify the SiPM signal. Temperature dependence of second and third dimmest pattern measured with both set-ups, third dimmest pattern used to scale. (b) Flasher brightness converted into an illumination level per camera pixel as function of temperature cycling measurements for the same 20 LED combinations as used in (a). Different cycle lengths were used for measurements with and without ND filter. Points showing the data (results of the measurements), lines showing the "corrected" data after applying the temperature correction factor deduced from the polynomial fit of the datasets in (a). Adapted from (Zorn et al., 2018) [106].

that the mean camera temperature varies over 8°C over a complete day with the largest change occurring during sunrise and sunset. This effect could be corrected for by changing the chiller temperature accordingly to the ambient temperature. As shown by temperature cycling tests (Fig. 5.14b), the camera temperature can be controlled and maintained on a certain level by adapting the chiller temperature.

The temperature dependence of the baseline[7] of all 2048 pixels was investigated using the same chiller temperature cycle runs shown in Fig. 5.14b, in which externally triggered 45-minutes runs at 3 Hz for each chiller temperature were taken. In order to observe a relative change in the baseline with temperature, all 45-minutes run data was subtracted from a fast (600 Hz) reference pedestal run taken at the beginning of the temperature cycle runs at a chiller temperature of 5°C. The resulting baseline-shift temperature dependence is fitted with a linear function $g(T) = a\,T + b$ with temperature $T$ and fit parameters $a$ and $b$ for the camera mean and for each pixel individually. The results show that the mean camera baseline shift is about 0.36 mV/°C (cf. Fig. 5.15). A spread in the temperature dependence between individual pixels is observed (some of them even with opposed sign, cf. Fig. 5.16a) with minimum and maximum temperature coefficient of $a_{\min} \sim -0.26$ mV/°C

---

[7]The baseline is defined as the waveform mean in absence of light.

a

b
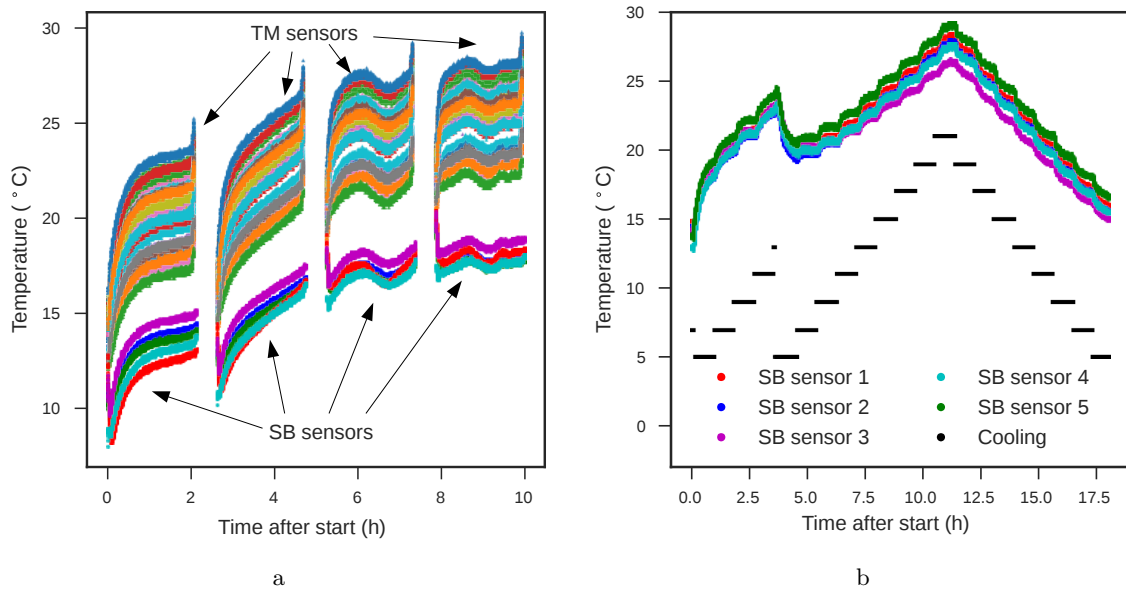
**Figure 5.14** Camera temperature as a function of time (a) measured with the TM temperature sensors (upper data points) and the five SB sensors (lower data points) during four power cycles keeping the chiller temperature at a fixed value of 5°C and (b) measured with the SB sensors when the chiller cooling temperature was changed by one degree every hour while the camera was on and data was taken. Adapted from (Zorn et al., 2018) [106].

and $a_{max} \sim 1.18 \, \text{mV}/°\text{C}$, respectively. This spread can be attributed to different temperature behaviours of either the ASICs or the external DACs providing the input signal `Vped` to each ASIC[8]. This is illustrated by Fig. 5.16b where it can be observed that pixels connected to the same ASIC and external DAC show similar baseline temperature coefficients. However, even though the baseline of different pixels have different temperature dependencies, only a small temperature dependence of the pixel baseline RMS is observed (cf. Fig. 5.15). This means that all 16384 storage cells of one pixel have similar temperature dependencies. Thus, one linear correction factor per pixel is enough to characterise or correct for the temperature dependence.

An uncertainty on the baseline of $\pm$ 0.5 mV is not expected to affect the camera performance in terms of charge resolution. However, in case the camera is not kept at a constant temperature level within $\pm$ 1°C, either a pixel dependent linear correction factor has to be used or the pedestal must be remeasured every time the camera temperature changes by more than 1°C. A pedestal measurement takes about 30 s and the HV needs to be off or the lid closed. Thus, this approach would cause a maximum dead time of ~0.8% per night (according to a very simplified calculation, assuming a linear temperature drift of 8°C within an eight-hours night). To avoid that, a pedestal determination could be done "online" during observation instead, either with interleaved events or by using parts of the waveforms/pixels with no signals – the latter option being the long-term plan for the future.

To investigate the camera warm-up, two relevant quantities were investigated: first, the change in trigger rate with closed lid and HV off, indicating whether the trigger threshold is stable and the camera is ready for triggering, and second, a possible shift in the baseline

---

[8]In TARGET-C used in CHEC-S, the offset `Vped` is not supplied by an external DAC anymore but by the ASIC itself.
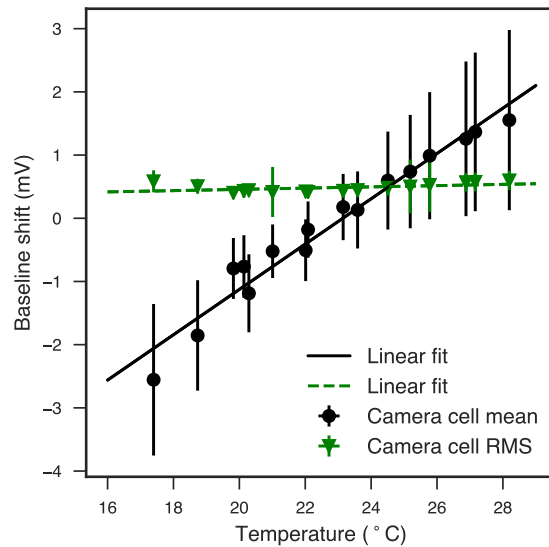
**Figure 5.15** Camera pedestal mean and RMS as function of the temperature for the dataset shown in Fig. 5.14b. The data is fitted with a linear function $g(T) = a\,T + b$ with temperature $T$ and resulting fit parameters of $a \sim 0.36$ mV/°C and $b \sim -8.30$ mV for the pedestal mean and $a \sim 0.01$ mV/°C and $b \sim 0.26$ mV for the RMS. Adapted from (Zorn et al., 2018) [106].

indicating whether the camera is ready for data taking. To measure the trigger rate change during warm-up, the trigger threshold was set in the electronic noise causing the trigger rate to be very sensitive to electronic noise changes expected to occur during warm-up[9]. Fig. 5.17a shows the trigger rate change as function of the time after camera power up. It is fitted with an exponential function $g(t) = a\,(1 - \exp(-t/\tau_{\mathrm{t}})) + b$ with time $t$ and fit parameters $a$, $b$, and $\tau_{\mathrm{t}}$, showing an increase over time with a time constant of $\tau_{\mathrm{t}} \simeq 1193$s. This increase is connected with a temperature increase during warm-up (as shown by Fig. 5.17b) and very likely caused by the baseline drift with temperature explained above. An increasing baseline in fact reduces the threshold, causing a higher trigger rate. Thus, the mean camera baseline is expected to show an increase during warm-up which is shown by Fig. 5.17c. The resulting time constant is $\tau_{\mathrm{b}} \sim 849$s with a mean baseline drift of about 0.35 mV over $\sim$40 min being less than 1 p.e. In total, the camera is assumed to be stabilised/warmed up when the trigger rate change and the mean camera baseline drift is less than 5% compared to the asymptotic value $\lim_{t \to \infty} g(t)$. This is the case after $\sim 3\,\tau$ ($\sim$1 h for the trigger rate change and $\sim$45 min for the mean camera baseline drift).

The camera parameters investigated in this section (temperature, trigger rate change, and baseline drift) are the most basic ones which allow to characterise the general functionality of the camera and to answer the most basic questions like: Can the temperature be controlled and stabilised? By how much does the temperature change over a day? What is the temperature distribution and its spread inside of the camera? Can the camera be triggered reliably? Can data be taken reliably and is it affected by temperature or time?

---

[9]In observing mode, the trigger threshold will be set well above the electronic noise level so the trigger rate will be less sensitive to electronic noise changes. It will be dominated by NSB and Cherenkov events.

a

b
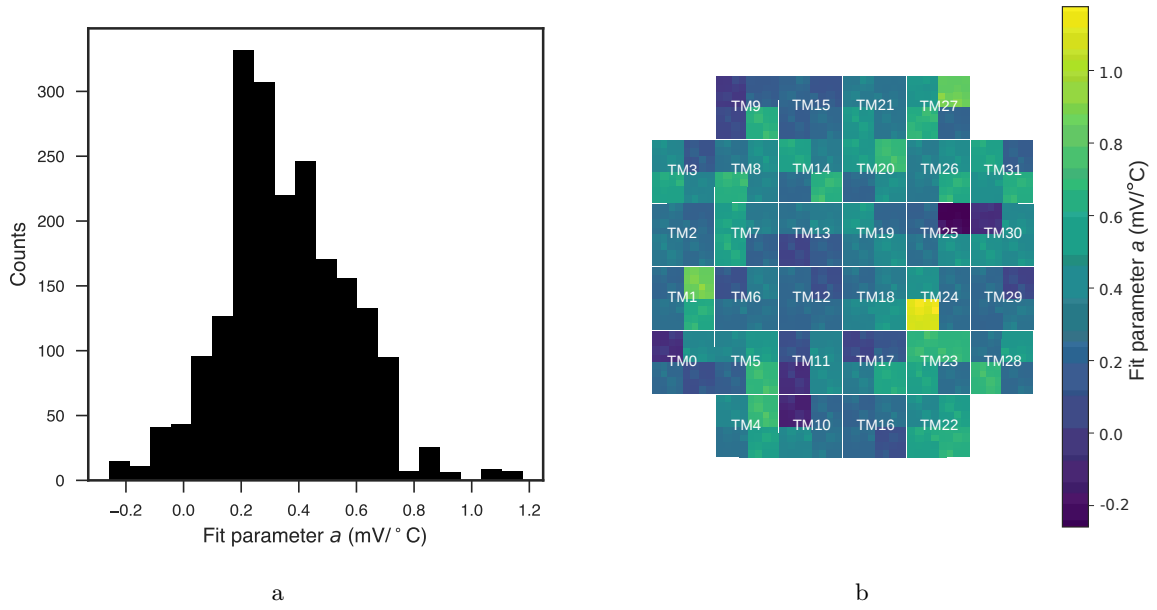
**Figure 5.16** (a) Distribution of all 2048 pixel baseline temperature coefficients (fit parameters $a$ in linear fits, $g(T) = a\,T + b$) giving a mean of $\sim$0.35 mV/°C and a standard deviation of $\sim$0.22 mV/°C. (b) Camera image illustrating the 2048 pixel baseline temperature coefficients. Each block of 16 pixels is connected to the same ASIC and external DAC on the given TM. Adapted from (Zorn et al., 2018) [106].

## 5.11 Cherenkov events

First Cherenkov light with CHEC-M was observed in November 2015 during a first campaign with the camera deployed on the GCT telescope prototype located at the Paris Observatory in Meudon near Paris [125]. A second campaign was carried out in Spring 2017.

Due to the high NSB light level in Meudon, estimated to be 20 to 100 times brighter than at the CTA site, the camera was operated at a low gain (mean HV of 800 V) and at trigger threshold setting 3 (cf. Fig. 5.6a), corresponding to roughly 11 p.e., pushing the trigger rate down to only $\sim$0.1 Hz. Two examples of on-sky events (telescope pointing to the sky, camera lid open, HV on) and one event with telescope in park position (0° elevation), camera lid closed, but HV switched on, all three recorded during the second campaign are shown in Fig. 5.18. The upper images show the intensity in p.e. (integrated charge) for each pixel, while the lower ones indicate the peak arrival time (after trigger) for each pixel for the same events. Furthermore, the white boxes indicate pixels surviving image cleaning (cf. Sec. 4.8.3). As expected for a Cherenkov flash from a shower, the timing plots of the Cherenkov events (Fig. 5.18d and 5.18e) show the image propagating across the focal plane in time. Whereas the first event (Fig. 5.18a & 5.18d) could have been a shower with a large impact distance thus showing a rather large time gradient of about 35 ns, the second event (Fig. 5.18b & 5.18e) could have been an inclined shower with the telescope being at the edge of the Cherenkov light pool causing all pixels with Cherenkov signal being illuminated at a very similar time. The event shown by Fig. 5.18c and 5.18f was recorded with closed lid in park position. It must have been a CR-induced particle travelling through the curved MAPM array of the camera. The unique geometry and fast time profile of such an event make it easy to be isolated from Cherenkov events in the analysis afterwards.

a                                b                                c
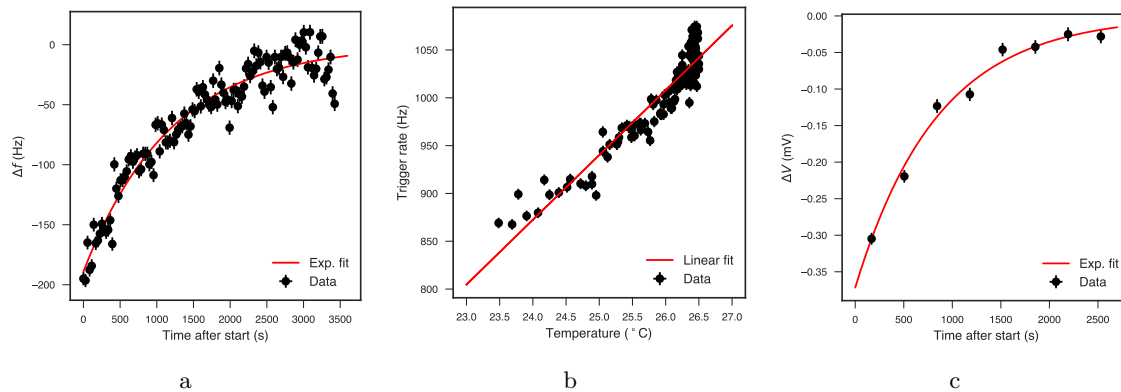
**Figure 5.17** (a) Trigger rate change $\Delta f$ as function of time after camera booting, fitted with an exponential function $g(t) = a\,(1 - \exp(-t/\tau_\mathrm{t})) + b$ with time $t$ and resulting fit parameters of $a \sim 189$ Hz, $b \sim 875$ Hz, and $\tau_\mathrm{t} \sim 1193$ s. The trigger rate change at time $i$ is defined as $\Delta f_i = f_i - \lim_{t \to \infty} g(t)$ with $f_i$ being the measured rate at time $i$. (b) Trigger rate as function of temperature for the same data as shown in (a), fitted with a linear function $g(T) = a\,T + b$ with temperature $T$ and resulting fit parameters of $a \sim 67.74$ Hz/°C and $b \sim -753.19$ Hz. (c) Camera mean baseline drift $\Delta V$ as function of time after camera booting, fitted with an exponential function $g(t) = a\,(1 - \exp(-t/\tau_\mathrm{b})) + b$ with time $t$ and resulting fit parameters of $a \sim 0.37$ mV, $b \sim 0.61$ mV, and $\tau_\mathrm{b} \sim 849$ s. The camera mean baseline drift at time $i$ is defined as $\Delta V_i = V_i - \lim_{t \to \infty} g(t)$ with $V_i$ being the measured camera mean baseline at time $i$. Adapted from (Zorn et al., 2018) [106].

The additional timing information in both the Cherenkov and direct CR-events is only possible due to the waveform sampling nature of the camera electronics and is useful for advanced image cleaning, background rejection, and event reconstruction algorithms. Additionally, images at the highest energies can take many tens of nanoseconds to cross the camera, as can be seen in Fig. 5.18d. Without a $\sim$100 ns readout window, such images would appear truncated, negatively impacting the analysis.

With the on-sky data taken with the CHEC-M camera, both the technical functionality of the camera and the existence of a data calibration and analysis chain have been proven. They both are crucial aspects for the camera to be used as an IACT camera. The on-telescope campaigns helped to verify interfaces and to improve operation procedures. Furthermore, the regular operation was used for understanding the system stability and reliability. In total, a few hundred meaningful Cherenkov and direct EAS particle events were recorded and analysed with the support of many people of all CHEC groups around the globe. However, the data taking was mainly performed by R. White and myself while the plots shown in Fig. 5.18 were mainly produced by J. J. Watson.

## 5.12 Summary and outlook

Regular operation of CHEC-M has shown that the camera control and data acquisition using the software `CHECInterface` and the calibration and waveform processing chain are robust and reliable. Intensive lab tests, presented in this chapter, led to a detailed characterisation of the camera performance. The main results are:

- CHEC-M can be read out at an efficiency of 95% at a mean random rate of 600 Hz, with an expected efficiency of 100% with the next TARGET ASIC generation used in
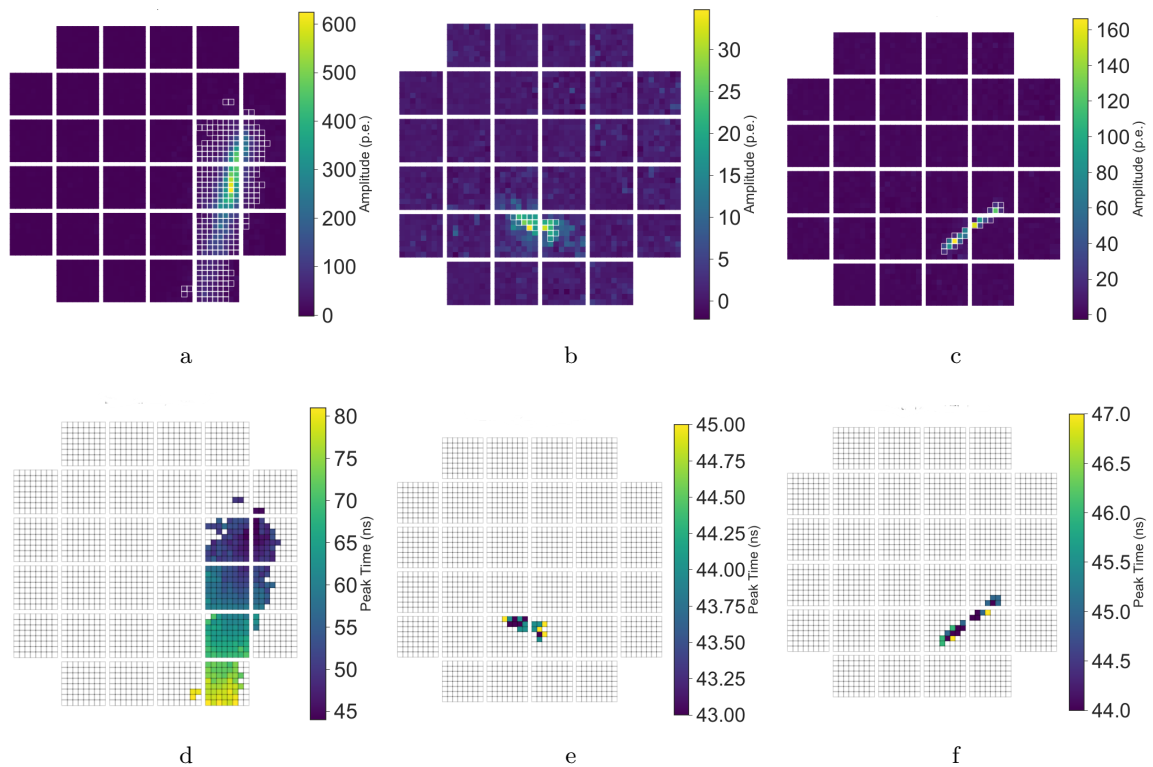
**Figure 5.18** Camera images of three different events, showing the intensity (a, b, and c) and the peak arrival time (d, e, and f) for each pixel. The white squares in (a), (b), and (c) indicate the pixels that remain after the tail-cut cleaning. All modules were active in this observation run. For further explanation refer to the text. Adapted from (Zorn et al., 2018) [106].

CHEC-S.

- While commissioning and testing of CHEC-M, 128 TARGET ASICs have been tested and tuned simultaneously confirming the results obtained in single TARGET ASIC tests (cf. [112]).

- Even after gain matching, the spread in gain between pixels is ~30% – the main limiting factor in trigger performance. This is due to the fact that in CHEC-M, the HV can only be set individually for each MAPM but not for each pixel – a fundamental feature of the MAPM design. The gain spread is expected to be reduced significantly when using SiPMs as photosensors as in CHEC-S.

- Camera trigger thresholds are characterised by 512 pairs of two ASIC parameters for each threshold which can be determined in lab measurements with a laser. In this way, five different threshold sets were defined for on-site tests between ~2 and ~170 p.e., intermediate thresholds can be identified by interpolation. A trigger bias scan over these settings can be used to identify the camera operating point on site.

- Reading out TARGET-5 modules leads to additional, false, triggers resulting in increased dead-time and the need of an increased trigger threshold. Both issues are addressed by decoupling sampling and triggering into two separate ASICs in the latest TM generation used in CHEC-S.

- The pulse shape characteristics (FWHM and 10–90% risetime) fulfil the requirements for trigger performance optimisation (5–10 ns and 2–6 ns, respectively).

- The time resolution between different pixels hit simultaneously by the same laser flash is better than 1 ns for illumination levels >6 p.e. confirming the expected behaviour.

- The crosstalk reaches a maximum of 6% between neighbouring pixels, affecting charge resolution, trigger efficiency, and camera image reconstruction.

- The dynamic range of the signal recording chain (MAPM, preamplifier, and TARGET module) covers a range from the sub-p.e. level to ~1000 p.e. at the highest possible HV of 1100 V and can be shifted towards higher signal amplitudes (factor ~6) by reducing the gain.

- The LED calibration flashers were shown to be appropriate devices for regular camera calibration and monitoring in terms of absolute gain and dynamic range determination. However, for the future, a design iteration is desired and on-going to avoid different temperature dependencies and to improve the predictability of absolute and relative brightnesses of different LED patterns.

- The camera and temperature stability were assessed showing that
    - the camera temperature can be controlled and (if required) kept at a constant level by adapting the chiller temperature,
    - the camera warm-up time is of the order of one hour, and
    - a mean baseline drift with temperature of 0.8 ADC/°C is observed and is mitigated by maintaining a constant camera temperature within 1°C or by taking regular 30 s pedestal calibration runs.

The on-telescope campaigns have not only provided a useful test-bed to assess operational and maintenance procedures, but have also – for the first time – demonstrated the use of Schwarzschild–Couder optics to collect atmospheric Cherenkov light. Data taken during the two campaigns have proven useful in the development of the data analysis chain and in understanding the levels of calibration that will be required for CTA.

Furthermore, understanding the factors limiting the performance were a critical input to the design of the second camera prototype CHEC-S. Those mainly are the limited readout rate of 600 Hz, the non-uniformity in gain, the trigger noise incurred with sampling enabled, and the trigger performance in general. Furthermore, the use of SiPMs in CHEC-S comes along with a number of advantages as explained in Sec. 4.2.2.

In the following chapter, I will present results of the commissioning, testing, and characterisation of CHEC-S where those limiting factors were addressed.

---

## CHEC-S commissioning, testing, and characterisation

---

> "It isn't enough to pick a path – you must go down it. By doing so, you see things you couldn't possibly see when you started out; you may not like what you see, some of it may be confusing, but at least you will have, as we like to say, explored the neighbourhood."

---

<div align="right">Ed Catmull</div>

In this chapter, I will present measurements and results of the commissioning, testing, and characterisation of CHEC-S. Beside basic studies such as the power consumption (cf. Sec. 6.1) and thermal distribution (cf. Sec. 6.2), I focused on measurements investigating the parameters that were mainly limiting the CHEC-M performance, such as the gain calibration (cf. Sec. 6.3) and the trigger performance (cf. Sec. 6.4). For those studies, I used not only laboratory measurements but also on-telescope data recorded while CHEC-S was installed on the ASTRI-Horn telescope. In Sec. 6.5, I will further show Cherenkov events from this on-telescope campaign before I conclude with a summary in Sec. 6.6. In addition to that, I discovered stability issues during the trigger performance studies with details given in App. B.

## 6.1 Power consumption

The power and current consumption of CHEC-S during the different steps of power-up and during nominal operation was investigated. For this purpose the current and voltage values of the BP (recorded by the SB) and of the PSU (recorded by the PSU controller) have been monitored. Fig. 6.1a shows the current drawn by the BP during power-up of the 32 TMs with a time delay of 10 s between each TM. The increase in BP current draw is about 34 A giving $\sim$1.05 A drawn per module (without being configured) with a supplied voltage of $\sim$12 V. The resulting power consumption of all modules is about 34 A$\times$12 V=408 W. This can also be inferred from Fig. 6.1b showing the power consumption during the different steps of power-up and initialisation: (1) X-DACQ power-up and initialisation, (2) BP power-up and initialisation, (3) TM power-up, (4) TM connection and initialisation, and (5) TM sampling and data sending. The difference between the power measured by the PSU and the SB ($\sim$150 W) is the power consumption by the PSU controller and fans, the Ethernet switches in the camera and in the PSU box, and the PB and SB. Hence, the overall camera

a



b
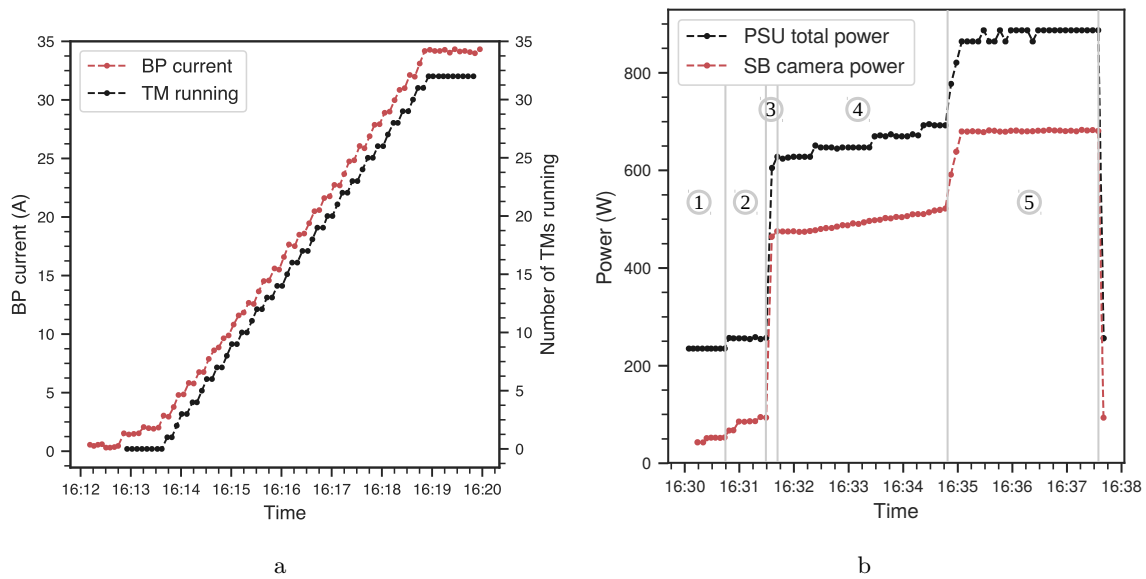
**Figure 6.1** (a) Current drawn by the BP (red data points, left y-axis) during power-up of the 32 TMs, measured by the SB. Also indicated is the number of TMs being running (black data points, right y-axis). (b) Power consumed by the camera as measured by the SB and by the whole system (camera + auxiliaries + PSU) as measured by the PSU controller during the different steps of component power-up and initialisation as well as nominal operation (for more details refer to text). Both measurement were done on 2017, Nov 3rd.

consumption (without chiller) is ∼900 W during nominal operation. Since a non-negligible part of this power is transferred into heat, it gives an upper limit for the cooling power the chiller must be able to provide.

## 6.2 Warm-up and thermal distribution

The temperature distribution in the camera and the warm-up were investigated using

- the TM on-board temperature sensors – one sensor for each board (primary, auxiliary, and power board; cf. Fig 4.8b),

- the SiPM temperature sensor, and

- five additional temperature sensors – four attached to the camera rack and one attached to the fan tray –, monitored by the SB.

The time the camera requires to stabilise in temperature in case of a constant ambient temperature (measurement performed in the lab) is about 45 min (cf. Fig. 6.2a).

The temperature spread between different TMs in the camera is quite large (∼27°C) with a few TMs having quite high temperatures (primary board temperatures of 40–50°C) even with the chiller temperature set to 12°C (being the case in the measurement shown in Fig. 6.2a). The spread is also significantly higher than in CHEC-M (cf. Sec. 5.10), being consistent with the generally higher power consumption of the TARGET-C modules compared to the TARGET-5 ones (cf. Sec. 6.1). However, most of the primary board temperatures lie between 25 and 35°C and even the hottest modules are within the temperature specification.

a                              b
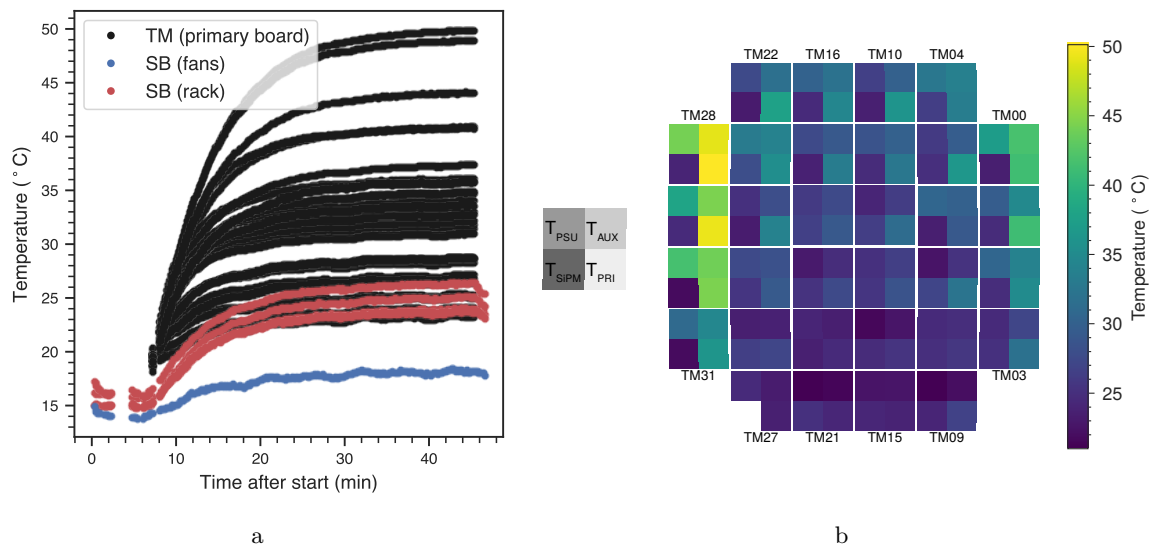
**Figure 6.2** (a) Monitoring of TM primary board temperature sensors as well as of SB temperature sensors mounted at the fan tray and at the camera rack during camera warm-up when the chiller was set to 12°C. The SB monitoring starts earlier and last longer since the SB is always monitoring while the TM temperature monitoring is only enabled in case the TM is powered and not being configured. (b) Camera image showing for each TM the temperature of the three TM boards – primary (PRI), auxiliary (AUX), and power (PSU) – and of the SiPM. The measurement was taken after a warm-up of ∼45 min, i.e. the image shows the distribution for the last data point in (a). The grey box on the left indicates which quarter on each TM represents which temperature sensor. The SiPM temperature sensor of the SiPM attached to TM 27 was not working and is therefore masked.

The reason for such a high spread may be inferred from Fig. 6.2b showing a snapshot of the TM temperatures (all four boards) at the end of the measurement shown in Fig. 6.2a (last data point), i.e. ∼45 min after camera boot-up. It can be observed that

- the hottest board on each TM is the primary board (which is why Fig. 6.2a shows the most extreme case),

- the modules on the bottom of the camera which are closest to the fan tray have the lowest temperatures while

- the modules on the vertical camera boundaries, where all the auxiliary boards are installed (like XDACQ-board on the right), have higher temperatures,

- the modules on the left vertical boundary, where the power entry panel is installed and cables are routed, are particularly hot (primary board temperatures > 40°C), and

- even though the TM temperatures and their spread are quite high, this is not as extreme for the SiPM temperatures which lie between 22 and 28°C.

Those observations stress the need of a temperature-dependent calibration of the modules when being calibrated in a stand-alone procedure in a temperature chamber. Furthermore, in case a smaller temperature spread is aimed for, the thermal in the camera housing needs to be optimised, e.g. by using baffles to guide the windflow or through-holes in the camera rack – the latter solution was used for CHEC-S as a follow-up of those measurements improving
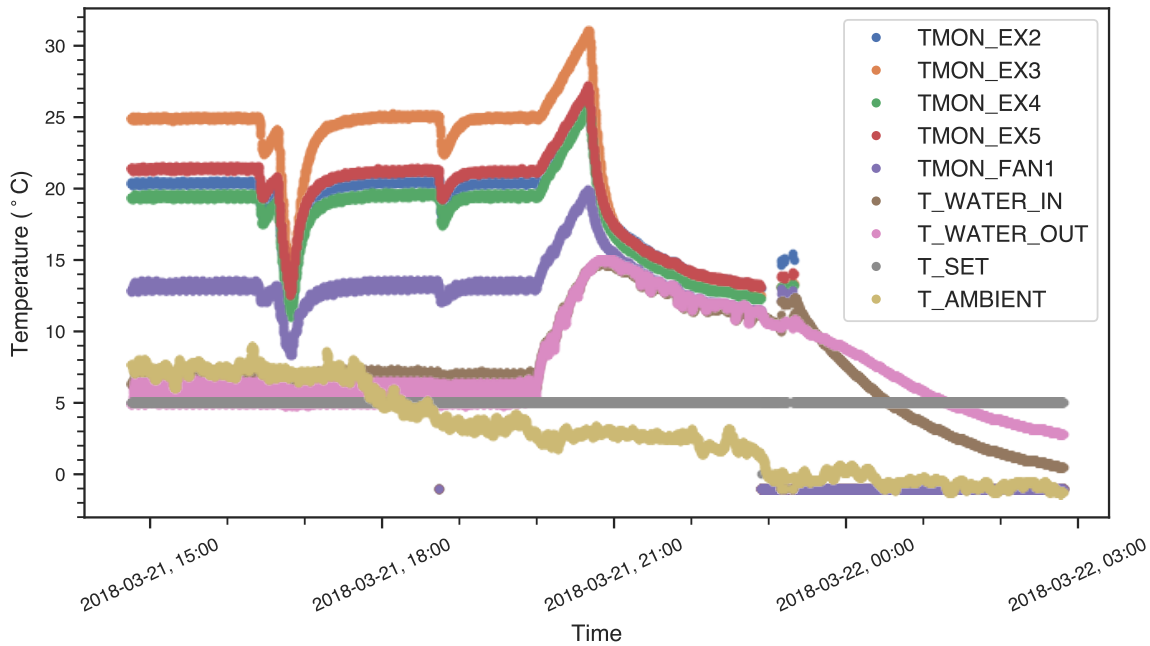
**Figure 6.3** Monitoring of several temperatures in the camera on 2018, March 21st (TMON_EX$i$, $i \in [2,5]$, being the SB sensors attached to the camera rack and TMON_FAN1 the one attached to the fan tray) as well as temperatures measured by the chiller unit (T_WATER_IN and T_-WATER_OUT being the inlet and outlet temperature, T_SET the set-point temperature, and T_-AMBIENT the temperature outside of the chiller unit, i.e. outdoor temperature). The downward spikes in the temperatures of the SB sensors are due to camera power cycles. Clearly visible is the failure of the chiller cooling around 8 p.m. when the in- and outlet temperatures started to increase causing also the SB sensor temperatures to increase. At around 8:45 p.m. TMON_EX3 exceeded 30°C causing the software to take action and sending the camera to `Safe`. The decrease of all temperatures indicates the success of this action. At around 11 p.m. the camera was power cycled for a quick investigation before it was switched off completely.

the situation slightly[1]. In any case, a precise monitoring of all temperatures, especially the TM board temperatures and the SiPM temperatures, is crucial not only for calibration but also for camera safety. For the latter one, not only an alert-action-feedback (cf. Sec. 4.6.1) provided by the SB (programmed in its firmware) but also a higher level alert system has been integrated into the control software regularly checking the monitor reading of all components against their predefined limits. The software takes action and sends the camera to `Safe` in case e.g. the temperatures of the SB temperature sensors exceed 30°C, as happened on 2018, March 21st when the chiller fan-speed-controller failed and the chiller stopped cooling (cf. Fig. 6.3).

## 6.3  HV matching and gain calibration

This section aims to describe the amplitude matching and gain calibration procedure used for CHEC-S and the analyses in the following sections. The aim of the amplitude matching is to equalise the response to a Cherenkov/laser signal of same intensity between all pixels. This

---

[1]Beyond CHEC-S, it has recently been discussed to add a second set of fans to the rack and to add thermo-electric cooler (TEC) elements to each sampling ASIC.

equalisation can in general be done on several levels, like extracted charge in p.e. (through gain equalisation), extracted intensity in photons (through PDE*gain equalisation), or signal amplitude in mV. It is of minor importance for image reconstruction (since different signal responses can be corrected for offline by the application of flat-field coefficients) but of crucial importance for trigger uniformity. Since the (L1) trigger logic is based on the discrimination of the signal sum of four neighbouring pixels (in mV), a non-uniform response in terms of pulse amplitude (in mV) to the same light level would result in single SPs dominating the trigger. The consequence would be a non-uniform acceptance to Cherenkov signals hitting the camera from different direction which is not desired.

The HV-amplitude-matching procedure consists of illuminating the camera with a reasonable laser light level (filter wheel attenuation of 56, cf. App. A) and adjusting the over voltage of each SP iteratively until the predetermined signal amplitude in mV is reached. More in detail, each iteration consists of (1) taking a laser run, (2) calibrating the events (pedestal subtraction and TF application, cf. Sec. 4.8), (3) calculating a new HV DAC value for each SP based on the difference between the goal signal amplitude and the extracted one from the current run, (4) applying the new HV DAC values, and (5) taking a new laser run. The iteration stops when all pixel amplitudes equal the predefined goal amplitude (within a given uncertainty range). The result is an HV configuration file with 512 individual DAC values. Instead of adapting the HVs until the amplitude of all pixels match the predefined value, the matching could also be performed on the L1 trigger, i.e. the HV of each SP is modified iteratively until the L1 trigger rate matches a predefined value. More in detail, this means that in the procedure of the so-called L1-rate-HV matching, step 2 and 3 in the HV-amplitude-matching procedure are replaced by (2) measuring the L1 trigger rates at the predefined threshold level and (3) calculating a new HV DAC value for each SP based on the difference between the goal L1 trigger rate and the measured one in the current run. Trigger measurements using both methods of HV-matching were performed showing no significant difference.

Sets of different HV-amplitude-matched configurations may be defined to be used for different applications and conditions, like for high and low NSB or for single p.e. measurements. Since a certain change in the HV DAC value corresponds to the same SiPM over voltage change for all pixels, the same PDE*OPCT*gain change corresponds to a certain DAC change. Thus, one HV-amplitude-matching measurement, performed to equalise the signal amplitudes of all pixel to 100 mV, is sufficient to determine multiple sets of different HV-amplitude-matched configuration files by shifting all DAC values by the same amount. The original HV configuration file resulting from the measurement is referred to as "DAC nudge 0" while the others are named after the DAC nudge which has been applied relative to their DAC values in "DAC nudge 0". Fig. 6.4a shows the extracted signal amplitudes from measurements with different DAC nudges. The relative spread in amplitude of 11% is limited by the DAC resolution and the fact that one bias voltage is set to four camera pixels, i.e. gain differences between those four pixels cannot be equalised. However, it is significantly lower than in CHEC-M (30% after gain-matching, cf. Sec. 5.3) where only one HV value could be set per 64 pixels. Furthermore the relative spread is constant for different DAC nudges proving the functionality of the procedure of determining different HV-amplitude-matched configuration files based on the same constant DAC shift for all SPs.

To convert the extracted charge of a pixel in units of cc (cf. Sec. 4.8.2) into number of p.e. (and photons), the gain (and PDE) as function of the over voltage must be known. For this purpose, the SPE distribution was measured for different DAC nudges and fitted with a multi-parameter function being a convolution of a Poisson distribution with individual Gaus-

a



b



c



d
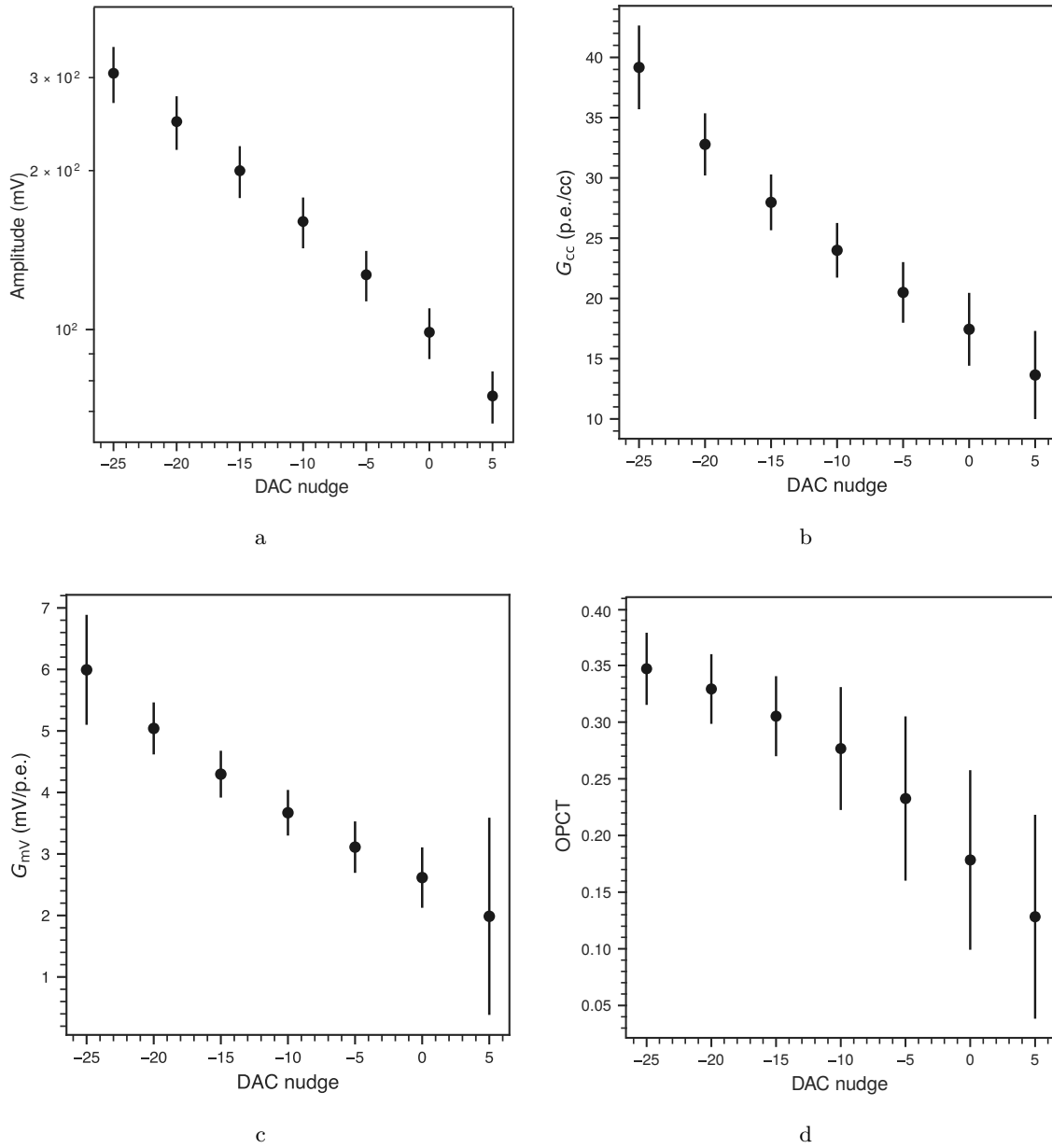
**Figure 6.4** (a) Measured signal amplitude at filter wheel attenuation 56, (b) $G_{cc}$ and (c) $G_{mV}$, and (d) OPCT as function of DAC nudge (for details refer to text). In all cases the errorbars indicate the standard deviation and thus the spread between all 2048 pixels.

sians including the influence of OPCT (cf. [107] & [126] for details about the fit function and fitting procedures). The resulting fit parameters are – among others – the mean illumination level $\lambda$ in units of p.e. and the OPCT. Hence, the gain $G_{cc}$ in units of cc/p.e. and defined as

$$G_{cc} = \frac{\overline{Q_{cc}}}{\lambda} \tag{6.1}$$

($\overline{Q_{cc}}$ being the mean of the SPE spectrum in units of cc) could be determined from the SPE distribution. To reach a better convergence of the fit, measurements at slightly different filter wheel attenuations were combined. Fig. 6.4b shows the resulting $G_{cc}$ for different DAC

nudges. It should be emphasised that – as already mentioned in Sec. 4.2.2 – a p.e. is defined as an electron-hole pair produced either directly by a photon hitting the microcell or via OPCT. Thus, $G_{cc}$ and the resulting signal in p.e. includes both, the amplification factor of a microcell and the OPCT. Since the PDE has not been measured yet for the CHEC-S SiPM tiles, the extracted OPCT from the SPE fits at different DAC nudges (cf. Fig. 6.4d) and the OPCT-PDE-dependence (given by the characteristic SiPM curves, cf. Fig. 4.7) were used to estimate the PDE at each DAC nudge. The PDE then is used to estimate the illumination in number of photons (hitting the camera focal plane) in all analyses in the following sections. However, due to possible differences between single SiPM tiles and since the PDE curve shown in Fig. 4.7 was measured at a wavelength of 408 nm (while the laser wavelength is 398 nm, cf. App. A), the stated number is an estimation only in all cases.

The gain $G_{mV}$ in units of mV/p.e. can be determined using the amplitude $A_{mV}$ in units of mV (cf. Fig. 6.4a), the charge $Q_{cc}$ in units of cc (both extracted at any but the same illumination level), and $G_{cc}$. It is given by

$$G_{mV} = \frac{A_{mV} \, G_{cc}}{Q_{cc}}.$$ (6.2)

Fig. 6.4c shows the resulting dependence of $G_{mV}$ on the DAC nudge.

For measurements with another HV configuration than one of the explicitly defined DAC nudge configurations, the values of $G_{cc}$, $G_{mv}$, and OPCT were determined using an interpolation between the two closest DAC values of the DAC nudge configurations or using an extrapolation in case the DAC value lies below/above the lowest/highest DAC value given in one of the DAC nudge configurations.

## 6.4 Trigger

One of the key performance parameters of CHEC-S assessed and optimised in the scope of this thesis is the trigger. The trigger calibration of CHEC-S follows another procedure than in CHEC-M: The individual ASIC parameters (`Pmtref4` and `Thresh`) were determined during the commissioning of the TARGET-C modules by injecting electrical signals. Those measurements were done in a temperature chamber at a fixed temperature by the CHEC-group at ECAP producing 16 look-up tables (one for each SP) for each TM. They link a given threshold in mV to a combination of `Pmtref4` and `Thresh` and set the required `Vped`-value for the corresponding SP. The full-chain camera testing, assessed in this work, consisted of using those look-up tables and validating them when all 32 TMs were used in parallel together with the BP and with the buffer board and SiPM connected. More in detail, the full-camera investigations performed in the scope of this thesis and presented in the following subsections are

1. trigger calibration verification and attempts to correct for mis-calibration (cf. Sec. 6.4.1),

2. mapping verification (cf. Sec. 6.4.2),

3. verification of the L2 trigger algorithm (cf. Sec. 6.4.3),

4. investigation of the influence of data sending on the trigger (cf. Sec. 6.4.4),

5. trigger efficiency investigation (cf. Sec. 6.4.5),

6. performance under different circumstances like NSB level, zenith angle, and DAC nudge (cf. Sec. 6.4.6),

7. comparison of data and trigger signal chain (cf. Sec. 6.4.7), and

8. minimum image amplitude investigation (cf. Sec. 6.4.8).

As mentioned in Sec. 3.2.1, a typical characteristic trigger measurement of an IACT-camera is the trigger bias scan. Due to the two-level trigger algorithm used in CHEC, it is distinguished between the L1 and L2 trigger bias scan/curve, depending on whether the 512 L1 trigger rates or the (single) L2 trigger rate is measured as function of the 512 L1 trigger thresholds applied.

### 6.4.1 L1 trigger measurements, calibration verification, and attempts to correct for mis-calibration

The procedure of the trigger calibration verification consisted of a continuous measurement-feedback-loop including the following steps:

1. measurements with a certain set of trigger look-up tables were performed with the whole camera,

2. issues were observed,

3. attempts to solve the issues were undertaken (if possible),

4. feedback to the CHEC-group at ECAP was given,

5. the CHEC-group at ECAP took actions to solve the issues and provided a new set of look-up tables,

6. the same iteration was initiated.

In the scope of this work, the loop was passed through three times.

The **first set** of trigger look-up tables showed quite a few mis-calibrated modules (cf. Fig. 6.5a). An attempt to resolve the mis-calibration based on changing `Thresh`, being one of the two ASIC parameters determining the L1 trigger threshold for each SP (cf. Sec. 4.3), was undertaken. However, identifying the cause of the mis-calibration[2] and producing a **second set** of trigger look-up tables lead to better results with only a few mis-calibrated SPs being left over (cf. Fig. 6.5b). While the first set of trigger threshold look-up tables was produced with positive input signals and up to a maximum amplitude of 200 mV only, the second set already contained look-up tables with trigger thresholds down to $-10$ mV. This is of special interest to identify the noise peak which should be centred around 0 mV in the L1 trigger bias scans. Furthermore, the ability to set thresholds higher than 200 mV is desirable for high-NSB conditions on site (e.g. for moonlight observations). Hence, a **third set** of threshold look-up tables containing thresholds from $-10$ mV up to 350 mV (instead of 200 mV) was produced for all TMs but the ones in slot 2, 3, 4, and 8[3]. Fig. 6.6a shows an L1 trigger bias scan using the third set of trigger look-up tables (except the four TMs in slot 2, 3, 7, and 8).

---

[2]In most cases, the cause of the mis-calibration was the look-up table production algorithm not leading to a convergence in the interpolation between different pairs of `Thresh` and `Pmtref4`.

[3]The production of the third set of trigger look-up tables took place in parallel to the HV stability repairing (cf. App. B) for which the TMs had to be taken out of the camera anyway. However, four modules not showing any HV stability issues were kept in the camera for further trigger tests (TMs in slot 2, 3, 7, and 8). Hence, the third set of trigger look-up tables with thresholds > 200 mV could not be produced for them.
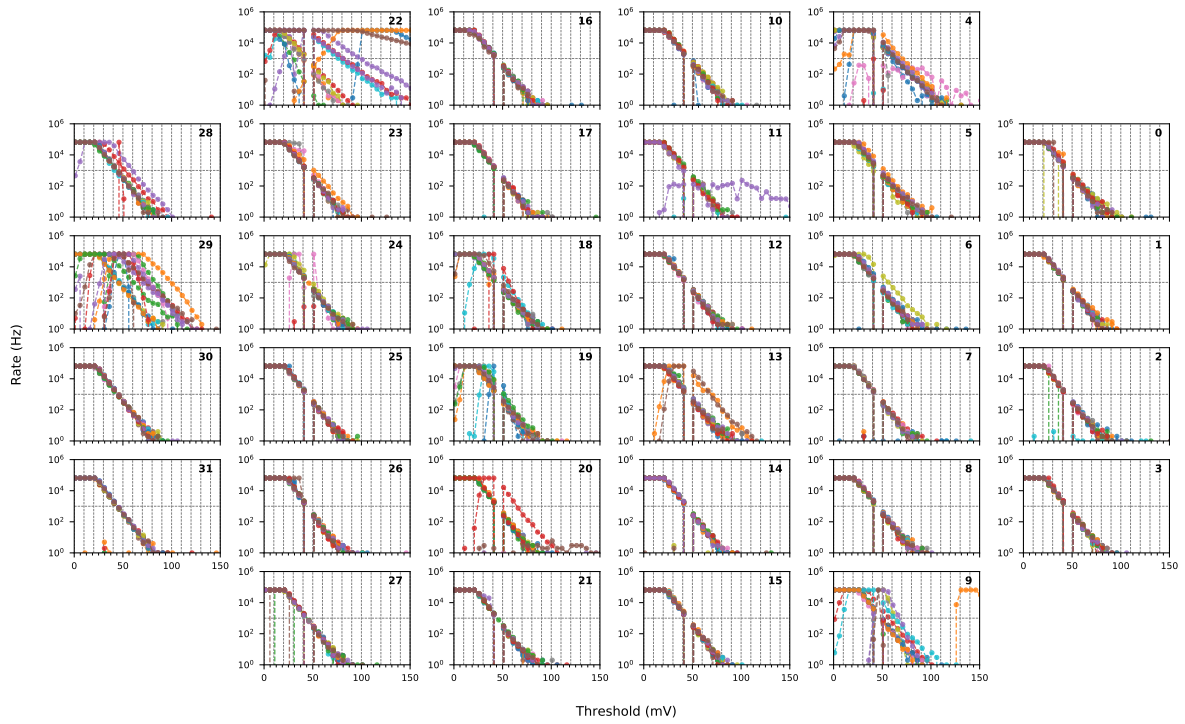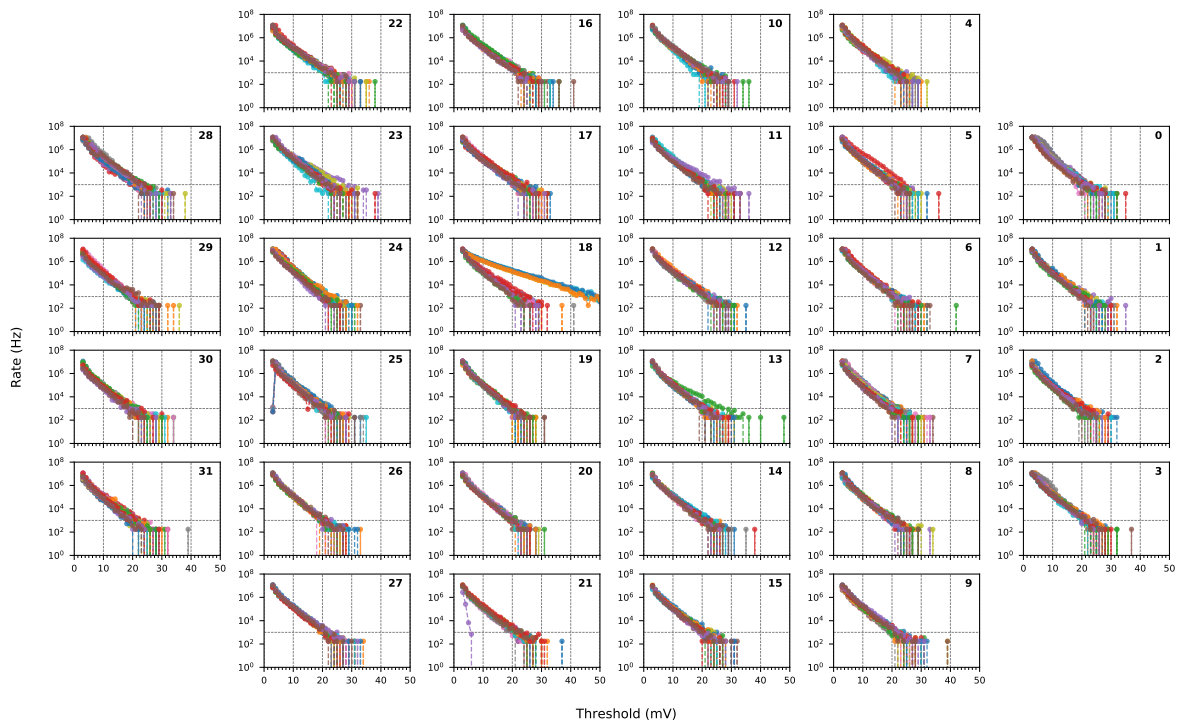
**Figure 6.5** L1 trigger bias scans (different colours indicating different SPs on each TM) with an amplitude-HV-matched camera using the (a) first set and (b) the second set of trigger look-up tables.
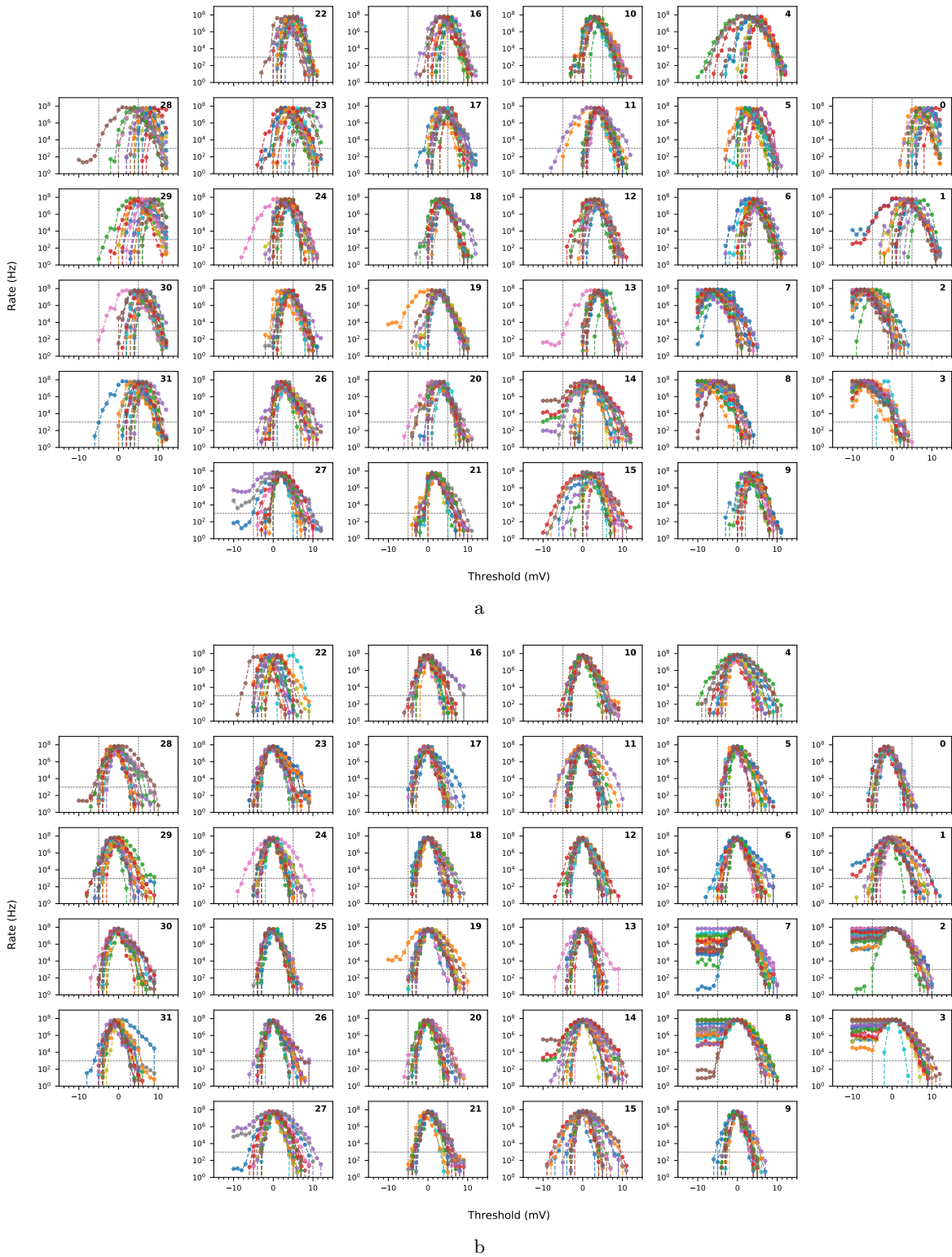
**Figure 6.6** L1 trigger bias scans (different colours indicating different SPs on each TM) with HV being off and using the third set of look-up tables (a) without and (b) with noise peak shifting applied.
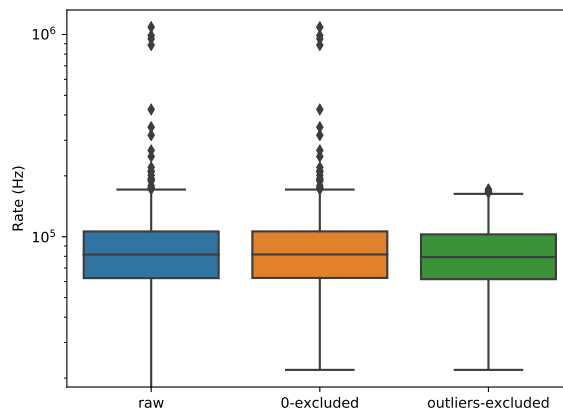
**Figure 6.7** Plot showing the distribution of the L1 trigger rates shown in Fig. 6.5b as measured ('raw', left), after exclusion of the L1 trigger rates = 0 ('0-excluded', middle), and after exclusion of the L1 trigger rates identified as outliers based on the IQRM with $x = 1.5$. In each case, the distributions of L1 trigger rates lying within $\Delta_{\mathrm{IQR}}$ (box) and within the intervals $[q_1 - x\,\Delta_{\mathrm{IQR}}, q_1]$ and $[q_3, q_3 + x\,\Delta_{\mathrm{IQR}}]$ (bars), and the values of L1 trigger rates identified as outliers (data points) are shown.

Since nearly all SPs show a noise peak being offset from 0 mV in Fig. 6.6a, a mis-calibration resulting in a constant offset for each SP could be assumed. This may be corrected for by shifting all thresholds of each SP by that offset resulting in a **shifted third set** of look-up tables. A measurement with such a shift applied is shown in Fig. 6.6b. It can be inferred that the shifting procedure worked for all SPs but for those on TM in slot 22 due to the known mapping issue (wrong mapping between L1 trigger counter reading and TM SP setting, cf. Sec. 6.4.2). It has further been validated in trigger efficiency measurements in the lab (cf. Sec. 6.4.5) and has been shown by on-telescope measurements (cf. Sec. 6.4.7) to result in a higher trigger uniformity than without the shift applied. Furthermore, it can be inferred that the noise wall reaches to thresholds of 5–10 mV/SP confirming stand-alone measurements with the T5TEA ASIC only (no SiPM, no buffer board) using electrical signals as inputs [113][4].

For cases of a remaining mis-calibration of a few SPs (as for example two SPs on module in slot 18 in Fig. 6.5b) or in case of a mis-functionality of an SP due to component failure during nominal operation, an algorithm to exclude those SPs is desired to achieve a certain degree of uniformity and to avoid those faulty SPs dominating the L2 trigger. An algorithm found to give good results is the so-called interquartile range method (IQRM). This method declares a data point to be an outlier in case its value $y$ does not lie in the interval $[q_1 - x\,\Delta_{\mathrm{IQR}}, q_3 + x\,\Delta_{\mathrm{IQR}}]$ where $q_1$ ($q_3$) is the 25th (75th) percentile. $x$ is typically set to 1.5, but can be defined differently based on the application and selection strictness. The box plots in Fig. 6.7 show the different steps of the algorithm (raw data, L1 rates = 0 excluded, and L1 outlier rates excluded) with $x = 1.5$ applied on the L1 trigger bias curves shown in Fig. 6.5b. In this case, 21 SPs were declared as outliers. Fig. 6.8 indicates to which L1 trigger bias curves they correspond to. Furthermore, the algorithm outputs a camera configuration file, containing the SPs to be masked from the trigger, to be applied in the following measurements.

---

[4]A small increase of noise on a sub-mV level is expected due to the use of 4×32 T5TEA-ASICs together with them connected to the SiPMs and buffer boards.
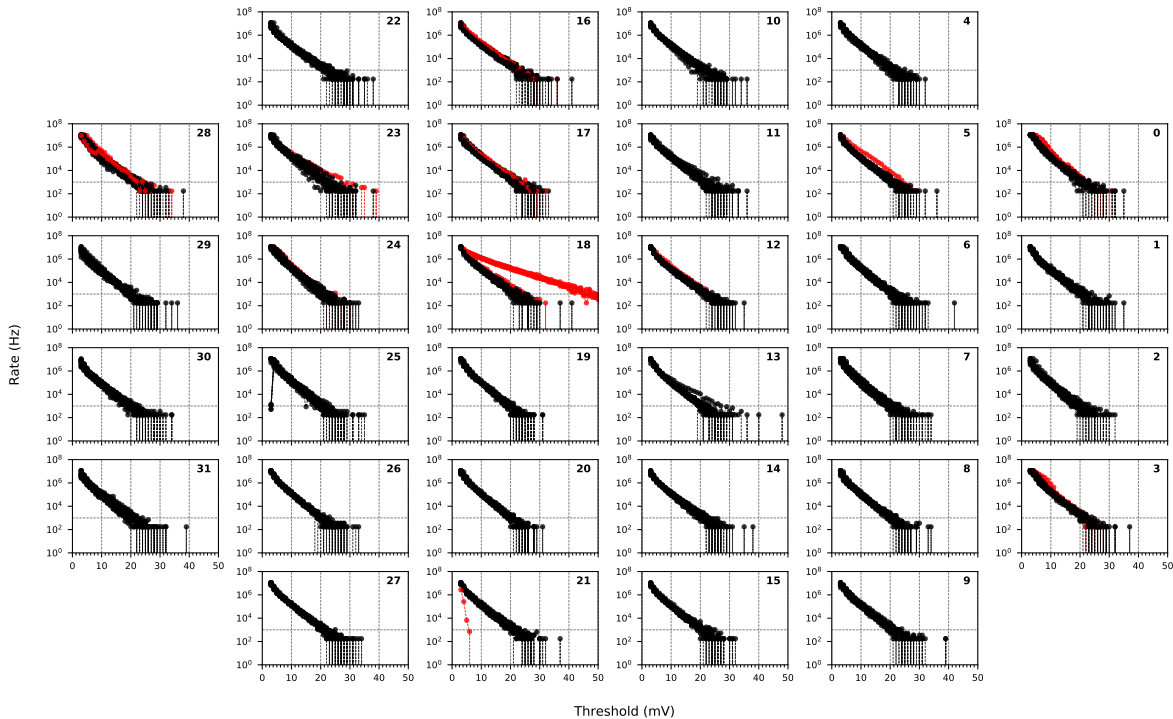
**Figure 6.8** Same L1 trigger bias scans as shown in Fig. 6.5b but with curves being identified as outliers (based on the IQRM with $x = 1.5$) marked as red.

## 6.4.2 Mapping

Each time the TFPGA was flashed with a new firmware the mapping between TM and BP SP indexing had to be validated. There are three main locations where the mapping is relevant and may incorrectly be implemented. This is between

1. SP L1 trigger line masking and SP L1 trigger counter reading (both on BP),

2. SP HV enabling (on TM) and SP L1 trigger counter reading (on BP), and

3. SP HV enabling (on TM) and SP L1 trigger line masking (on BP).

Once (1) and (2) are checked, (3) can inferred from them. Fig. 6.9 shows exemplary results of such validation measurements for different firmware versions. Fig. 6.9a reflects the different FEE module orientations when installed in the camera (cf. Fig. 4.4), i.e. modules with orientation B (slot 0, 2, 5, etc.) have the wrong mapping between setting their SP L1 trigger mask and reading their SP L1 trigger counter. The altering orientation was not taken into account in this BP TFPGA firmware (version d2017-03-31). Fig. 6.9b shows a mismatch between the TM SP (HV enabling) and the BP SP definition (L1 trigger counter reading). It could be inferred that in this BP TFPGA firmware (version d2017-10-03) the pixel and SP indexing was still following the "old" CHEC-M definition.

The measurements presented above are examples of measurements that were performed each time a new BP TFPGA firmware version was used. A first solution to correct the wrong mapping was to add a mapping conversion function in the camera software so that for the user the pixel and SP index definition was the same independent of setting the HV, reading the L1 trigger counter, or masking an L1 trigger line.
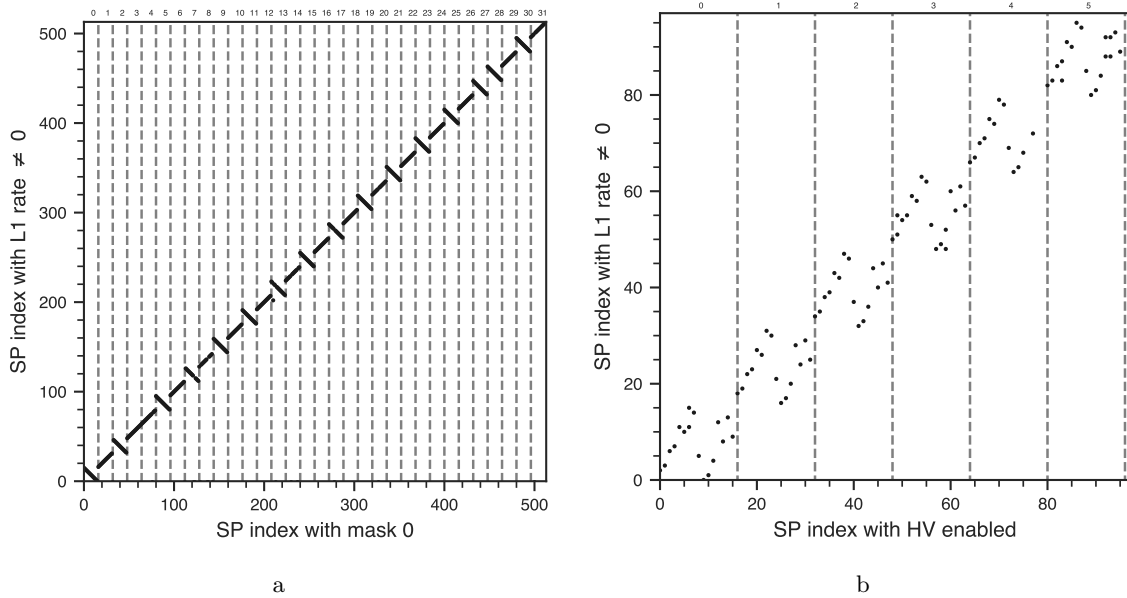
**Figure 6.9** Measurement showing which SP L1 trigger counter index increased (a) as function of the SP L1 trigger line index being un-masked (i.e. for which the TFPGA accepts an L1 trigger) for BP TFPGA firmware version d2017-03-31 and (b) as function of the SP index whose HV was enabled (zoom into the first 6 slots) for BP TFPGA firmware version d2017-10-03. Numbers on top and grey dashed lines help to show which SP indices correspond to which TMs.

However, to rule out more serious problem in the firmware logic, such as SPs being defined as neighbours in the firmware but not being physical neighbours (crucial for the correct formation of an L2 trigger), laser measurements with a physical mask were performed. In those measurements, the HV was enabled to two neighbouring SPs (according to the TM SP indexing) and a physical mask was installed in front of the focal plane leaving a hole only on top of those two SPs believed to be the selected ones. All L1 trigger lines but the ones corresponding to the two SPs (according to the determined TM-BP-mapping conversion) were masked and the L1 trigger counters were recorded. Recording the waveforms in those measurements could additionally confirm the pixel indexing in the data analysis pipeline at the same time. A few spot checks of this kind did not reveal any issues. However, a full systematic check during the NN-logic scan (cf. Sec. 6.4.3.1) confirmed such an issue in slot 22 for the BP TFPGA firmware version d2018-08-24 (the one used for most of the trigger performance measurement presented in this chapter).

### 6.4.3 L2 trigger algorithm

The correct implementation of the L2 trigger algorithm (NN algorithm with a coincidence window of 8 ns, cf. Sec. 4.4.1) in the BP TFPGA firmware had also to be verified each time a new TFPGA firmware version was loaded. The verification consists of two aspects: (1) the NN logic, i.e. whether two NN SPs, both with positive L1 trigger, actually fire an L2 trigger, and (2) the combinatorics, i.e. whether the measured L1 trigger rates result in the from combinatorics expected L2 trigger rate.
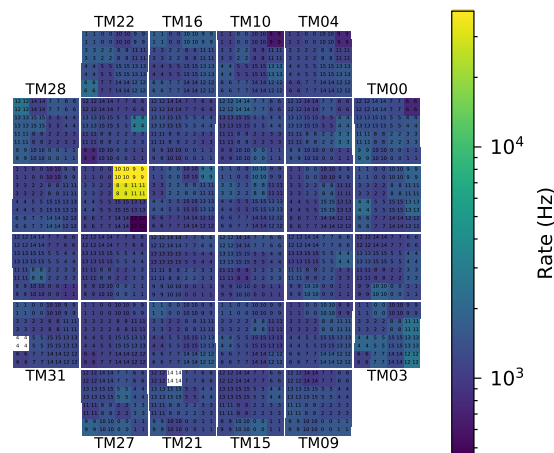
**Figure 6.10** L1 trigger rates at a threshold of 15 mV/SP. The amplitude-HV-matched camera was illuminated by the laser with a rate of 1 kHz and an illumination of ∼50 p.e./pixel.

### 6.4.3.1  NN logic testing

To verify the correct implementation of the NN logic in the BP TFPGA firmware (version d2018-08-24), an NN-logic scan looping over all 1910 valid NN combination (cf. Eq. 4.14) was performed. For this purpose, the amplitude-HV-matched camera was illuminated by the laser (rate of 1 kHz, illumination of ∼50 p.e./pixel). First, an L1 trigger bias scan was performed to determine a trigger threshold to be used in the NN-logic scan. A threshold of 15 mV/SP was chosen to be used since it sat well above the electronic noise wall with all but two SPs being triggering on the laser signal (cf. Fig. 6.10). The NN-logic scan consisted of a loop over all 1910 valid NN combinations. In each step, only the two corresponding NN SPs were enabled in the trigger mask and also the HV was enabled to those two SPs only. Then the trigger was enabled for a certain amount of time and the resulting L2 trigger rate was compared to the laser rate. The result of this measurement is shown in Fig. 6.11a. Fig. 6.12a shows the same measurement but with the HV enabled to all SPs in the whole measurement. It could be inferred from both measurements that the NN logic seems not to work for several SPs (issue 1) and that there is a mapping problem between the physical position of the SPs and the L1 trigger lines for the TM in slot 22 (issue 2) which is why all SPs show an efficiency equal to 1 in case the HV is enabled to all of them but not when only the HV of the ones physically next to each other is enabled.

Issue 2 was identified as a bug in the BP firmware code. To identify the source of issue 1 whether it is due to mapping issues in the BP firmware or due to instabilities of the L1 trigger signals from the FEE modules, the L1 trigger counters of all SPs were recorded in each step of the NN-logic scan in addition to the L2 trigger counter resulting in an "L1-efficiency" shown in Fig. 6.12b. Comparing Fig. 6.12a with Fig. 6.12b shows that the non-triggering NN patterns are coincident with at least one SP of the given NN pair not sending L1 triggers. This reveals not the NN logic in the BP TFPGA firmware being the cause of the issue but the FEE modules not sending L1 triggers to the BP. However, since all SPs (but two) were providing L1 triggers just before starting the NN-logic scan (cf. Fig. 6.10), it seemed to be a time-dependent issue meaning that all SPs send L1 trigger signals at the beginning but they disappear with advanced time. The NN-logic scan takes about 16 hours (30 seconds per pattern) starting with patterns in slot 0 and ending in slot 31. And indeed, when starting the NN-logic scan from behind (camera being rebooted in between), all valid patterns in slot
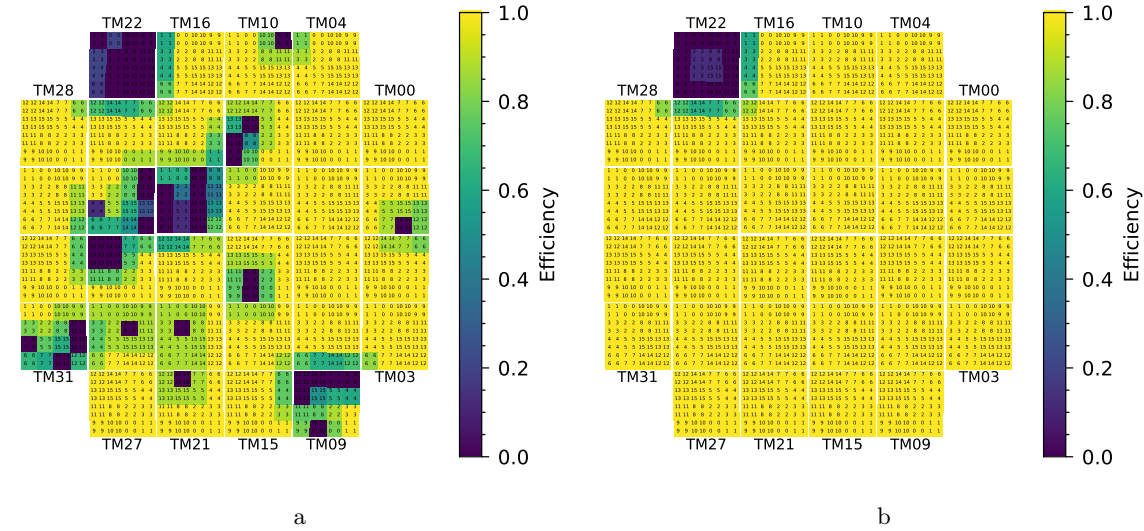
**Figure 6.11** NN logic test showing the efficiency of each SP forming an L2 trigger, i.e. the number of NN combinations containing this SP that formed an L2 trigger divided by the expected number of combinations that should form an L2 trigger. In case an SP and its neighbour did not trigger, for both the efficiency decreases. For those SPs having an efficiency of 0, they never triggered with their neighbours. The HV only is enabled to SP pairs for which the NN logic is checked at the given step. (a) before, (b) after fixing the HV stability issue (further details given in text).

31 triggered. In addition to that, the NN-logic test was repeated after FEE modules together with their SiPMs had been physically swapped around. The non-triggering pattern moved with the FEE modules being another indication that the problem was connected to the FEE (including SiPM) and not to the BP.

The issues discovered in the NN-logic tests were investigated in detail and were identified to be related to the TM HV stability (further details given in App. B).

After the HV stability issue was solved, the NN-logic scan was repeated showing no issues but the known mapping issue in slot 22 (cf. Fig. 6.11b).

### 6.4.3.2 Combinatorics

To verify the trigger combinatorics, a trigger bias scan was performed with an emulated NSB of $\sim$100 MHz and a mean camera gain of $G_{\mathrm{mV}} \simeq 4.5$ mV/p.e. while recording both, the L1 and L2 trigger rate(s). A `Wbias`-value of 1219 was used, expected to correspond to a coincidence window of $\sim$8 ns [5] and 26 SPs were excluded from the L2 trigger (result of the IQRM with $x = 1.3$) resulting in $1910 - 173 = 1737$ valid NN combinations. Fig. 6.13 shows the measured and predicted L2 trigger bias curves. The prediction is calculated from the measured L1 trigger bias curves using Eq. 4.13. Beside the predicted and measured L2 trigger rates, the two limits indicated in Fig. 6.13 are

- the L1 counter limit resulting from the maximum L1 trigger rate measurable with the BP TFPGA. It follows from the limited range of the 16 bit L1 counter and the integration time of 5 ms used in this measurement. Its value of $\sim$2.4 GHz is calculated using $f_{\mathrm{a,ji}}^{\mathrm{L1}} = f_{\mathrm{b,ji}}^{\mathrm{L1}} = (2^{16} - 1)/(4 \times 10^{-3}\ \mathrm{s})$ in Eq. 4.13, and

---

[5]This value was extrapolated from [114] and spot checked by R. White and A. Zink by probing the L1 trigger signal of a few SPs with an oscilloscope.
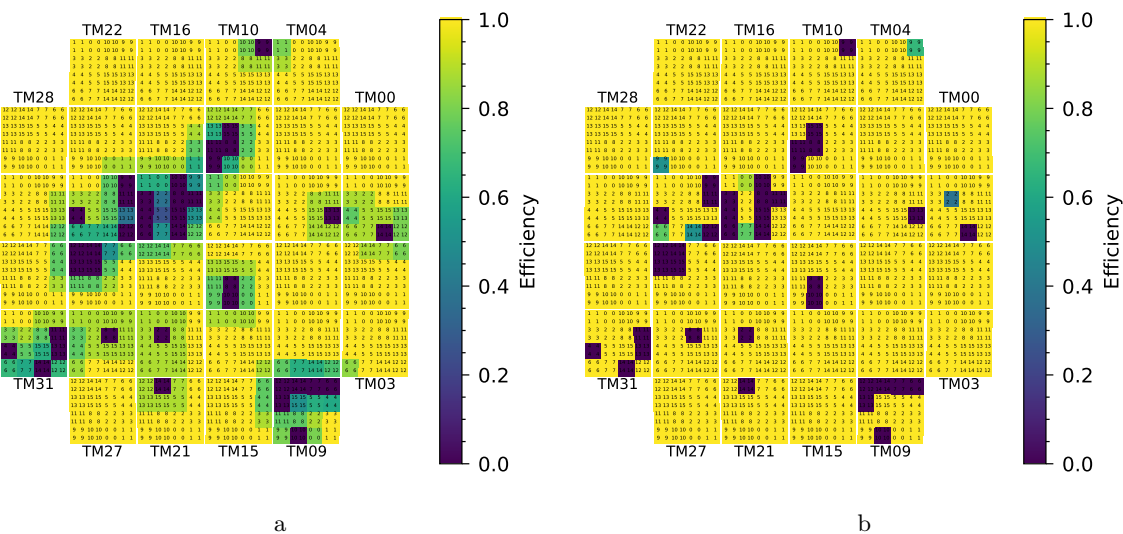
**Figure 6.12** (a) NN logic test showing the efficiency of each SP forming an L2 trigger (same definition as in Fig. 6.11a) with HV enabled to all SPs during the whole measurement. (b) L1 trigger efficiency of each SP sending an L1 trigger defined as the relative frequency of the L1 trigger counter of each SP being $\neq 0$ divided by the expected relative frequency this counter should be $\neq 0$ (HV enabled to all SPs).

- the L2 dead time limit following from the used BP HO time of 1 $\mu$s in this measurement and resulting in a maximum L2 trigger rate of $1/(1 \times 10^{-6}$ s$) = 1$ MHz.

Since the expected L2 trigger bias curve is calculated from the L1 trigger bias curves, it saturates at the L1 counter limit. Furthermore, as expected, the measured L2 trigger rate saturates at the L2 dead time limit. Similar to the L1 dead time limit, a new L2 trigger can only be fired in case the L2 trigger bit, which increased to 1 in case of an NN L1 trigger coincidence, decreased back to 0 before a new coincidence occurs. The probability of an NN L1 trigger coincidence arriving in the time the L2 trigger bit still being equal to 1 increases with an increasing number of L1 triggers, hence with decreasing threshold. Thus, the number of actual measured L2 triggers will decrease as soon as this probability is $\neq 0$. This is why the measured L2 trigger rate decreases for threshold of $<20$ mV towards lower thresholds. The observed plateau at $\sim$1 Hz in the measured L2 bias curve at a threshold of $\sim$60 mV is due to the counting accuracy given the used integration time of 1 s in the L2 trigger bias scan.

Beside the agreement with the system-based and theoretical rate limits, the measurement revealed a consistency between the measured L2 trigger bias curve and the predicted one. This does not only verify the full camera trigger logic but also the calibration of `Wbias`, meaning that a value of 1219 in fact corresponds to a coincidence window of 8 ns.

### 6.4.4 Influence of data sending

In CHEC-M the data sending process was observed to cause additional triggers due to noise pick-up by the trigger circuitry (cf. Sec. 5.4). This was one of the main inputs for the development of the new TARGET generation used in CHEC-S. The trigger and digitisation process was split into two different ASICs to prevent an influence of the data sending process on the trigger performance. Fig. 6.14, showing an L2 trigger bias scan with and without TACK
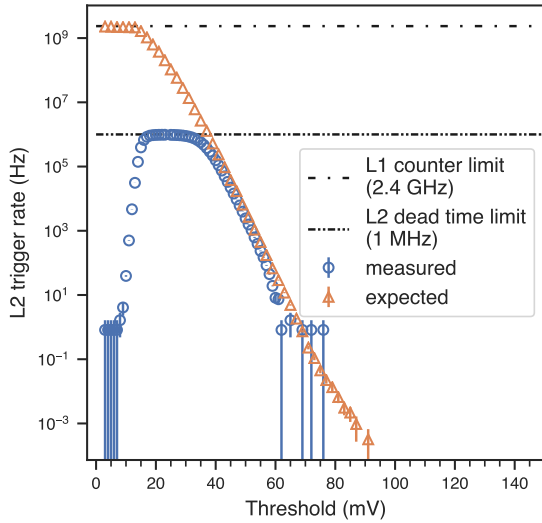
**Figure 6.13** L2 bias scan measured and expected from the combinatorics of the 486 measured L1 trigger bias scans (26 SPs were excluded). In addition two system-based limits are shown. For further explanations refer to text.
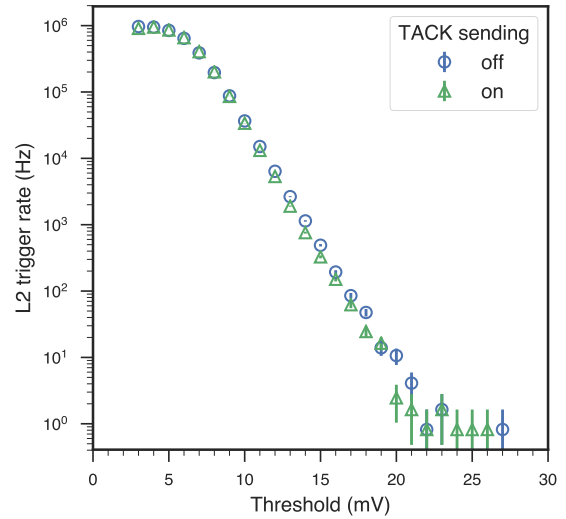
**Figure 6.14** L2 bias scan with and without TACK sending enabled. The observed saturation at 1 MHz is due to the L2 dead time limit following from the used BP HO time of 1 $\mu$s in this measurement (cf. Sec. 6.4.3.2).

sending enabled[6] verified that the data sending has no influence on the trigger performance. Hence, it can be concluded that the separation of the trigger and digitisation chain into two different ASICs solved the issue observed in CHEC-M.

### 6.4.5  Trigger efficiencies

Both, the L1 and L2 trigger efficiencies were investigated. Fig. 6.15a shows 510 (two SPs excluded from the measurement due to malfunctionality, identified using the IQRM) L1 trigger efficiency curves measured by looping through different laser illumination levels with the camera being amplitude-HV-matched. A rather low gain (DAC nudge +10, resulting in a mean gain of $G_{\mathrm{mV}} \simeq 1.5$ mV/p.e.) was used to keep the OPCT, negatively affecting the trigger uniformity, at a reasonably low level of $\sim$10%. Such an OPCT is comparable to the OPCT expected from SiPMs of the current generation being used in future camera iterations[7]. The threshold was set to 25 mV/SP using the shifted third set of trigger look-up tables except for TMs in slot 2, 3, 7, and 8. The resulting trigger amplitude, being defined as the illumination with a trigger efficiency of 50%, is 24.3 p.e./SP (mean out of all 510 curves) with a standard deviation of 2.8 p.e./SP (cf. Fig. 6.15b). The later one gives a measure for the trigger uniformity, being of the order of 12%. This is of similar order as the remaining relative spread in signal amplitudes after HV-amplitude matching (cf. Sec. 6.3), being the limiting factor for a higher trigger uniformity. Taking into account the pixel-wise PDE estimation at DAC-nudge +10, the trigger amplitude can be given in units of photons, being $(123.8 \pm 24.4)$ ph/SP. The spread in photons being a bit higher than 12% is due to the spread in PDE between different pixels.

---

[6]The sending of a TACK from the BP TFPGA to the TM FPGA initiates the data readout process, cf. Sec. 4.4.1.

[7]SiPMs of latest developments promise to have an improved OPCT-gain and OPCT-PDE dependence, i.e. a lower OPCT while keeping the gain and PDE at the same level.
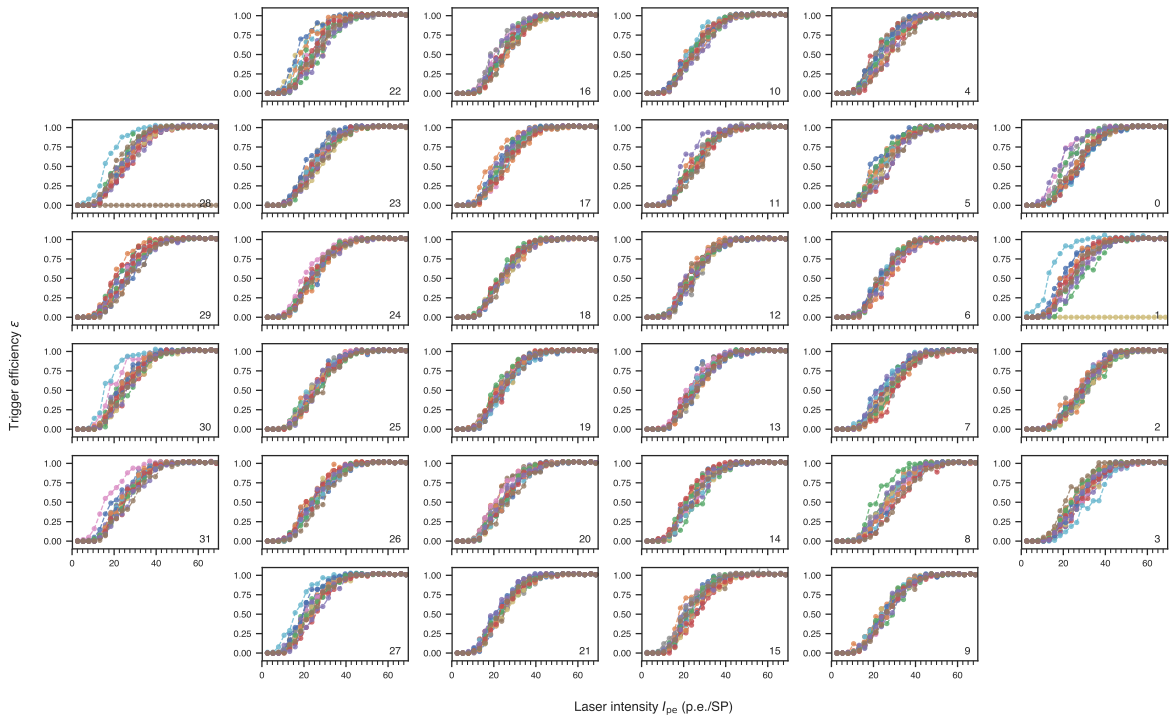
a
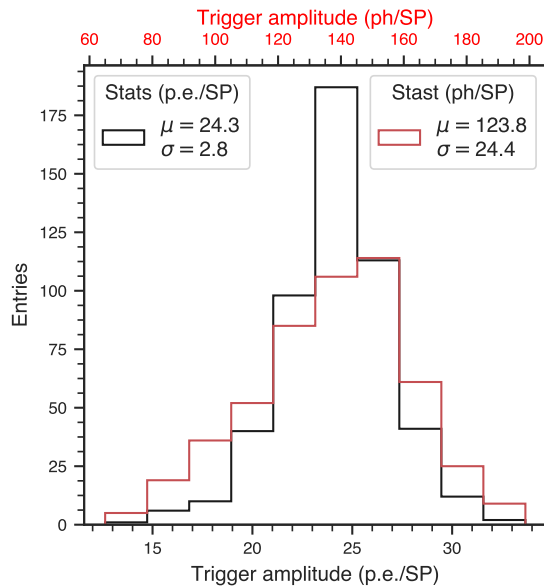


b

**Figure 6.15** L1 trigger efficiency measurements (with shifted trigger look-up tables) at gain of $G_{mV} \simeq$ 1.5 mV/p.e. and a threshold of 25 mV/SP. (a) L1 trigger efficiency as function of laser intensity in units of p.e./SP. (b) Trigger amplitude distribution extracted from measurements shown in (a) in units of p.e./SP and photons/SP.

The L2 trigger efficiency was investigated using a small representative subset of valid
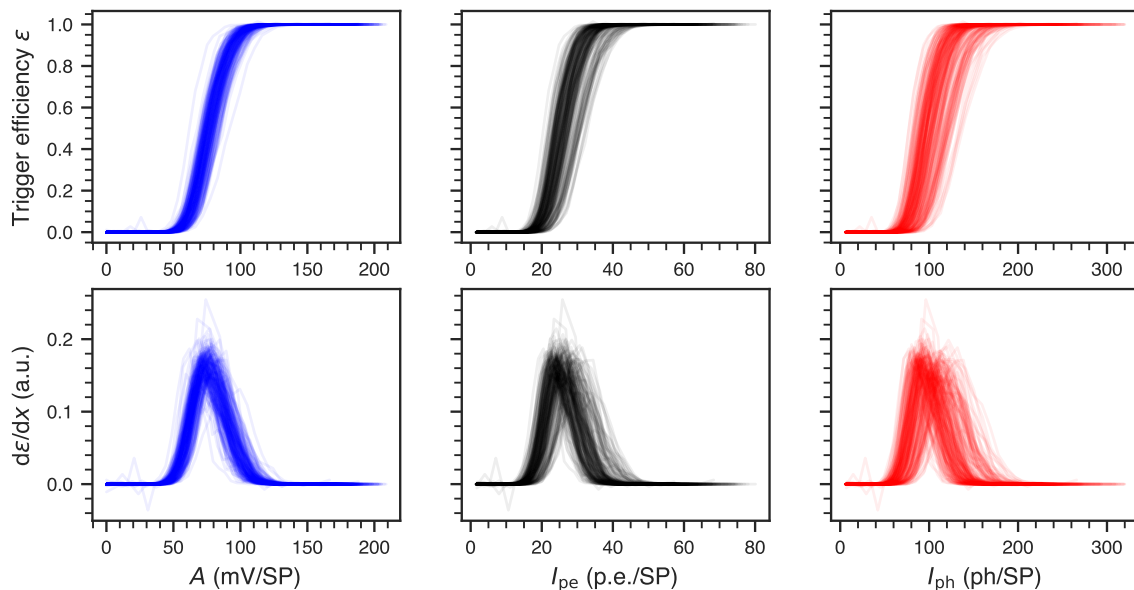
**Figure 6.16** L2 trigger efficiency $\epsilon$ (upper panels) and its derivation $\mathrm{d}\epsilon/\mathrm{d}x$ (lower panels) as function of signal amplitude $A$ (left panels) and laser intensity in units of p.e. $I_{\mathrm{pe}}$ (middle panels) as well as in units of photons $I_{\mathrm{ph}}$ (right panels) with the camera set to a threshold of 60 mV/SP and a mean gain $G_{\mathrm{mV}} \simeq 2.9$ mV/p.e. .

NN combinations only[8]. The result of a measurement with 210 valid NN combinations (all combinations between SPs on modules in slot 2, 3, 7, and 8 using the second set of trigger look-up tables) under the influence of an emulated NSB of ∼60 MHz, with the camera set to a threshold of 60 mV/SP and a mean gain $G_{\mathrm{mV}} \simeq 2.9$ mV/p.e. is shown in Fig. 6.16. The x-axis is given in three different units, reflecting the different steps of calibration (as explained in Sec. 6.3): extracted signal amplitude in mV, extracted charge in p.e. (using $G_{\mathrm{mV}}$ for conversion), and extracted illumination in photons (additionally using the estimated PDE). In addition, the derivation of the efficiency curve is shown which is used to determine the trigger amplitude and noise being the mean and standard deviation of a Gaussian fit to that curve. The extracted values for trigger amplitude and noise are shown in Fig. 6.17. The spread in trigger amplitude in units of p.e. is slightly lower in this measurement than in the previous L1 trigger efficiency measurement (∼10% compared to ∼12%) likely because of the smaller subset of SPs used in the L2 trigger efficiency measurements. Again, the spread in trigger amplitude in units of photons is slightly higher due to the spread in PDE. The trigger noise being a measure for the steepness of the efficiency curve, i.e. how efficient the trigger switches from "not triggering" to "100% triggering", increases with the presence of NSB. Its spread between all SPs of ∼11% (in units of p.e.) is slightly higher than the trigger amplitude spread being a hint for a non-uniform NSB distribution (as expected from the lab set-up, cf. App. A.3.4). The value of the mean trigger amplitude of 26.0 p.e./SP is consistent with the mean trigger amplitude of 24.3 p.e./SP extracted from the L1 trigger efficiency measurements (cf. Fig. 6.15b) since a gain ratio between the L1 and L2 trigger efficiency measurements of $1.5/2.9 \simeq 0.5$ and a ratio in threshold of $25/60 \simeq 0.4$ results in an expected ratio between

---

[8]Recording L2 trigger efficiency curves out of all 1910 valid NN combinations at different thresholds would take ∼1 month (depending on the accuracy of the measurement like step size in laser illumination, etc.). This is why only a small subset was used.
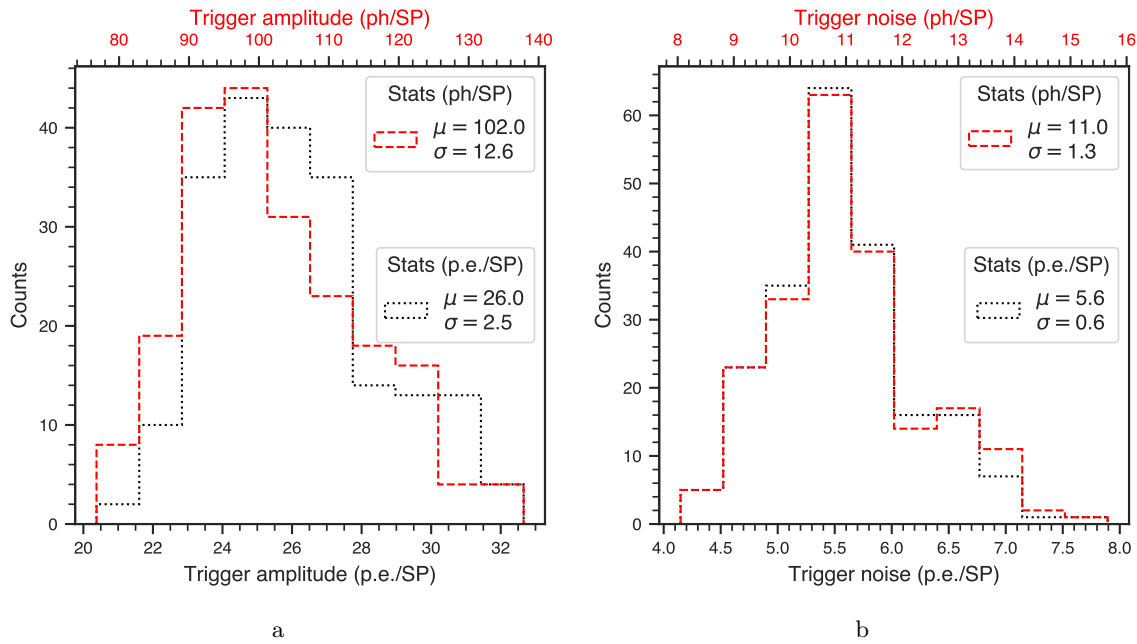
**Figure 6.17** Distributions of (a) trigger amplitude and (b) trigger noise (both in units of p.e./SP and ph/SP) deduced from L2 trigger efficiency curves shown in Fig. 6.16 (camera being set to a threshold of 60 mV/SP and a mean gain $G_{mV} \simeq 2.9$ mV/p.e.).

trigger amplitude of $\sim 1.2$. This is consistent with what is observed ($26.0/24.3 \simeq 1.1$) with the slight difference likely resulting from the fact, that L1 trigger measurements are compared to L2 trigger measurements. In the latter case, a smaller subset of SPs was used and the combinatorics of two SPs are taken into account (by design of the L2 trigger) causing the trigger efficiency curve to be slightly steeper.

The L2 trigger efficiency was further measured at eight more thresholds (keeping the gain at $G_{mV} \simeq 2.9$ mV/p.e.) using five valid NN combinations instead of 210. Those five combinations are formed by SP 0, 1, 2, and 3 on TM in slot 3. The resulting efficiency curves and extracted trigger amplitudes as function of threshold are shown in Fig. 6.18. The lower threshold of 24 mV is the lowest possible at this gain in case the maximum accepted accidental L2-trigger rate (induced by noise and dark counts) should be limited to $\leq 6$ Hz. It is significantly larger than the minimum threshold measured without NSB and HV (cf. Fig. 6.6 and [113]) being of the order of 5–10 mV/SP. This is due to charge induced by NSB, SiPM dark counts, and OPCT (cf. Sec. 6.4.6). The HV settings used in these measurements had been deduced by the L1-rate-HV matching procedure performed at 25 mV. This is why the spread in trigger amplitude is – by definition – at a minimum at 24 mV in the plot shown in Fig. 6.18b. The reason for the generally increasing spread with increasing amplitude might result from an intrinsic gain spread in the four ASIC channels forming an SP. This effect gets more visible at higher signal amplitudes. Furthermore, a slight discrepancy between applied and measured threshold in mV/SP can be observed which might be an indication for a remaining mis-calibration. Hence, this measurement could be utilised as a look-up table to provide improved calibration of the trigger threshold.
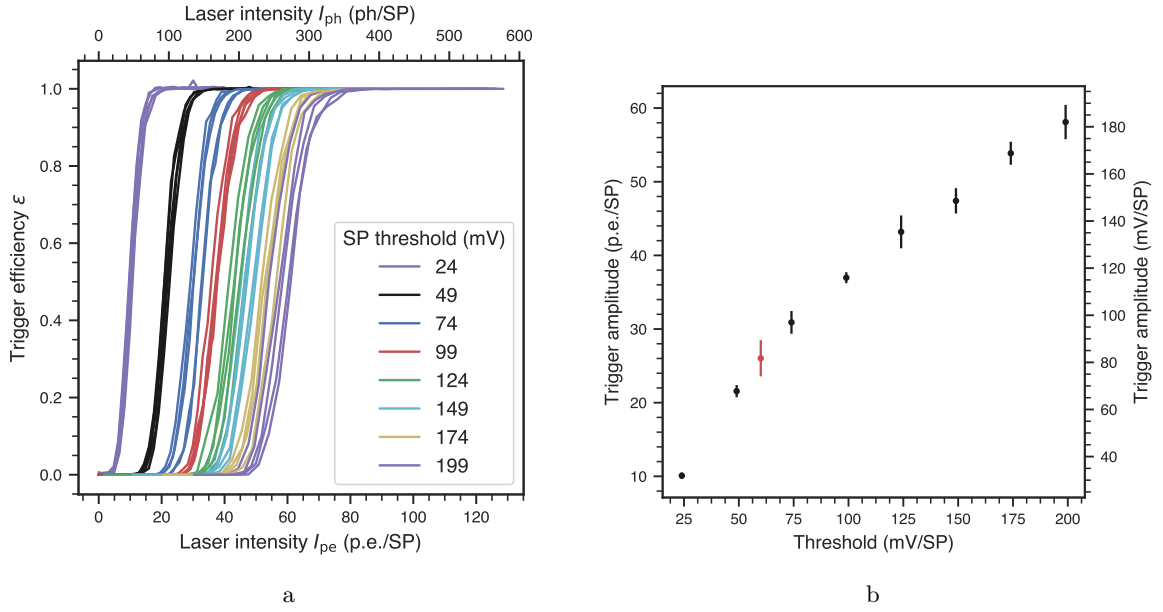
**Figure 6.18** (a) L2 trigger efficiency as function of laser intensity $I_{pe}$ and $I_{ph}$ for five different valid NN combinations and at different thresholds. (b) From (a) extracted trigger amplitudes as function of threshold. The errorbars indicate the spread between the five different valid NN combinations. The red data point shows the trigger amplitude extracted from the previous measurement (cf. Fig. 6.17a) with 210 valid NN combinations at a threshold of 60 mV.

## 6.4.6 Performance under different circumstances

The performance of the trigger under different circumstances was investigated in the laboratory and on the ASTRI-Horn telescope structure.

**L2 trigger rate and NSB level**  Fig. 6.19 shows L2 trigger bias scans with different NSB levels as emulated in the lab at a mean gain of $G_{mV} \simeq 4.5$ mV/p.e. and as measured on telescope at a mean gain of $G_{mV} \simeq 2.7$ mV/p.e. (DAC nudge 0). The observed saturation in Fig. 6.19a at 5 MHz for the measurement without NSB and at 1 MHz for the other measurements with NSB is due to the L2 dead time limit following from the used BP HO time of 200 ns and 1 $\mu$s, respectively (as explained in Sec. 6.4.3.2). Also the reason for the observed decrease of the L2 trigger rate towards lower thresholds is the same as explained in Sec. 6.4.3.2, being due to the fact that a new L2 trigger can only be fired in case the L2 trigger bit decreased back to 0 before a new coincidence occurred. The integration time in the measurement was set to 1 s being the reason for the saturation at an L2 trigger rate of 1 Hz. While in the laboratory measurements, the emulated NSB level was known from the DC UV LED calibration, on telescope it was estimated using the measurement of the slow signal.

The trigger bias curve without HV and NSB (blue data points in Fig. 6.19a) is in agreement with L1 trigger bias curves and stand-alone ASIC measurements showing a minimum achievable threshold (where no triggers are observed) of the order of 5–10 mV/SP (cf. Fig. 6.6 and [113]). The increase of minimum threshold under the presence of NSB (and HV) is due to accidental triggers resulting from NSB photons, SiPM dark counts, and OPCT charges. Both, the lab and on-telescope measurements nicely display the influence of different levels of NSB: the NSB wall (defined in Sec. 3.2.1) is shifted to higher thresholds for higher NSB
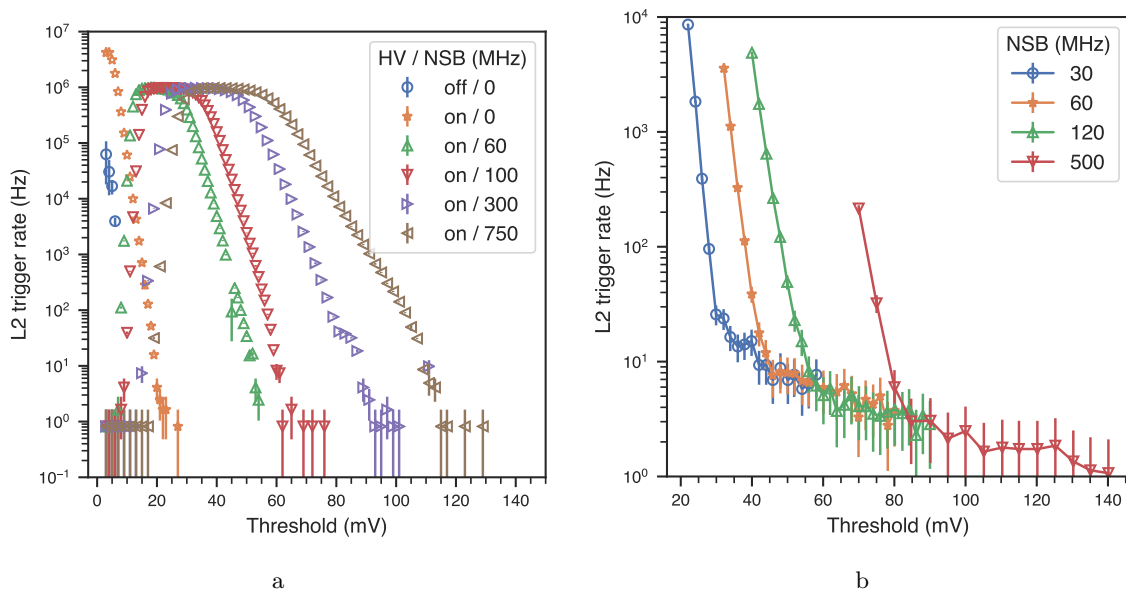
**Figure 6.19** L2 trigger bias scans measured (a) with emulated NSB in the laboratory and (b) on telescope at a mean gain of (a) $G_{\mathrm{mV}} \simeq 4.5$ mV/p.e. and (b) $G_{\mathrm{mV}} \simeq 2.7$ mV/p.e. .

levels. On telescope (cf. Fig. 6.19b), additionally the influence of the CRs can be observed. Since the CR rate, deduced from the CR flux (cf. Eq. 2.2) is independent of the NSB level, all curves in Fig. 6.19b asymptotically approach the CR rate curve at higher thresholds. In the CR-dominated part of the bias curve, the L2 trigger rate is given by Eq. 3.11, resulting in

$$ f_{\mathrm{L2}} = A\,\Omega\,\Phi_{\mathrm{CR}} = A\,\Omega \left(\frac{E}{1\,\mathrm{TeV}}\right)^{-2.7} 9.6 \times 10^{-2}\,\mathrm{m}^{-2}\,\mathrm{s}^{-1}\,\mathrm{TeV}^{-1}\,\mathrm{sr}^{-1}, \qquad (6.3) $$

with $A = \pi \times (100\,\mathrm{m})^2$ being the area of the Cherenkov light pool and $\Omega = 4\,\pi\,\sin^2\left(\frac{\alpha}{4}\right) \simeq 0.019$ sr the solid angle covered by CHEC (FoV of $\alpha \simeq 9°$). Using the transition point (defined in Sec. 3.2.1) as operation point, the energy threshold for given observing conditions can be calculated. For the observation under an NSB level of 30 MHz (blue curve in Fig. 6.19b), the transition point is at a threshold of $\sim$30 mV with an L2 trigger rate of $f_{\mathrm{L2}} \simeq 17$ Hz. Isolating $E$ from Eq. 6.3, the energy threshold for those specific observation conditions is given by

$$ \frac{E_{\mathrm{thr}}}{1\,\mathrm{TeV}} = \left(\frac{A\,\Omega\,9.6 \times 10^{-2}\,\mathrm{m}^{-2}\,\mathrm{s}^{-1}\,\mathrm{TeV}^{-1}\,\mathrm{sr}^{-1}}{f_{\mathrm{L2}}}\right)^{(1/2.7)} \simeq 1.58. \qquad (6.4) $$

**L2 trigger rate and zenith angle** L2 trigger bias scans were also recorded as function of telescope zenith angle $\theta_z$ (cf. Fig. 6.20a). It roughly follows the expected dependence (cf. Fig. 6.20b) given by [127]

$$ \frac{f_{\mathrm{L2}}(\theta_z)}{f_{\mathrm{L2}}(0°)} \propto \cos(\theta_z)\, e^{1-1/\cos(\theta_z)}\, [1 - \ln(\cos(\theta_z))], \qquad (6.5) $$

where $f_{\mathrm{L2}}(\theta_z)$ and $f_{\mathrm{L2}}(0°)$ are the L2 trigger rates at zenith angle $\theta_z$ and $0°$, respectively[9]. The deviations from the fit in Fig. 6.20b may result from varying NSB conditions with zenith

---

[9]The $\cos(\theta_z)$-dependence results from the fact that CRs arriving at some zenith angle $\theta_z$ have travelled a pathlength through the atmosphere that increases as $1/\cos(\theta_z)$. Hence, the Cherenkov light yield gets
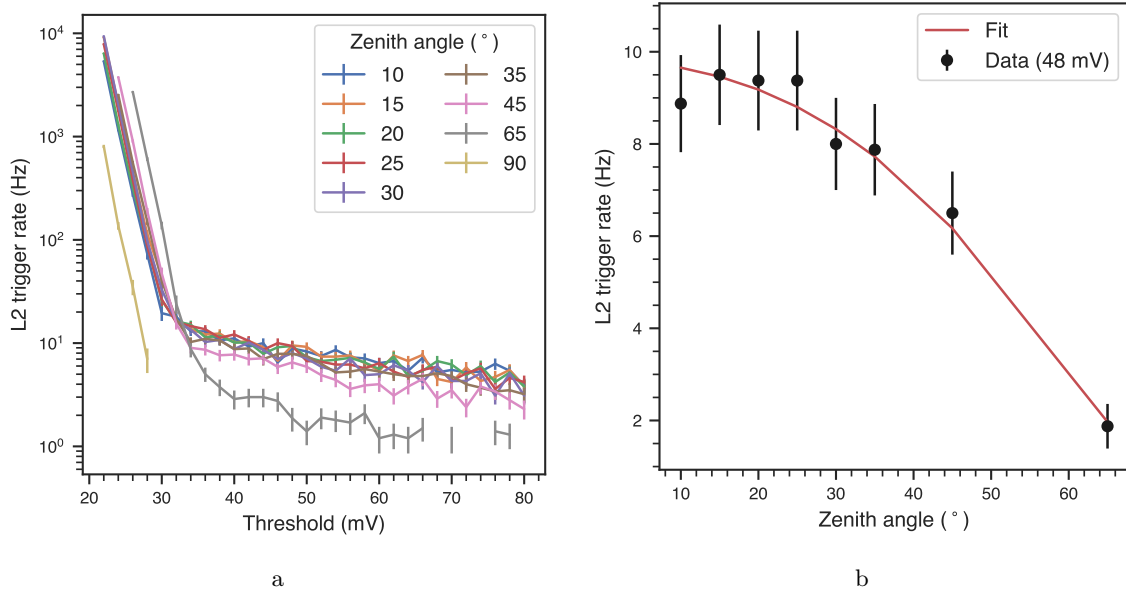
**Figure 6.20** (a) On-telescope L2 trigger bias scans measured at different zenith angles. (b) Dependence of the L2 trigger rate at a threshold of 48 mV on the zenith angle. The fit function is given by Eq. 6.5. Plots look similar for other thresholds.

angle due to clouds and fog as well as due to the surroundings of the telescope. The slight dependence of the position of the NSB wall on the zenith angle also hints at this aspect. Especially at $\theta_z = 90°$ (parking position of the telescope), the NSB wall is significantly shifted to lower thresholds due to trees in the FoV, appearing as dark background and thus low NSB.

**L2 trigger rate and DAC nudge** Fig. 6.21 shows L2 bias scans for different DAC nudges. As expected, the whole bias curve shifts to higher thresholds for lower DAC nudges due to the increased gain and PDE. Furthermore, in addition to the shift of the bias curve in $x$-direction, the overall CR rate increases due to the increase of the PDE. This can nicely be monitored with the increase of the L2 trigger rate at the transition point for each DAC nudge (compare for example transition point rate of ∼10 Hz at DAC nudge 0 and ∼15 Hz at DAC nudge −25 which is consistent with an increase of 50% in PDE between those two DAC nudges).

**In general**, the measurements presented in this section are in good agreement with expectations as well as with MC simulations (cf. Fig. 6.22). The latter reveals an optical throughput of the ASTRI-Horn telescope of ∼55%. With the next-generation of SiPMs, featuring a higher PDE and lower OPCT, and an increased performance of the telescope optics reaching the expected throughput of 80–90%, an increase of factor ∼4 in number of photoelectrons may be reached. This would lead to an increase of the L2 trigger rate at the transition point (blue curve in Fig. 6.19b) to ∼70 Hz and hence to a decrease of the energy threshold to ∼400 GeV. Additionally, when being part of an array of telescopes, a threshold slightly below the transition point might be used as operation point (due to the shift of the

---

reduced by the same factor through atmospheric extinction and scattering. However, this only is an approximation. The additional factors $e^{1-1/\cos(\theta_z)}$ and $[1-\ln(\cos(\theta_z))]$ are corrections to the approximation resulting from the accurate handling of the atmospheric pressure and the $\theta_z$-dependence of the photon density at the focal plane. See [127] for further details.
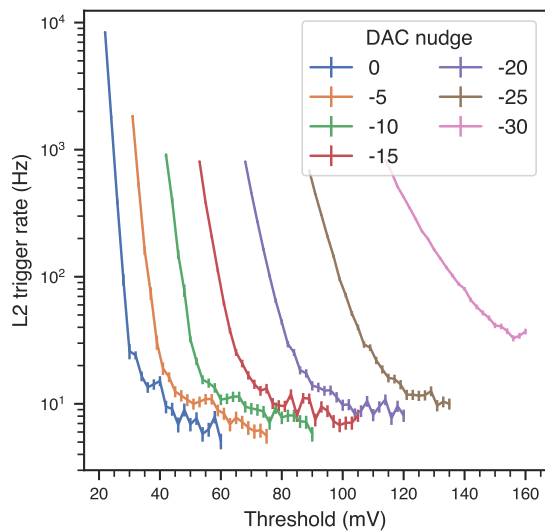
**Figure 6.21** On-telescope L2 trigger bias scans measured for different DAC nudges.
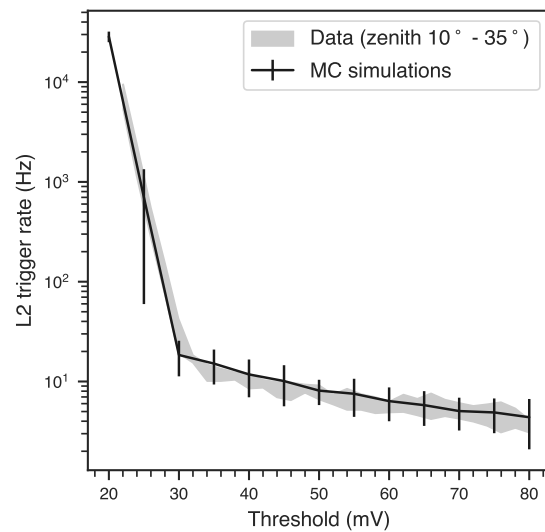
**Figure 6.22** Comparison of measured and simulated on-telescope L2 trigger bias curves.

NSB wall to lower thresholds in the array trigger bias curve, cf. Fig. 3.11). In this way, an L2 trigger rate of ∼300 Hz, being the required event rate an SST camera must be able to deal with, could be reached.

### 6.4.7 Comparison of data and trigger signal chain

Two different ASICs are used in the CHEC-S TARGET module for triggering and digitisation (cf. Sec. 4.3). To check consistency between the trigger and digitisation chain, the trigger efficiency can be compared to the extracted signals from data. For this purpose, the camera was set to internal triggering and illuminated by the laser (periodic frequency of 50 Hz). A mean gain of $G_{mV} \simeq 4.5$ mV/p.e. and an emulated NSB of 60 MHz were used. An L2 trigger bias scan was performed and data was recorded in case the L2 trigger rate was between 10 and 600 Hz. Fig. 6.23a shows the L2 trigger efficiency $\epsilon$ as function of threshold. Three parts can be identified: (1) the NSB-dominated part with $\epsilon > 1$ for thresholds <50 mV (same as green data points in Fig. 6.19a, (2) the laser-dominated part for thresholds between ∼50 and ∼125 mV with $\epsilon = 1$, and (3) the part with the threshold being close to or higher than the laser amplitude causing $\epsilon \to 0$.

In each NN combination, both SPs need to have signal amplitudes above the threshold to fire an L2 trigger. Consequently, it can be assumed that out of all valid NN combinations the second SP with the highest amplitude (referred to as "second-brightest SP") determines whether an L2 trigger is fired or not. Fig. 6.23b shows distributions of the difference of the second-brightest SP amplitude $A_{2ndSP}$ and threshold as function of threshold applied. Comparing Fig. 6.23a and 6.23b, the trigger efficiency should be similar to the fraction of $A_{2ndSP}$ being above the threshold. At the 50%-efficiency point being at ∼145 mV, more than half of $A_{2ndSP}$ is already below the threshold. This is an indication for a slight difference in trigger and digitisation chain or for a slight mis-calibration of the threshold – the latter one being more likely since the second set of threshold look-up tables was used in this measurement.

Fig. 6.24a shows the distribution of $A_{2ndSP}$ for on-telescope measurements with the threshold set to 55 mV using the shifted third set of threshold look-up tables. The peak of the dis-

*J. Zorn*
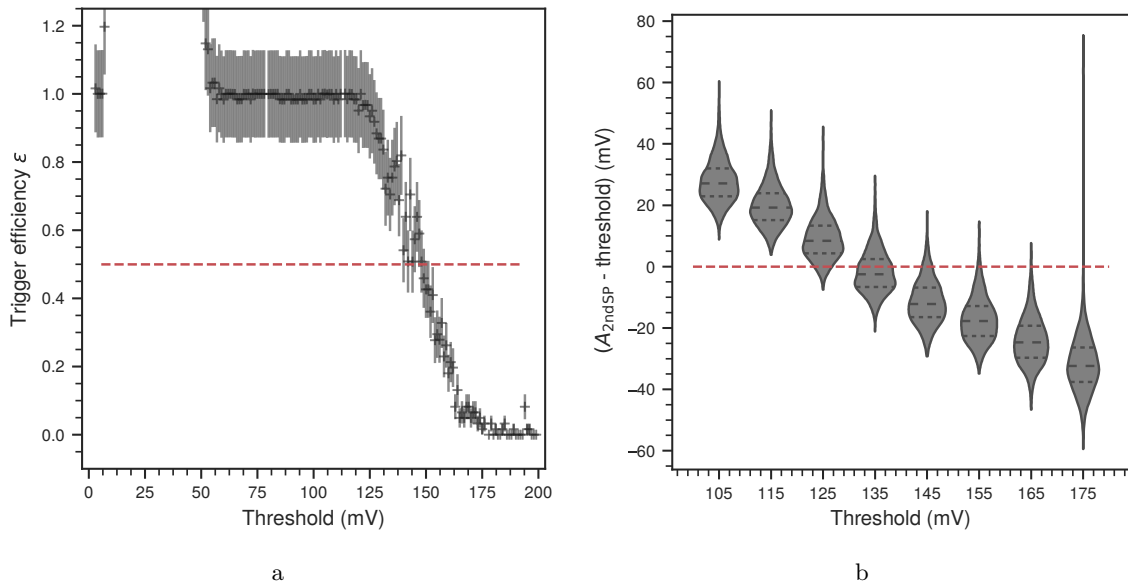
**Figure 6.23** (a) L2 trigger efficiency $\epsilon$ as function of threshold, measured at a mean gain of $G_{mV} \simeq$ 4.5 mV/p.e. and an emulated NSB of 60 MHz. (b) Distributions showing the difference of the second-brightest SP amplitude $A_{2ndSP}$ and threshold as function of threshold applied.

tribution is at 55 mV and therefore in agreement with the threshold being set. Fig. 6.24b also shows the distribution of $A_{2ndSP}$ but for another run (and night). In this case the threshold was set to 32 mV using the **un-shifted** third set of threshold look-up tables. Two peaks, both being at $A_{2ndSP}$ larger than the threshold, can be identified in the distribution. They indicate a non-uniformity in the trigger resulting from the mis-calibration of the thresholds which was not corrected for by using the noise-peak-shifting algorithm. The comparison of both measurements (Fig. 6.24a & 6.24b) is another proof of the noise peak shifting being a valid method to correct for mis-calibration of the trigger look-up tables. Furthermore, it proves that once the corrected trigger look-up tables are used, the signal processing in the trigger and digitisation chains are consistent.

### 6.4.8 Minimum image amplitude

In addition to the second-brightest SP amplitude, the distribution of image amplitudes for a certain run can be extracted using a Hillas analysis. Fig. 6.25 shows such a distribution for run 12714 (trigger threshold of 55 mV) revealing a minimum image amplitude of $\sim$35 photons at the focal plane (no telescope throughput taken into account). The minimum image amplitude is another characteristic property of the trigger. In this observation run, a rather high threshold was used due to a quite high NSB of $\sim$120 MHz. Hence, a lower minimum image amplitude might be reached for lower thresholds.

## 6.5 Cherenkov events and further analyses

Fig. 6.26 shows a Cherenkov event recorded during the on-telescope campaign when CHEC-S was installed on the ASTRI-Horn telescope structure in Sicily (Italy) end of April/beginning of May 2019. Those events have not only been used for performance analyses as presented in
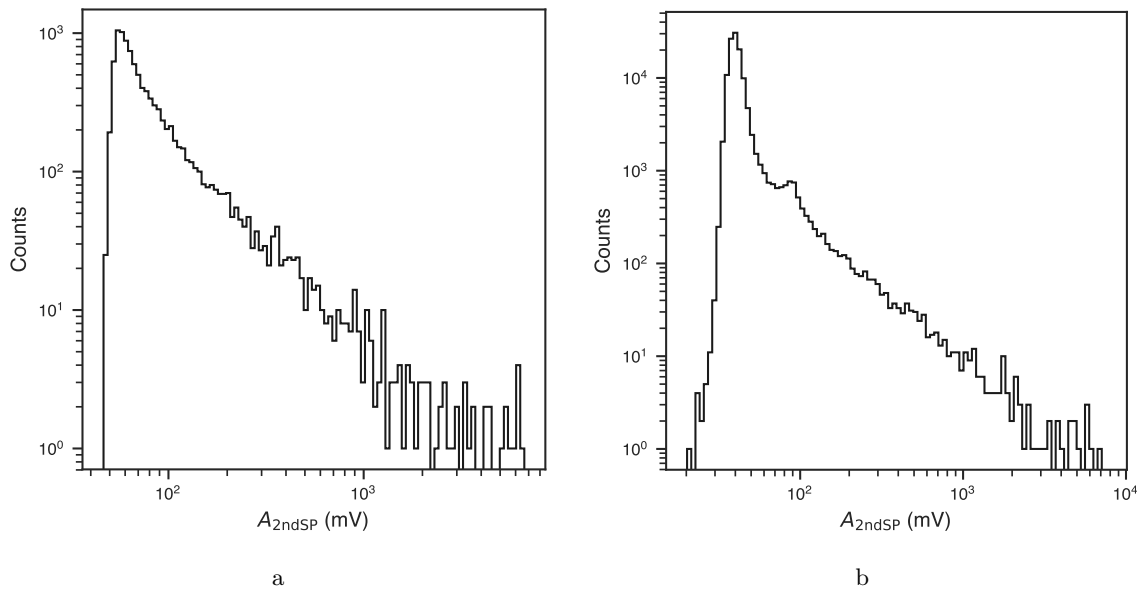
**Figure 6.24** Histograms showing distributions of the second-brightest SP amplitude $A_{2ndSP}$ for two different on-telescope observation runs (12714 & 12827, in two consecutive nights) with (a) the threshold set to 55 mV using the shifted third set of threshold look-up tables and (b) the threshold set to 32 mV using the un-shifted third set of threshold look-up tables.

the previous sections but also for astrophysical analyses which are currently on-going. Similar as with CHEC-M (cf. Sec. 5.11), many events like the one shown in Fig. 6.26 with very long time gradients (>100 ns), typically being VHE events at high impact distances, have been recorded. Only the full-waveform readout with a window of 128 ns avoids the images to be truncated what would negatively impact the analysis. More details about advantages of full-waveform readout are presented in Ch. 8 in the scope of H.E.S.S. IU.

## 6.6 Summary and outlook

A selection of studies performed in the scope of this work during the commissioning, testing, and characterisation of CHEC-S has been presented in the preceding sections. The investigations were selected according to their relevance for future design iterations, such as the power consumption of and thermal distribution inside the camera, and to prove that the issues observed with CHEC-M, such as the gain calibration and trigger performance, were tackled and solved. The main results of those investigations are:

- The total power consumption of CHEC-S (∼900 W) is significantly higher than in CHEC-M (∼600 W) due to the increased current draw of the TARGETs-C modules being equipped with more electrical components, such as additional slow-ADCs for slow signal readout and eight ASICs instead of four.

- Given the increased power consumption, also more heat is produced inside CHEC-S. The thermal distribution inside the camera is significantly worse than in CHEC-M with a maximum spread between TMs of ∼27°C (compared to ∼6°C in CHEC-M), and with TM temperatures reaching 40–50°C even with the chiller set to 12°C and despite of the use of six instead of four fans. The high temperature spread stresses the need of a
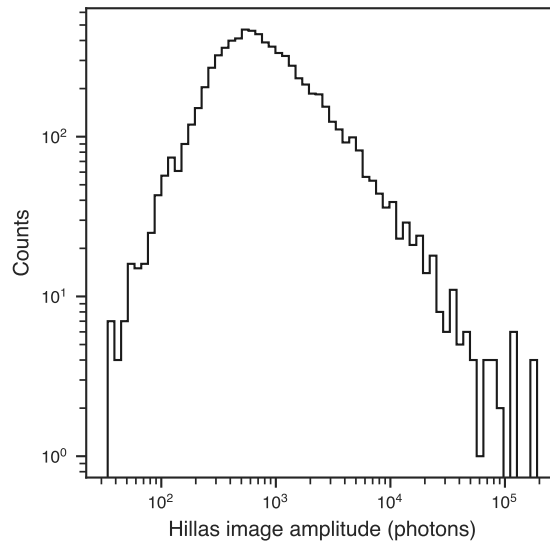
**Figure 6.25** Histogram showing the Hillas image amplitude distribution for run 12714.

temperature-dependent calibration of the TMs when being calibrated in a stand-alone procedure. For future design iterations, an improved heat distribution and exchange is required, for example via adding a second set of fans to the rack and TEC elements to each sampling ASIC.

- In spite of the higher temperatures inside the camera, the SiPM temperature lie in an acceptable range of 22 to 28°C (with the chiller set to 12°C) proving the functionality of the cooled focal plane plate.

- The warm-up time is ~45 min, being similar as for CHEC-M.

- The main reason for adjusting the SP HV values is to aim for a uniform trigger response. In contrast to MAPMs, where only the gain depends on the HV, this is different for SiPMs with three parameters – the PDE, gain, and OPCT – being dependent on the HV. Thus, gain matching, i.e. adjusting the HV of all SPs to result in the same SPE value, would not result in a uniform trigger response. Instead, in CHEC-S, the SP HV values are adapted to equalise the SP signal amplitudes (in mV) since this is what is discriminated by the L1 trigger. Since the HV is settable per SP instead of per TM as in CHEC-M, the achievable amplitude spread between all camera pixels is significantly lower: ~11% compared to ~30%. It is limited by the resolution of the DAC, setting the SiPM bias voltage, and the fact that only one voltage value is settable per four pixels. In future design iterations, both of those topics might be addressed.

- Seven HV-amplitude matched configuration files were produced with mean pixel gains in the range of 2–6 mV/p.e. to be used for lab and on-telescope measurements.

- Unlike CHEC-M, the trigger thresholds were calibrated individually for each TM in stand-alone tests. The resulting look-up tables linking a threshold in mV to a pair of the ASIC parameters `Pmtref4` and `Thresh` were provided by the CHEC-group at ECAP. In the scope of this work, those look-up tables were tested when being used in parallel with 32 TMs installed in the camera. The results were used to fix bugs in the
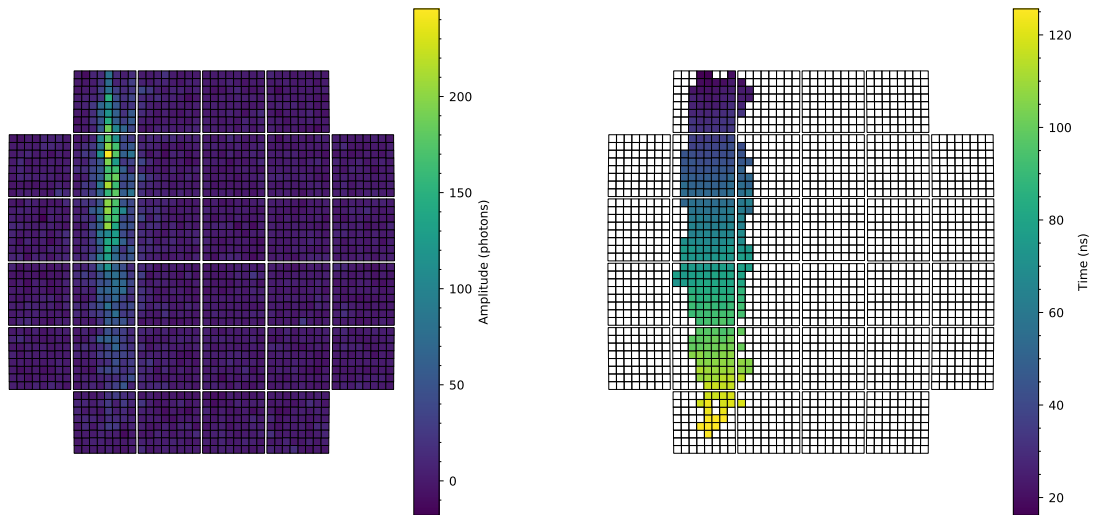
**Figure 6.26** Camera image of a ∼120 ns long Cherenkov event showing the intensity and peak arrival time for the pixels that remain after image cleaning. Images provided by J. J. Watson.

look-up table production scheme and to improve it. In this way, final look-up tables were produced and their performance verified.

- The BP trigger mapping, NN trigger logic, and NN combinatorics were verified.

- It was shown that sending data while triggering does not affect the trigger performance. This was one of the major issues observed in CHEC-M and solved with CHEC-S by splitting the triggering and digitisation into two ASICs.

- Trigger bias scans were performed for different circumstances such as different NSB levels, telescope zenith angles, and HV settings, all verifying the expected performance of the camera. In addition, the bias curves were compared to MC measurements showing a good match.

- Trigger efficiency measurements were performed recording both, the 512 L1 triggers and the L2 trigger. They revealed the following main results:
  - The spread in trigger uniformity is ∼12% as expected from the minimum achievable spread in signal amplitude.
  - The resulting trigger amplitudes, measured at an NSB level of 60 MHz and a gain of $G_{mV} \simeq 2.9$ mV/p.e., lie between ∼10 p.e./SP and ∼58 p.e./SP for thresholds between 24 mV and 199 mV. The factor 4 higher minimum threshold (24 mV/SP) than in measurements without NSB and HV is expected due to the influence of NSB, SiPM dark counts, and OPCT.
  - The L1 and L2 trigger efficiency measurements are consistent.

- CHEC-S can be read out with an efficiency of 100% at the required mean event rate of 600 Hz. Thanks to the increased bandwidth of the X-DACQ board installed in CHEC-S, a maximum mean rate of ∼1.25 kHz can even be reached.

- CHEC-S was installed on the ASTRI-Horn telescope during dedicated on-telescope campaigns and therefore – since CHEC-M has already been installed on the GCT structure

in 2015 and 2017 – proving the compatibility of CHEC with both SST structures, GCT and ASTRI-Horn. Furthermore, those campaigns were used not only for performance tests but also for astrophysical observations with the analyses currently being on-going.

To conclude, both CHEC prototypes, CHEC-M and CHEC-S, were invaluable steps towards a reliable and high-performance product for CTA. The recent decision that the final SST design will be based on the ASTRI-Horn telescope structure equipped with a CHEC-like camera enables possibilities for design iterations in the very near future. For this process, the results presented in this and the previous chapter can be used as valuable input.

While the chapters about CHEC illustrated the need of hardware development and testing of an atmospheric Cherenkov camera, the following two chapters about H.E.S.S. IU will demonstrate the importance of MC simulations and analysis software development for the ability to analyse data recorded with a Cherenkov camera.

# H.E.S.S. IU simulations and performance verification

> "Nature isn't classical, dammit, and if you want to make a simulation of nature, you'd better make it quantum mechanical, and by golly it's a wonderful problem, because it doesn't look easy."
>
> Richard P. Feynman

As described in Sec. 3.2.5, deep MC simulations reflecting (1) the EAS properties, (2) the optical properties of the telescope, and (3) the electronics of the camera are one of the steps needed for the reconstruction of measured Cherenkov events. Hence, any hardware exchange, such as the electronics upgrade of the H.E.S.S. I cameras (cf. Sec. 3.2.2.2), affecting the optical properties of the telescope or the camera electronics results in the need of an adaptation and a re-validation of the simulation chain. In the scope of this work, I performed such an adaptation and re-validation of the H.E.S.S. IU HD MC simulation chain and I will present details in this chapter.

First, in Sec. 7.1, I will introduce the MC parameters that needed updating and explain the procedure used to determine their values. Then, in Sec. 7.2, I will explicitly go through all the different steps of the validation study I performed for each of the MC parameters. In Sec. 7.3, I will present the results of my performance tests of the H.E.S.S. IU cameras using the updated MC parameters and newly created IRFs. Finally, I will summarise the main results of this chapter in Sec. 7.4.

## 7.1 H.E.S.S. IU MC simulation chain and updated parameters

As stated in Sec. 3.2.5, the MC simulations for the HD simulation chain of H.E.S.S. are based on two simulation frameworks `CORSIKA` and `sim_telarray`. Since the latter is used for the telescope simulations, its parameters characterising the optical throughput of the telescope, the Cherenkov signal detection by the PMTs, and the signal processing by the camera electronics need to be updated for the use with H.E.S.S. IU. While many of the parameters could be experimentally determined in the laboratory, such as the pulse shape of the single p.e. entering the flash-ADC (FADC, [128]), a few others (see below) required an iterative procedure comparing telescope data to MC simulations. The latter consisted of a four-step approach of

1. a best-guess for the MC parameter,

2. running the MC simulation,

3. comparison with measurements,

4. adapting the MC parameter and repeating step 2 and 3.

Since the H.E.S.S.-group at Deutsches Elektronen Synchrotron (DESY) in Zeuthen was responsible for the full camera upgrade including R&D and integration of the electronics parts into the camera, they performed the specific measurements that were needed as input to `sim_telarray`. The determination of the parameters based on the iterative approach using MC simulations were performed by myself and is presented in this chapter. Those parameters are

1. `fadc_sum_offset` and `laser_pulse_offset` setting the position of the readout window and of laser pulses (when externally triggered) w.r.t. the trigger time,

2. `fadc_amplitude` ($P_{\mathrm{mean,SPE}}$) determining the overall gain (PMT and electronics) in ADC/p.e.,

3. `mirror_degraded_reflection` determining the mirror reflectivity and hence the optical throughput of the telescope, and

4. `discriminator_threshold` determining the pixel threshold for triggering.

The procedures and analyses performed for the determination and validation of those four parameters are presented in detail in the following section.

## 7.2 MC parameter validation study

As explained in the previous section, four MC parameters needed updating using an iterative approach based on MC simulations. All analyses performed to determine and validate their values are presented in the following subsections.

### 7.2.1 `fadc_sum_offset` and `laser_pulse_offset`

The parameter `fadc_sum_offset` sets the readout window[1] w.r.t. the trigger time, `laser_pulse_offset` sets time difference between the trigger time of the camera and the time the external laser device is triggered – it therefore can also be negative. While the first parameter is used in all simulations, the second one is needed for the simulation of externally triggered laser events. Such events are used for SPE simulations required for the determination of `fadc_amplitude` (cf. Sec. 7.2.2).

The values of both parameters were determined by comparing simulations of internally and externally triggered[2] laser events with laser (flat-field) measurements read out in SM (cf. Fig. 7.1). First the amplitude of the simulated laser pulse was adapted to result in the same pulse height as of the measured one. As a next step, `fadc_sum_offset` was iteratively adapted until the peak time of the internally triggered simulated pulse and the measured

---

[1]For more details about the H.E.S.S. readout system refer to Sec. 3.2.2.2.

[2]The camera can be triggered externally by another device via an electronic pulse or internally by setting a pixel threshold (cf. Sec. 3.2.2).
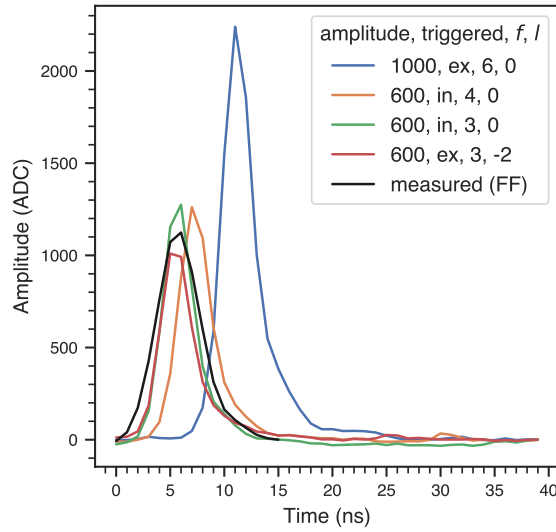
**Figure 7.1** Simulated laser and measured flat-field (FF) waveforms with different amplitudes (in number of photons hitting the camera focal plane), internally (in) or externally (ex) triggered, and different values for the parameters `fadc_sum_offset` $f$ and `laser_pulse_offset` $l$. It can be concluded that out of all values for `fadc_sum_offset` and `laser_pulse_offset`, the pulses resulting from simulation with those values set to $f = 3$ and $l = -2$ match best the measured FF pulse.

pulse matched best. A value of `fadc_sum_offset` $= 3$ was deduced. Once this parameter was fixed, `laser_pulse_offset` was iteratively modified until the peak time of the externally triggered simulated pulse was matched best to the peak time of the measured one resulting in a value of `laser_pulse_offset` $= -2$.

### 7.2.2 `fadc_amplitude`

In H.E.S.S., the gain is measured with dedicated SPE measurements illuminating the cameras with a very faint light source without exposure to the NSB. A typical resulting SPE spectrum is shown in Fig. 7.2. A convolution of a Poisson distribution with a Gaussian for both, the pedestal $G_P$ and subsequent p.e. peaks $G_T$, provides a good approximation to the spectrum.
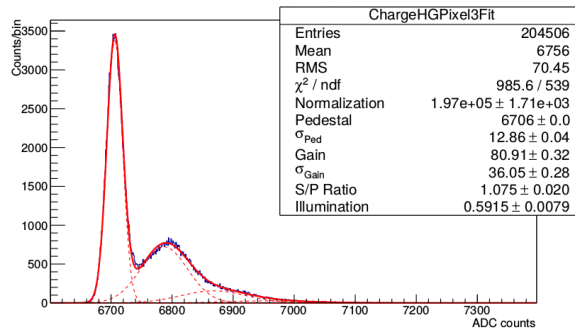


**Figure 7.2** Example of a measured SPE spectrum overlayed with the fit function given by Eq. 7.1. Adapted from [78].
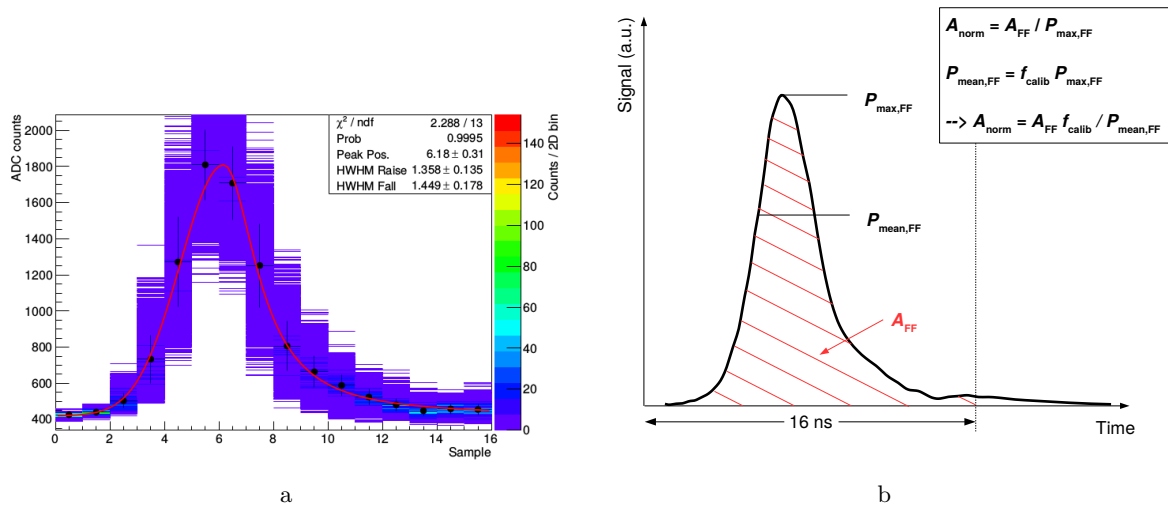
**Figure 7.3** (a) Typical PMT pulse from FF measurements taken in SM. Adapted from [78]. (b) Annotated FF pulse.

More in detail, the fit function is given by

$$G(x) = N(G_P(x) + G_T(x)), \qquad (7.1)$$

with

$$G_P(x) = \frac{\exp(-\mu)}{\sqrt{2\pi}\sigma_P} \exp\left[-0.5\left(\frac{x-P}{\sigma_P}\right)^2\right] \qquad (7.2)$$

and

$$G_T(x) = \kappa \sum_{n=1}^{n=\infty} \frac{\exp(-\mu)}{\sqrt{2\pi}\sqrt{\sigma_p^2 + n\,\sigma_{\gamma_e}^2}} \frac{\mu^n}{n!} \exp\left[-0.5\left(\frac{x - (P + n\gamma_e^{ADC})}{\sqrt{\sigma_p^2 + n\,\sigma_{\gamma_e}^2}}\right)^2\right]. \qquad (7.3)$$

$N$ is a normalisation factor, $x$ is the charge in ADC, $\sigma_P$ is the electronic noise as shown by the pedestal, $\sigma_{\gamma_e}$ the PMT resolution for 1 p.e., $P$ the position of the pedestal mean, $\mu$ the mean illumination, and $N$ and $\kappa$ normalisation factors. In the H.E.S.S. calibration procedure, the gain $\gamma_e^{ADC}$ is defined as the **most probable** charge[3] (measured in ADC) that is produced by an SPE. Since the gain of each PMT (pixel) depends on the HV (cf. Sec. 4.2.1), the HV of each pixel is adjusted so that the mean value of $\gamma_e^{ADC}$ (over all 960 PMTs of a camera) is ∼80 ADC. The measured electronic noise is in the order of 12 ADC (∼0.15 p.e.).

In `sim_telarray`, the corresponding parameter determining the gain is `fadc_amplitude` ($P_{\mathrm{mean,SPE}}$). It is defined as the **mean** amplitude of an SPE pulse output from the FADC of the high-gain channel, hence given in units of ADC. Pulse shape measurements (cf. Fig. 7.3a) were used to find a first guess for $P_{\mathrm{mean,SPE}}$. To do so, a relation between the area $A_{\mathrm{FF}}$, the peak amplitude $P_{\mathrm{max,FF}}$, the mean amplitude $P_{\mathrm{mean,FF}}$, and the normalised area $A_{\mathrm{norm}} \equiv A_{\mathrm{FF}}/P_{\mathrm{max,FF}}$ of the measured FF pulse (cf. Fig. 7.3b for definitions of the variables) was used. The calibration scale factor $f_{\mathrm{calib}}$, defined as

$$f_{\mathrm{calib}} \equiv \frac{P_{\mathrm{mean,FF}}}{P_{\mathrm{max,FF}}}, \qquad (7.4)$$

---

[3]Since in the nominal CM data readout, "the charge" is a 16 ns-integration of the signal, it is the area under the signal, hence a "pulse area".
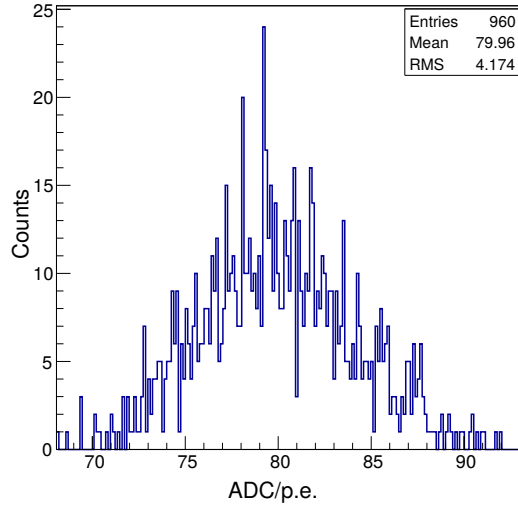
**Figure 7.4** Distribution of the extracted gain from SPE MC simulations $\gamma_{e,\mathrm{MC}}^{ADC}$ (with $f_{\mathrm{calib}} = 0.91$ and $P_{\mathrm{mean,spe}} = 22.78$), using the same calibration software as used for measurements.

takes into account the difference between the two gain definitions used in the calibration and MC chain. Its value is determined by the ENF of the used PMTs, being 0.85, convolved with the influence of the electronics and digitisation circuity attached to the PMTs. Under the assumption that the pulse shape does not depend on the intensity of the light/Cherenkov signal (being a valid assumption in a first-guess determination of $P_{\mathrm{mean,SPE}}$), $A_{\mathrm{norm}}$ can also be expressed in terms of the area $A_{\mathrm{SPE}}$ and the peak amplitude $P_{\mathrm{max,SPE}}$ of an SPE pulse. Furthermore, since also for an SPE pulse, it then holds that $P_{\mathrm{mean,SPE}} = f_{\mathrm{calib}} P_{\mathrm{max,SPE}}$, it follows that

$$A_{\mathrm{norm}} = \frac{A_{\mathrm{FF}}\, f_{\mathrm{calib}}}{P_{\mathrm{mean,FF}}} = \frac{A_{\mathrm{spe}}\, f_{\mathrm{calib}}}{P_{\mathrm{mean,spe}}}. \tag{7.5}$$

Solving this equation for $P_{\mathrm{mean,spe}}$ results in

$$P_{\mathrm{mean,spe}} = \frac{A_{\mathrm{spe}}\, f_{\mathrm{calib}}}{A_{\mathrm{norm}}} = \frac{\gamma_e^{ADC}\, f_{\mathrm{calib}}}{A_{\mathrm{norm}}}. \tag{7.6}$$

Given the definition of the gain in the H.E.S.S. calibration procedure (see above), it follows that $A_{\mathrm{SPE}} \equiv \gamma_e^{ADC} \simeq 80$ ADC which was used in the last step in the equation above.

The value of $A_{\mathrm{norm}}$ could be deduced from the FF pulse shape measurement (cf. Fig. 7.3a), being $\sim$3.20. To evaluate the correct value for $P_{\mathrm{mean,spe}}$, SPE simulations using `sim_telarray` with different values for $P_{\mathrm{mean,spe}}$ (determined by $f_{\mathrm{calib}}$) were performed. As a first guess, the pre-upgrade value of $f_{\mathrm{calib}}$, being 0.92, was used, resulting in $P_{\mathrm{mean,spe}} = 23.03$ (using Eq. 7.6). However, an iteration on that value showed that $f_{\mathrm{calib}} = 0.91$ (giving $P_{\mathrm{mean,spe}} = 22.78$) resulted in the best agreement between the distributions of $\gamma_e^{ADC}$ (with a mean of $\sim$80 ADC, extracted from SPE measurements) and of $\gamma_{e,\mathrm{MC}}^{ADC}$ (extracted from SPE MC simulations). In both cases, SPE measurements and SPE MC simulations, the gain was extracted using the calibration software. Hence, their values were directly comparable. Fig. 7.4 shows the resulting $\gamma_{e,\mathrm{MC}}^{ADC}$ distribution for the final value of `fadc_amplitude` being 22.78. As can be observed, the mean value of the distribution is compatible with 80 ADC.
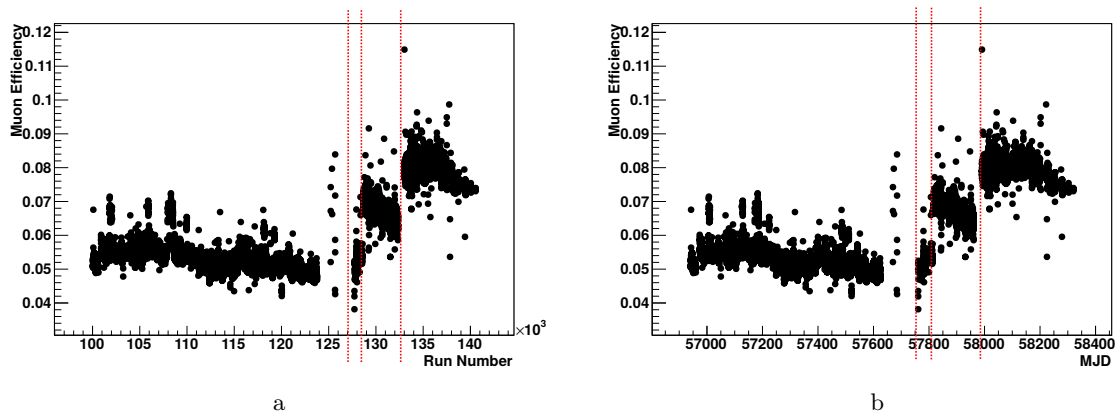
**Figure 7.5** Extracted muon efficiency from data for CT3 as function of (a) run number and (b) date in MJD (Modified Julian Day, [130]). The red lines indicate the transition between different muon phases, refer to text for details.

**Table 7.1** H.E.S.S. IU muon phases. The ID and date of the first run of each phase is given as well as a description giving the reason for the definition of a new phase.

| Phase | run ID | date (MJD) | date (MM-YYYY) | description |
|-------|--------|-----------|----------------|-------------|
| 2c0 | 127700 | 57760 | 01-2017 | H.E.S.S. IU starts operation |
| 2c1 | 128600 | 57816 | 03-2017 | exchange of PMT light cones (CT1-4) |
| 2c2 | 132350 | 57965 | 07-2017 | exchange of mirrors (CT3) |

### 7.2.3 `mirror_degraded_reflection`

To determine the value of the parameter `mirror_degraded_reflection`[4], first the optical efficiencies of the four H.E.S.S. I telescopes had to be evaluated for the time after the upgrade. A general approach to monitor changes in the optical throughput of an IACT is the use of muon events [68, 129]. For this purpose, muon events are separated from other Cherenkov events in the calibration procedure by using their characteristic ring-like shape. From the correspondence of the ring radius to the muon energy, the expected Cherenkov light yield and its intensity distribution around the ring image can be found. The ratio between the detected and the analytically predicted amount of light results therefore in a measure of the mirror reflectivity and is quantified by a muon efficiency parameter $\epsilon_\mu$. Its evolution with time around the upgrade phase of the H.E.S.S. I cameras is shown for CT3 in Fig. 7.5. Each time, the optical throughput, monitored by the muon efficiency, changes significantly (e.g. due to hardware exchanges), a new muon phase is defined. Since the beginning of operation of H.E.S.S. IU in January 2017 (57760 MJD), three periods (referred to as phase 2c0, 2c1, and 2c2) were identified (cf. Tab. 7.1). To reflect those muon efficiencies in simulations, muon events were simulated with different values of `mirror_degraded_reflection`. To extract $\epsilon_\mu$, the same algorithm was used for the simulated data as for the measured data. The final values for `mirror_degraded_reflection` were then deduced iteratively while the

---

[4]More in detail, this parameter is the fraction of the current reflectivity to the nominal one measured after the production of the mirror. It therefore indicates by which fraction the mirror reflectivity is worse or has degraded.
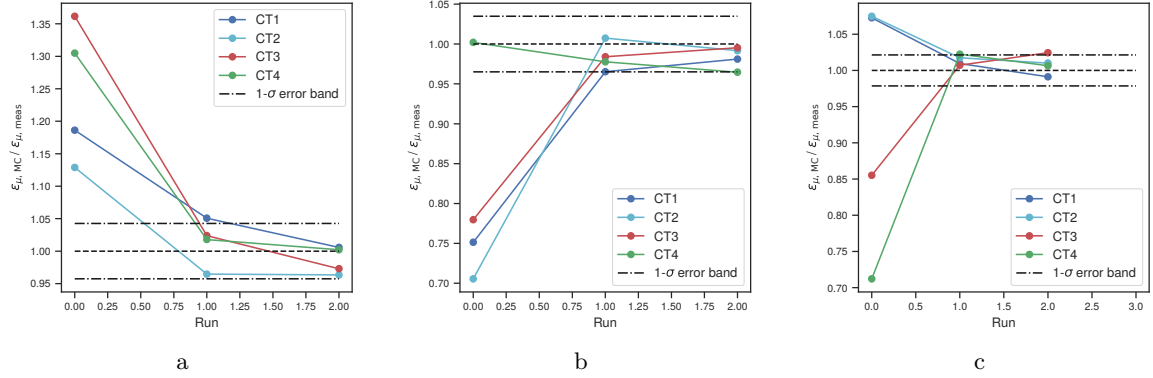
**Figure 7.6** Iterative determination of the values for `mirror_degraded_reflection` for all four H.E.S.S. IU telescopes for the three muon phases (a) 2c0, (b) 2c1, and (c) 2c2. Shown is the ratio of muon efficiencies extracted from MC simulations $\epsilon_{\mu,\mathrm{MC}}$ and measurements $\epsilon_{\mu,\mathrm{meas}}$ as function of the number of MC simulations (runs) performed until the ratio lied within the 1-$\sigma$ error band of the measured muon efficiency.

**Table 7.2** Muon efficiencies $\epsilon_\mu$ extracted from measurements and `mirror_degraded_reflection` $r$ determined from MC simulations for all four H.E.S.S. IU telescopes and all three phases.

| Phase | $\epsilon_{\mu,\mathrm{CT1}}$ | $\epsilon_{\mu,\mathrm{CT2}}$ | $\epsilon_{\mu,\mathrm{CT3}}$ | $\epsilon_{\mu,\mathrm{CT4}}$ | $r_{\mathrm{CT1}}$ | $r_{\mathrm{CT2}}$ | $r_{\mathrm{CT3}}$ | $r_{\mathrm{CT4}}$ |
|---|---|---|---|---|---|---|---|---|
| 2c0 | 0.057 | 0.056 | 0.052 | 0.053 | 0.670 | 0.653 | 0.603 | 0.601 |
| 2c1 | 0.076 | 0.077 | 0.065 | 0.071 | 0.880 | 0.891 | 0.760 | 0.843 |
| 2c2 | 0.069 | 0.071 | 0.075 | 0.071 | 0.809 | 0.840 | 0.898 | 0.843 |

iteration continued until the muon efficiencies extracted from MC simulations and data were in agreement (within a 1 $\sigma$ uncertainty band), i.e. until $\epsilon_{\mu,\mathrm{MC}} = \epsilon_{\mu,\mathrm{meas}}$ (cf. Fig. 7.6). Their numbers with the corresponding values for $\epsilon_\mu$ (extracted from measurements) are given in Tab. 7.2.

### 7.2.4 `discriminator_threshold`

`discriminator_threshold` parameterises the L0 trigger threshold (cf. Sec. 3.2.2) in `sim_telarray`. To determine its value, trigger bias scans were simulated and compared to measured ones. The NSB level $f_{\mathrm{NSB}}$ of the bias scan measurement was needed as an input to the bias scan simulations as it determines the shape and location of the NSB wall. To determine its value for a given measurements, the relation

$$\sigma_{\mathrm{ped}} = q_0 \sqrt{f_{\mathrm{NSB}} + q_1} + q_2 \iff f_{\mathrm{NSB}} = \frac{(\sigma_{\mathrm{ped}} - q_2)^2}{q_0^2} - q_1 \tag{7.7}$$

was used, with $\sigma_{\mathrm{ped}}$ being the pedestal width and $q_i$ ($i \in [0,3]$) constant parameters being characterised by the camera electronics. The extraction of $\sigma_{\mathrm{ped}}$ is part of the nominal H.E.S.S. calibration chain. The constants $q_i$ ($i \in [0,3]$) were determined from MC simulations with different NSB levels fitting the extracted pedestal widths with Eq. 7.7 (cf. Fig. 7.7). Since $f_{\mathrm{NSB}}$ is defined as NSB level before entering the optical system of the telescope, the
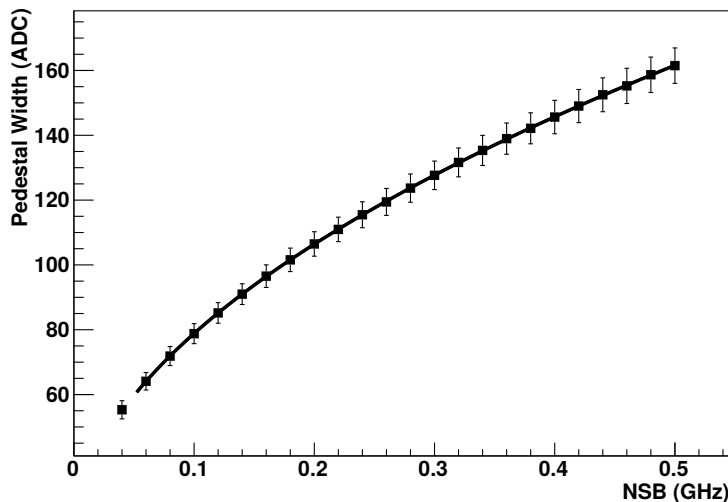
**Figure 7.7** Pedestal width as function of NSB level, simulated for muon phase 2c1 and CT4. Also shown is the fit to the data using Eq. 7.7 as fit function.

**Table 7.3** Characteristics of the trigger bias scan measurements such as muon phase, run number, observed source, zenith angle $\theta_z$, and extracted NSB levels $f_{NSB}$ in units of MHz.

| Phase | Run | Source | $\theta_z$ (°) | $f_{NSB,CT1}$ | $f_{NSB,CT2}$ | $f_{NSB,CT3}$ | $f_{NSB,CT4}$ |
|-------|-----|--------|----------------|---------------|---------------|---------------|---------------|
| 2c0 | 128014 | PKS 0447-439 | 22.5 | 79 | 84 | 90 | 90 |
| 2c0 | 127921 | HESS J0632+057 | 29.6 | 159 | 168 | 170 | 173 |
| 2c1 | 128658 | PMN J0850-1213 | 31.6 | 130 | 132 | 139 | 135 |
| 2c1 | 129254 | Vela pulsar | 34.0 | 191 | 195 | 204 | 199 |

optical throughput (parameterised by `mirror_degraded_reflection`, cf. Sec. 7.2.3) had also to be taken into account. Hence, one trigger bias scan simulation was performed for each set of NSB level and muon phase.

An overview of the trigger bias scan measurements used for comparison with MC simulations is given in Tab. 7.3. The MC simulation parameters were chosen accordingly to best reflect the observational conditions. Then, the simulation was performed in two steps: for different values of `discriminator_threshold`, (1) NSB events were simulated and the corresponding single-telescope trigger rates were extracted, (2) proton EASs with primary energies between 0.03 and 150 GeV were simulated. The single-telescope trigger rate was calculated for each value of `discriminator_threshold` from the trigger effective area $A_{\text{eff,trig}}$ using Eq. 2.2 & 3.11. To correct for other primary hadrons not being simulated but contributing to the CR-rate, the extracted camera rate was multiplied by a factor of 1.34 [131].

Fig. 7.8 shows measured and simulated trigger bias curves fitted with a broken power-law function with four fit parameters $q_i$ ($i \in [0, 4]$) given by

$$f(t) = \Theta(t + q_0/q_1)\, 10^{q_0 + q_1\, t} + \Theta(t + q_2/q_3)\, 10^{q_2 + q_3\, t} \tag{7.8}$$

with $\Theta$ being the Heaviside function. A disagreement between measured and simulated trigger bias curves can be observed. This was not unexpected due to the new design used for the L0 comparator output (cf. Sec. 3.2.2.2), being difficult to reproduce in `sim_telarray` without
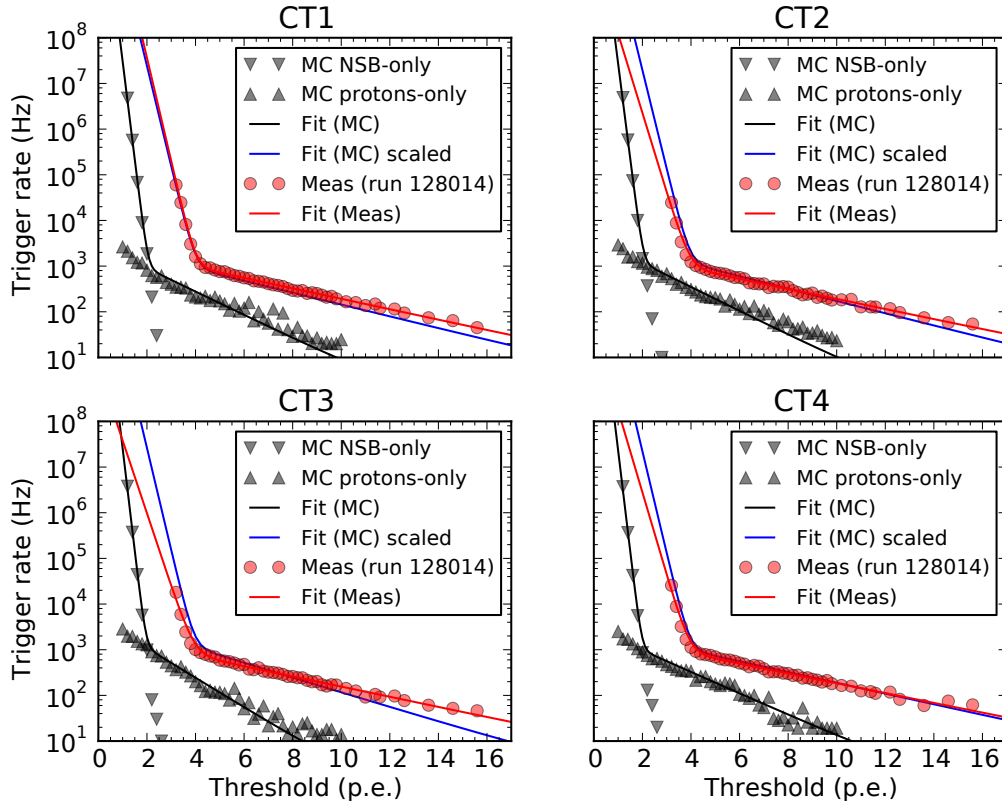
**Figure 7.8** Bias scan measured and simulated for muon phase 2c0 fitted with a broken power law given by Eq. 7.8. For more details refer to text.

significant changes [131]. Hence, it was decided trying to match measurements and simulations experimentally, i.e. finding a sensible scaling factor between p.e. definitions in data and MC. The blue curve in Fig. 7.8 shows such a try using the ratio between the transition points of measurements and MC simulations as scaling factor. The shape of the measured bias scan cannot perfectly be reflected by MC simulations when using such a single scaling factor resulting in an underestimated camera trigger rate in MC simulations. Attempts to obtain a better match by iterations on other `sim_telarray` trigger parameters, such as `discriminator_-sigsum_over_threshold`[5], were not successful. Hence, as a preliminary conclusion, a single scaling factor of ~1.7 between MC threshold (parameterised by `discriminator_threshold`) and camera threshold was used – the value being an average obtained from all telescopes and experimental bias scan measurements (listed in Tab. 7.3) for which a comparison between measurement and simulations was performed.

Two L0 camera thresholds were (are) used for data runs in the H.E.S.S. IU era: 4.5 p.e. (5.5 p.e.) for data runs before (after) the light cones were exchanged, i.e. for muon phase 2c0 (2c1 and 2c2). Hence, given the scaling factor of ~1.7, this results in values for `discriminator_-threshold` of 2.65 p.e. for muon phase 2c0 and 3.24 p.e. for muon phase 2c1 and 2c2.

---

[5]This sets the value of integrated signal required to be over the threshold to issue an L0 trigger.
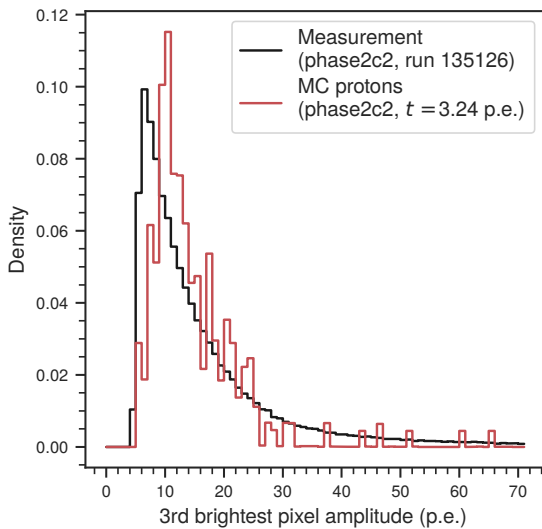
**Figure 7.9** Third-brightest pixel distributions of CT1 measured (run 135126) and simulated (using a `discriminator_threshold` of $t = 3.24$ p.e.), both for muon phase 2c2.
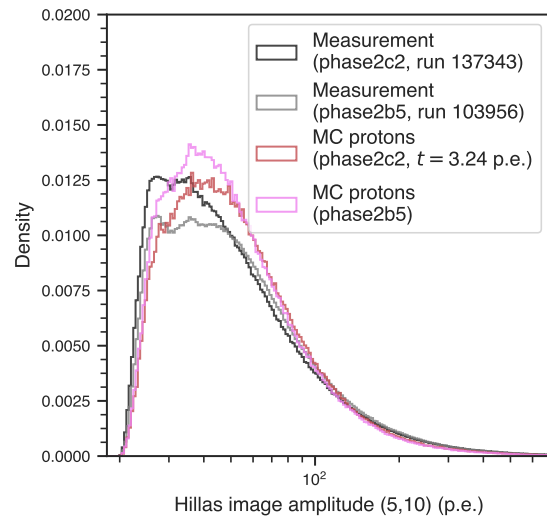
**Figure 7.10** Hillas image amplitude distributions, using tail cuts of (5,10), for pre- and post-upgrade measurements and simulations (muon phase 2b5 and 2c2, respectively).

## 7.3 Performance verification

The performance of the H.E.S.S. IU HD MC simulation chain being based on the parameters determined in the previous section was tested and verified in different studies presented in this section.

**Third-brightest pixel distribution**   Since an L1 trigger is issued whenever at least $N = 3$ pixels in a camera trigger sector are triggering simultaneously (cf. Sec. 3.2.2), the amplitude value of the third-brightest pixel in data reflects the pixel threshold. Hence, the third-brightest-pixel distribution of measurements and simulations can be used to verify the trigger implementation in the MC simulation chain[6]. Fig. 7.9 shows such a comparison for CT1 and muon phase 2c2. The agreement between MC and measured third-brightest pixel distribution is only moderate with the rise of the distribution, i.e. the onset of the trigger, being at similar amplitudes but with an offset of 4 p.e. between the peaks of the distributions.

**Hillas image amplitude**   Beside the third-brightest pixel distribution, a comparison of the Hillas image amplitude deduced from measurements and MC simulations is another parameter to verify the trigger implementation in MC[7]. Similar to the third-brightest pixel distribution, the distributions of Hillas image amplitudes of MC simulations and measurements only show a moderate match (cf. Fig. 7.10). However, they both indicate a similar minimum image amplitude of ∼30 p.e. . Furthermore, the pre-upgrade (muon phase 2b5) and post-upgrade (muon phase 2c2) simulated distributions are of similar shape with a similar (only moderate) agreement with measurements in the corresponding muon phases.

---

[6]A similar study, using the second-brightest SP distribution, was performed when verifying the trigger performance of CHEC-S (cf. Sec. 6.4.7).

[7]Also in the CHEC-S trigger performance tests, such an analysis was performed (cf. Sec. 6.4.8).
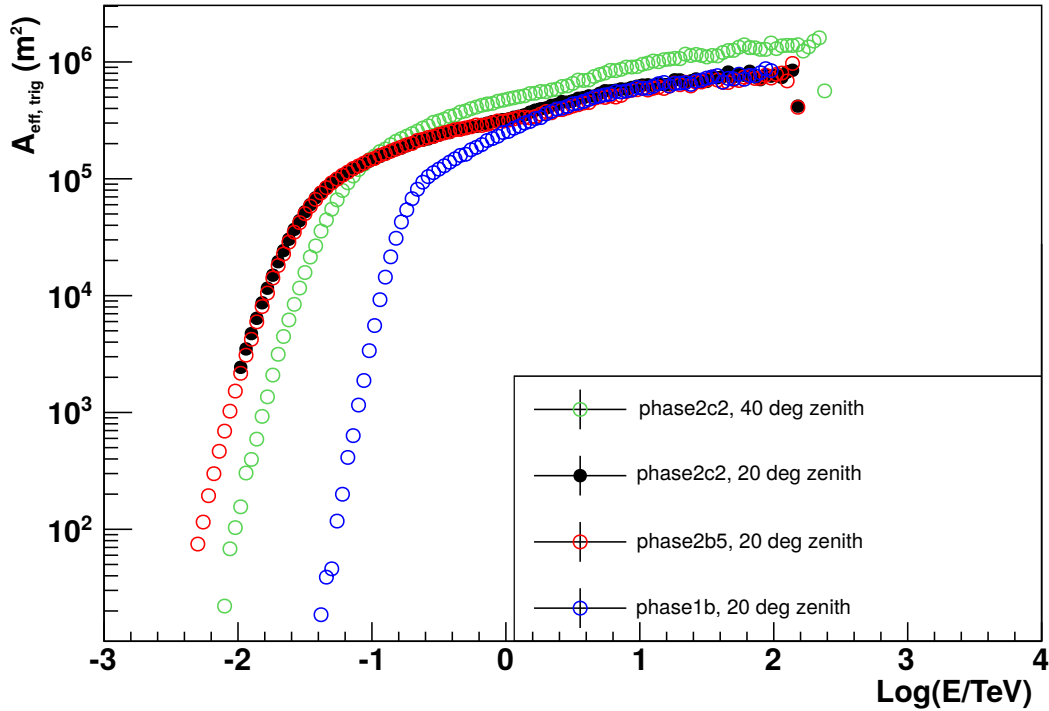
**Figure 7.11** Trigger effective area extracted from MC simulations for different muon phases.

**Trigger effective area**   Another third parameter used for performance verification is the trigger effective area. Fig. 7.11 shows trigger effective areas extracted from MC simulations for different muon phases. They show a good agreement between pre- and post-upgrade simulations (phase 2b5 vs. 2c2). Furthermore, as expected, the trigger effective area is much lower for muon phase 1b, being a phase in the H.E.S.S. I era, for low energies due to the absence of CT5 and is – for higher zenith angles – lower for low energies and higher for high energies.

**Crab data analysis**   As a final performance verification test, data of the Crab Nebula taken with H.E.S.S. IU was analysed using preliminarily produced H.E.S.S. IU IRFs. Fig. 7.12 shows the resulting spectrum including two fit models (power law with and without exponential cutoff, [95]) analysed with H.E.S.S. IU IRFs. The resulting index $\alpha_\gamma = 2.30 \pm 0.04$ and flux at $E_\gamma = 1$ TeV being $\Phi_{\gamma,1 \text{ TeV}} = (3.07 \pm 5.34) \times 10^{-11} \text{ cm}^{-2} \text{ s}^{-1} \text{ TeV}^{-1}$ (corresponding to 91.7% of the "Crab-Meyer flux" [132]) are by 10% lower than index and flux reported in [95] ($\alpha_\gamma = 2.39 \pm 0.03$ and $\Phi_{\gamma,1 \text{ TeV}} = (3.76 \pm 0.07) \times 10^{-11} \text{ cm}^{-2} \text{ s}^{-1} \text{ TeV}^{-1}$ ).

## 7.4  Summary and outlook

In the scope of this work, parameters required for the implementation of the H.E.S.S. IU HD MC simulation chain were determined. The determination procedure of those parameters and the resulting values were presented n this chapter – cf. Tab. 7.4 for a summary. While with the determined values for `fadc_sum_offset`, `laser_pulse_offset`, `fadc_amplitude`, and `mirror_degraded_reflection`, a good match between measurements and simulations could
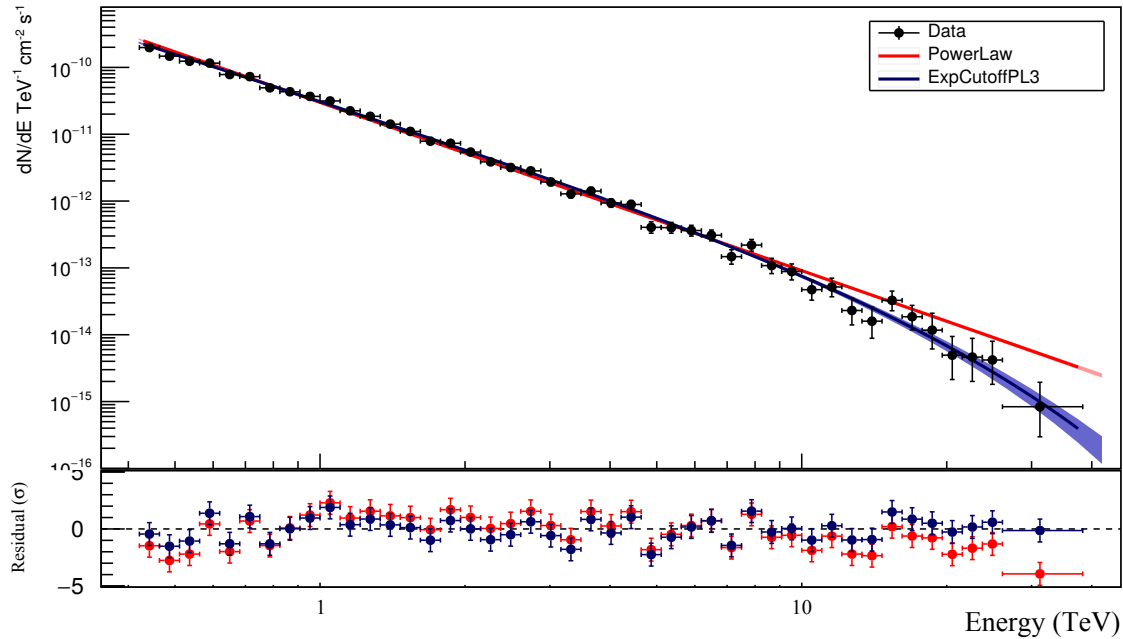
**Figure 7.12** Spectrum including two fit models resulting from observations of the Crab Nebula and analyses using H.E.S.S. IU IRFs.

be observed, an uncertainty remains on the value for `discriminator_threshold` and on the trigger implementation in the HD MC simulation chain in general. The comparison of trigger bias scans revealed a difference in the p.e.-definition in the settings of the camera electronics and `sim_telarray`. This was expected and could, in principle, be corrected for by a simple scaling factor. However, not only the bias scans but also performance verification studies using the third-brightest pixel and Hillas amplitude distributions suggest that a single scaling is not enough to match measurements and MC simulations. Several attempts were undertaken to improve the agreement with the results presented in this chapter found to be the best ones that could be achieved. The 10% difference, observed in the Crab measurements, may also result from the mismatch in the trigger performance, even though the trigger effective area shows a good agreement between measurements and simulations. Moreover, an influence of the new calibration scheme used for the H.E.S.S. IU data cannot be excluded.

Further cross-checks between pre and post-upgrade analyses, performed by other H.E.S.S. members on other sources than the Crab Nebula, did not show differences between pre- and post-upgrade analyses of the order of more than 10%. Hence, despite the observed differences, a first set of full IRFs for the H.E.S.S. IU era was produced. Careful and regular cross-checks of the results obtained through analyses using these IRFs against pre-upgrade analyses and a comparison with results obtained via the PA analysis chain will help to conclude whether the current implementation of the HD MC simulation chain is acceptable or needs to be revised. In the latter case, a better match between measurements and simulations might be achievable with an improved/correct implementation of the new trigger design on its most basic level in the HD MC simulation chain. As already mentioned, this requires significant changes in the `sim_telarray` source code which was beyond the scope of this work.

**Table 7.4** Summary of MC parameter values determined for the H.E.S.S. IU era in the scope of this work.

| Parameter name | Muon phase | Telescope | Value |
|---|---|---|---|
| `fadc_sum_offset` | 2c0–2c2 | CT1–4 | 3 |
| `laser_pulse_offset` | 2c0–2c2 | CT1–4 | $-2$ |
| `fadc_amplitude` | 2c0–2c2 | CT1–4 | 22.78 |
| `mirror_degraded_reflection` | 2c0 | CT1 | 0.670 |
| | | CT2 | 0.653 |
| | | CT3 | 0.603 |
| | | CT4 | 0.601 |
| | 2c1 | CT1 | 0.880 |
| | | CT2 | 0.891 |
| | | CT3 | 0.760 |
| | | CT4 | 0.843 |
| | 2c2 | CT1 | 0.809 |
| | | CT2 | 0.840 |
| | | CT3 | 0.898 |
| | | CT4 | 0.843 |
| `discriminator_threshold` | 2c0 | CT1–4 | 2.65 |
| | 2c1 & 2c2 | CT1–4 | 3.24 |

---

## H.E.S.S. IU full-waveform processing and performance improvements

---

"God loves the noise as much as the signal."

Lewis M. Branscomb

In nominal data acquisition mode, i.e. CM, the 1 GHz-sampled signal is integrated over a fixed window of 16 ns in case trigger conditions are met. As explained in Sec. 3.2.2.2, the H.E.S.S. IU cameras enable the readout of full-sampled waveforms of 40 ns length in parallel to CM. As described in Sec. 3.2.4, this allows a higher flexibility in data analysis and is expected to increase the performance at both, the low and high end of the energy range of H.E.S.S. .

I have already shown some of the context, that I will present in this chapter, at the International Cosmic-Ray Conference (ICRC) 2019. This is summarised in the proceedings (Zorn, 2019) [69]. Concerning the structure of this chapter, I will first give an overview of the SM readout scheme (cf. Sec. 8.1). Then, I will present the charge extraction algorithm that I implemented (cf. Sec. 8.2) and I will give details about how I integrated SM into the existing analysis framework of H.E.S.S. (cf. Sec. 8.3). Furthermore, I will show results of SM data integrity investigations (cf. Sec. 8.4) and of performance studies (cf. Sec. 8.5) that I performed in the scope of this work. Finally, I will summarise the results of this chapter and discuss next steps (cf. Sec. 8.6).

## 8.1 Readout scheme

The current SM readout scheme (cf. Fig. 8.1a) is based on two considerations:

1. The separation from the CM readout chain to reduce the risk of possible effects on the data taken in CM and thus ensuring a stable and reliable nominal data taking while SM is introduced and validated.

2. The readout and storage of 40-sample waveforms of all pixels without data reduction or other on-site operations to keep flexibility for further investigation.

Due to the SM data being 40 times bigger in size[1] and the limited data transfer rate from

---

[1]140 GB per camera for a 28 min run, assuming a mean trigger rate of 500 Hz
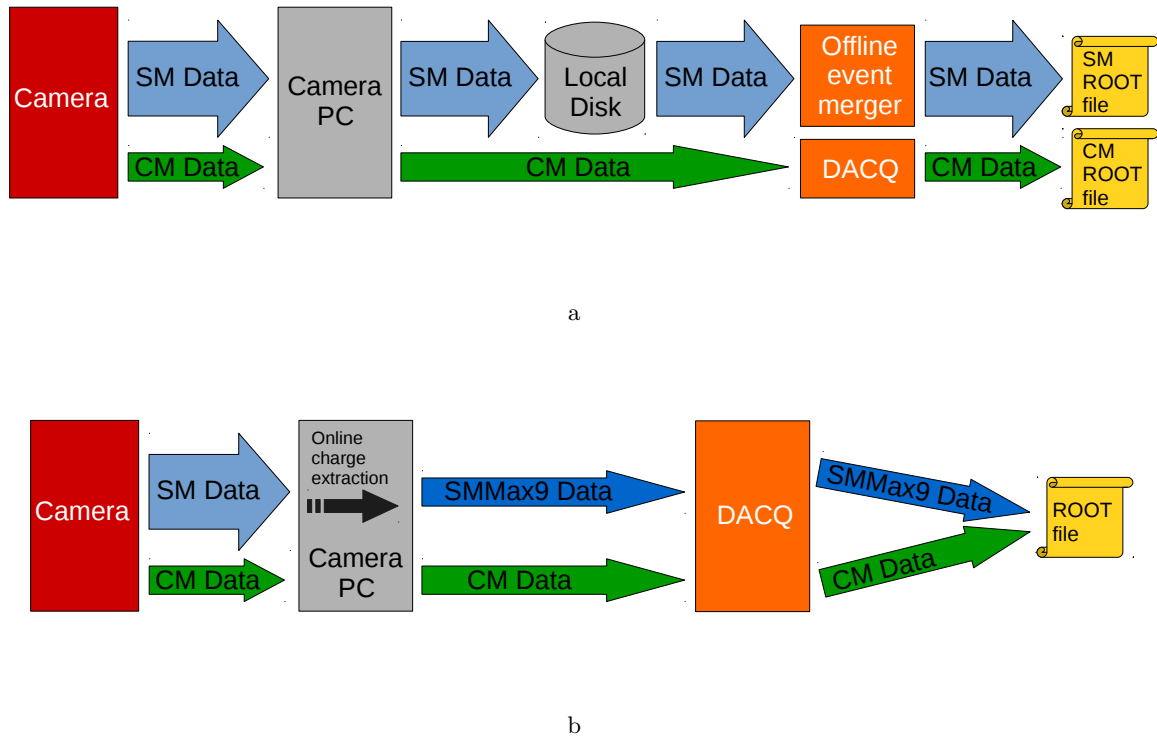
**Figure 8.1** Box diagram showing the (a) current and (b) future SM readout scheme. "SMMax9" stands for the charge extraction based on the integration around the peak maximum of each pixel in a 9 ns window (cf. Sec. 8.2).

the camera PCs to the DACQ process, the SM data is not transferred to the DACQ in real time in contrast to CM data. Instead, it is stored locally on the camera PCs. An offline event merger process, running after the observing shift (during daytime), builds the appropriate events from the runs stored on the different camera PCs. Consequently, CM and SM data are stored in two different data files.

SM data readout is planned to be enabled in all observation runs in the near future. To do so, it will be reduced online and then transferred and processed in the same way as CM data via the DACQ, and stored as another dataset in the same data file (cf. Fig. 8.1b). The data reduction will be based on the same charge extraction mechanism that will be presented in the following section.

## 8.2 Charge extraction

In general, there are two questions involved which are: (1) How to extract the charge and (2) where, i.e. which part of the waveform to use? Amongst others, the following possibilities can be used for charge extraction [131]:

- using a box-type window integration with a fixed window size,

- using a correlation function with reference pulse shape,

- fitting the waveform with a parameterised reference pulse shape, or

- shaping the pulse, with the peak amplitude after shaping being the measure for the charge.

For the choice which part of the waveform to use, it may be decided to

- use a fixed window/position w.r.t. to the trigger or readout,

- use a fixed window around the "global peak", derived after adding up all (to some level) significant pixels,

- search for the signal peak in every pixel by itself (resulting in a bias because of picking positive fluctuations),

- search for a peak in neighbour pixels only,

- search for a peak in some combination of pixel itself and neighbours, or

- fit a linear time gradient along a first iteration image major axis.

For some combinations, there may be the third question to answer: "How long to integrate?"

Relying on neighbours only to find the peak position in each pixel is good against picking up all afterpulse signals. However, in regions of very low signal, this results in an integration in a randomly defined window. Even though this might seem unsatisfactory, it does not matter since all pixels passing the typically used two-level tail cut cleaning have some signal in at least one neighbour. A time gradient fit may give a more reasonable integration window position in dark parts of the camera but has a risk of discarding image features not following the time gradient, such as a (partial) muon ring on top of a shower image. The integration window size also has an influence: the shorter the integration window, the bigger the differences between the different methods; the longer the integration window, the more NSB noise is integrated. In general, finding the right compromise is tricky.

Charge extraction optimisation studies for NectarCAM (being one of the prototypes for the CTA MST cameras and also using Nectar ASICs such as the H.E.S.S. IU cameras) [133] resulted in the use of a two-fold method [131]. It consists of (1) finding the peak time in each pixel and (2) integrating the waveform in a 9 ns window around that peak time with a shift to both, the left and right of the peak time, of 3 ns. The same method, being also very similar to what was used for the charge extraction in CHEC-M (cf. Sec. 4.8.2), was decided to be used for the H.E.S.S. IU SM data. The so-called NN peak finding algorithm is used to identify a Cherenkov signal in each pixel. It sums the waveforms of all pixels adjacent to the PoI and takes the time of the maximum value as peak time for the PoI. By default, the high-gain channel is used for this algorithm. In case the signal in at least one of the adjacent pixel exceeds the limit in which the signal response is linear, the low-gain channel is used for all pixels in the NN peak finding of the PoI. Once the peak time of the PoI is found (same peak time used for high- and low-gain channel), the signal is integrated in a 9 ns window around that peak resulting in one charge number per pixel for each gain channel. The extracted charge is referred to as "SMMax9". In case the peak finding algorithm would result in the definition of an integration window with edges falling outside the readout window, i.e. lower edge $<0$ ns or upper edge $>39$ ns, the integration window is shifted by the corresponding number of samples exceeding the readout window. In this way, it is ensured that always a valid part of the waveform is integrated.

The NN peak finding algorithm is an effective search for Cherenkov signals. Due to the use of the NNs and the typically small time gradient of the Cherenkov signal, the likelihood
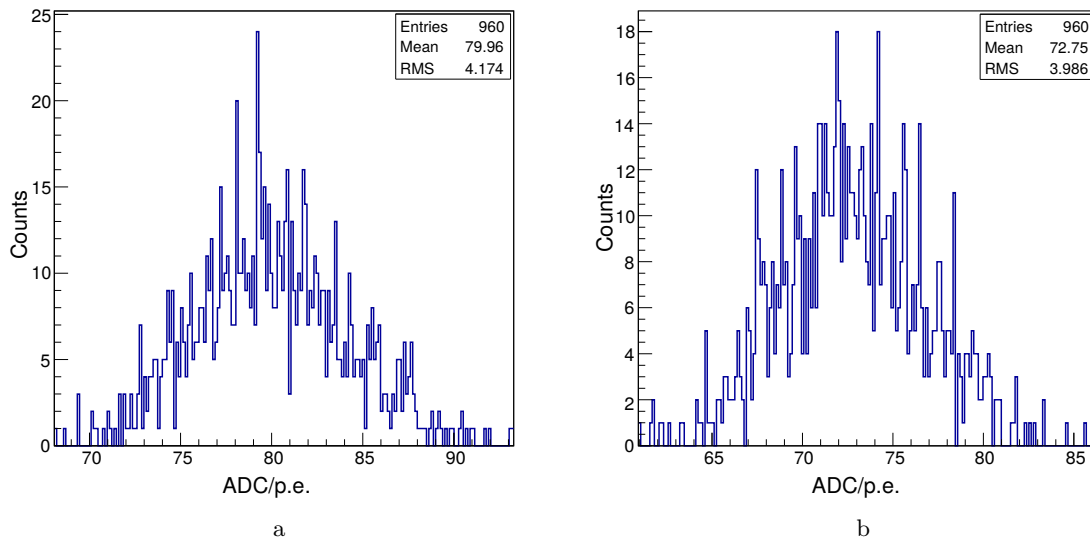
**Figure 8.2** SPE value distribution (in ADC/p.e.) for all 960 pixels of CT1 extracted from MC simulations for (a) CM and (b) SMMax9. Adapted from (Zorn, 2019) [69].

of a mis-identification of an NSB photon as a Cherenkov photon is decreased, especially important for low-signal pixels. If for example just the time of the signal maximum in the PoI was taken as peak time, a mis-identification would happen very often as soon as the signal amplitude of Cherenkov and NSB photons are of the same order. Furthermore, using the sum of the NN waveforms leads to a higher weight of pixels with Cherenkov signal than those without. Another advantage of the algorithm is that no distinction between pixels with and without signals is needed. Hence, the same algorithm can be used for the pedestal estimation which is based on signal-free pixels. Due to the uncorrelated appearance of NSB signals in adjacent pixels, a summation of the waveforms smooths out any NSB signal. This prevents a bias to higher amplitudes in the integration which would lead to a higher (wrong) pedestal estimation.

The use of a shorter integration range results in a different ADC-to-p.e. conversion factor (SPE value). Fig. 8.2 shows distributions for SPE values extracted from SPE simulations for CM and SMMax9 and revealing a factor of ∼0.91 between the two SPE values. This ratio is expected from the integration of the signal pulse shape (being used as an input to the simulation chain, cf. Fig. 7.3) in the two different windows (first 16 ns and 9 ns around the peak of the pulse).

## 8.3 Integration into analysis framework

Thanks to the simpleness of the charge extraction (being a simple integration of the signal in a fixed window around the signal peak, cf. previous section) and the same handling of pixels with and without Cherenkov signal, the integration of SM into the analysis framework is straight forward. Only one additional charge extractor is needed preceding the nominal extraction method.

After the charge extraction, the integrated SM data (SMMax9) is handled in the same way as CM, i.e. the image processing (such as image cleaning) is performed on the integrated

signal. However, due to the lower signal integrated in SMMax9 than in CM, new cuts for image cleaning and parameterisation (cf. Sec. 3.2.5) had to be defined. Due to the integration of 9 ns instead of 16 ns, the noise is reduced by a factor of $\sqrt{16/9}$. Furthermore, since the difference in SPE value (factor $\sim$0.91, cf. Sec. 8.2) is not taken into account at the stage of the image cleaning, the values for tail cut cleaning should be reduced by a factor of $\sqrt{16/9} \times 0.91$ for SMMax9 compared to CM. Hence, a lower-image-amplitude cut of $\sim$54 p.e. and tail cuts of (3,7) were determined to be used in the image cleaning of SMMax9 data.

The determination of other analysis parameters like background rejection cuts and local distance cuts, the optimisation of the Hillas direction reconstruction algorithm for the correct handling of long images, and the production of new `ImPACT` templates for SMMax9 will be required but is not covered by the work presented in this thesis.

Similar to the calibration chain, SM was incorporated into the MC simulation chain. All H.E.S.S. IU simulations were performed in SM by default. For the production of CM IRFs, the first 16 samples were summed afterwards. For SM, the simulated samples are processed in the same way as for measurements, i.e. the same charge extraction based on NN peak finding and integration around peak maxima is applied. The MC parameter determined in Ch. 7 are therefore valid for both, SM and CM.

## 8.4 Data integrity investigation

The data integrity of data taken in SM was investigated. For this purpose, different aspects, parameters, and characteristics of the data taken in SM and CM were compared.

**Event- and pixel-wise charge**   The charge of same events (matched by telescope participation and combination of bunch and event number, details below) of data runs taken in both, SM and CM, was compared. To do so, the SM data was integrated in two ways, (1) over the first 16 samples, referred to as "SMFirst16", and (2) over 16 samples around the waveform maximum – maximum being determined in same way as above via NN peak finding –, referred to as "SMMax16". Both were then compared to the CM charge of the same event. Fig. 8.3a shows such a comparison for $2 \times 10^7$ waveforms revealing no difference between CM and SMFirst16 (as expected). As also shown by the histogram in Fig. 8.3b, the difference between CM and SMMax16 is for most cases uniformly centred around 0. Those cases are events without Cherenkov signal or with the Cherenkov signal lying in the first 16 ns of the waveform. In cases of Cherenkov signals with time gradients $>$16 ns, the difference becomes more pronounced (spikes in Fig. 8.3a) since in such cases, SMMax16 contains the Cherenkov signal while it is truncated in CM and SMFirst16.

**Pedestal investigation**   Even though the event- and pixel-wise charge comparison already prove the SM data integrity on a "microscopic" scale, a further check on a "macroscopic" scale was performed. For this purpose, soft-trigger runs ($\equiv$ externally triggered runs with HV off and lid closed) in CM and SM were taken and analysed. In CM, a dependence of the pedestal on the location of the readout electronics the camera pixel is connected to was observed with pixels connected to channels located on the right side of a Nectar card being more noisy (i.e. showing a higher charge RMS) than those on the left. Hence, a good way to check consistency in the pedestals between CM and SM was to investigate whether this effect was also observed in SMMax16. Fig. 8.4 displays the pedestal RMS distribution for SMMax16 and CM showing that indeed the same effect was observed with a mean pedestal RMS of $\sim$12.5 ADC (corresponding to $\sim$0.15 p.e.) for the "left" pixels and of $\sim$17.8 ADC

a

b
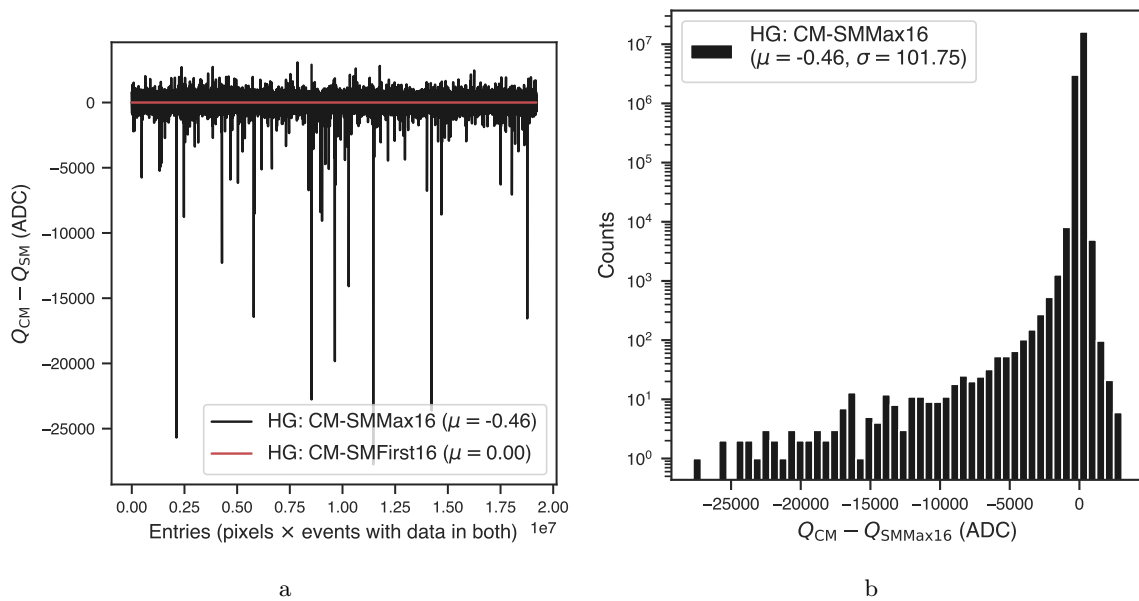
**Figure 8.3** Difference between CM charge $Q_{CM}$ and SM charge $Q_{SM}$ (a) as function of entry number for two ways of SM charge extraction: SMMax16 and SMFirst16. In addition, the mean $\mu$ for both distributions is given. (b) Histogram shown for the charge difference between CM and SMMax16 with the mean $\mu$ and standard deviation $\sigma$ indicated. As a reminder: The gain is $\sim$80 ADC/p.e. and the electronic noise 12 ADC, i.e. $\sim$0.15 p.e. . Refer to text for more details.

($\sim$0.22 p.e.) for the "right" pixels. As in CM, the mean pedestal RMS of the "left" pixels is $\sim$12.5 ADC (corresponding to $\sim$0.15 p.e.) and $\sim$17.8 ADC ($\sim$0.22 p.e.) of the "right" pixels.

**Event timing and identification** The timestamps of same events (matched by telescope participation and combination of bunch and event number) of observation runs taken on the Crab Nebula and Wd1 in both, SM and CM, was compared. Fig. 8.5a shows the difference of the *global* event timestamps between same events taken in SM and CM revealing a time difference between 2 and 7 $\mu$s. In nominal DACQ, the *global* event timestamp is given by the central trigger. However, since in the current readout scheme, the SM data is first stored on the camera PCs and then merged offline, it does not contain information from the central trigger. Hence, in the offline event merging process, the *telescope* event time[2] of one of the participating telescopes is used as *global* event time. This is why the SM *global* event timestamp is equal to the *telescope* event timestamp of at least one of the participating telescopes (cf. Fig. 8.5b). In future, when the SM data will also be processed in real time, the timestamp provided by the central trigger will also be used as *global* event time for SM.

The identification and matching of same events in CM and SM data files can therefore currently not be based on the *global* event time. However, the combination of event and bunch number, being used in the real time event processor on the DACQ to merge CM events of different telescopes, should be a unique event identifier in a given run. Fig. 8.6a shows – for all CM and SM events with same combination of event and bunch number – the telescope combination consistency as function of SM file entry. The later is defined to be 1 in case the

---

[2]The *telescope* event time with a resolution of 1 $\mu$s is the trigger time of the telescope. Depending on the geometry of the EAS, a difference of 1 $\mu$s between *telescope* event times of different telescopes is possible.
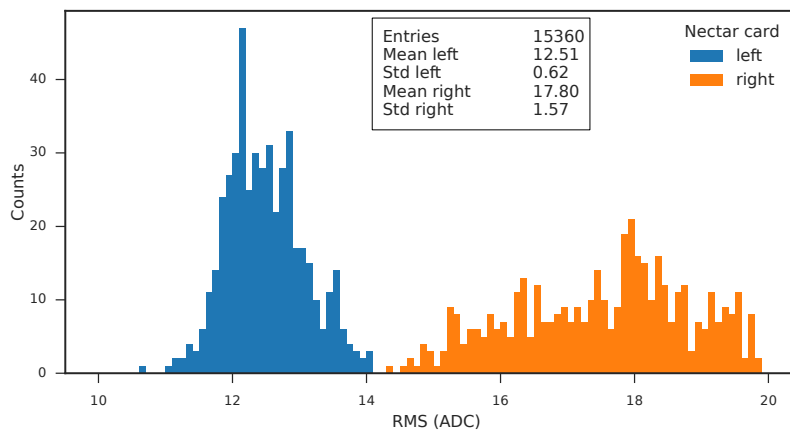
a
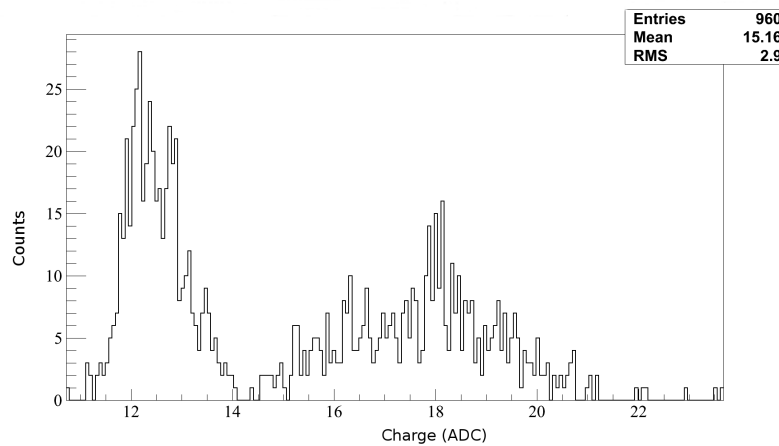


b

**Figure 8.4** RMS charge distribution for all pixels of CT1 for (a) SMFirst16 and (b) CM, extracted from soft-trigger runs. The SMMax16 histogram was filled with the event-wise charge per pixel of 16 events. This is the reason for the higher number of entries than in the CM histogram that was taken from the general output of the H.E.S.S. calibration chain where it is filled with the pixel-wise mean RMS.

telescopes participating in the array trigger[3] are the same for both, SM and CM event, and 0 if not. It is observed, that the telescope participation in each SM event is the one expected from the corresponding CM event in case the events were matched via the same combination of bunch and event number. In the previous investigation of pixel- and event-wise charges, this matching algorithm was already been used and resulted in a 100% match between CM and SMFirst16 charges. Hence, it can be concluded that the combination of bunch and event number is a unique event identifier. This was expected and verified to be the case also for SM data. It can therefore be used for comparison or matching of CM and SM events.

---

[3]The array (central) trigger looks for time coincidences between different telescopes. During regular observations, an array trigger is issued in case CT5 issued an L2 (telescope) trigger or in case of a time coincidence of at least two telescopes.

a



b
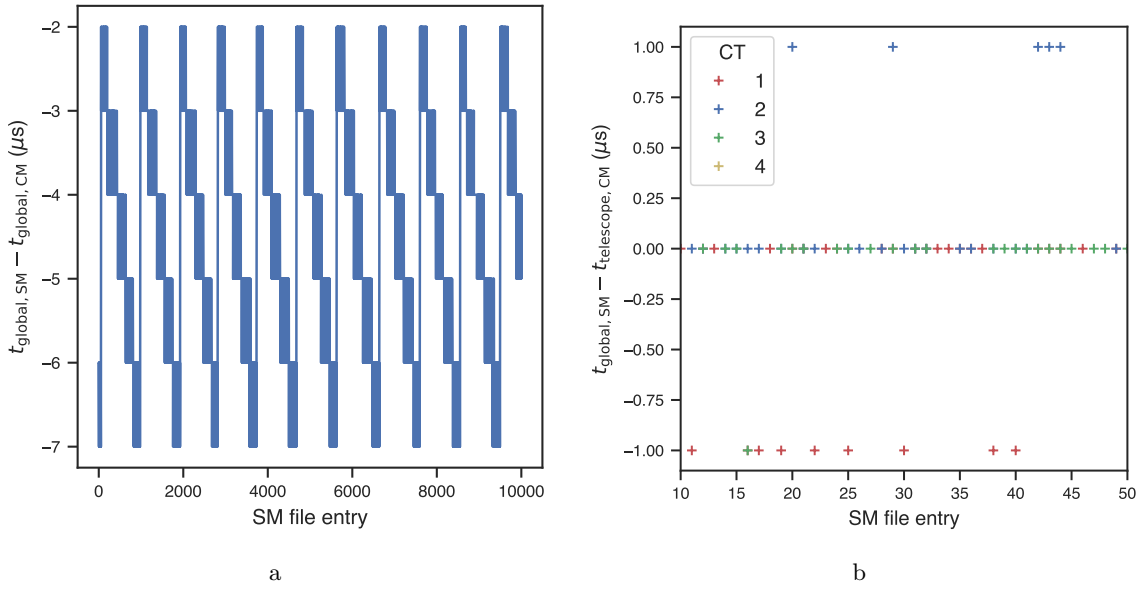
**Figure 8.5** (a) Difference of SM and CM *global* event timestamps and (b) difference of SM *global* and CM *telescope* event timestamp for all four telescopes, both as function of SM file entry number.



a



b
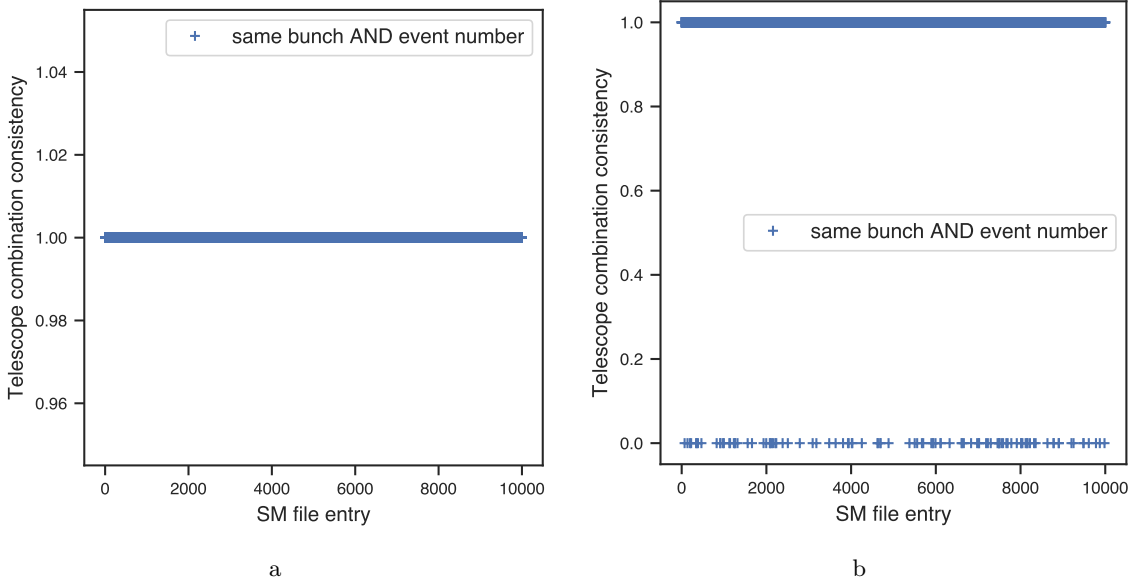
**Figure 8.6** Telescope participation consistency (refer to text for definition) as function of SM file entry number for events with same combination of event and bunch number for run (a) 135247 and (b) 129930.

**Missing SM data**  In the investigation of telescope participation consistency for events with same event and bunch numbers, a consistency $\neq 1$ was observed for several events and even full runs taken on the Crab Nebula and Wd1 (cf. Fig. 8.6b for an example of the Wd1 run 129930). The inconsistency is due to missing SM data of some telescopes; in case of Wd1 data, approximately 1% of the events are affected.
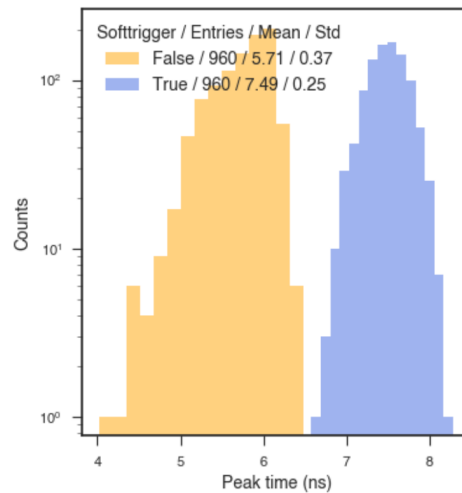
**Figure 8.7** Peak time distribution (pixel-wise mean out of all events) for CT1 extracted from FF
runs interleaved with soft-trigger events. Yellow (blue) histograms show the distributions for events
with (without) FF signal.

The issue was reported and further investigated by G. Giavitto[4] revealing a problem in
the offline event merger. However, the missing data was found to be still located on the
camera PCs of the corresponding telescopes allowing a recovery of the events. Thanks to the
online charge extraction and incorporation into the nominal data processing via the DACQ
system in future, such a problem is not expected to happen again.

## 8.5 Performance studies

**NN peak finding algorithm**  The performance of the NN peak finding algorithm was
investigated using FF runs interleaved with soft-trigger events. For those runs, only 16
samples were read out instead of the nominal value of 40. Fig. 8.7 shows a distribution of
extracted peak time (mean over all FF or soft-trigger events for each pixel) for events with
and without FF signals for all pixels of CT1. The histogram filled with the mean peak time
of soft-trigger events of each pixel is centred around 7.5 ns. This is expected since for a
soft-trigger event, the probability of a peak to occur in any sample between 0 and 15 ns is
expected to be the same. Hence, a distribution filled with the event-wise peak time of all
soft-trigger events is expected to be flat. The mean of a flat distribution with 16 bins between
0 and 15 is 7.5, as being observed. From this analysis, it could therefore be concluded that
no bias towards any sample is observed in the NN peak finding algorithm. This also proved
that the same charge extraction algorithm can be used for pixels with and without Cherenkov
signal, as explained in Sec. 8.3. The histogram filled with the mean peak time of FF events of
each pixel is centred around 5.71 ns being a measure for the time delay between the FF unit
and camera trigger. The spread of the distribution results from the different arrival times of
the photons from the FF unit at the individual camera pixels[5].

The performance of the NN peak finding was also investigated using observation data.

---

[4]G. Giavitto from DESY Zeuthen is the responsible person for the technical implementation of SM readout.

[5]Since the distance between the FF unit and the camera pixels depends on the position of the pixel within the
camera (outer pixels have a bigger distance), the arrival time of the photons from the FF varies between
camera pixels.
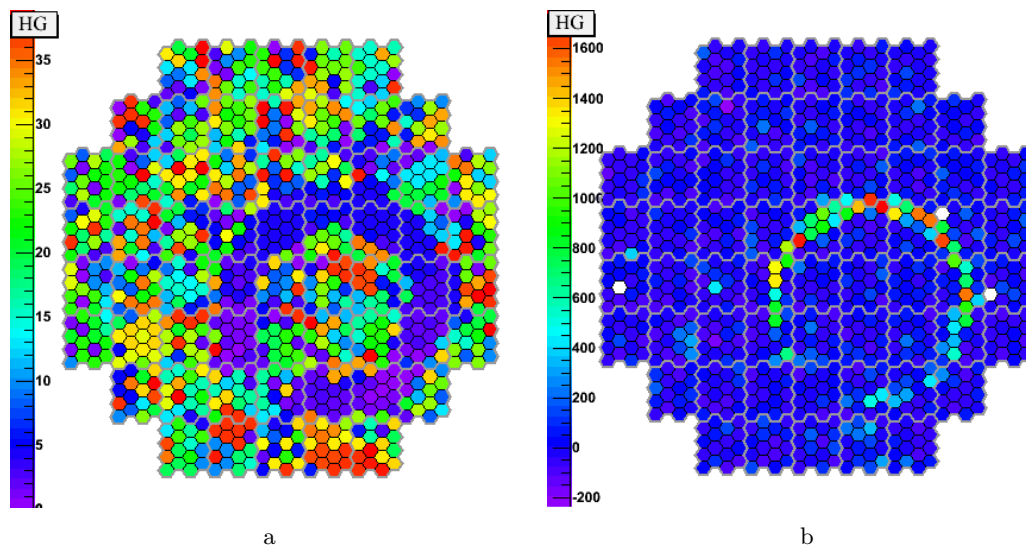
**Figure 8.8** Camera images showing (a) the peak time in ns and (b) the extracted charge SMMax9 in a.u., both indicated by the colour scale.
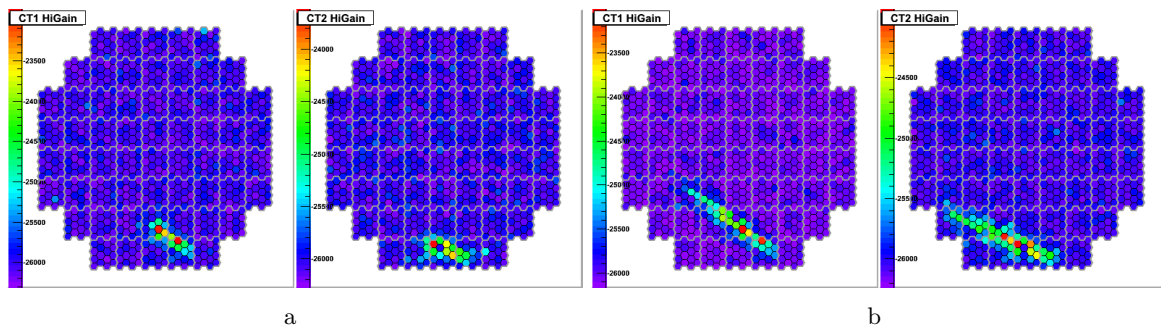


**Figure 8.9** Camera images of a Cherenkov event detected during observations of the Crab Nebula showing the (a) CM and (b) SMMax9 charge in ADC (indicated by the colour scale) for CT1 and CT2.

Fig. 8.8 shows camera images (peak time and extracted charge) for a muon event of a Crab Nebula observation run. As expected for a muon event, a ring-like image with all pixels of that ring having the same peak time (with a possible spread of 1–2 ns depending on the orientation of the muon Cherenkov cone w.r.t. the telescope axis) can be observed. Furthermore, the ring in the peak time camera image shows to be thicker by two rows than the ring in the charge camera image. The reason is the functionality of the NN peak finding: A pixel without Cherenkov signal but being a one-sided neighbour to a pixel with a Cherenkov signal (having an amplitude significantly higher than the baseline) is associated with the peak time of the signal pixel.

Both examples, the FF investigation and muon ring event, indicate the correct implementation of the NN peak finding algorithm resulting in the expected performance.

**Camera image parameterisation**  In SM, the number of truncated images is expected to get reduced, i.e. longer images are expected to be observed. Exemplary, Fig. 8.9 shows an event detected during observations of the Crab Nebula and recorded in both, SM and CM. It
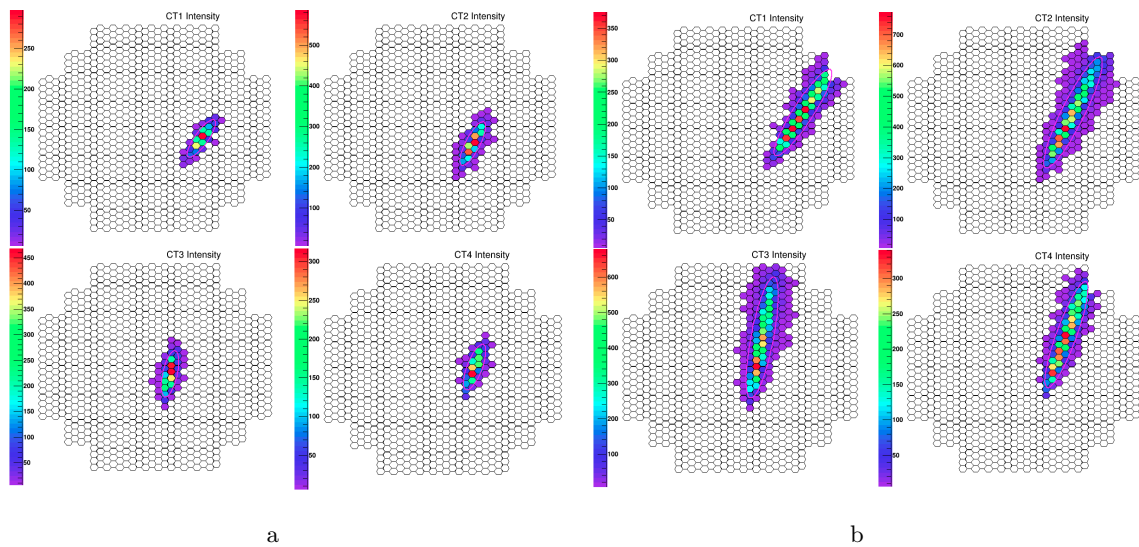
**Figure 8.10** Simulated camera images showing the pixel-wise intensity in units of p.e. (indicated by the colour scale) after tail cut cleaning for (a) CM and (b) SMMax16. They result from an EAS at a zenith angle of 45°, being offset by 2° from the optical axis of the telescope, with an impact distance of 925 m, and initiated by a $\gamma$-ray with an energy of 223 TeV. Adapted from (Zorn, 2019) [69].

can nicely be observed that the image is truncated in CM while it is much longer in SMMax9. The same effect is observed in MC simulations: Fig. 8.10 shows camera images of the same MC Cherenkov event resulting from a high-energy, high-impact-distance EAS ($E \simeq 223$ TeV, $d \simeq 925$ m) in CM and SMMax16[6]. Due to the truncation in CM, the Hillas reconstruction results in different Hillas ellipses with a significant increased length in SMMax16.

To quantify this effect, Fig. 8.11 shows the ratio of SMMax9 and CM Hillas length, extracted from the parameterised camera image after image cleaning (tail cuts and lower image amplitude cuts applied[7]), for different image amplitude cuts and as function of the impact distance and MC energy of the primary $\gamma$-ray. As emphasised by the example shown in Fig. 8.10, Cherenkov images recorded in SM are in general longer than those recorded in CM (cf. Fig. 8.11a). For images with low image amplitudes, for a few events even a factor 3 between SMMax9 and CM Hillas length is observed. In most of the cases, longer images in SMMax9 are observed for events with high impact distances (cf. Fig. 8.11b). Furthermore, Fig. 8.11c shows that not only the very high-energy events gain from being recorded in SM, also low-energy events may produce longer images in SM due to a reduced noise integration. There are also cases in which the Hillas length is slightly smaller in SM than in CM. In those cases, typically one more low-intensity pixel was cleaned away in SM than in CM resulting in a slightly reduced Hillas length.

**Effective area** As discussed in Sec. 8.3, the determination of all cuts and the full optimisation of the reconstruction algorithm based on Hillas and `ImPACT` is beyond the scope of

---

[6]To better compare the pixel-wise intensity in units of p.e. the same integration window length as for CM (16 ns) was used in this example.

[7]As explained in Sec. 8.3, new tail cuts were defined for SMMax9 – (03,07) – to account for the reduced noise being integrated and the smaller SPE value. Furthermore, the latter one results in a lower image amplitude cut for SMMax9 being 54 p.e. .
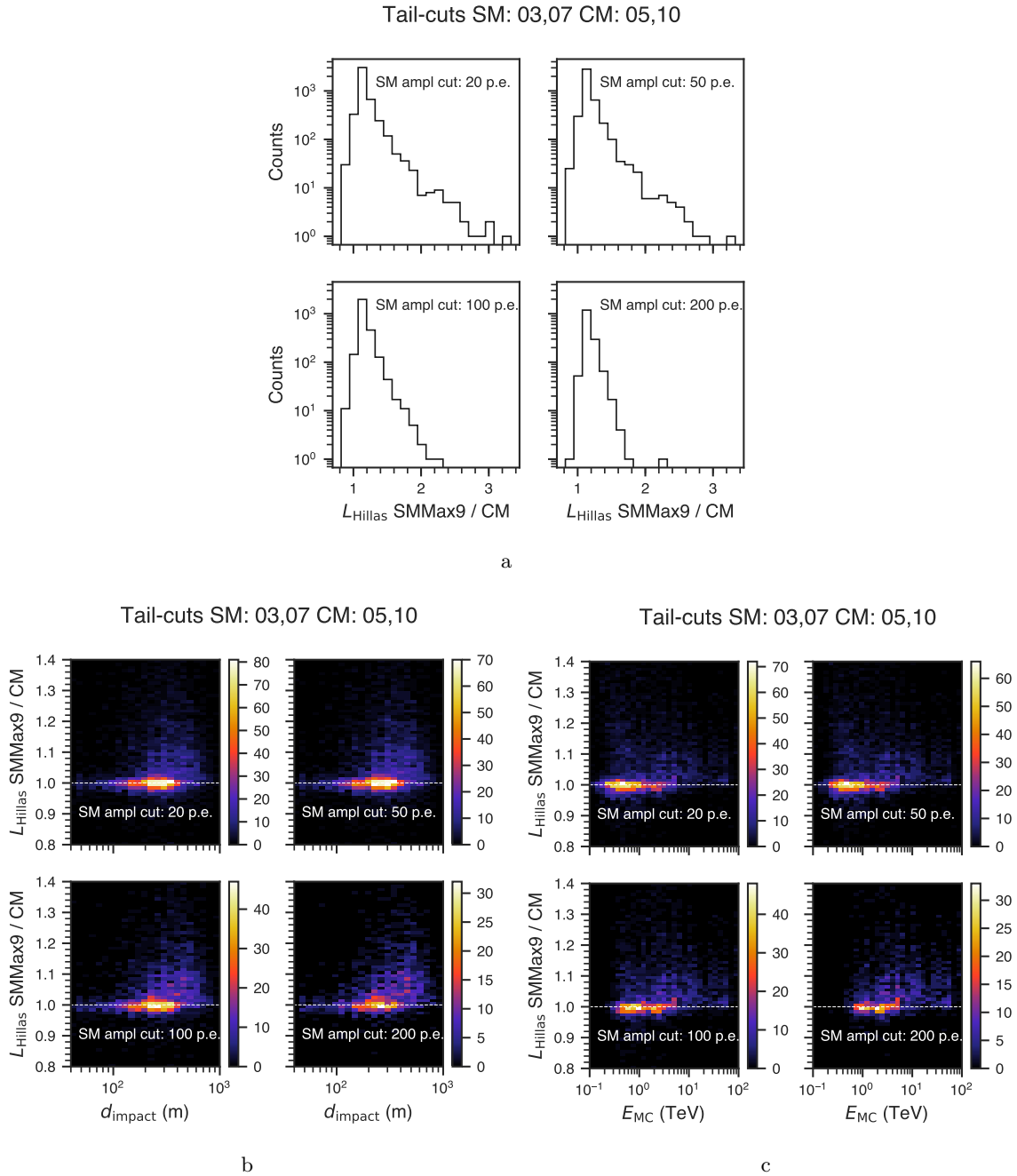
**Figure 8.11** Simulations of SMMax9 and CM Cherenkov events. Shown are the ratio of SMMax9 and CM Hillas length $L_{\mathrm{Hillas}}$ for different Hillas amplitude cuts applied (20, 50, 100, and 200 p.e.) as (a) a 1D histogram, (b) function of impact distance $d_{\mathrm{impact}}$ of the primary $\gamma$-ray (2D histogram), and (c) function of energy $E_{\mathrm{MC}}$ of the primary $\gamma$-ray (2D histogram). The colorscale given by the colorbar indicates the number of counts in a bin for the 2D histograms. (b) & (c) are reproduced from (Zorn, 2019) [69].

this thesis. Hence, the difference in effective area was analysed using tail and lower-image-amplitude cuts only. Fig. 8.12 shows such a comparison. As expected, the effective area is higher in SM at low energies due to the reduced NSB integration. At high energies, it is similar for SM and CM what is expected since no further cuts are applied yet. Once all cuts
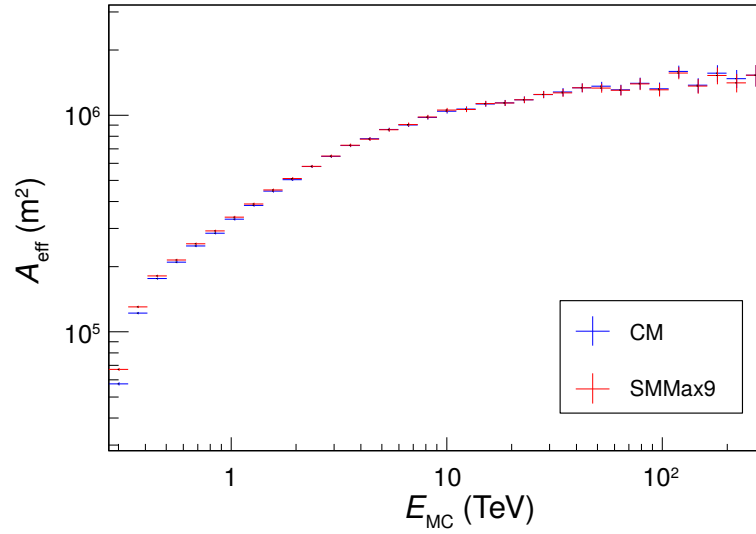
**Figure 8.12** Comparison of CM and SMMax9 effective areas $A_{\text{eff}}$ as function of MC energy $E_{\text{MC}}$ with lower-image-amplitude cut applied only. Adapted from (Zorn, 2019) [69].

have been redefined for SM, the effective area is expected to improve at both, the low- and high-energy end of the energy range, since in general more images will be extracted in the analysis.

**Angular resolution**   The angular resolution of the H.E.S.S. system is derived from point-source $\gamma$-ray MC simulations. For this purpose a distribution of squared angular distance $\theta^2$ between the true and the reconstructed direction of the MC $\gamma$-rays is generated. Two different values, the 68%- and the 90%-containment radius, are typically extracted and used as angular resolution quantifier.

Similar as for the effective area, only preliminary results from angular resolution comparisons can be shown. Since the Hillas direction reconstruction algorithm has not been optimised yet for SM, the values are expected to change in future. However, as shown by Fig. 8.13, even without algorithm optimisation for SM, the angular resolution is better for SMMax9 than CM for primary $\gamma$-ray energies $> 10$ TeV (red data points lying below the blue ones in Fig. 8.13b) and large offsets from the optical axis of the telescope ($2°$ in the example shown). A possible interpretation for this observation is that for high offsets, the camera images can be significantly longer in SMMax9 than in CM without hitting the camera edge. In CM the images are typically shorter due to truncation reducing the direction reconstruction capabilities. The situation looks different in case of no offset where the angular resolution is observed to become worse for SMMax9 at high energies. This observation might be explained by the fact that even though also in this case, the SMMax9 images are longer than the CM ones, due to geometry the chance of SMMax9 images hitting the camera edge is much higher than at high offsets. The current direction reconstruction algorithm might not be optimised to handle such events, possibly also since no local distance cut is used (as mentioned above). This could be the reason for the angular resolution to be worse for SMMax9 than CM for on-axis events.

**Energy bias and resolution**   The energy bias and resolution of the H.E.S.S. system is derived from point-source $\gamma$-ray MC simulations. The energy bias is defined as the mean
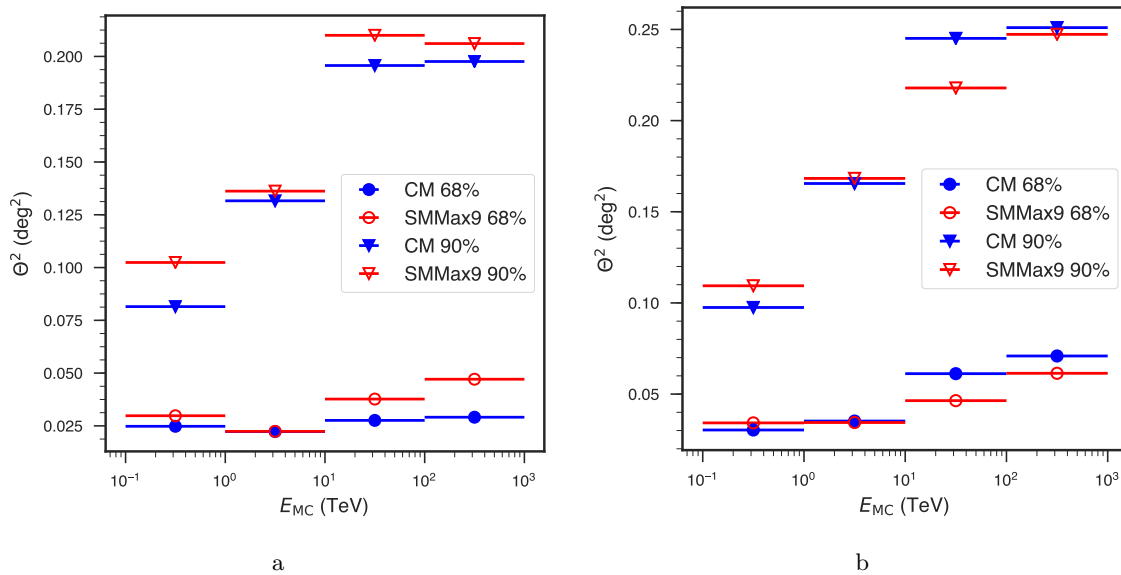
**Figure 8.13** Simulations of SMMax9 and CM Cherenkov events. Shown are the 68%- and the 90%-containment radii of the $\theta^2$-distribution as function of primary $\gamma$-ray energy and for two different offsets from the optical axis: (a) 0° and (b) 2°. The errorbars indicate the size of the energy bins used to generate the corresponding $\theta^2$-distribution.

difference between reconstructed and true (MC) energy of the primary $\gamma$-ray normalised by the true (MC) energy, i.e. $(E_{\mathrm{reco}} - E_{\mathrm{MC}})/E_{\mathrm{MC}}$. It can be corrected for in the analysis. The energy resolution is defined as the spread of the energy bias, i.e. the event-wise scatter around the bias. Since its value is not predictable on an event-wise basis, the energy resolution cannot be corrected for.

Similar as for the effective area and angular resolution, only a preliminary comparison of energy bias and resolution between CM and SMMax9 can be shown. Fig. 8.14 shows the energy bias for CM and SMMax9 as function of true MC energy of the primary $\gamma$-ray for two offsets from the optical axis of the telescope (0° and 2°). The energy bias is observed to be smaller for SMMax9 than CM at low energies ($\lesssim 300$ GeV) for all offsets likely due to the reduced noise integration. At high energies and high offsets, the energy bias is negative for SMMax9, i.e. the reconstructed energy is underestimated. No obvious explanation could be found for this behaviour at the current state of the investigation.

To determine the energy resolution, the event-wise energy bias was filled into a histogram and the central part fitted with a Gaussian. The resulting standard deviation $\sigma$ determines the energy resolution. Fig. 8.15 shows such a distribution for $E_{\mathrm{MC}} \in [10, 100]$ TeV for CM and SMMax9 and two different offsets from the optical axis of the telescope (0° and 2°). The resulting fit parameters and energy resolution (cf. Tab. 8.1) indicate an increased energy resolution for SMMax9 at an offset of 2° even without the optimised analysis chain for SM being in place. This improvement might be explained – similar as for the angular resolution – by the fact that images recorded in SM are in general longer and not truncated at high offsets. This should then allow a better and more stable energy reconstruction, hence result in an improved energy resolution.
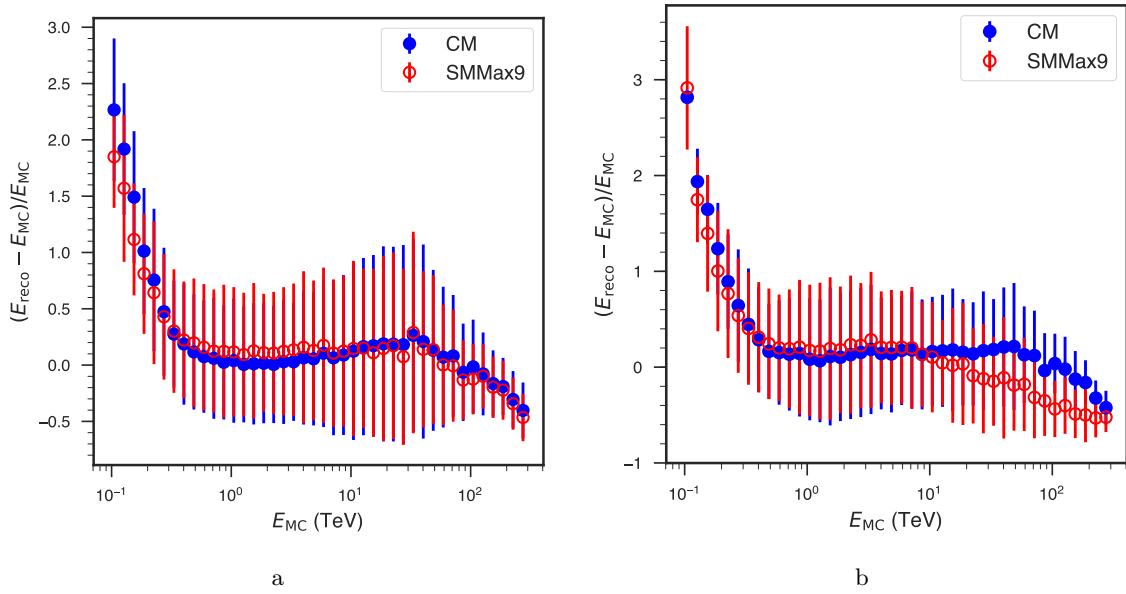
**Figure 8.14** Simulations of SMMax9 and CM Cherenkov events. Shown is the energy bias as function of true MC energy of the primary $\gamma$-ray for two different offsets from the optical axis: (a) $0°$ and (b) $2°$.

**Table 8.1** Energy resolution (in %) for $E_{MC} \in [10, 100]$ TeV for CM and SMMax9 and two different offsets from the optical axis, deduced from the standard deviation $\sigma$ of the Gaussian fits to the energy bias distributions shown in Fig. 8.15.

| Offset (°) | CM | SMMax9 |
|---|---|---|
| 0.0 | 10.8 | 10.9 |
| 2.0 | 25.0 | 21.0 |

## 8.6 Summary and outlook

In this chapter, the current and future SM readout scheme, the charge extraction algorithm being based on a NN peak finding with an integration in a fixed window around the peak, and the integration into the analysis framework has been presented. Extensive SM data integrity tests were performed revealing only minor issues that will be solved by design when using the new readout scheme in future. The performance of H.E.S.S. improves in several aspects when using SM data in the analysis. It was shown that, compared to CM, SM camera images are significantly longer since less images are truncated. Furthermore, due to the smaller integration window less noise is integrated. The latter aspect was shown to result in increased statistics at the lower end of the H.E.S.S. energy range. An improvement is also expected at the higher end once the full set of new analysis cuts, new BDTs, and new `ImPACT` templates have been defined, retrained, and produced for SM. Data taken in SM will therefore especially be useful in combination with the high-energy-optimised analysis methods currently being developed within H.E.S.S..

Furthermore, an improvement of energy and angular resolution at high energies and high offsets has been shown. The behaviour of the energy resolution at low offsets, showing to
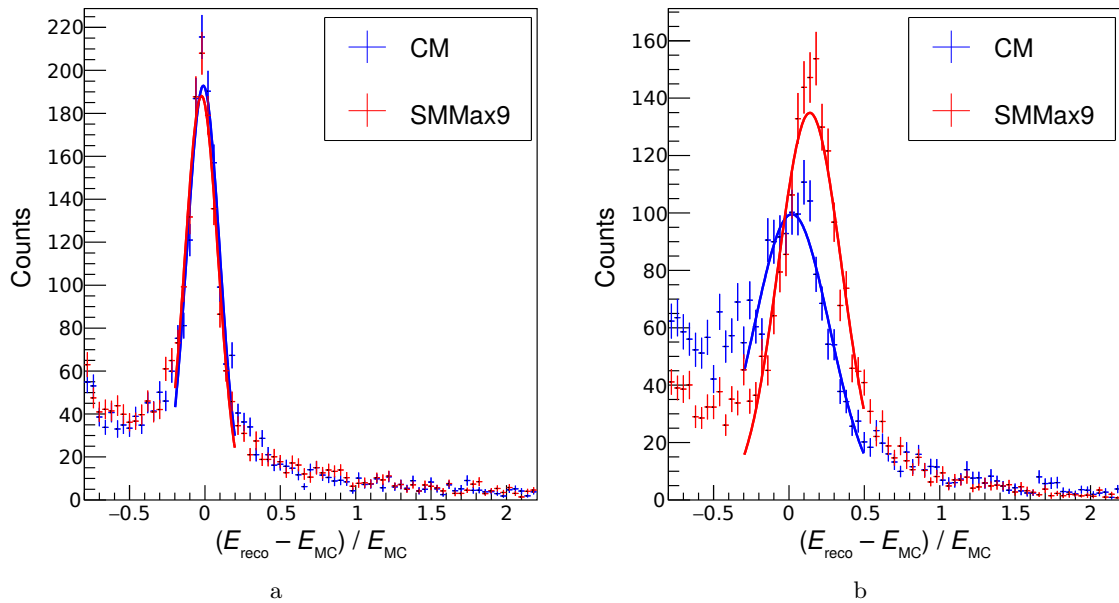
**Figure 8.15** Simulations of SMMax9 and CM Cherenkov events. Shown is the energy bias distribution for $E_{MC} \in [10, 100]$ TeV and a Gaussian fit to the central part for two different offsets from the optical axis: (a) 0° and (b) 2°.

be worse for SM, and of the energy bias at high offsets, showing an underestimation of the reconstructed energy for SM events, is not fully understood yet. It might be related to the current direction reconstruction not yet being optimised for long images hitting the camera edge. A deeper study of this behaviour and of the Hillas direction reconstruction algorithm as well as the determination of other analysis parameters like $\zeta_{BDT}$ and local distance cuts and the production of new `ImPACT` templates for SM were beyond the scope of this work but have to be tackled in the near future.

So far, SM data was taken in two explicit observation campaigns only: ∼20 hours of Crab Nebula and ∼60 hours of HESS J1646–458, being a very extended VHE γ-ray source in the direction of Wd1. However, thanks to the studies presented in this chapter, showing that the integration of SM into the analysis framework is simple and straight forward and promising better performance for all kind of observations, it will be used by default in all observation runs in the near future. To be able to handle the increased amount of data, the SM data will be reduced online by using the same charge extraction mechanism as presented above. Thanks to the readout in parallel to CM, CM data will not be affected and will further be available for standard analyses and backwards compatibility.

As soon as the final SM data analysis scheme is in place, the ∼60 hours of SM data taken on HESS J1646–458 can be combined with the ∼168 hours taken in CM (cf. Ch. 9). This promises to increase the performance especially at the upper end of the spectrum being crucial for the possible identification of HESS J1646–458 as a PeVatron. As the work on the implementation of such a combined analysis is not finalised yet, the recently acquired CM data of HESS J1646–458 was used for the analysis in this thesis, presented in the following chapter.

Westerlund 1 and HESS J1646–458

HESS J1646–458 is an extended VHE $\gamma$-ray source located in the direction of the young, very massive SC Westerlund 1 (Wd1, cf. Fig. 9.1). It was shown to have a relatively hard spectrum with a spectral index of $\alpha \simeq 2.19$ and a flux normalisation at 1 TeV of $\Phi_0 \simeq 9.0 \times 10^{-12}\,\mathrm{TeV}^{-1}\,\mathrm{cm}^{-2}\,\mathrm{s}^{-1}$ without indication for a cutoff for energies >10 TeV [134]. Such observations of Wd1 and of other Galactic massive SCs have recently triggered studies suggesting that those SCs are factories of GCRs possibly even with the potential to act as Galactic PeVatrons [47].

In this chapter, I will present a new analysis of HESS J1646–458. To do so, I will first introduce Wd1 and other astronomical objects that are located in the direction of HESS J1646–458 (cf. Sec. 9.1). Then, I will give details about the datasets (cf. Sec. 9.2) that I used for the investigations presented in Sec. 9.3. Based on those, I will discuss different scenarios that may explain the observed VHE $\gamma$-ray emission with the goal to identify the underlying physical processes (cf. Sec. 9.4). Finally, I will summarise the main results of this chapter and conclude with an outlook (cf. Sec. 9.5).

## 9.1 HESS J1646–458 and astronomical objects in the field of view

To explain the origin of the VHE $\gamma$-ray emission of HESS J1646–458, Wd1 but also other astronomical objects located in its direction should be considered. These are introduced in the following subsections.

### 9.1.1 Westerlund 1

Wd1, named after its discoverer Bent Westerlund in 1961 [138], is located [139] at a right ascension of $r_{\mathrm{J2000}} \simeq 16^{\mathrm{h}}47^{\mathrm{m}}04^{\mathrm{s}}$ and a declination of $d_{\mathrm{J2000}} \simeq -45°51'04''$ or (in Galactic coordinates) at a longitude of $l \simeq 339.55°$ and a latitude of $b \simeq -0.40°$. With an estimated mass of $\sim 4.75 \times 10^5\, M_\odot$, it is the most massive SC in the Galaxy observed so far [140] and even
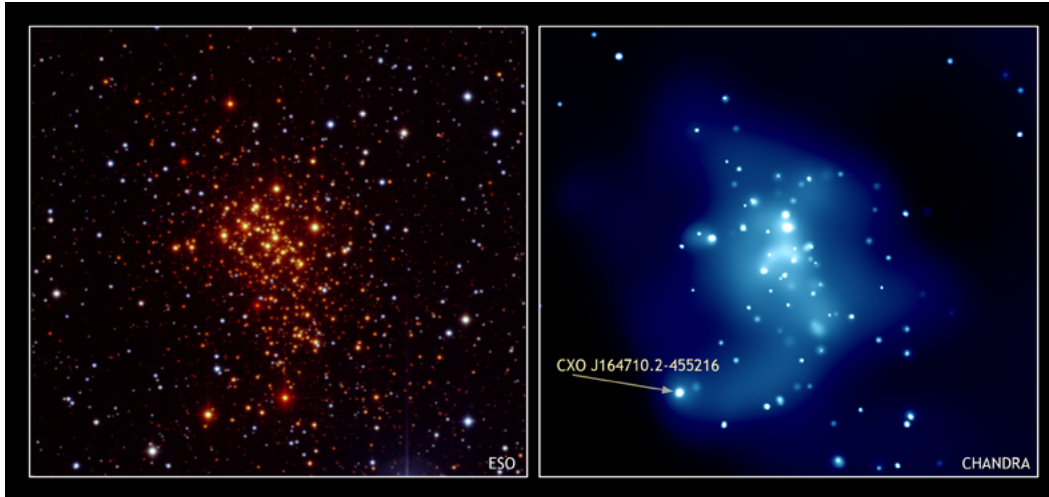
**Figure 9.1** Images of Wd1 (300" × 270") combining optical observations by the European Southern Observatory in Chile [135] (left) and in X-rays taken by the Chandra X-ray telescope [136] (right) with the magnetar CXO J164710.2–455216 being indicated. Adapted from [137]. For more details about the X-ray observations, refer to text.

more massive than other known SCs such as R136 ($\sim$4.5$\times$10$^5$ $M_\odot$), Arches ($\sim$4.3$\times$10$^5$ $M_\odot$), or the Galactic centre ($\sim$4.0$\times$10$^5$ $M_\odot$). A new distance estimation of Wd1 was recently derived with Gaia data (data release 2) [141] resulting in

$$d_{\mathrm{Wd1}} = (3.2 \pm 0.4)\,\mathrm{kpc}. \tag{9.1}$$

Furthermore, its radial velocity was deduced from HI observations to be [142]

$$v_{r,\mathrm{Wd1}} = (-55 \pm 3)\,\mathrm{km/s}. \tag{9.2}$$

95% of the $\sim$200 known cluster members were found to lie within 2' of the nominal cluster core corresponding to a size of $\sim$2 pc at the given distance. 25% of the stars have been spectroscopically investigated, all showing masses of >30 $M_\odot$ [140]. In total, at least 24 Wolf-Rayet stars (>70% of them expected to be bound in binary systems [143]), more than 80 OB supergiants, one luminous blue variable, one sgB[e], six yellow hypergiants (out of 12 in the whole Galaxy), and three red supergiants (RSGs) have been identified up to now [144], including one of the largest star known in our Galaxy: the RSG Westerlund 1-26 with a radius of 1530–2550 solar radii [145, 146].

Assuming a typical initial mass function and given the masses of the observed stars today, Wd1 is expected to have contained a huge number of very massive stars. As the age of Wd1 is estimated to lie in the range of 3.5–5 Myr [140], higher than the typical lifetime of such stars, Muno et al. [144] concluded that $\sim$80–150 stars with initial masses >50 $M_\odot$ should have exploded as SNe since the cluster was 3 Myr old. This would result in an average SN rate of one every 7–13 kyr. Observations carried out with the Chandra X-ray telescope [136] in 2005 revealed point-like and diffuse X-ray emission within Wd1 [144, 147], similar to what is seen in a few young stellar associations in the Galaxy, such as RCW 38 [148], and in the Large Magellanic Cloud (LMC) in 30 Doradus C [149]. While the point-like emission is coincident with stars, the extended emission shows a 5' halo around Wd1 which might be interpreted as a thermal plasma or non-thermal emission produced by stellar light being IC-scattered off MeV electrons. While the Chandra observation did not show any feature of an SNR shell,

the magnetar CXO J164710.2–455216, with an estimated age of 65–90 kyr, was detected as an X-ray pulsar with a spin-down power of $\dot{E} \leq 3 \times 10^{33}$ erg/s (cf. Fig. 9.1) [150]. Being a possible remnant of an SN, it is the only compact object that was observed within Wd1 up to now. The mass of its progenitor star is estimated to be >40 $M_\odot$.

The very massive stars in Wd1 are observed to experience mass loss with rates in the order of $\dot{M}_* \simeq (0.1 - 7.2) \times 10^{-5} M_\odot$ yr$^{-1}$. It should be either triggered by phases of instability or by interactions with other stars when bound in binary systems, and result in stellar winds with velocities of 200–2100 km/s [151]. According to Sec. 2.2.2.3, the individual stellar winds may have merged into a superwind forming an SpB. Indeed, a gas cavity with a radius of ~0.73°, corresponding to ~41 pc at the distance of Wd1, is seen in HI observations [142] with a dynamic age similar to the age of Wd1. The total superwind wind luminosity can be estimated from the observed individual stellar mass-loss rates and wind velocities (listed in [151]) (cf. Eq. 2.48):

$$L_{\text{SC,wind}} = \sum L_{*,\text{wind}} = \frac{1}{2} \sum \dot{M}_* v_{*,\text{wind}}^2 \simeq 4 \times 10^{38} \text{ erg/s} \equiv L_{\text{Wd1,wind}}. \qquad (9.3)$$

### 9.1.2 Other objects

There are other astronomical objects than Wd1 in the direction of HESS J1646–458 that could act as counterparts and sources for the observed VHE $\gamma$-ray emission. Of special interest is the low-mass X-ray binary 4U 1642–45 (also named as GX 340+0) at a distance of 8.5–11.5 kpc with an accreting NS [152, 153, 154]. As pointed out in the publication from 2012 [134], so far only *high*-mass X-ray binaries were associated with *point-like* and *variable* VHE $\gamma$-ray sources. Since 4U 1642–45 is a *low*-mass X-ray binary, the observed VHE $\gamma$-ray emission is *not point-like* (even at distances of 8.5–11.5 kpc), and *no variability* in the VHE $\gamma$-ray emission at the position of 4U 1642–45 was observed, an association of 4U 1642–45 with the VHE $\gamma$-ray emission region of HESS J1646–458 was deduced to be unlikely.

In contrast to that, pulsars and their extended nebulae have been proven to produce extended VHE $\gamma$-ray emission, actually accounting for the largest proportion of Galactic objects in the TeV sky. Fig. 9.2 shows $\dot{E}/d^2$ of known pulsars in the FoV as a function of the radial distance to Wd1 revealing two pulsars with $\dot{E}/d^2 > 8 \times 10^{33}$ erg/(s kpc) that are considered as possible counterparts, similar to the selection criterion used in [155]:

- PSR J1648–4611 with an estimated distance of (4.9±0.7) kpc, a measured spin-down power of $\dot{E} \simeq 2.1 \times 10^{35}$ erg/s, and a characteristic age of $\tau \simeq 1.1 \times 10^5$ yr [156, 157, 158], and

- PSR J1650–4601 with a measured spin-down power of $\dot{E} \simeq 2.9 \times 10^{35}$ erg/s and a characteristic age of $\tau \simeq 1.3 \times 10^5$ yr [159], but unknown distance[1].

Their possible influence on the observed $\gamma$-ray emission was considered in the analysis.

## 9.2 Datasets

Wd1 has been observed at different wavelengths, either as part of a survey or in dedicated observations. In addition to $\gamma$-ray data taken with H.E.S.S. (cf. Sec. 9.2.1), radio data taken

---

[1]As the distance of this pulsar is unknown, it was artificially set to the distance of Wd1 resulting in $\dot{E}/d^2 > 8 \times 10^{33}$ erg/(s kpc). This choice is of course arbitrary, however the pulsar was considered in the following investigations.
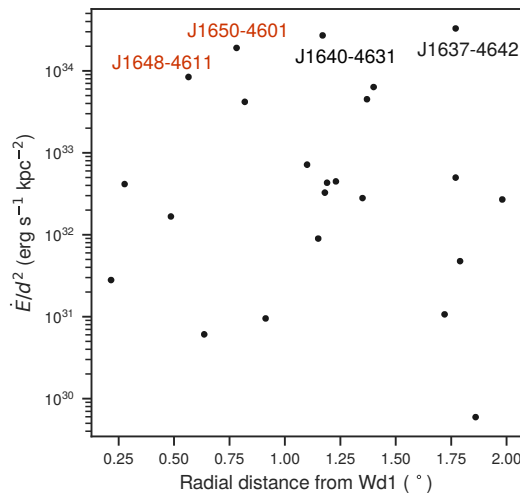
**Figure 9.2** Pulsars in the FoV of HESS J1646–458. For the four labelled ones, it holds that $\dot{E}/d^2 > 8 \times 10^{33}$ erg/(s kpc). The red-labelled ones are potential counterparts of HESS J1646–458 while the black-labelled ones are spatially coincident with other known VHE $\gamma$-ray sources located in the FoV of HESS J1646–458. Since the distance of PSR J1650–4601 is not known, it was (arbitrarily) set to the expected distance of Wd1 to position it in this plot.

with the Mopra radio telescope [160] tracing molecular material (CO and CS) and data from the HI4PI survey [161] tracing atomic hydrogen (HI) (cf. Sec. 9.2.2) was used for the analysis and physical interpretation of the observed $\gamma$-ray emission presented in Sec. 9.3.

### 9.2.1 Gamma ray (H.E.S.S.) data

A first observation of the region around Wd1 with H.E.S.S. was performed during the H.E.S.S. Galactic plane survey (HGPS) in 2004 and 2007 [162, 163], followed by explicit follow-up observations pointing towards Wd1 in summer 2008, resulting in a total of ∼45 hours of data. For the analysis published in 2012 [134], observations at zenith angles $\theta_z > 55°$ were excluded in addition to the standard exclusion of data taken under unstable weather conditions or with malfunctioning hardware[2]. Thus, a total of ∼34 hours remained. The analysis of this data resulted in the detection of the extended VHE-$\gamma$-ray source HESS J1646–458 with a diameter of ∼2.2°. It showed a hard spectrum with a spectral index of 2.2 and no cutoff up to $\gamma$-ray energies of ∼20 TeV. Due to the spatial coincidence with Wd1, the $\gamma$-ray emission was assumed to result (at least partially) from particle acceleration and physical processes within and in the vicinity of the SC.

Since the publication in 2012, a lot more data was acquired (1) as a side product in deep observations of HESS J1641–463 (∼72 hours in 2010, 2011, and 2015) and of HESS J1640–465 (∼15 hours in 2014), both lying in the FoV of Wd1, and (2) in additional dedicated observations of HESS J1646–458 in 2017. In the latter observations, a large dataset of ∼80 hours (with SM readout enabled in ∼60 hours) was collected.

The combined dataset contains data in three different hardware phases: H.E.S.S. I era, H.E.S.S. II era before H.E.S.S. IU (simply referred to as H.E.S.S. II era), and H.E.S.S. II era with H.E.S.S. IU (simply referred to as H.E.S.S. IU era). As shown by Fig. 9.3a, the dataset contains data taken in a range of different zenith angles between 20° and 65°. Different to the

---

[2]cf. [164] for details about standard data quality selection procedure

a                                    b
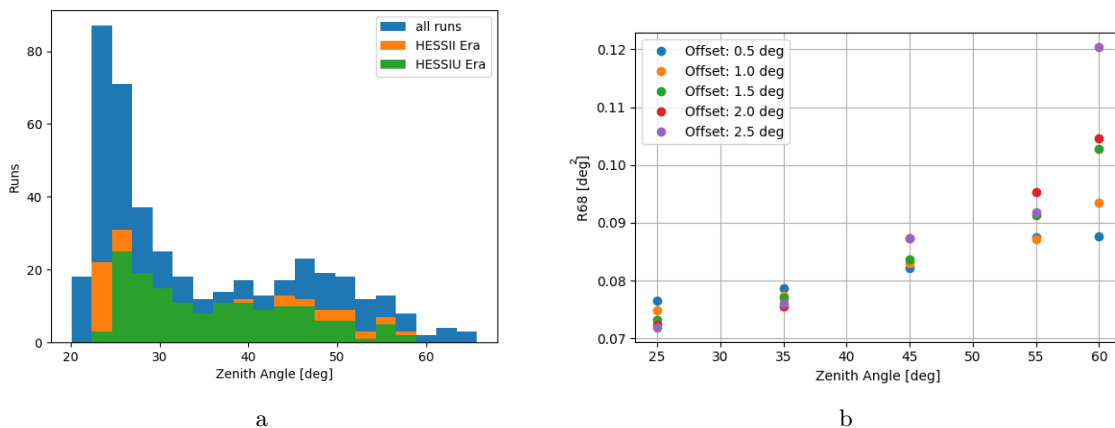
**Figure 9.3** (a) Zenith angle distributions of runs taken on HESS J1646–458, subdivided into different hardware eras. (b) 68% containment radius of the PSF as function of zenith angle for different offsets, deduced from MC simulations. Studies performed and plots provided by R. Rauth (University of Innsbruck).

**Table 9.1** Full HESS J1646–458 dataset after zenith angle and data quality selection cuts applied, grouped by number of runs and hours taken in the three different hardware phases.

| Era | Runs | Hours |
|---|---|---|
| H.E.S.S. I | 172 | 80 |
| H.E.S.S. II | 33 | 15 |
| H.E.S.S. IU | 157 | 73 |

previous analysis presented in [134], a higher cut on zenith angle of $60°$ was used in the data selection procedure for the combined dataset. This is reasonable since the analysis methods have improved significantly since 2012, e.g. thanks to the use of `ImPACT`. As a result, a 68% containment radius of the point spread function (PSF) of $\leq 0.12°$ at $\theta_z = 60°$ (cf. Fig. 9.3b) is still acceptable for the analysis of extended sources. Furthermore, as shown by Fig. 9.4, a cut on $\theta_z = 55°$ was expected to result in an exclusion of $\sim 25\%$ of the events in the highest energy bins, while for a cut on $\theta_z = 60°$, only 10% of those events were expected to be thrown away. As especially the high-energy end of the spectrum is of special interest in the possible identification of HESS J1646–458 as a PeVatron, throwing away a huge fraction at those energies was not desired. Consequently, after the application of the $60°$ zenith angle and the standard data quality selection cuts, a total of $\sim 168$ hours of HESS J1646–458 data remained, five times more than in the previous 2012 analysis. Tab. 9.1 shows how they are grouped by the three different hardware eras.

### 9.2.2 HI and CO data

For a hadronic interpretation of a the VHE $\gamma$-ray emission of HESS J1646–458, the abundances of HI and $H_2$ in the vicicnity of the Wd1 have to be derived from radio observations. HI column densities were extracted from the HI4PI survey. It combines two all-sky HI surveys: the Effelsberg-Bonn HI Survey [165] and the Galactic All-Sky Survey [166]. The survey

a

b
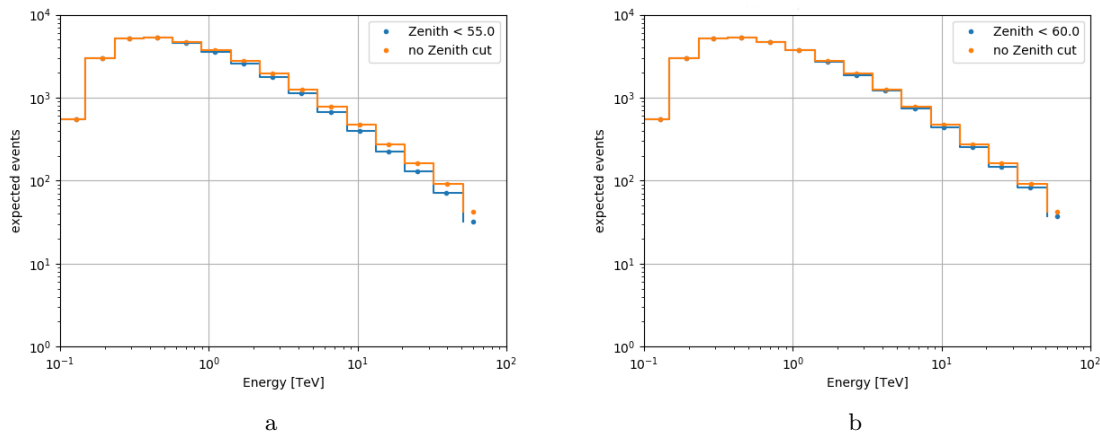
**Figure 9.4** Expected number of events as function of energy without cut on zenith angle (orange histograms) and with cut on (a) $\theta_z = 55°$ and (b) $\theta_z = 60°$ (blue histograms). The number of expected events was calculated from the energy-dependent effective area and exposure convolved with the published spectrum [134] (flux normalisation at 1 TeV of $\Phi_0(1\,\mathrm{TeV}) = 9 \times 10^{-12}\,\mathrm{TeV}^{-1}\,\mathrm{cm}^{-2}\,\mathrm{s}^{-1}$ and spectral index of $\alpha_\gamma = 2.19$). Studies performed and plots provided by R. Rauth.

covers a velocity range from $-600$ to $600$ km/s with a step size of 1.29 km/s. With a map pixel size of 5'×5' and an angular resolution of 16.2', the oversampling factor calculates to $f_{\mathrm{HI4PI}} \simeq 14$ (cf. Eq. 2.60).

New Mopra observations tracing $^{12}$CO (1-0)[3] was used to extract the $H_2$ column densities (following the steps outlined in Sec. 2.3.2). The data is not publicly available but was provided by G. Rowell and C. Snoswell (both from University of Adelaide) for the scope of this work. It covers a solid angle around Wd1 of approximately $\Delta l \times \Delta b = (341 - 338)° \times (0.3 - (-1.3))°$ and a velocity range from $-150$ to $50$ km/s with a step size of 0.088 km/s. Given a map pixel size of 30"×30" and a CO beam size of 0.6', the oversampling factor is $f_{\mathrm{Mopra}} \simeq 1.6$.

As a consistency check, the Mopra data was compared to CO data from (Dame et al., 2001) [167], which was used for multi-wavelength analyses in the 2012 publication of HESS J1646–458 [134]. Fig. 9.5 shows a Mopra CO map with Dame et al. contour lines overlayed (both integrated in the velocity range from $-57$ to $-41$ km/s) for the FoV of Wd1. As expected, both datasets are consistent, with Mopra showing a significantly better spatial resolution. Furthermore, the latter reveals a few additional small-scale CO structure in the near vicinity of Wd1 which promises to enhance the physical interpretation of the observed $\gamma$-ray emission (cf. Sec. 9.3).

## 9.3  New analysis

Thanks to the preparatory work, i.e. the validation of the H.E.S.S. IU MC simulation chain (cf. Ch. 7), IRFs for the H.E.S.S. IU era could be produced enabling the analysis of the combined dataset. Fig. 9.6 shows an excess map using the combined dataset and the background estimation method 3F (cf. Sec. 9.3.1), overplotted with other astronomical objects acting as possible counterparts of the observed VHE $\gamma$-ray emission (cf. Sec. 9.1.2). To avoid contribution from the two pulsars (PSR J1648–4611 and PSR J1650–4601) and from the three

---

[3]As mentioned in Sec. 2.2.2.4, for simplicity, $^{12}$CO (1-0) is referred to CO throughout the thesis.
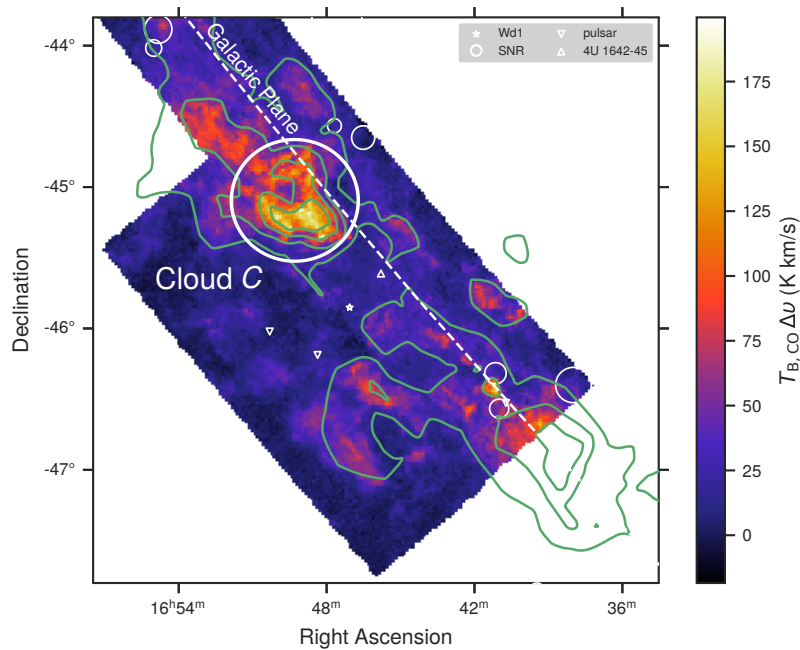
**Figure 9.5** Map showing the CO brightness temperature integrated in the velocity range from $-57$ to $-41$ km/s. The colours show the Mopra data, the contour lines (20, 40, 60, and 80 K km/s) the data from (Dame et al., 2001). The difference in absolute values results from different oversampling factors of both datasets. The positions of Wd1 and other known sources are overplotted and the position of the cloud $\mathcal{C}$ (refer to Sec. 9.3.3 for its definition) is indicated.

other known VHE $\gamma$-ray emitters in the FoV (namely HESS J1641–463, HESS J1640–465, and HESS J1634–472), the regions around them were excluded in the following analyses, such as radial profile investigations (cf. Sec. 9.3.2). The corresponding exclusion regions are overplotted in Fig. 9.6.

### 9.3.1 Gamma ray background estimation studies

Due to the very extended emission (diameter of $\sim 2.2°$) covering about half of the FoV of the H.E.S.S. I telescopes (5°, cf. Sec. 3.2.2), the background subtraction turned out to be difficult. Two different background estimation methods were compared: the AR and the FoV method (cf. Sec. 3.2.5) including different exclusion regions defined in the H.E.S.S. analysis chain. Two different tables with exclusion regions, both based on the known sources from the most-recent HGPS [168] are available in the standard H.E.S.S. analysis: HGPS-standard and HGPS-large. They differ in the radius of the circle used as exclusion region around each source position. In Tab. 9.2, the different combinations of background estimation model and exclusion regions, that were investigated, as well as the resulting mean and width of the significance distribution are listed. For Wd1, the background estimation method 3F, which uses the FoV background estimation method with the HGPS-large table and an additionally defined exclusion region around the centre of HESS J1646–458 with a radius of 1.5°, resulted in the best background estimation with acceptable values for the mean and width of the background distribution. Fig. 9.7 shows the resulting significance map with exclusion regions and the corresponding distributions for this method.
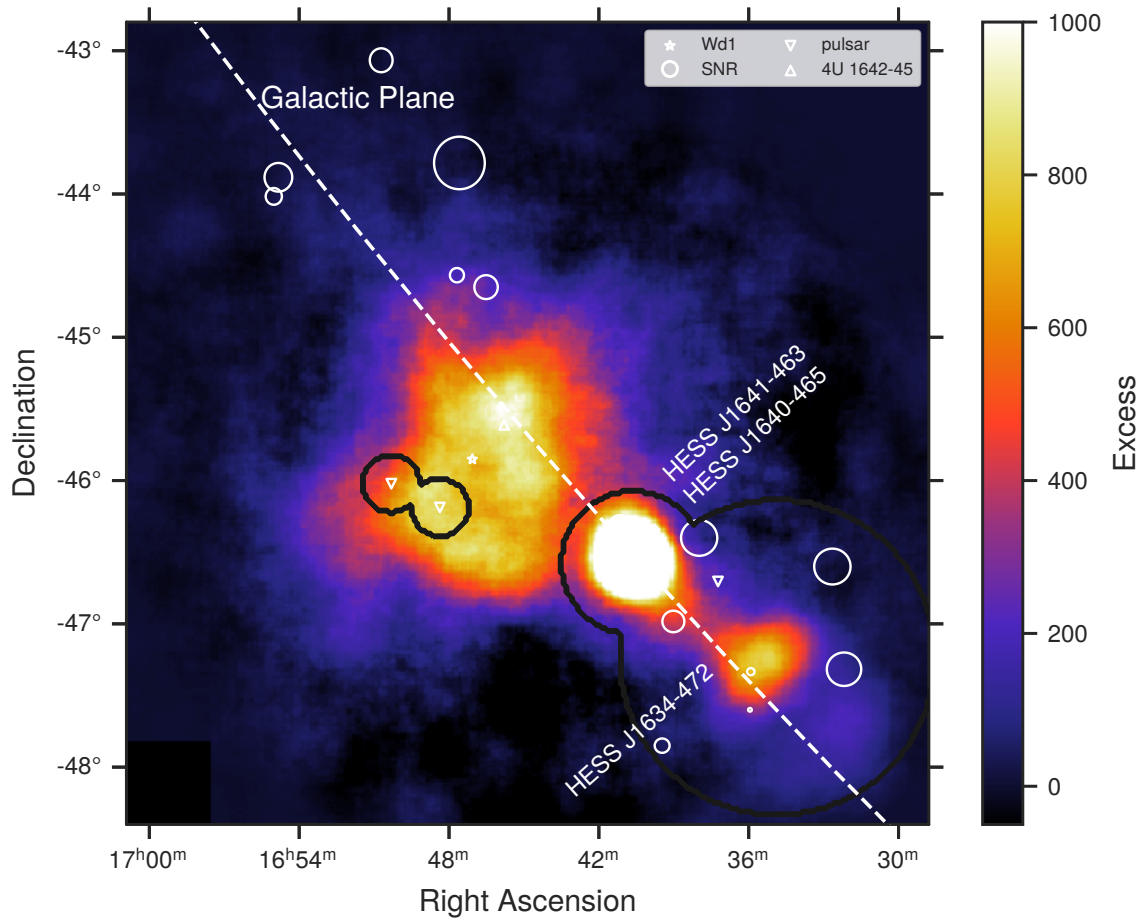
**Figure 9.6** Map showing the $\gamma$-ray excess resulting from all H.E.S.S. data ($\sim$168 hours) taken in the given FoV of HESS J1646–458 in equatorial coordinates. The positions of Wd1, other known objects, and exclusion regions (black circles) used in the following analysis are overplotted.

### 9.3.2 Gamma ray excess and energy dependence

The observation of Wd1 at different offsets and zenith angles resulted in a varying energy threshold over the FoV of Wd1. To prevent systematic effects in the analysis, the same energy threshold should be used for all image pixels. A preliminary study performed by R. Rauth revealed the highest pixel-wise energy threshold to lie at $\sim$350 GeV determining the lowest energy bin to use in the analysis.

Evaluating the excess in different energy bands and comparing the resulting maps and distributions helps in general to investigate the energy dependence of the morphology of the observed VHE $\gamma$-ray emission. For this purpose, six different energy bands were defined and their individual excess computed (cf. Tab. 9.3 for their definitions and statistics).

To measure the radial extent of HESS J1646–458 in each energy band, an approach using the radial profile with the position of Wd1 in the centre was adopted. In the computation of the radial profiles, the previously defined exclusion regions (cf. Fig. 9.6) were used as masks to avoid contamination from the pulsars and known VHE $\gamma$-ray emitters in the FoV. Furthermore, it was particularly important to ensure that any asymmetries in the relative exposure of the dataset to different regions of the sky were taken into account. This was

**Table 9.2** Results of AR and FoV background estimation method with different exclusion regions applied and defined in the H.E.S.S. analysis chain (refer to text for further explanations). Given are the mean and width of the significance distribution extracted from the significance map with exclusion regions.

| Index | Exclusion regions | Background method | Mean | Width |
|---|---|---|---|---|
| 1A | HGPS-standard | AR | 0.18 | 1.40 |
| 1F | HGPS-standard | FoV | −0.19 | 1.29 |
| 2A | HGPS-large | AR | 0.25 | 1.25 |
| 2F | HGPS-large | FoV | −0.18 | 1.21 |
| 3A | HGPS-large + 1.5° around HESS J1646–458 | AR | 0.22 | 1.15 |
| 3F | HGPS-large + 1.5° around HESS J1646–458 | FoV | −0.13 | 1.14 |
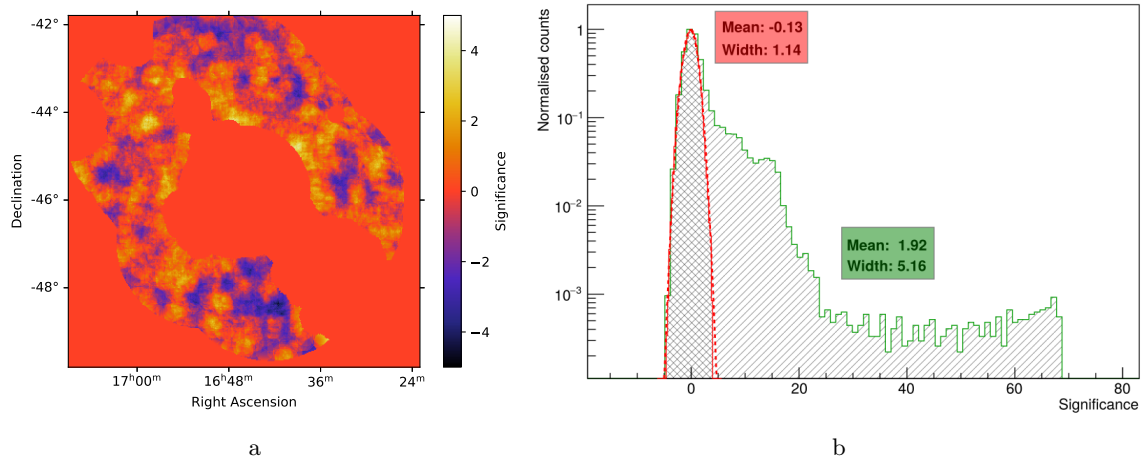


**Figure 9.7** (a) Significance map with exclusion regions and (b) significance distribution extracted from (red) regions used for the background estimation and (green) source region using the background estimation method 3F (cf. Tab. 9.2).

ensured by using acceptance-corrected excess maps[4],[5]. Furthermore, it was important to use uncorrelated acceptance-corrected excess maps to get statistically independent bins in the radial profiles.

The error on the (acceptance-corrected) excess of each pixel in the map was approximated by the error on the number of ON events ($\Delta N_{\mathrm{excess}} \simeq \Delta N_{\mathrm{on}}$). This is a valid method since the FoV background method was used for the evaluation of the excess, for which $\alpha \to 0$ (cf. Sec. 3.2.5). Since the measurement of ON events is a Poisson process, it follows that $\Delta N_{\mathrm{on}} = \sqrt{N_{\mathrm{on}}}$ and hence $\Delta N_{\mathrm{excess}} \simeq \sqrt{N_{\mathrm{on}}}$.

The resulting radial profiles are shown in Fig. 9.8–9.10, alongside with the excess map of each energy band (produced with a correlation radius of $r_{\mathrm{c}} = 0.22$ and overlayed with

---

[4]Since no H.E.S.S. IU radial acceptance look-up tables have been produced yet, the pre-upgrade tables were used. As the upgrade of the H.E.S.S.-I cameras is not expected to affect the radial acceptance, using the old tables is considered as a valid approach.

[5]In acceptance-corrected excess maps, the excess profiles are divided by the acceptance profiles, which provide the number of expected $\gamma$-ray events at a particular position in the sky given the exposure and sensitivity of the dataset.

**Table 9.3** Energy band definitions for the combined Wd1 dataset. Additionally, the corresponding statistics (integrated excess and significance in a 1° circle around Wd1) and the reference to the excess map figures are given.

| Name | Energy range (TeV) | Excess | Significance | Figure |
|------|------|------|------|------|
| Low | 0.35–0.65 | 2710 | 19.6 | 9.8a |
| Medium | 0.65–1.30 | 4639 | 30.1 | 9.8c |
| High | 1.30–5.00 | 3765 | 27.4 | 9.9a |
| Above 5 TeV | >5 TeV | 1109 | 20.3 | 9.9c |
| Above 10 TeV | >10 TeV | 250 | 7.7 | 9.10a |
| Above 20 TeV | >20 TeV | -4 | -0.5 | 9.10c |

significance contours). No radial profile was produced for the energy band "above 20 TeV" due to an insufficient number of excess events. Furthermore, it should be emphasised that the energy bands "above 5 TeV", "above 10 TeV", and "above 20 TeV" overlap. Hence, they are not statistically independent.

The radial profiles of all energy bands have a similar shape being rather irregular in the centre (i.e. close to the Wd1 position) up to a radial distance of $r_{\max}$ of 0.1°–0.4°, then showing a rather regular decrease towards higher radial distances. To determine the extent of the $\gamma$-ray emission region in the five different energy bands, a similar approached as in the analysis of HESS J1825–137 [129, 169] was followed. This means, first a moving average was used to find the radial distance $r_{\max}$, then the radial distributions were fitted with an exponential for distances $> r_{\max}$. The resulting fits and their residuals (defined as $(y_i - f_i)/f_i$, with $y_i$ being the data and $f_i$ the resulting fit values at radial distance $i$) are also shown in Fig. 9.8–9.10. The distance $r_{1/e}$, at which the fitted exponential dropped to the fixed fraction $1/e$ of the peak value, was used as a measure for the radial extent of the $\gamma$-ray emission region[6].

To further study the energy dependence of the radial extent, the resulting dependence of $r_{1/e}$ on the energy (cf. Fig. 9.11) was fitted with two models, while the goodness of the fit was estimated with a $\chi^2$ statistic (giving a $p$-value and a reduced $\chi^2$ value ($\chi^2_{\mathrm{red}}$) for each fit):

- Assuming an energy-independent, constant extent of the source, as would be expected for an underlying hadronic CR population (cf. Sec. 9.4 for more details), the data points in Fig. 9.11 were fitted with a constant resulting in $r_{1/e} \simeq 0.91°$ ($\chi^2_{\mathrm{red}} \simeq 3.38$, $p \simeq 0.01$). This corresponds to $\sim$51 pc at the distance of Wd1.

- Under the assumption of dominating cooling losses, as expected in case of a leptonic CR population[7] (cf. Ch. 2), the radial extent can be expressed by (cf. Eq. 2.44)

$$r_{1/e} \propto E_{\mathrm{e}}^{(\delta-1)/2}, \tag{9.4}$$

with $E_{\mathrm{e}}$ being the energy of the underlying electron population. Furthermore, since $E_{\mathrm{e}} \propto E_{\gamma}^{1/2}$ in case of dominating synchrotron and IC losses (for IC emission in the

---

[6]As in [129, 169], the fraction $1/e$ was chosen since it is often used to estimate typical time or distance scales in physical processes showing exponential dependencies.

[7]The leptonic CR population considered here are electrons and positrons.

a



b



c



d
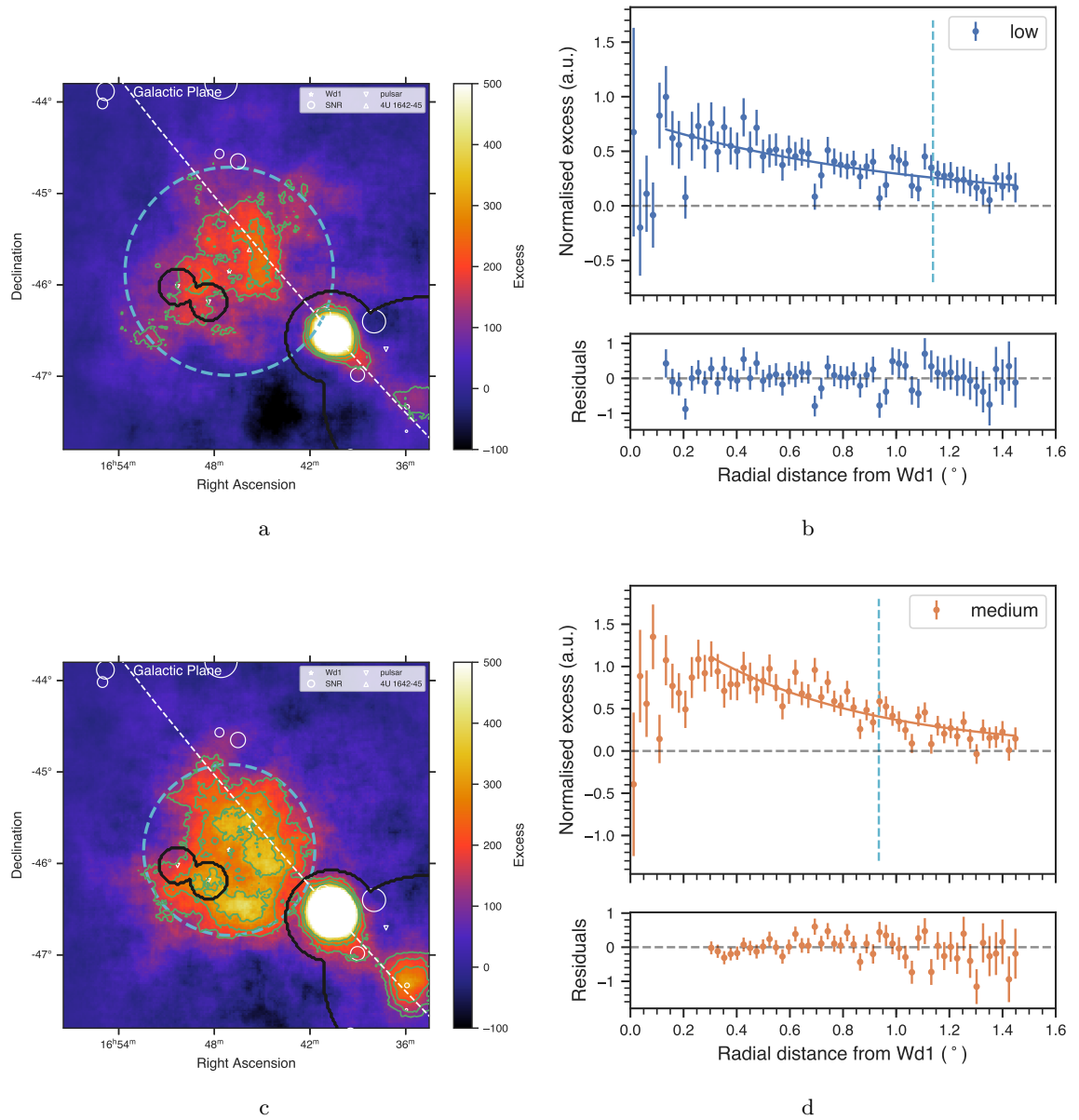
**Figure 9.8** Correlated excess maps alongside with corresponding radial profiles for the (a & b) low and (c & d) medium energy band. In the excess maps, significance contours of (5, 7, and 9) $\sigma$ (in green) are overlayed. Exclusion regions (black circles) and the determined size of the emission (cyan circle with radius $r = r_{1/e}$, refer to text for details) are also shown. In the radial profile plots, the exponential fit (solid line), the resulting residuals (refer to text for a definition), as well as the determined size (dashed cyan line) are shown in addition to the data points.

Thomson regime, cf. Eq. 2.15 & 2.21), it follows that

$$r_{1/e} \propto E_\gamma^{(\delta-1)/4}. \tag{9.5}$$

Thus, the data in Fig. 9.11 was fitted with a power law ($\chi^2_{\mathrm{red}} \simeq 0.86$, $p \simeq 0.46$) yielding a diffusion index of $\delta \simeq 0.5$ as expected for energy-dependent diffusion in the Galaxy (cf. Sec. 2.1.1).

a



b



c



d
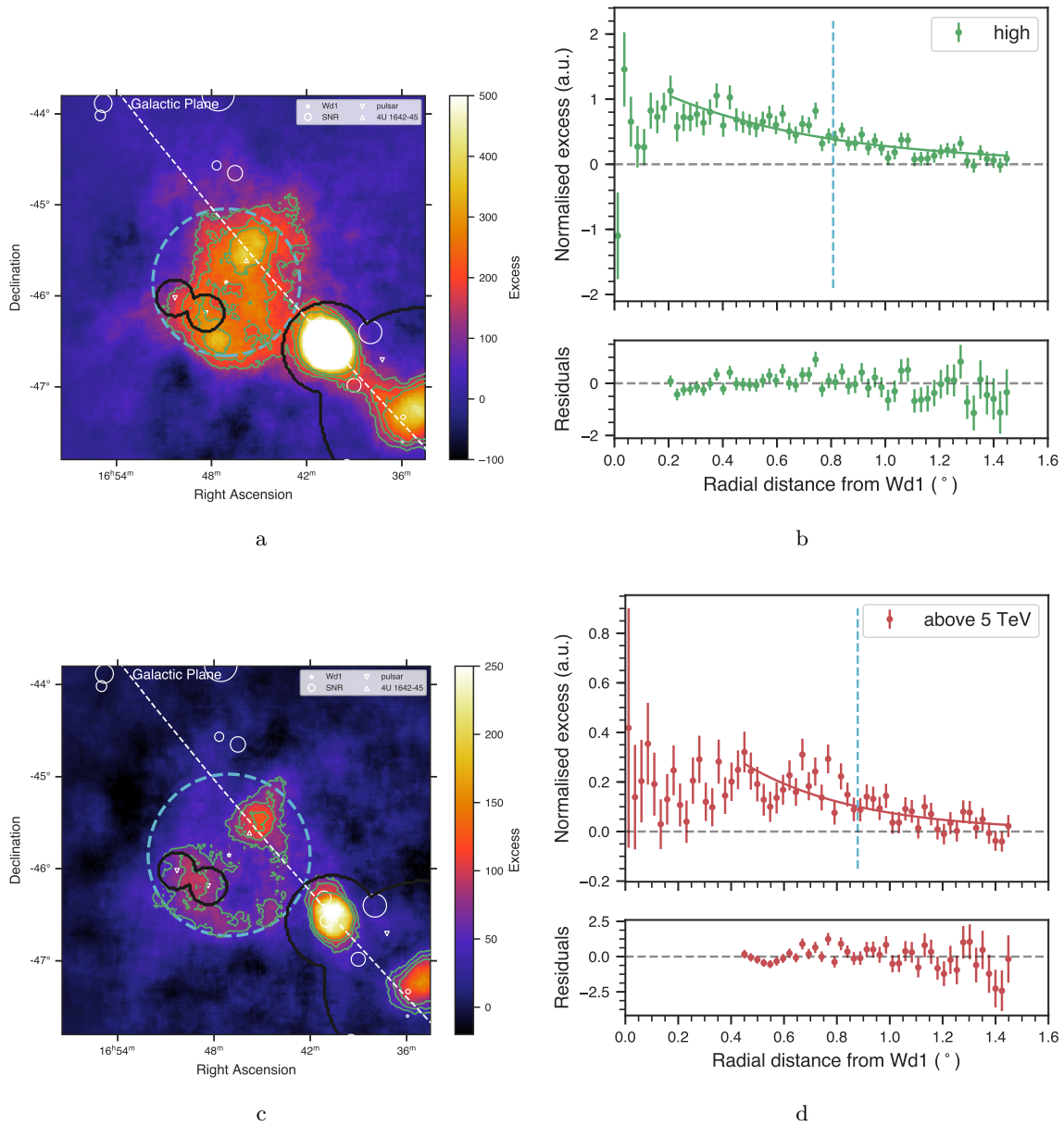
**Figure 9.9** Same as in Fig. 9.8 but for the (a & b) high and (c & d) "above 5 TeV" energy band (colour scale adapted).

A similar study was performed for the PWN HESS J1825–137 [129, 169] which is why it is also shown in Fig. 9.11. Due to the acceleration of electrons and their much faster cooling compared to hadrons, PWNe typically show energy dependencies in their morphology and size as it is the case for HESS J1825–137. The dependence of the radial extent of HESS J1646–458 on the energy might be explainable by both models (cf. Sec. 9.4 for further discussion).

### 9.3.3 Gas distribution

To extract the gas column density from the HI4PI and Mopra data, the steps described in Sec. 2.3.2 were followed. For the HI data, a velocity integration range of $\pm 5$ km/s around the

a



b



c
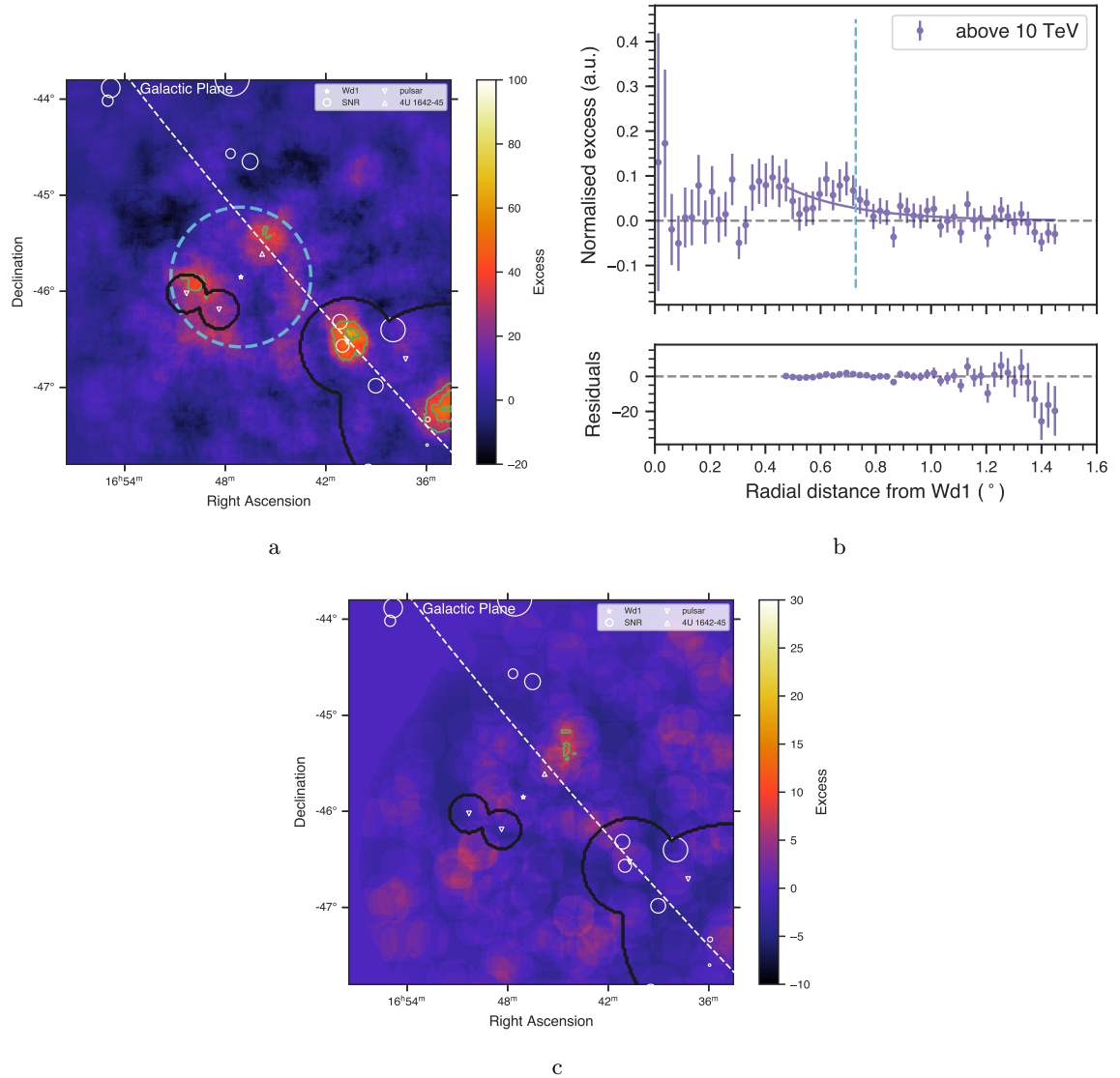
**Figure 9.10** Same as in Fig. 9.8 but for the (a & b) "above 10 TeV" and (c) "above 20 TeV" energy band (colour scale adapted). No radial profile computed and shown for "above 20 TeV" due to insufficient statistics.

expected radial velocity of Wd1 ($-55$ km/s, cf. Sec. 9.1.1) was used. For CO data, the velocity integration range was deduced from the brightness temperature spectrum shown in Fig. 9.12. At least four gas clouds were identified (peaks in the brightness temperature spectrum) in the line of sight of Wd1, one of them at a mean radial velocity of $\sim -41.0$ km/s. This is close to the expected radial velocity of Wd1 which is why that cloud is likely to be located in the vicinity of Wd1. The cloud observed at $r_{\rm J2000} \simeq 16^{\rm h}49^{\rm m}18$ and $d_{\rm J2000} \simeq -45°4'10''$ (referred to as "cloud $\mathcal{C}$", cf. Fig. 9.5) has a diameter of $\sim 0.5°$ corresponding to $\sim 30$ pc at the distance of Wd1. Clouds with such sizes are observed to have typical velocity dispersions of $\sim 5$ km/s [170]. Hence, the CO data was integrated in the velocity range $(-41 \pm 5)$ km/s.

Resulting multi-wavelength maps are shown in Fig. 9.13. Fig. 9.13a shows the H.E.S.S. excess map overlayed with contour lines of HI and $H_2$ column densities (determined from HI4PI
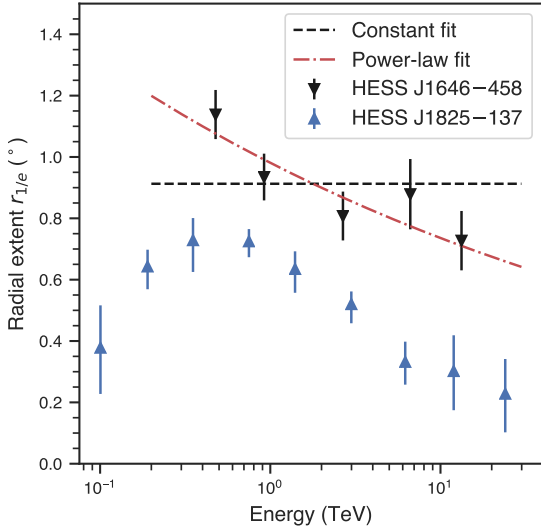
**Figure 9.11** Radial extent $r_{1/e}$ as function of energy for HESS J1646–458 fitted with a constant and a power law, and for HESS J1825–137. For details refer to text.
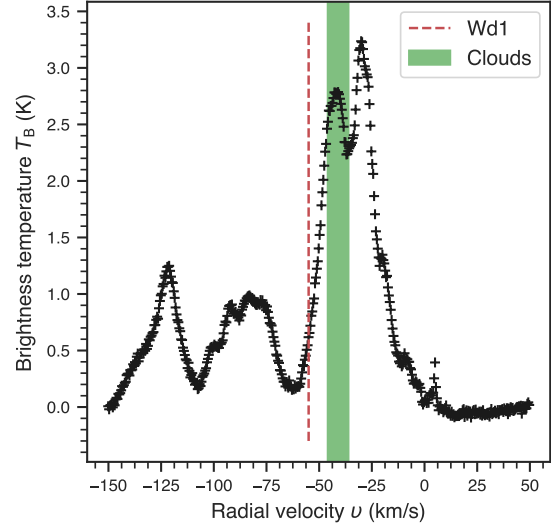
**Figure 9.12** Mopra CO brightness temperature for the Wd1 FoV as function of radial velocity. The red dashed line indicates the expected radial velocity of Wd1, the green band the velocity range used for integration of the CO data.

and Mopra CO brightness temperatures using Eq. 2.58 & 2.59) as well as velocity-integrated Mopra CS flux densities. While the HI data shows features on larger scales distributed over the whole VHE $\gamma$-ray emission region of HESS J1646–458 with an increase towards HESS J1641–463 and HESS J1640–465, $H_2$ was found to be clumped in clouds such as the cloud $\mathcal{C}$ located at the Western edge of that region. The detection of additional CS(1-0) emission in that cloud indicates that it is particularly dense. Fig. 9.13b shows a map for the same FoV with the resulting total hydrogen column density $N_{\mathrm{H,total}}(l,b) = N_{\mathrm{HI}}(l,b) + 2\,N_{\mathrm{H_2}}(l,b)$ overlayed with H.E.S.S. significance contours.

Dividing $N_{\mathrm{H,total}}$ by the expected diameter of the region (in $z$-direction), assumed to be in the order of 100 pc, resulted in an estimate for the particle number density $n_{\mathrm{H,total}}$ with a mean of $\sim$15 cm$^{-3}$, similar to what was reported in the 2012 publication [134]. A radial profile of $n_{\mathrm{H,total}}$ w.r.t. the Wd1 position (cf. Fig. 9.14) revealed an SpB-like structure with a radius of $R_{\mathrm{SpB}} \simeq 39$ pc, which is of similar size as the feature B3 that was observed in [142] (cf. Sec. 9.1.1).

### 9.3.4 Hadronic cosmic ray density and total cosmic ray energy

To study the distribution of the hadronic CR energy density $\omega_{\mathrm{CR}}(\geq E_{\mathrm{CR}})$ for CRs with energies $> E_{\mathrm{CR}}$, the VHE $\gamma$-ray excess map was divided by the total H (gas) map resulting in a CR density map (cf. Fig. 9.15a). To calculate absolute values for $\omega_{\mathrm{CR}}(\geq E_{\mathrm{CR}})$ following Eq. 2.53, preliminary analyses of the $\gamma$-ray spectrum of HESS J1646–458, performed by E. O. Angüner (University of Aix Marseille), were used. In that analyses, HESS J1646–458 was divided into 12 subregions (squares with edge lengths of 0.4°, cf. Fig. 9.16) for which the spectra and their characteristics, such as flux normalisation and spectral index were determined separately (cf. Tab. 9.4). Due to the energy threshold of 350 GeV used in the analysis of HESS J1646–458 (cf. Sec. 9.3.2), being compatible with the fit range used by

a



b
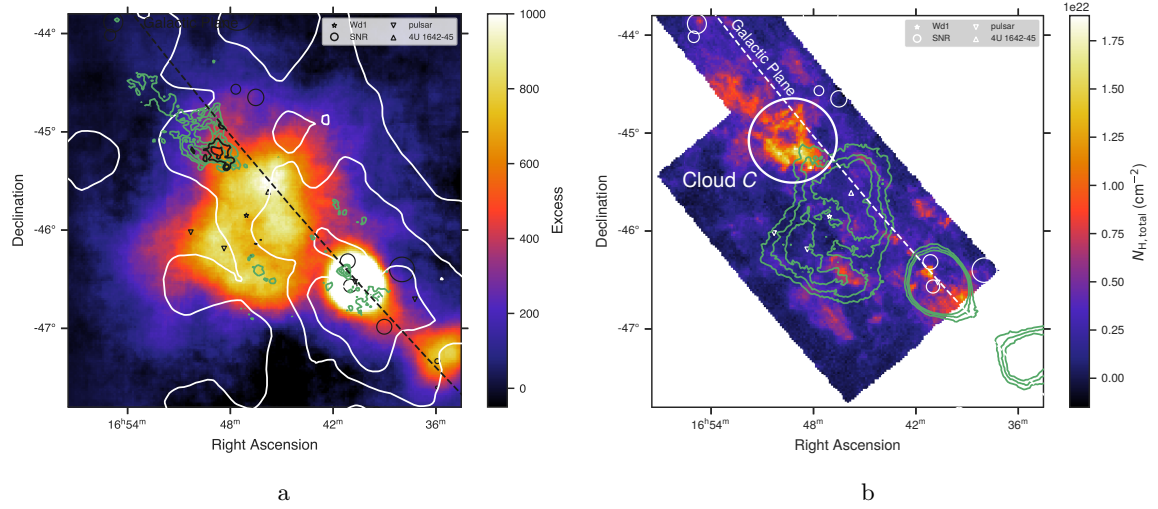
**Figure 9.13** Maps showing the FoV of HESS J1646–458 with (a) the VHE $\gamma$-ray excess overlayed with white, green, and black contours showing the HI (0.4, 0.7, and 1.0)$\times 10^{20}$ cm$^{-2}$ and H$_2$ (0.7, 1.1, and 1.3)$\times 10^{22}$ cm$^{-2}$ column densities as well as the velocity-integrated CS flux densities (3, 6, and 9) Jy/beam km/s, and (b) the total hydrogen column density $N_{\text{H,total}}$, overlayed with H.E.S.S. significance contours (11, 13, and 15) $\sigma$ in green and the position of the cloud $\mathcal{C}$.

E. O. Angüner in his spectral analyses, the CR density was determined for $\gamma$-ray energies $> E_\gamma = 350$ GeV, i.e. for CR energies $> E_{\text{CR}} = 10\,E_\gamma = 3.5$ TeV.

With the knowledge of the $\gamma$-ray spectrum, the $\gamma$-ray luminosity $L_{\gamma,i}(\geq 350\,\text{GeV})$ of each subregion $i$ (following Eq. 2.54) and the average luminosity, normalised to the solid angle of the subregions $\Omega_{\text{sub}}$, were determined. This resulted in[8]

$$L_\gamma(\geq 350\,\text{GeV}) = \frac{\sum_{i=1}^{12} L_{\gamma,i}(\geq 350\,\text{GeV})}{12\,\Omega_{\text{sub}}} = (3.2 \pm 0.6) \times 10^{34}\,\text{erg/(s\,deg}^2). \tag{9.6}$$

The gas mass, located in the vicinity of Wd1, was determined in a solid angle of $0.7° \times 0.7°$ around Wd1 (following Eq. 2.57), resulting in $M_{\text{H}} = (1.389 \pm 0.003) \times 10^5\,M_\odot/\text{deg}^2$. Hence, using Eq. 2.53 (with $\eta = 1.5$), the mean CR density for the vicinity of Wd1 was calculated to be

$$\omega_{\text{CR}}(\geq 3.5\,\text{TeV}) = (0.44 \pm 0.09)\,\text{eV/cm}^3, \tag{9.7}$$

resulting in an CR enhancement factor of $k = 97 \pm 8$ (cf. Eq. 2.55).

For the investigation of the radial distribution of the CR density, a radial profile was produced from the CR density map (cf. Fig. 9.15a) and scaled with $\omega_{\text{CR}}(\geq 3.5\,\text{TeV})$. It is shown in Fig. 9.15b together with two different models the radial distribution was fitted with reflecting underlying source scenarios:

1. In case of a steady-state acceleration of CRs within Wd1 which then diffuse away into the ISM, a radial distribution following a $1/r$-dependence would be expected (cf. Sec. 2.2.2.3). As the shown radial profile is a 2D-projection, the fit function used

---

[8]The stated uncertainties in the calculations are the systematic errors resulting from the spectral fits in the analysis of E. O. Angüner.
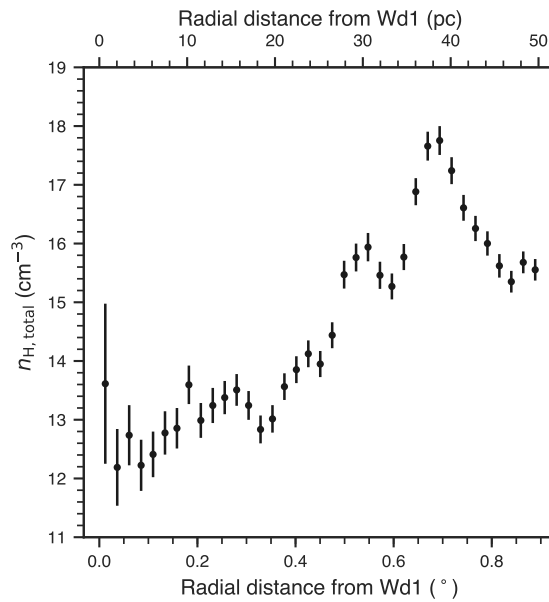
**Figure 9.14** Gas (total hydrogen) particle density $n_{\mathrm{H,total}}$ as function of the radial distance to Wd1 in degree and pc, deduced from the total hydrogen column density $N_{\mathrm{H,total}}$ and under the assumption of a uniformly distributed target material in the direction of the line of sight. .

for this scenario is a projected $1/r$-profile, given by [47]

$$f(r) = A \, \frac{\log\left(\frac{r_0 + \sqrt{r_0^2 - r^2}}{r}\right)}{\sqrt{r_0^2 - r^2}}, \tag{9.8}$$

with $A$ being a normalisation factor and $r_0$ a size scale of the emission region.

2. In case of a burst-like injection of CRs from an SN followed by CR acceleration in the vicinity of the SNR, particles are expected to leave the acceleration site after some time and diffuse away. Hence, the radial distribution is expected to have a Gaussian shape which was used as a fit function in this scenario.

With the assumption that the VHE $\gamma$-ray emission, observed at the position of cloud $\mathcal{C}$, results from hadronic interactions of CRs with the gas in that cloud, an upper limit on the CR density within that cloud could be inferred. For this purpose, the $\gamma$-ray luminosity of subregion 4A in Fig. 9.16 (being approximately spatially coincident with the position of cloud $\mathcal{C}$) and the gas mass $M_{\mathrm{cloud}}$ for that region were determined. With $L_{\gamma,4\mathrm{A}}(\geq 350\,\mathrm{GeV}) = (3.6 \pm 1.1) \times 10^{34}\,\mathrm{erg/(s\,deg^2)}$ and $M_{\mathrm{cloud}} = (2.876 \pm 0.010) \times 10^5\,M_\odot/\mathrm{deg}^2$, an upper limit for the CR density of

$$\omega_{\mathrm{CR,cloud}}(\geq 3.5\,\mathrm{TeV}) \leq (0.22 \pm 0.07)\,\mathrm{eV/cm^3} \tag{9.9}$$

and for the CR enhancement factor of $k_{\mathrm{CR,cloud}} \leq 26 \pm 8$ was calculated. To use this value for a possible constraint on one of the fit models shown in Fig. 9.15b, a radial distance range for the cloud $\mathcal{C}$ from Wd1 was determined. The minimum distance is given by the angular separation of $\sim 0.65°$, corresponding to $d_{\mathrm{min}} \simeq 36\,\mathrm{pc}$ at the distance of Wd1. To determine an estimate for the maximum distance $d_{\mathrm{max}}$, the difference in mean radial velocity of the
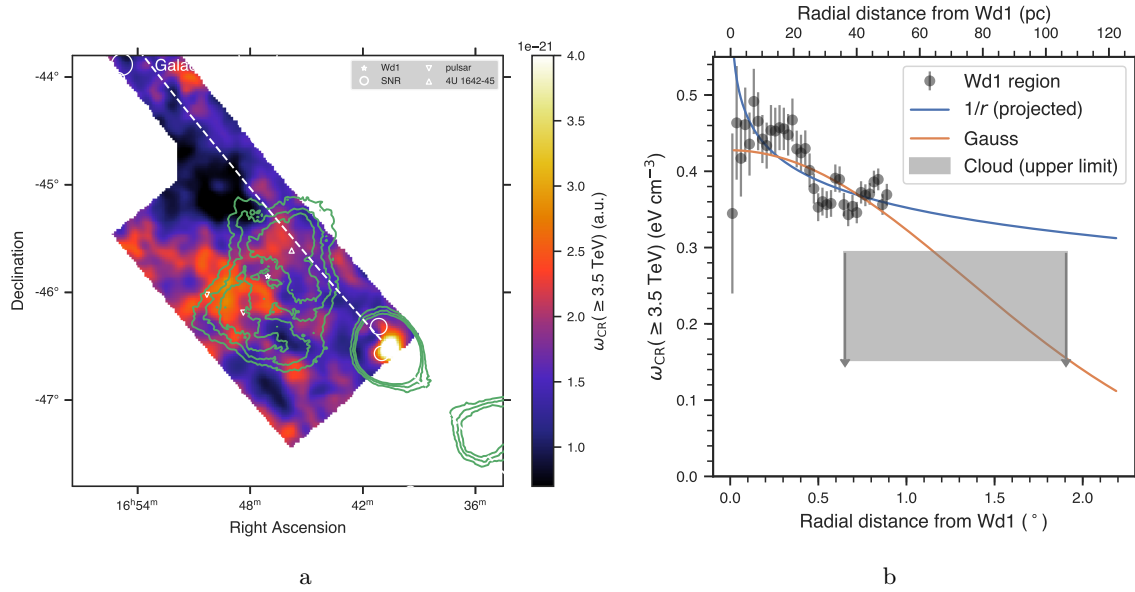
**Figure 9.15** (a) Map showing the CR density $\omega_{\mathrm{CR}}(\geq 3.5\,\mathrm{TeV})$ for the FoV of Wd1 overlayed with H.E.S.S. significance contours (11, 13, and 15) $\sigma$ in green. (b) $\omega_{\mathrm{CR}}(\geq 3.5\,\mathrm{TeV})$ as function of the radial distance to Wd1 in degree and pc (errorbars showing statistical errors). Also shown are a projected $1/r$- and Gaussian fit to $\omega_{\mathrm{CR}}(\geq 3.5\,\mathrm{TeV})$, as well as the upper limit deduced from the $\gamma$-ray emission observed at the position of the cloud. Refer to text for more details.

cloud ($-41.0$ km/s, cf. Fig. 9.12) and the expected radial velocity of Wd1 ($-55$ km/s) was calculated and then converted to a distance $d_{\mathrm{Wd1-cloud}} \simeq 100$ pc (using the Galactic rotation curve model given in [142]). Hence, $d_{\mathrm{max}} = \sqrt{d_{\mathrm{min}}^2 + d_{\mathrm{Wd1-cloud}}^2} \simeq 106$ pc. The resulting upper limit for the CR density within the cloud for the range of possible distances between $d_{\mathrm{min}}$ and $d_{\mathrm{max}}$ is indicated in Fig. 9.15b.

The total CR energy confined inside HESS J1646–458 was determined by integrating the $\omega_{\mathrm{CR}}(\geq 3.5\,\mathrm{TeV})$ in a spherical volume around Wd1 with a radius of $0.91°$ (51 pc), which is the size of the VHE $\gamma$-ray emission region determined in Sec. 9.3.2. This revealed a total CR energy of

$$W_{\mathrm{CR}}(\geq 3.5\,\mathrm{TeV}) = (1.1 \pm 0.2) \times 10^{49}\,\mathrm{erg}. \tag{9.10}$$

Assuming the same spectral index of the observed VHE $\gamma$-ray emission down to $E_\gamma = 1$ GeV, the total CR energy associated with HESS J1646–458 is $W_{\mathrm{CR}}(\geq 10\,\mathrm{GeV}) \simeq 3.1 \times 10^{50}$ erg.

## 9.4 Discussion of different scenarios

The results presented in the previous section mainly offer three different scenarios for the origin of the extended VHE $\gamma$-ray emission of HESS J1646–458. Fig. 9.17 shows a flowchart illustrating the procedure to identify the underlying physical processes and astronomical objects in case of an observation of an extended Galactic VHE $\gamma$-ray source in the direction of an SC in general and applied to HESS J1646–458 and Wd1 in particular. The following discussion will follow the logic of that diagram.

The energy dependence of the morphology of an observed VHE $\gamma$-ray emission is typically used for the discrimination between a hadronic and a leptonic underlying CR population. In case of the latter, the size of the observed VHE $\gamma$-ray emission region is typically expected
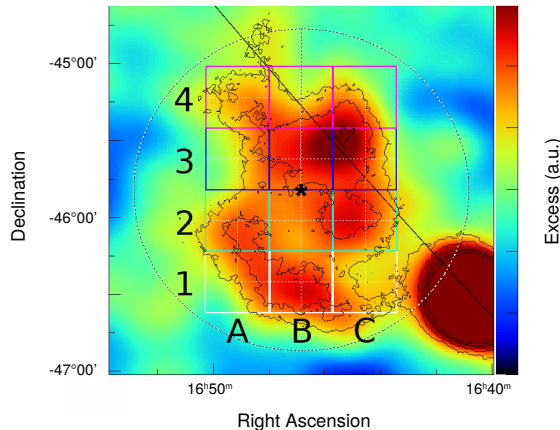
**Figure 9.16** Excess map of HESS J1646–458 (excess given by the colour scale in arbitrary units) with 12 subregions indicated that were used in the spectral analysis performed by E. O. Angüner, overlayed with H.E.S.S. significance (5, 7, 10, and 12) $\sigma$ contours and a dotted circle of radius 1° around Wd1 (indicated by the asterisk). Reproduced from a plot provided by E. O. Angüner.

to decrease with increasing energy due to the increasing cooling losses of electrons with energy (cf. Ch. 2). Even though the morphology of HESS J1646–458 has not yet been fully investigated, its energy dependence was estimated by the energy dependence of the radial extent of the source. From the $\chi^2$ statistic of the corresponding fits (cf. Sec. 9.3.2), a decrease of the radial extent with energy seems more likely, however, a constant, energy-independent radial extent cannot be excluded. Hence both, a leptonic and a hadronic scenario are possible and will be discussed in the following subsections.

### 9.4.1 Leptonic scenario

Several questions need to be addressed to estimate the likelihood of HESS J1646–458 being associated with a leptonic scenario, i.e. with a PWN.

**Pulsar(s) in the FoV?** Two pulsars are located in the FoV of HESS J1646–458 (cf. Sec. 9.1.2): PSR J1648–4611 and PSR J1650–4601.

**Resulting values for the diffusion of electrons sensible?** The published VHE $\gamma$-ray spectrum of HESS J1646–458 [134] extends up to energies of ~10 TeV. If this was caused by VHE electrons IC-scattered off CMB photons ($E_{\rm CMB} \simeq 6 \times 10^{-4}$ eV, $u_{\rm CMB} \simeq 0.25$ eV/cm$^3$), the underlying electrons would have energies of ~22 TeV (cf. Eq. 2.21). The corresponding synchrotron cooling time (assuming a typical Galactic $B$-field of 4 $\mu$G) and IC cooling time would have values of $\tau_{\rm sync} \simeq 33.4$ kyr and $\tau_{\rm IC} \simeq 53.4$ kyr, resulting in a combined cooling time of $\tau_{\rm cool} \simeq 20.5$ kyr (cf. Eq. 2.43). Furthermore, with the power-law fit to the radial extent (cf. Sec. 9.3.2), the radial extent at 10 TeV can be estimated to be $r_{1/e}(E_\gamma = 10\,{\rm TeV}) \simeq$ 41 pc. With Eq. 2.8 the diffusion coefficient can further be determined giving a value of $D(E_{\rm e} = 22\,{\rm TeV}) \simeq 6.2 \times 10^{27}$ cm$^2$/s. This value is similar to the diffusion coefficient of $\simeq$ $2.7 \times 10^{27}$ cm$^2$/s that was measured for the PWN Geminga [30][9] what suggests commonalities

---

[9]The value of the diffusion coefficient for Geminga at 22 TeV was derived using Eq. 2.9 and the values of $D_0 = 4.5 \times 10^{27}$ cm$^2$/s at $E_0 = 100$ TeV and $\delta = 1/3$ taken from the publication [30].

**Table 9.4** Results of preliminary spectral analyses (performed by E. O. Angüner) for the 12 subregions of HESS J1646–458 defined in Fig. 9.16. Listed are flux normalisation $\Phi_0$ at 1 TeV in units of $(10^{-13}\,\mathrm{cm}^{-2}\,\mathrm{s}^{-1}\,\mathrm{TeV}^{-1})$, spectral index $\alpha_\gamma$, and their systematic errors $\Delta\Phi_0$ and $\Delta\alpha_\gamma$.

| Subregion | $\Phi_0$ | $\Delta\Phi_0$ | $\alpha_\gamma$ | $\Delta\alpha_\gamma$ |
|---|---|---|---|---|
| 1A | 7.22 | 1.22 | 2.1349 | 0.0963 |
| 1B | 5.65 | 1.54 | 2.9633 | 0.4209 |
| 1C | 4.14 | 1.21 | 2.3055 | 0.1997 |
| 2A | 8.68 | 1.34 | 2.3539 | 0.1152 |
| 2B | 3.59 | 1.35 | 2.1907 | 0.2455 |
| 2C | 4.93 | 1.32 | 2.6777 | 0.2792 |
| 3A | 5.94 | 1.23 | 2.2889 | 0.1324 |
| 3B | 5.36 | 1.47 | 2.7878 | 0.422 |
| 3C | 7.82 | 1.36 | 2.5177 | 0.1563 |
| 4A | 3.65 | 1.14 | 2.1463 | 0.1605 |
| 4B | 4.5 | 1.35 | 2.1902 | 0.1631 |
| 4C | 4.73 | 1.35 | 2.6765 | 0.2948 |

between both VHE $\gamma$-ray sources. Geminga is a very extended ($\sim 5.5°$) TeV-source of leptonic origin at a distance of $\sim 250$ pc and hence of similar size ($\sim 24$ pc) as HESS J1646–458 ($\sim 51$ pc or $\sim 78$ pc for HESS J1646–458, associated with either Wd1 or PSR J1648–4611).

The derived values for the electron cooling time and diffusion coefficient for HESS J1646–458 are therefore not only sensible but suggest similarities between HESS J1646–458 and the PWN Geminga.

**Pulsar energetics enough?** Using the observed $\gamma$-ray luminosity $L_\gamma(\geq 350\,\mathrm{GeV}) \simeq 3.2 \times 10^{34}$ erg/s (cf. Eq. 9.6) and the cooling time $\tau_{\mathrm{cool}} \simeq 64.9$ kyr of electrons producing $\gamma$-rays with TeV energies (with the same $B$-field and radiation fields as above), yields an estimate for the total electron energy of $W_{\mathrm{e}} \simeq 6.5 \times 10^{46}$ erg (cf. Eq. 2.42).

Given the spin-down power of $\dot{E} \leq 3 \times 10^{33}$ erg/s and a maximum estimated age of 90 kyr (cf. Sec. 9.1.1), resulting in a total released energy of $\sim 8 \times 10^{45}$ erg, CXO J164710.2–455216 cannot explain the observed $\gamma$-ray luminosity. However, with the expected number of about 100 SNe that might have exploded since the formation of Wd1 (cf. Sec. 9.1.1), the existence of another compact object within Wd1, not yet detected and associated with a pulsar is possible. To be able to explain the measured VHE $\gamma$-ray luminosity, it should have an age of $\mathcal{O}(10\,\mathrm{kyr})$ and a spin-down power of $\mathcal{O}(10^{35}\,\mathrm{erg/s})$.

On the other hand, if Wd1 was not responsible for the observed emission of HESS J1646–458 and only by coincidence located in the line of sight, the emission could also energetically be explained by a PWN powered by one of the pulsars, PSR J1648–4611 or PSR J1650–4601. Scaling the observed $\gamma$-ray luminosity of $L_\gamma(\geq 350\,\mathrm{GeV})$ (cf. Eq. 9.6) to the distance of PSR J1648-4611 (4.9 kpc, cf. Sec. 9.1.2), the total electron energy of $W_{\mathrm{e}}(E_\gamma \geq 350\,\mathrm{GeV}) \simeq 1.5 \times 10^{47}$ erg is by a factor $\sim 5$ smaller than the released energy of PSR J1648–4611, being $\sim 7.25 \times 10^{47}$ erg. Hence, assuming a high conversion efficiency $\epsilon$[10], PSR J1648–4611 might energetically be able to explain the observed VHE $\gamma$-ray emission. Similar considerations

---

[10]The conversion efficiency is defined as how efficient the released energy of an object is converted into CRs.
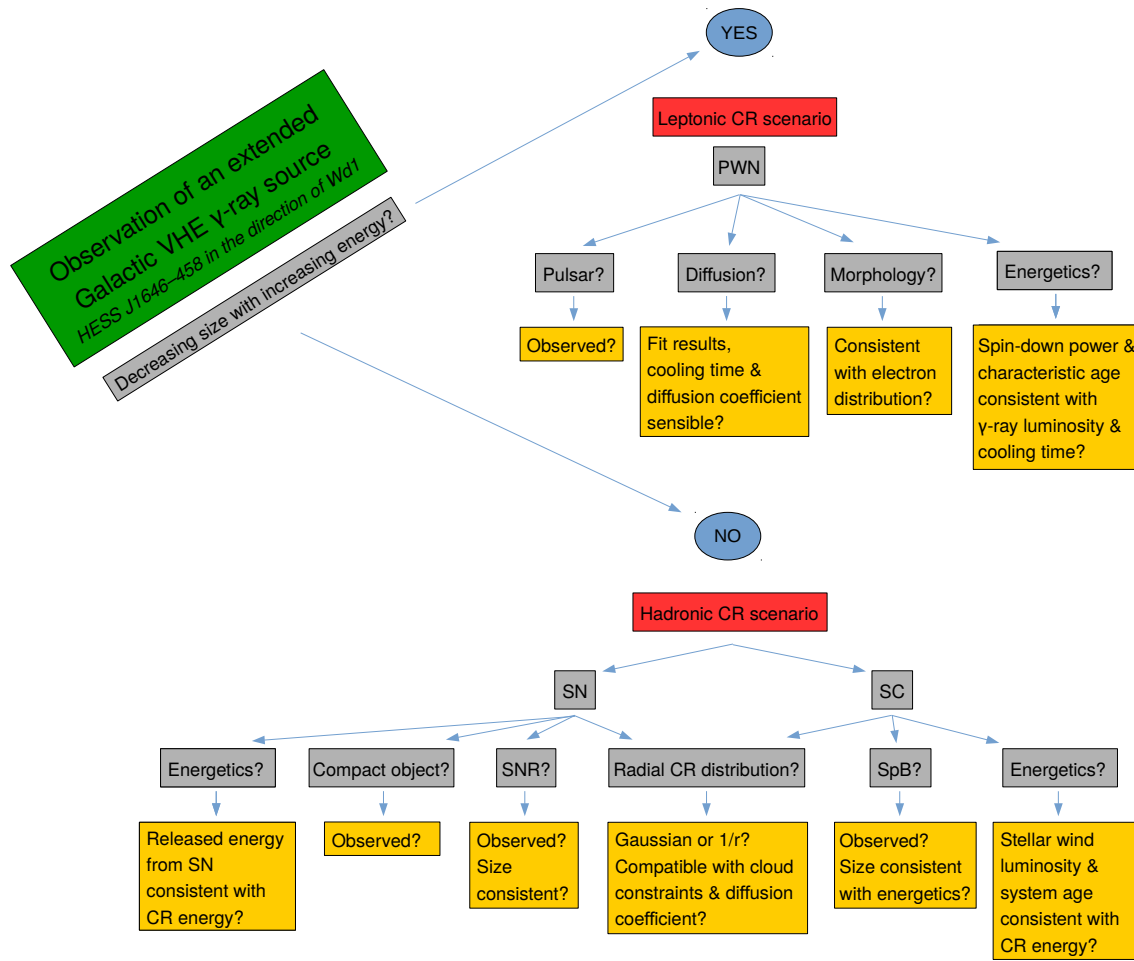
**Figure 9.17** Flowchart illustrating the procedure followed in this analysis to identify the origin of the extended VHE $\gamma$-ray emission from HESS J1646–458. Acronyms are defined as: PWN: pulsar wind nebula, SN: supernova, SNR: supernova remnant, SC: stellar cluster, SpB: superbubble. For more details and answers to the different questions refer to text.

in case of PSR J1650–4601, assuming it to be at the same distance as Wd1[11], resulted in a required conversion efficiency of 5% (given the total released energy of $\sim$1.84 $\times 10^{48}$ erg and the deduced total electron energy of $W_{\mathrm{e}} \simeq 6.5 \times 10^{46}$ erg as mentioned above). However, as no distance estimation for this pulsar exists yet, there is a very high uncertainty on this value.

**Morphology?**  The bolometric stellar radiation luminosity $L_{\mathrm{rad,SC}}$ of an SC is typically in the order of $\sim$500 $L_{\mathrm{wind,SC}}$ [171], resulting in $L_{\mathrm{rad,Wd1}} \simeq 2 \times 10^{41}$ erg/s in case of Wd1. Thus, the thermal radiation density of Wd1 is

$$u_{\mathrm{rad,Wd1}} = \frac{L_{\mathrm{rad,Wd1}}}{\pi\, c\, R^2} \simeq 34.8\,\mathrm{keV/cm^3} \tag{9.11}$$

---

[11]The distance of PSR J1650–4601 is not known (cf. Sec. 9.1.2) which is why it was arbitrarily positioned at the distance of Wd1 for this study.

(with $R \simeq 2$ pc being the radius of Wd1 (cf. Sec. 9.1.1) and $c$ the velocity of light)[12]. Assuming a nominal $1/r^2$-decline with distance, $u_{\mathrm{rad,Wd1}}$ reaches a typical energy density of 1 eV/cm$^3$ at a distance of $\sim$373 pc from Wd1. Hence, if Wd1 was responsible for the observed emission of HESS J1646–458 in a leptonic scenario, the IC losses by scattering off star light should dominate the $\gamma$-ray production towards the centre of HESS J1646–458 which in turn should result in a sharp increase in the radial $\gamma$-ray distribution. However, the morphology of HESS J1646–458 rather suggests a plateau or in some energy bins even a cavity at the position of Wd1 (cf. Sec. 9.3.2). This is therefore an argument against the association of Wd1 with a leptonic scenario.

If instead one of the pulsars (PSR J1648–4611 or PSR J1650–4601) was associated with HESS J1646–458, the observed morphology may be explainable as it is similar to the plateau-like structure that is seen, for example, in the radial profile of the PWN HESS J1825–137 [129, 169]. Furthermore, also the displacement of the pulsar from the centre of the VHE $\gamma$-ray emission[13] of about 0.3°, corresponding to 26 pc at the pulsar distance, is similar to the displacement of PSR B1823–13 from HESS J1825–137.

**Summary** In case of an underlying electron population, the association of HESS J1646–458 with Wd1 seems unlikely since this would imply a sharp increase in the VHE $\gamma$-ray emission towards Wd1 what has not been observed. However, an association with one of the two pulsars (PSR J1648–4611 or PSR J1650–4601), located in the same direction as Wd1 and HESS J1646–458, seems possible even though it would be a very rare coincidence if the observed emission, perfectly aligned with Wd1, was only associated with a pulsar and not at all with Wd1.

## 9.4.2 Hadronic scenario

If the VHE $\gamma$-ray emission of HESS J1646–458 was of hadronic origin, basically two underlying source scenarios, both associated with Wd1, are likely and discussed in the following subsections, addressing the questions outlined in Fig. 9.17.

### 9.4.2.1 Supernova in Westerlund 1

**Compact object found?** The magnetar CXO J164710.2–455216 was found to be located within Wd1 and is expected to have formed in the SN explosion of a very massive star with $M > 40\,M_\odot$ about 65–90 kyr ago (cf. Sec. 9.1.1).

**Released SN energy enough?** The typical energy transferred onto an SNR in an SN is assumed to be of the order of $10^{51}$ erg. Given the high mass of the progenitor star of CXO J164710.2–455216, the released SN and therefore the SNR energy might even be higher than in typical SNe. Given the total observed CR energy of $W_{\mathrm{CR}}(\geq 3.5\,\mathrm{TeV}) \simeq 1.1 \times 10^{49}$ erg (observed) and $W_{\mathrm{CR}}(\geq 10\,\mathrm{GeV}) \simeq 3.1 \times 10^{50}$ erg (expected, cf. Sec. 9.3.4), $\lesssim$10% of the SNR should have been transferred onto CRs to explain the VHE $\gamma$-ray emission of HESS J1646–458.

---

[12]More in detail, Eq. 9.11 results from the thermal stellar radiation luminosity, given by $L_{\mathrm{rad}} = 4\,\pi\,R^2\,\sigma\,T^4$ with $\sigma$ being the Stefan-Boltzmann constant and $T$ the stellar temperature, combined with the energy density of radiation in thermodynamic equilibrium, given by $u = 4\,\sigma\,T^4/c$.

[13]As explained in Sec. 2.2.2.2, such as displacement is expected due to the pulsar's net drift velocity at its birth and asymmetric crushing effects in the PWN.

**SNR observed?**   In case of an isolated SNR with an age of 65–90 kyr, its shell is expected to lie at a radial distance of about 20 pc (cf. Eq. 2.35). This may actually be the origin of the plateau-like structure observed in the radial CR distribution (cf. Fig. 9.15b) reaching up to ∼20 pc. However, considering the fact, that the SNR is expected to evolve in an SpB, even assuming very high ejecta masses in the order of the mass of the progenitor star, it should have already entered the Sedov-Taylor phase after latest ∼30–40 kyr (cf. Eq. 2.51) and its current size should be of the order of 70–80 pc (cf. Eq. 2.52).

In any case, an evidence for an SNR shell surrounding Wd1 at either of those distances has not been observed yet in other wavelengths. However, this may be expected since due to the low gas density inside an SpB, the appearance and therefore the detectability of an SNR might be significantly different. In some studies (e.q. [150, 172]), the authors argue that a typical radio and X-ray SNR should not be expected when an SN occurs in an evacuated cavity, such as the SpB of an SC, as long as the remnant has not encounter the boundaries of the SpB itself. Now, following this argument, if the SpB radius was given by the size of the observed gas cavity $R_{SpB} \simeq 39$ pc (cf. Sec. 9.3.3), the SNR should have already catched up with the SpB shell and an SNR-like structure would be expected to be observable at this distance also in other wavelengths. But, if the SpB size was at the distance as expected from the assumed superwind luminosity, i.e. at∼124–153 pc (cf. Sec. 9.4.2.2), the SNR would not yet have reached the SpB edge what may explain why an SNR has not been observed yet.

**Radial CR distribution compatible with expectations?**   As explained in Sec. 9.3.4, the CR distribution is expected to follow a Gaussian shape in this scenario. The fit does not only show to be consistent with the data but also includes the upper limits on the CR density, set by the VHE $\gamma$-ray observations from the direction of the cloud $\mathcal{C}$ (cf. Sec. 9.3.4, Fig. 9.15b).

Furthermore, if the CR distribution was explained by the SN related to the formation of the magnetar CXO J164710.2–455216, its expected age of $t = 65$–90 kyr and the width of the fitted Gaussian distribution $\sigma$ would yield an estimate for the CR diffusion coefficient in the vicinity of Wd1 of

$$D_{Wd1} \simeq \frac{\sigma^2}{4\,t} \simeq 1.3 \times 10^{28} \, \text{cm}^2/\text{s}. \tag{9.12}$$

This value is well within the limits set by observations of Geminga ($D \simeq 3 \times 10^{27} \, \text{cm}^2/\text{s}$, cf. Sec. 9.4.1) and the value typically assumed for the Galactic disk ($D(3.5\text{TeV}) \simeq 5.6 \times 10^{29} \, \text{cm}^2/\text{s}$, cf. Eq. 2.9 using $\delta = 0.5$).

**Summary**   Given that

- a magnetar with a very massive progenitor star was found to be located inside of Wd1,

- the derived total CR energy is in agreement with the typical conversion efficiency of 10% assumed for SNRs, and

- the Gaussian fit to the radial CR distribution is in agreement with the upper limit provided by the cloud $\mathcal{C}$,

the scenario of a single SN being responsible for the observed VHE $\gamma$-ray emission of HESS J1646–458 seems likely. The main caveat for this scenario is actually given by the fact that no SNR has been observed yet in other wavelengths. However, this may be explained by fundamental differences of the SNR evolution inside an SpB or by observational constraints given by the large diameters expected for the SNR and SpB (cf. following paragraph).

### 9.4.2.2 Stellar winds of Westerlund 1

**Superbubble observed?** As explained in Sec. 2.2.2.3, the individual stellar winds of the massive stars within Wd1 should form a so-called superwind which in turn should result in an SpB with a size according to the age of the system. An SpB-like structure is actually observed in the radial gas density distribution of the vicinity of Wd1 (cf. Sec. 9.3.3). However, its radius $R_{\mathrm{SpB}} \simeq 39$ pc is incompatible with the predicted age of Wd1 (3.5–5 Myr) and superwind luminosity of $L_{\mathrm{SC,wind}} \simeq 4 \times 10^{38}$ erg/s. According to Eq. 2.49, a radius of $R_{\mathrm{SpB}} \simeq 124$–153 pc would be expected to be observed for an external ISM density of $n_0 \simeq 16$ cm$^{-3}$ (deduced from Fig. 9.14) and for the age and superwind luminosity of Wd1.

**Stellar wind energetics enough?** The total energy provided by stellar winds and converted into CRs $E_{\mathrm{CR,wind}}$ is determined by the total superwind luminosity, a conversion efficiency $\epsilon$, and the CR diffusion timescale $\tau$. Replacing the latter by the size of the VHE $\gamma$-ray emission region $R$ and the diffusion coefficient $D$ (cf. Eq. 2.8) results in

$$E_{\mathrm{CR,wind}} = \epsilon \, L_{\mathrm{Wd1,wind}} \, \tau = \frac{\epsilon \, L_{\mathrm{Wd1,wind}} \, R^2}{2 \, D}. \tag{9.13}$$

Inserting expected numbers (deduced from previous analyses: $L_{\mathrm{Wd1,wind}}$ taken from Eq. 9.3, $R = r_{1/e} \simeq 50$ pc deduced from the constant fit to the radial extent, cf. Sec. 9.3.2, and $D$ taken from Eq. 9.12) for the given parameters, the equation converts into

$$E_{\mathrm{CR,wind}} \simeq 4.8 \times 10^{49} \left( \frac{L_{\mathrm{Wd1,wind}}}{4 \times 10^{38} \, \mathrm{erg/s}} \right) \left( \frac{\epsilon}{0.1} \right) \left( \frac{R}{50 \, \mathrm{pc}} \right)^2 \left( \frac{D}{10^{28} \, \mathrm{cm^2/s}} \right)^{-1} \, \mathrm{erg}. \tag{9.14}$$

A comparison of $E_{\mathrm{CR,wind}}$ with the total CR energy $W_{\mathrm{CR}}(\geq 3.5 \, \mathrm{TeV}) \simeq 1.1 \times 10^{49}$ erg (cf. Eq. 9.10) shows that the observed CR energy could be explained by the stellar winds and their luminosity in case of a conversion efficiency of $\epsilon \simeq 0.03$.

**Radial CR distribution compatible with expectations?** The stellar winds of an SC provide continuous injection of CRs which is why in the SC scenario, a steady-state acceleration of CRs and a $1/r$-dependence of their radial distribution are expected (cf. Sec. 2.2.2.3). This however, is not in agreement with the upper limits of the CR density set by the deduced mass of the cloud $\mathcal{C}$ and the VHE $\gamma$-ray emission observed from its direction (cf. Sec. 9.3.4, Fig. 9.15b).

**Summary** The SC scenario is supported by the energetic consideration demonstrating that the stellar winds are in principle able to explain the observed VHE $\gamma$-ray luminosity. The fact that no SpB has been observed yet at the radial distance of 124–153 pc, as predicted by theory, may be explained by (1) a significant lower super wind power than assumed e.g. in case a significant fraction of it is lost in other processes such as radiative cooling (as discussed in [173]) or (2) observational constraints such as limited FoV or a wrong attribution of the observed HI data to the correct location in the line of sight. Finally, the deduced radial CR distribution, not being in agreement with the upper limits set by the cloud $\mathcal{C}$, may exclude this scenario even though CR data points to a higher radial distance would be desirable as it may influence the final fit.

### 9.4.3 Multi-source scenario

In general, given the number of astronomical objects located in the emission region of HESS J1646–458 (at least two pulsars, an SC, and a low-mass X-ray binary), also a multi-source scenario should be considered. The morphology of the observed VHE $\gamma$-ray emission for energies exceeding 5 TeV (cf. excess maps for the three highest energy bands, Fig. 9.9c, 9.10a & 9.10c) may support such a scenario. Even though an association with the low-mass X-ray binary 4U 1642–45 was deduced to be unlikely in the publication from 2012 [134] (cf. Sec. 9.1.2), one of the two emission regions that remain for energies >5 TeV lies near it. The other emission region (south of the Galactic plane) seems to be spatially coincident with PSR J1648–4611. If the emission at those energies was only associated with these objects and not with Wd1, this would (1) result in the discovery of low-mass X-ray binaries as a new class of VHE $\gamma$-ray emitters and (2) be an argument against Wd1 to be a PeVatron. However, given the low statistics at energies above 5 TeV, this could not be further constrained with the results of this analysis but should be considered in future investigations.

## 9.5 Summary and outlook

HESS J1646–458 is an extended VHE $\gamma$-ray source observed in the direction of the SC Wd1 with H.E.S.S. . New analyses of this source were presented in this chapter using a significantly larger dataset than in the publication of 2012 [134] (168 instead of 34 hours). For the interpretation of the observed VHE $\gamma$-ray emission, CO data, taken with the Mopra radio telescope, and HI data extracted from the HI4PI survey, were used.

Since HESS J1646–458 appears very extended in terms of the H.E.S.S. FoV – a diameter of $\sim$1.8° was derived in this analysis –, with other VHE $\gamma$-ray sources close to it (namely HESS J1641–463, HESS J1640–465, and HESS J1634–472), the background estimation is rather difficult. It was shown that using the FoV background estimation method instead of the AR method, which is commonly used in H.E.S.S. for nominal analyses, give slightly better results.

The resulting $\gamma$-ray excess was computed and analysed in six different energy bands with an energy threshold of 350 GeV, chosen based on the highest pixel-wise energy threshold. The radial distribution of the $\gamma$-ray excess in those energy bands was investigated relative to the position of Wd1. It revealed a rather irregular distribution in the centre up to a radial distance of $r_{\mathrm{max}}$ of 0.1°–0.4°, followed by a more regular decrease towards higher radial distances which was fitted with an exponential function. The distance $r_{1/e}$, where the fitted exponential dropped to the fixed fraction $1/e$ of the peak value, was taken as an estimate for the size of the emission. The energy dependence of $r_{1/e}$ was tested on two scenarios for the underlying CR population being (1) of leptonic origin with $r_{1/e} \propto E_\gamma^{(\delta-1)/4}$, $\delta$ being the diffusion index, or (2) of hadronic origin with $r_{1/e} = \mathrm{const}$. Even though the power-law fit (leptonic scenario) showed a better agreement with the measurements, a hadronic origin with a resulting constant radial extent of $r_{1/e} \simeq 0.91°$, corresponding to $\sim$51 pc at the distance of Wd1 ($\sim$3.2 kpc), could not be excluded.

In a next step, the gas column and particle number density distributions were derived using the CO Mopra and the HI4PI data. This revealed (1) a mean number density of $\sim$15 cm$^{-3}$ for the vicinity of Wd1, (2) an SpB-like structure around Wd1 with a radius of $\sim$0.7° ($\sim$39 pc), and (3) a gas cloud at a distance of $\sim$0.65° from Wd1, corresponding to a distance between 36 and 106 pc, depending on its exact location in the line of sight.

With the knowledge of the spatial distribution of both, VHE $\gamma$-rays and gas, the CR

density and its spatial distribution were determined. For this purpose, a preliminary spectral analysis was used to infer the VHE $\gamma$-ray luminosity of HESS J1646–458 of $L_\gamma(\geq 350\,\text{GeV}) \simeq 3.2 \times 10^{34}\,\text{erg/s}$. The resulting hadronic CR density for CR energies >3.5 TeV is $\omega_{\text{CR}}(\geq 3.5\,\text{TeV}) \simeq 0.44\,\text{eV/cm}^3$. Integrated in a spherical volume this yielded the total CR energy confined in the emission region of $W_{\text{CR}}(\geq 3.5\,\text{TeV}) \simeq 1.1 \times 10^{49}\,\text{erg}$ for CR energies >3.5 TeV and $W_{\text{CR}}(\geq 10\,\text{GeV}) \simeq 3.1 \times 10^{50}\,\text{erg}$ for CR energies >10 GeV, respectively. The radial CR distribution was fitted with two different models for the origin of the hadronic CRs, either produced and accelerated by stellar winds of Wd1 or by a single SNR resulting from an SN in Wd1. Furthermore, an upper limit on the CR density inside a gas cloud located in the vicinity of Wd1 was determined and also used for a discrimination between those scenarios.

Given those analysis results, a few scenarios that may explain the observed VHE $\gamma$-ray emission were considered. It was concluded that

- a leptonic scenario associated with Wd1 as underlying source is quite unlikely,

- a leptonic scenario associated with a PWN powered by PSR J1648–4611 or PSR J1650–4601 as underlying source seems possible,

- a hadronic scenario associated with Wd1 and based on SC winds seems rather unlikely, and

- a hadronic scenario associated with Wd1 and based on a single SN seems likely even though no SNR has been experimentally observed yet in other wavelengths.

In addition to that, a multi-source scenario with a contribution of several sources located in the FoV of HESS J1646–458 was discussed. From the VHE $\gamma$-ray excess maps, a combination of for example Wd1, the pulsar PSR J1648–4611, and the low-mass X-ray binary seems to be possible. However, this assumption is highly speculative and needs further investigations in the future.

The study presented in this thesis should be considered as a first glance on HESS J1646–458 using the full dataset of 168 hours taken in three different hardware eras with H.E.S.S. . In future, the analysis capabilities may improve for example by

- the use of the final results of spectral analyses of the full dataset,

- a combined analysis with the 60 hours of data taken in SM (possible as soon as the final analysis scheme is in place, cf. Ch. 8),

- the use of new high-energy-optimised analysis methods currently being developed within H.E.S.S., especially useful in combination with SM data,

- a combined analysis with $\gamma$-ray observations conducted in the HE range (e.g. including Fermi data),

- the use of gas maps reaching to further distances from Wd1, and

- the development and application of a 3D model including a multi-source scenario.

Furthermore, as the spectrum of Wd1 continues up to 20–30 TeV without an indication of a cutoff or a break, future observations with CTA, promising a significantly higher sensitivity at the highest energies, should improve the discrimination of different scenarios. Moreover, given these $\gamma$-ray energies, the energy spectrum of parent hadrons should not break at least until 0.5 PeV. This makes Wd1 (and massive SCs in general) potential sources of multi-TeV neutrinos with a fair chance to be detected by the cubic-km volume neutrino detectors.

Conclusion

"I think and think for months and years. Ninety-nine times, the conclusion is
false. The hundredth time I am right."

Albert Einstein

This thesis is dedicated to several aspects in highest-energy $\gamma$-ray astronomy, being (1)
the prototyping of corresponding hardware to detect $\gamma$-rays with such energies, (2) the de-
velopment of analysis techniques to improve their detection, and (3) the investigation of an
astronomical source from which direction $\gamma$-rays with those energies were detected.

The first part of the thesis covered the hardware development and testing of two proto-
types for the CHEC camera, dedicated for the detection of $\gamma$-rays with energies ranging from
1 TeV to several hundreds of TeV. I was heavily involved in the testing and characterisation
of both prototypes, named CHEC-M and CHEC-S, both, in the lab and during on-telescope
campaigns.

While with CHEC-M, on the one hand, I could verify general operation procedures such as
camera control and readout as well as the calibration and waveform processing chain, on the
other hand, I identified limiting performance aspects, such as data readout, gain calibration,
and trigger performance. This was used as valuable input for the development of CHEC-
S. The investigations, that I performed with CHEC-S and which I presented in this thesis,
showed that those limiting performance aspects were tackled and solved. Furthermore, with
extensive trigger calibration and trigger performance studies I could demonstrate a good
agreement of my measurements with expectations and MC simulations.

During the on-telescope campaigns with both prototypes, not only the results from my
laboratory measurements were used and verified but also a huge number of Cherenkov images
was recorded. Many of them showed to have large time gradients ($>$100 ns) demonstrating
the advantage of reading out full waveforms.

Moreover, as the final CTA SST design was recently chosen to be based on the ASTRI-
Horn telescope structure equipped with a CHEC-like camera, possible design iteration are
currently under investigation. The performance results of both camera prototypes that I
presented in this thesis are a very valuable input for this iteration process.

In the second part of the thesis, I presented full-waveform (referred to as SM) readout that was introduced to be used also with the H.E.S.S. IU cameras. Unlike the investigations in the first part, the studies I performed in this part were not related to hardware but analysis development. To be able to use SM data with the H.E.S.S. data analysis framework, I implemented SM charge extraction and calibration schemes and investigated the difference in performance when using SM instead of nominal (CM) data. Thanks to my charge extraction algorithm, the integration window moves along the time gradient of a Cherenkov event resulting in significantly longer images in SM which mainly improves the reconstruction of high-energy events. In addition, due to the smaller integration window used in SM, the detection capabilities of dim, typically low-energy events also improves, resulting in an increased sensitivity at the lower end of the H.E.S.S. energy range. Furthermore, I showed that the SM energy and angular resolution is better for high-energy (>1 TeV) events recorded at high offsets (2°) from the telescope axis. Such an improvement is expected for all offsets and energies, once all new SM-specific analysis settings were derived. An optimisation study of those was beyond the scope of this work and should be performed in the future.

In addition to SM investigations, I verified the new H.E.S.S. IU MC simulation chain, used to analyse both, CM and SM H.E.S.S. IU data. In the corresponding studies, I found a mismatch of the order of 10% between MC simulations and measurements most likely resulting from a difference in the trigger algorithm implementation between camera hardware and MC simulation software. Despite those differences, a first set of full IRFs for the H.E.S.S. IU era was produced. Careful and regular cross-checks of post-upgrade against pre-upgrade analyses and a comparison with results obtained with the second (PA) analysis chain will help to conclude on the quality of the current MC implementation and whether it needs to be revised. Such a revision would most likely include a more realistic implementation of the new H.E.S.S. IU trigger algorithm in the MC simulation software `sim_telarray`.

In the final part of the thesis, I performed a new analysis of the VHE $\gamma$-ray source HESS J1646–458 using H.E.S.S. data with a significantly higher exposure than available for the published analysis on that source in 2012 (168 instead of 34 hours). I confirmed the large extent of the source (diameter of $\sim$1.8°) compared to the FoV of H.E.S.S. what is in agreement with previous analyses. As the centre of the VHE $\gamma$-ray emission is spatially coincident with the SC Wd1, the latter was proposed in the past to accelerate CRs which in turn may produce the observed VHE $\gamma$-ray emission. To investigate this and other scenarios, I used CO data taken by the Mopra radio telescope and HI data that I extracted from the HI4PI survey to determine the gas distribution and density in the vicinity of Wd1. Furthermore, as also two pulsars (one of them being PSR J1648–4611) are located in the line of sight of HESS J1646–458, I discussed their possible impact on the VHE $\gamma$-ray emission.

In the end, I identified four scenarios for underlying CR populations. Two of them are associated with a leptonic origin, with the source being either a PWN powered by PSR J1648–4611 or PSR J1650–4601, or Wd1. In the other two scenarios, both associated with a hadronic origin of the CRs in Wd1, the observed VHE $\gamma$-ray emission may result either from CRs being continuously injected by SC winds or from an SN that happened 65–90 kyr ago with the magnetar CXO J164710.2–455216 being the remnant object. I inferred from my analysis that the leptonic scenario with Wd1 as underlying source is rather unlikely, while none of the other three scenarios could be definitely excluded. Furthermore, I speculated on a possible multi-source scenario including Wd1, PSR J1648–4611, and the low-mass X-ray binary 4U 1642–45 based on the observed morphology of HESS J1646–458 at $\gamma$-ray energies exceeding 5 TeV.

Given the huge dataset, 60 hours of which were recorded in SM, further analyses going beyond the one I presented in the thesis promise to set stronger constraints on the different scenarios.

For more details on the studies and results of the individual investigations performed in the scope of the thesis, the reader is referred to the corresponding chapters, especially to the summary section at the end of each of them.

> "Without laboratories men of science are soldiers without arms."

<div align="right">Louis Pasteur</div>

Several set-ups and devices were and will be used for hardware development, testing, calibration, and performance measurements of the CHEC cameras. Those as well as their characterisation and calibration measurements that I performed in the scope of the thesis are presented in this chapter.

## A.1 Set-up

The general set-up for camera testing is installed in two rooms, a control room and a light-tight laser room. The rooms are equipped with

- (laser room) a laser, a laser box, a light baffle, a robot arm, SiPMs for monitoring, and the camera to be tested (either CHEC-M or CHEC-S), and

- (control room) a computer (referred to as "lab PC"), a DC power supply to power the SiPMs, an oscilloscope to record the SiPM signals, a "periodic" pulse generator (generating periodic output signals), and a "random" pulse generator (for randomly distributed output signals around a mean frequency) to trigger the laser and/or camera.

A close-up pictures of the laser room is shown in Fig. A.1. A schematic drawing of the complete set-up and a box diagram illustrating the cabling are shown in Fig. A.2 and A.3, respectively.

**Periodic pulse generator** The periodic pulse generator (PPG), used to trigger the laser and camera (if external triggered measurements are performed), is a four-channel BNC-577 pulse generator [174] with a USB serial port for remote control using the lab PC. It outputs rectangular pulses of an adjustable width and height at an adjustable periodic frequency (between 1 mHz to 20 GHz).
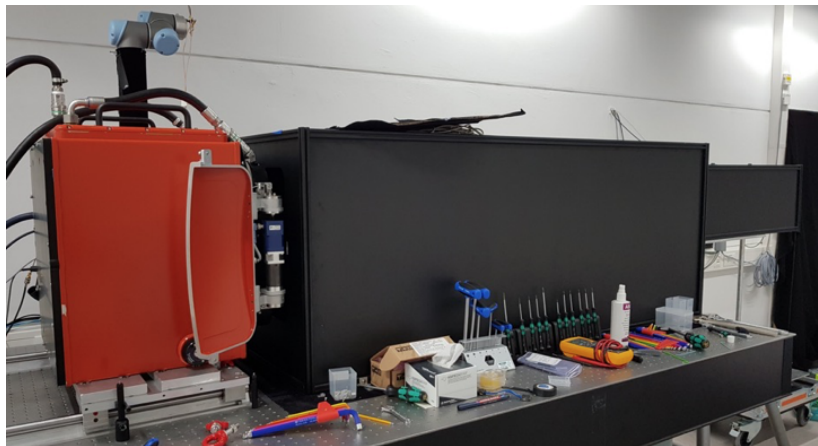
**Figure A.1** Close-up picture of the laser room with CHEC-S camera, light baffle, and laser box (left to right).

**Random pulse generator**  The random pulse generator (RPG) is a custom-designed device by J. D. Thornhill (University of Leicester) containing a 32 bit random number generator with a settable mean random rate. In case the camera should be triggered by the RPG, a series connection of RPG and PPG is used since the output signal amplitude of the RPG is not settable. In this case, the RPG triggers the PPG which then generates the same output signal shape as in case of periodic triggering which is then used as camera trigger signal.

**Oscilloscope**  The oscilloscope used to record and monitor the SiPM signals (laser flashes and background light level) is a Teledyne LeCroy WavePro HD Oscilloscope [175], controllable via Ethernet.

**Laser**  The laser is a PicoQuant PDL 800-B picosecond pulsed diode laser (class 3B, wavelength of 398 nm) [176].

**Laser Box**  The laser box (cf. Fig. A.4), similar to the one presented in [177], contains several devices which are

- a laser fibre coupling,

- a motorised, Ethernet-controllable OD4 filter wheel with a 12-bit DAC resulting in a dynamic range of 4–5 orders of magnitude for dynamic range measurements of the camera with the laser (cf. Fig. A.5a),

- a DC UV LED with a wavelength of 375 nm and a DAC with a 12-bit amplitude range for emulating different NSB levels (cf. Fig. A.5b),

- a diffuser system to illuminate the whole camera in a uniform way (cf. Fig. A.5c), and

- a lensing system for an optimised laser beam path.

**Robot arm**  The robot arm is a Universal Robots UR5 robot arm [178] used to scan the laser beam for uniformity measurements or to illuminate the camera from different angles. It can be either used via its own controller touch screen or remotely via Ethernet.
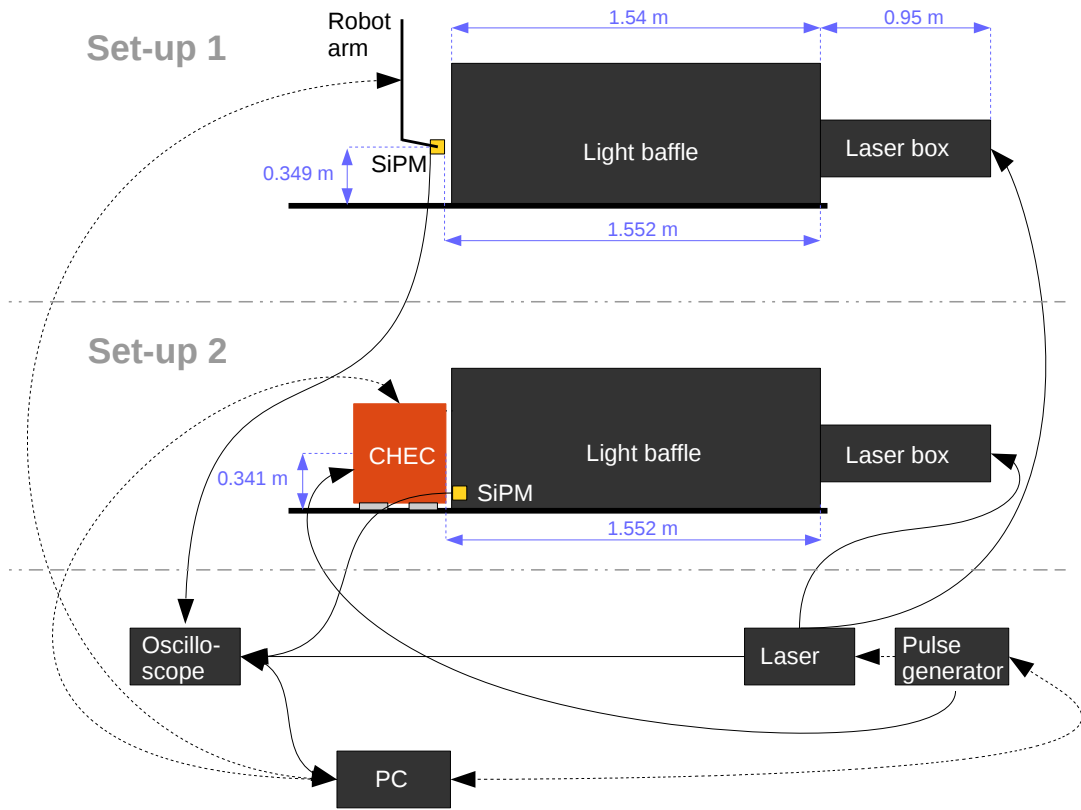
**Figure A.2** Schematic drawing of the laboratory set-up with either the robot arm (set-up 1) or the camera (set-up 2) installed in front of the light baffle.

**SiPMs**  The SiPMs[1] are used for monitoring the laser and background light in case of camera measurements and for several calibration measurements described in the following section. They are SensL MicroFJ-SMA-60035 SiPMs [179] with an area of $6 \times 6$ mm$^2$ (same as a camera pixel) and 22,292 microcells. Their typical operating bias voltage is 30 V, corresponding to an over voltage of ~6 V. Depending on the type of measurement a preamplifier is connected in series to amplify the SiPM signal. It is a ZFL-100LN+ low noise amplifier of the company Mini-Circuits [180] and typically operated at a voltage of 13 V corresponding to a gain of ~10.

When using SiPMs, a few characteristics have to be taken into account in the analysis. Those are:

- An intrinsic fluctuation of the order of

$$\frac{\Delta N_{\text{p.e.}}}{N_{\text{p.e.}}} = \frac{\sqrt{N_{\text{p.e.}}}}{N_{\text{p.e.}}}, \tag{A.1}$$

is expected due to Poisson fluctuations ($N_{\text{p.e.}}$ being the number of photoelectrons).

---

[1]Further details on the working principles of SiPMs are given in Ch. 4.2.2.

Cables between control and camera room:

**C1**: Camera External Trigger
**C2**: VBias for SiPM
**C3**: Signal from SiPM

**Figure A.3** Box diagram illustrating the cabling between the different components in the laboratory.

- The linearity of the SiPM decreases with increasing illumination following the equation

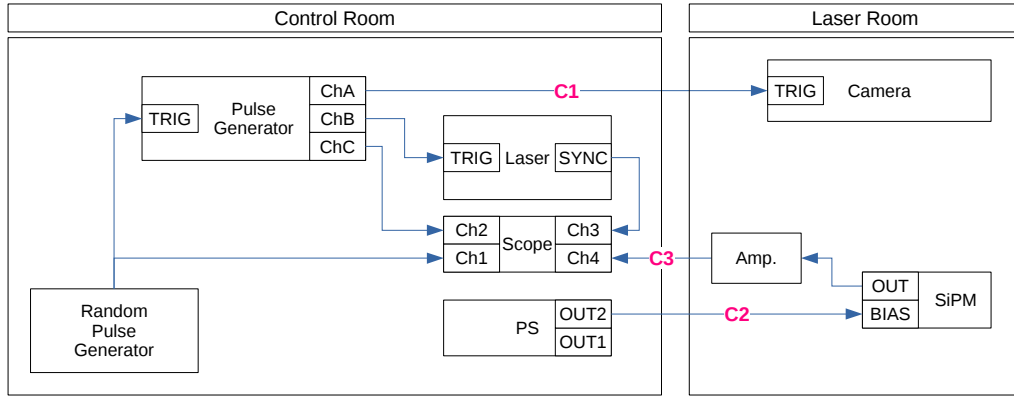$$N_{\mathrm{fired}} = M \left( 1 - \exp \left( -\frac{q\, N_{\mathrm{ph}}}{M} \right) \right) = M \left( 1 - \exp \left( -\frac{N_{\mathrm{p.e.}}}{M} \right) \right), \qquad (A.2)$$

where $N_{\mathrm{fired}}$ is the number of fired microcells in the SiPM being proportional to the signal measured by the oscilloscope, $M$ the total number of microcells in the SiPM (for the SensL SiPM, $M = 22{,}292$), $q$ the PDE, and $N_{\mathrm{ph}}$ the number of photons. Thus, one can extract the number of p.e. from the measured signal $S_{\mathrm{meas}}$ and the known SiPM gain $G$ by inverting the above equation, resulting in

$$N_{\mathrm{p.e.}} = -M \ln \left( 1 - \frac{N_{\mathrm{fired}}}{M} \right) = -M \ln \left( 1 - \frac{S_{\mathrm{meas}}}{G\, M} \right). \qquad (A.3)$$

- The dependence of the $G$ on the temperature $T$ is given by

$$G \propto a\, T[^{\circ}\mathrm{C}] + \mathrm{b}. \qquad (A.4)$$

with the parameters $a$ and $b$ being determined in a dedicated measurement. It follows that the temperature corrected signal $S_{\mathrm{corr}}$ is given by

$$S_{\mathrm{corr}} = \frac{S_{\mathrm{meas}}}{a\, T[^{\circ}\mathrm{C}] + \mathrm{b}}. \qquad (A.5)$$

The SensL SiPM contains two outputs, a fast signal (FS) and a slow signal (SS) output. They differ in SPE pulse shape characteristics. As suggested by the name, the typical FS SPE pulse length is much shorter (FWHM of $\sim$3 ns) than the SS one (FWHM of $\sim$30 ns). Depending on the measurement circumstances like photon rate $f_{\mathrm{ph}}$ of the light source and SPE pulse length $t_{\mathrm{pulse}}$, different SiPM quantities have to be used so extract the charge
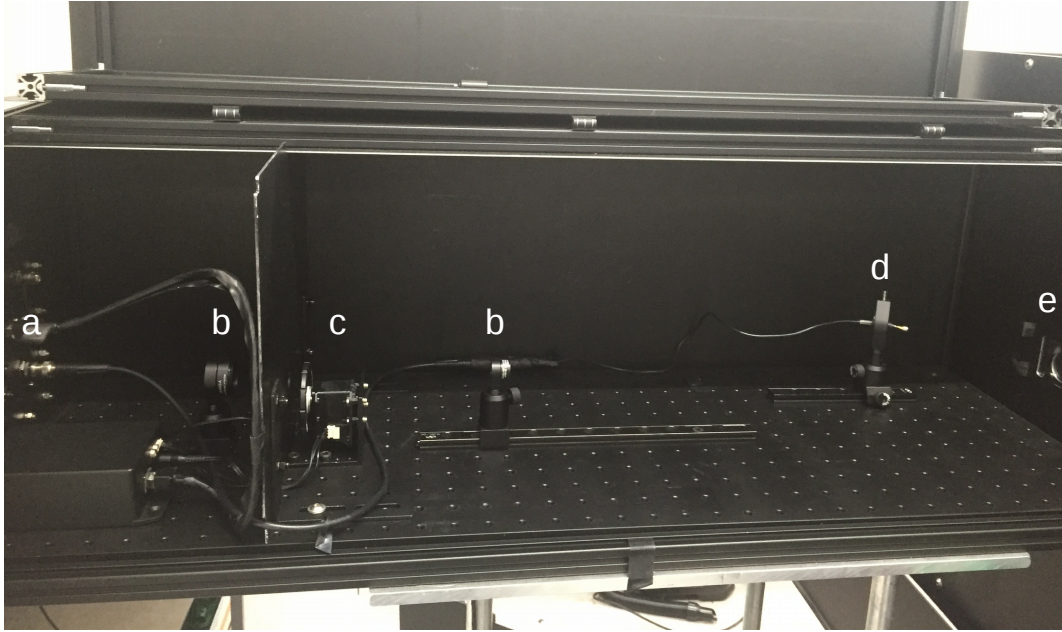
**Figure A.4** Picture of the open laser box with different components: (a) laser fibre coupling, (b) lensing system, (c) filter wheel, (d) DC UV LED, and (e) diffuser.

(in number of p.e.). For $t_{\text{pulse}} \ll 1/f_{\text{ph}}$, the amplitude or area of the measured pulse is proportional to the number of p.e. . If $t_{\text{pulse}} \gg 1/f_{\text{ph}}$, individual pulses can no longer be distinguished. In this case, the FS variance and the SS mean are proportional to the number of p.e. .

## A.2  Characterisation and calibration measurements

The devices presented in the previous section have been characterised and calibrated within the scope of this work. Measurement procedures and results for the individual devices are presented in the following subsections.



**Figure A.5** Pictures of (a) filter wheel, (b) NSB LED (highlighted by red circle), and (c) diffuser.

| Measure | P1:ddelay(C1,C2) | P2:wid@lv(C2) | P3:rise(C2) | P4:pkpk(C2) | P5:area(C2) | P6:--- | P7:--- | P8:--- |
|---|---|---|---|---|---|---|---|---|
| value | 523 ps | --- | 1.505 ns | 3.52 mV | 9.4680 pWb | | | |
| mean | 13.17 ns | 3.0796 ns | < 1.1077 ns | 6.253 mV | 17.32 pWb | | | |
| min | -9.359 ns | 463 ps | < 45 ps | 990 µV | -22.2920 pWb | | | |
| max | 48.349 ns | 12.180 ns | < 6.304 ns | 37.93 mV | 214.7160 pWb | | | |
| sdev | 17.37 ns | 940.9 ps | < 698.5 ps | 4.631 mV | 21.49 pWb | | | |
| num | 10.158e+3 | 4.665e+3 | 9.460e+3 | 10.163e+3 | 10.163e+3 | | | |
| status | ✓ | ⚠ | ⊓ | ✓ | ✓ | | | |

**Figure A.6** Oscilloscope screenshot showing waveform signal measurements (in persistence mode, i.e. overlayed waveforms of co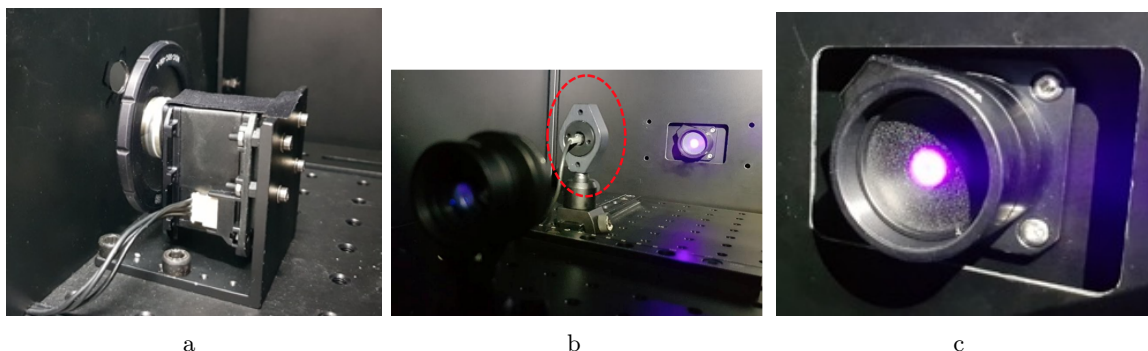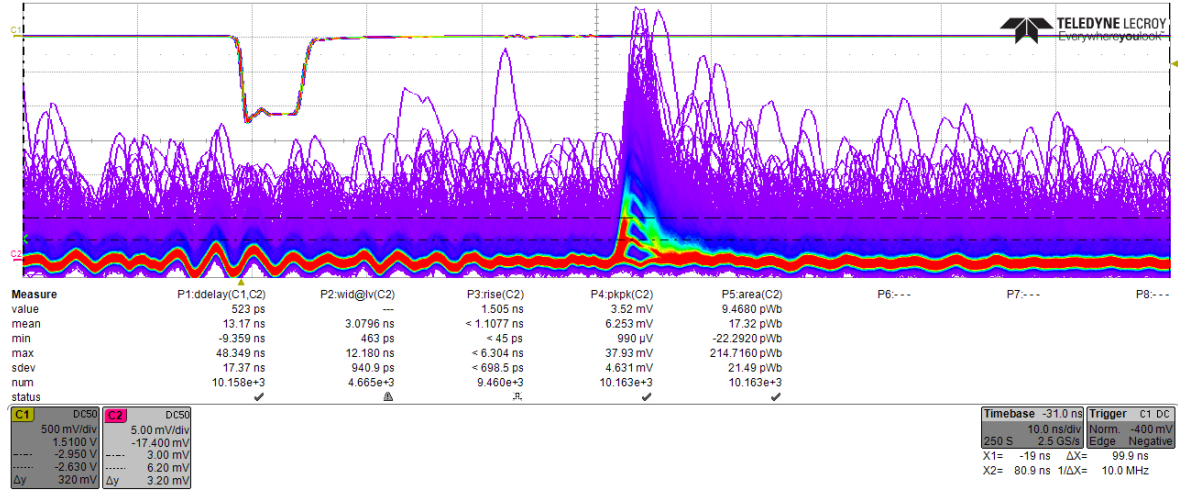nsecutive measurements where the colour indicates the frequency of occurrence) of the laser trigger output signal (channel C1, top curves, resolution of 500 mV/div) and the SiPM signal (channel C2, bottom curves, resolution of 5 mV/div) as a function of time (10 ns/div).

## A.2.1 SiPMs

The SiPM gain at a bias voltage of 30 V and a temperature of 20°C has been determined from low-laser-amplitude measurements with a preamplifier at 13 V connected in series. Fig. A.6 shows the resulting signal being recorded by the LeCroy oscilloscope. Beside many randomly distributed peaks in the SiPM signals (resulting from dark counts or background photons), an accumulation of peaks is observed at ∼35 ns after the laser trigger signal. This is the laser light pulse measured by the SiPM. The observed quantisation of the SiPM signal is due to the SPE counting. The gain (in mV/p.e.) can approximately be deduced from the amplitude difference between the different local maxima within the laser pulse. Such a measurement is indicated by the dashed lines, showing $\Delta V = 3.2$ mV. However, since the measurement was performed with a preamplifier connected in series, this is not the SiPM gain yet. To extract the gain without preamplifier, another measurement at a laser amplitude resulting in a measurable but un-saturated signal in the SiPM with and without preamplifier connected in series was performed. The pulse height ratio of these two measurements determines the preamplifier gain, measured to be ∼16.8 at 13 V. Thus, the resulting SiPM gain without preamplifier is given by $(3.2/16.8)\,\mathrm{mV/p.e.} \simeq 0.2$ mV/p.e. .

The gain-temperature dependence was deduced from temperature chamber measurements resulting in values for $a$ and $b$ (cf. Eq. A.4) of

$$
\begin{aligned}
a &\simeq -0.004\,(°\mathrm{C})^{-1} \\
b &\simeq 1.080.
\end{aligned}
\tag{A.6}
$$

## A.2.2 Laser

The laser stability was measured using a SensL SiPM and the LeCroy oscilloscope. To investigate the influence of the ambient temperature on the laser, measurements with it being installed inside and outside of the temperature chamber were performed. Furthermore, the laser characteristics at two different time scales were assessed:
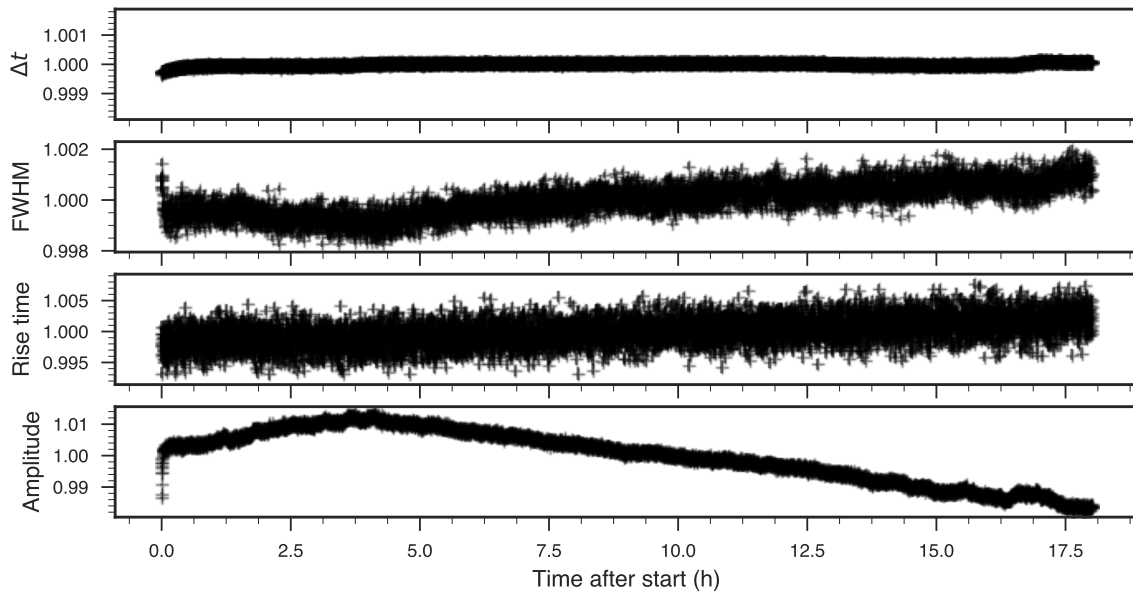
**Figure A.7** Time evolution of the quantities $\Delta t$, FWHM, rise time, and amplitude (all relative to their mean value) as function of time for an 18-hour measurement.

- Long-term over several hours to investigate the overall laser stability.

- Short-term over a few minutes to investigate the laser pulse-to-pulse variation.

In all measurements, the laser was triggered at 600 Hz (typical CHEC trigger rate) using the PPG while the oscilloscope was triggered by the trigger output signal of the laser. In the long-term measurements, the time delay between laser trigger output signal and measured laser pulse ($\Delta t$) as well as the FWHM, the rise time, and the amplitude of the laser pulse were measured. Every 10 seconds, the mean and standard deviation of the last 10 seconds of these quantities were recorded, i.e. each data point contains the mean and spread of 6000 measurements. In the short-term measurements, laser pulses were recorded at different intensities over a short period of a few minutes filling an amplitude histogram with ~15 000 entries.

### A.2.2.1 Long-term stability

The long-term stability was measured with both, the laser being placed inside and outside of the temperature chamber. No systematic difference between both configurations was observed. This is expected because of the active thermoelectric cooling mechanism coupled to the laser. However, a long-term drift of the recorded signal amplitude (and of the FWHM, but on a per-mill level) over time scales $\mathcal{O}(\text{h})$ of the order of ~0.2%/h has been observed (cf. Fig. A.7). Furthermore, a warm-up time of ~10 min, in which the amplitude increases by about 2%, can be inferred from Fig. A.7. Hence, to avoid %-level drifts during a measurement, the laser should be powered and triggered for 10 minutes before starting a measurement.

### A.2.2.2 Pulse-to-pulse fluctuations

The short-term measurements provide information about the pulse-to-pulse fluctuation of the laser. Histograms and Gaussian fits for all four short-term measurements performed at four

a



b



c



d
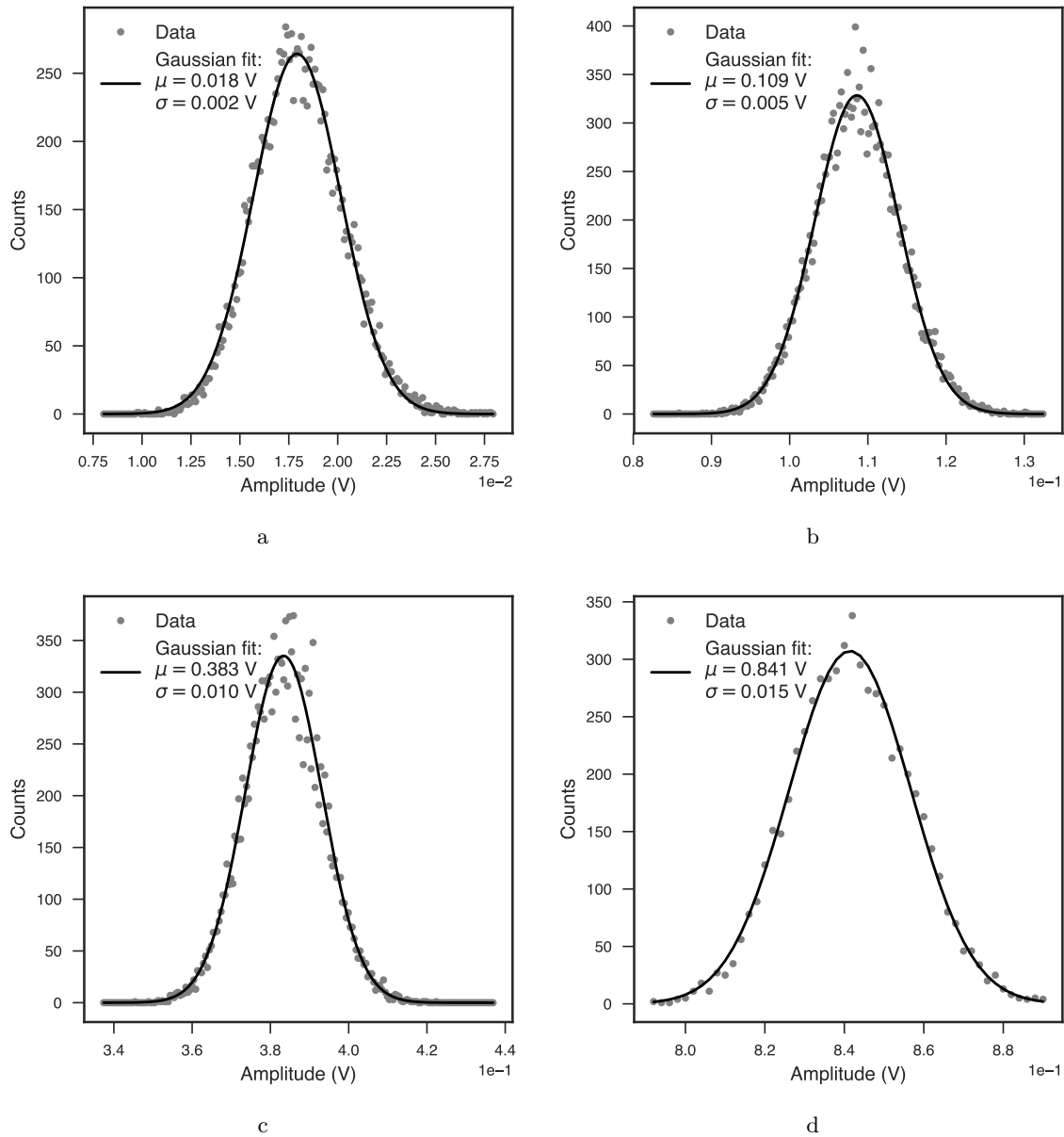
**Figure A.8** Amplitude histograms (each with approximately 15 000 entries) and Gaussian fit for different laser amplitudes. The laser illumination (in p.e.) can be calculated using the recorded mean signal $\mu$, the SiPM gain of $\sim$0.2 mV/p.e., and Eq. A.3 resulting in mean laser amplitudes of (a) $\sim$90 p.e., (b) $\sim$552 p.e., (c) $\sim$ 2002 p.e., and (d) $\sim$4934 p.e. .

different laser amplitudes are shown in Fig. A.8. The measurements were performed without preamplifier, thus, the mean $\mu$ (in V) of the Gaussian fit can be converted into number of p.e. using Eq. A.3. Then, the expected fluctuation due to Poisson statistics (ref. Eq. A.1) can be compared to the measured fluctuation ($\sigma/\mu$, both resulting from the Gaussian fit). Results are shown in Tab. A.1. The measured fluctuations are in the range of Poisson fluctuations. This implies that the lowest Poisson fluctuation value given in Tab. A.1 (1.7%) is an upper limit for the laser pulse-to-pulse fluctuations.

**Table A.1** Measurements with different laser amplitudes resulting in a measured mean $\mu_{\text{fit}}$ and standard deviation $\sigma_{\text{fit}}$ (both from Gaussian fit for $\sim$15 000 recorded laser pulses with the SensL SiPM). $N_{\text{p.e.}}$ is the number of photoelectrons, calculated with the gain value of 0.19 mV/p.e., and $\Delta N_{\text{p.e.}}$ is the Poisson fluctuation calculated from Eq. A.1.

| Measurement (Figure) | $\mu_{\text{fit}}$ (V) | $\sigma_{\text{fit}}/\mu_{\text{fit}}$ | $N_{\text{p.e.}}$ | $\Delta N_{\text{p.e.}}/N_{\text{p.e.}}$ |
|:---:|:---:|:---:|:---:|:---:|
| A.8a | 0.018 | 0.111 | 90 | 0.105 |
| A.8b | 0.109 | 0.046 | 552 | 0.043 |
| A.8c | 0.383 | 0.026 | 2002 | 0.022 |
| A.8d | 0.841 | 0.017 | 4934 | 0.014 |

### A.2.3 Laser beam uniformity

The laser beam uniformity was measured at a distance of 1.552 m from the laser box (camera position, cf. Fig. A.2) using a SensL SiPM attached to the robot arm. The robot arm was programmed to scan the laser beam in steps of 1 cm in $x$ and $y$ direction over the camera focal plane projected on a plane area. To remove possible temperature effects of the SiPM and laser brightness drifts, the robot arm was programmed to return to the centre position after each measurement. This could then be used as reference measurement in the analysis for each data point. Several attempts were undertaken to optimise the laser beam path and thus the beam profile[2]. The plot shown in Fig. A.9a results from a measurement of the beam profile used for the camera performance measurements presented in the following chapters. It shows a gradient in vertical direction with a maximum spread over the projected camera focal plane of $\sim$9%. This spread can be corrected for in the analysis by using a correction coefficient for each pixel resulting from a simple gradient model (cf. Fig. A.9b). Additionally taking into account the camera focal plane curvature (cf. Fig. A.9c) gives an overall correction coefficient for each pixel as shown in Fig. A.9d.

### A.2.4 Filter wheel

The filter wheel was calibrated with a similar set-up as used for the laser calibration measurements using a SensL-SiPM and the LeCroy oscilloscope. The SiPM was not temperature controlled since the measurement was done over $\sim$2 hours, a timescale in which the room temperature was measured to not vary by more than 1°C causing a change in breakdown voltage of $<$21.5 mV (according to [179]) and thus a gain change of $<$1% (being in the range of the laser stability). To be able to measure the full dynamic range correcting for saturation effects from the SiPM, a combination of different ND filters added to the output port of the laser box were used with several overlapping parts for scaling between the individual measurements[3]. The results of these measurements and the extracted combined, overall transmission are shown in Fig. A.10.

A second calibration measurement has been performed in February 2018 after the laser box light path set-up has been optimised. A comparison of both measurements is shown in Fig. A.11a. A combined dataset has been produced (cf. Fig. A.11b), taking the new measurement where data of both measurements do not agree and the older measurement

---

[2]The physical beam profile optimisation as well as the measurements were performed by myself. The resulting plots were produced by J. J. Watson and C. Duffy.

[3]For scaling, data points were used where the SiPM is operated in its linear range and no saturation effects are observed.
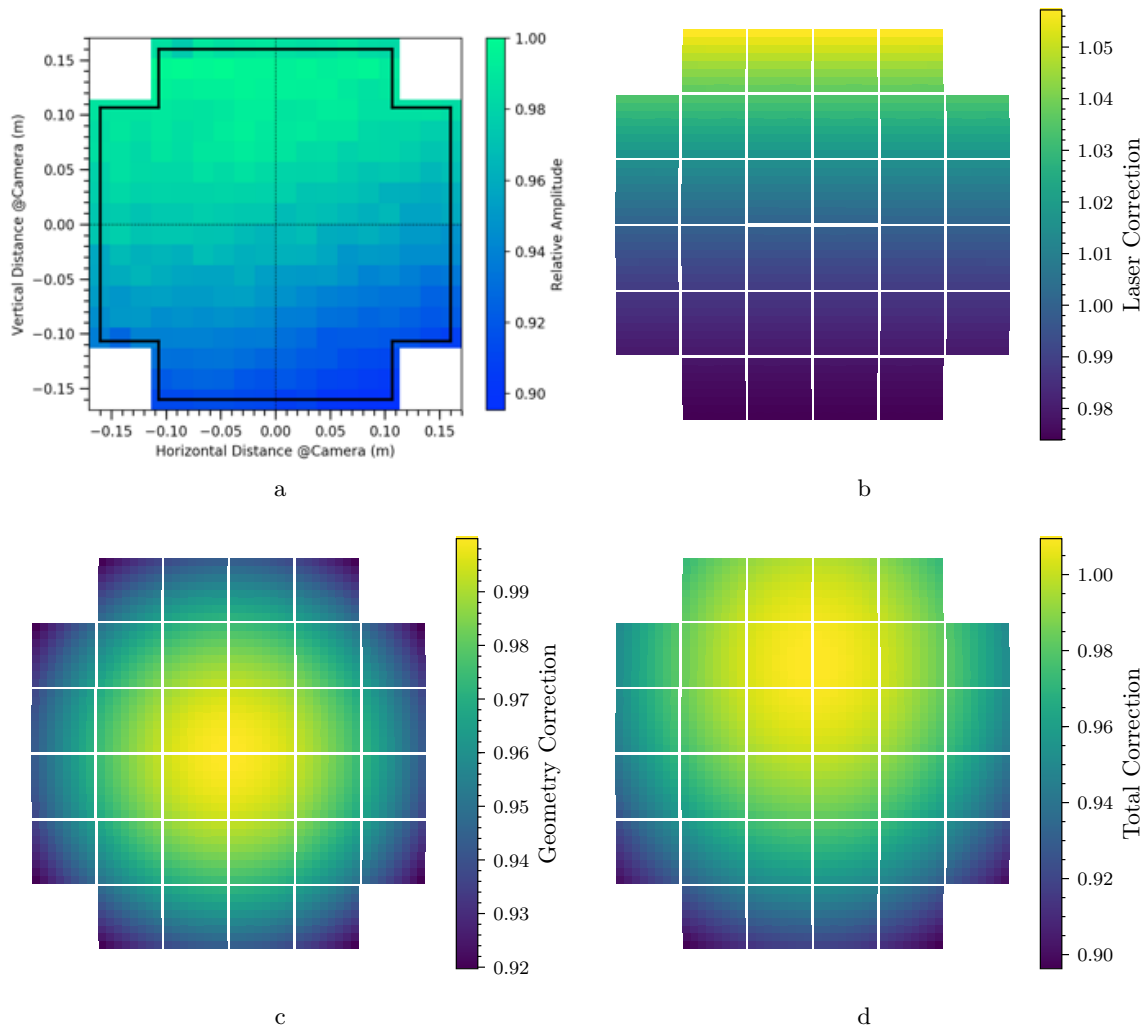
**Figure A.9** (a) Laser beam measurement showing the relative SiPM amplitude (normalised to the maximum amplitude measurement) as function of horizontal and vertical distance to the camera centre. (b) Laser beam profile correction coefficient resulting from measurement shown in (a) for each camera pixel. (c) Camera curvature correction coefficient for each camera pixel. (d) Total correction coefficient folding laser beam profile and camera curvature for each pixel. Drawings were produced by C. Duffy (a) and J. J. Watson (b–d).

where data points of both measurements overlap (since the older dataset contains more data points at lower illumination levels). The combined dataset is the final filter wheel calibration used afterwards. Even though the calibration measurements were not performed using all 4096 filter wheel positions, intermediate attenuation levels are deduced by linear interpolation between two data points in software.

Note: The "FlashCam-team" uses a filter wheel of similar type for their camera laser measurements. The calibration of their filter wheel showed similar results as illustrated by Fig. A.12.
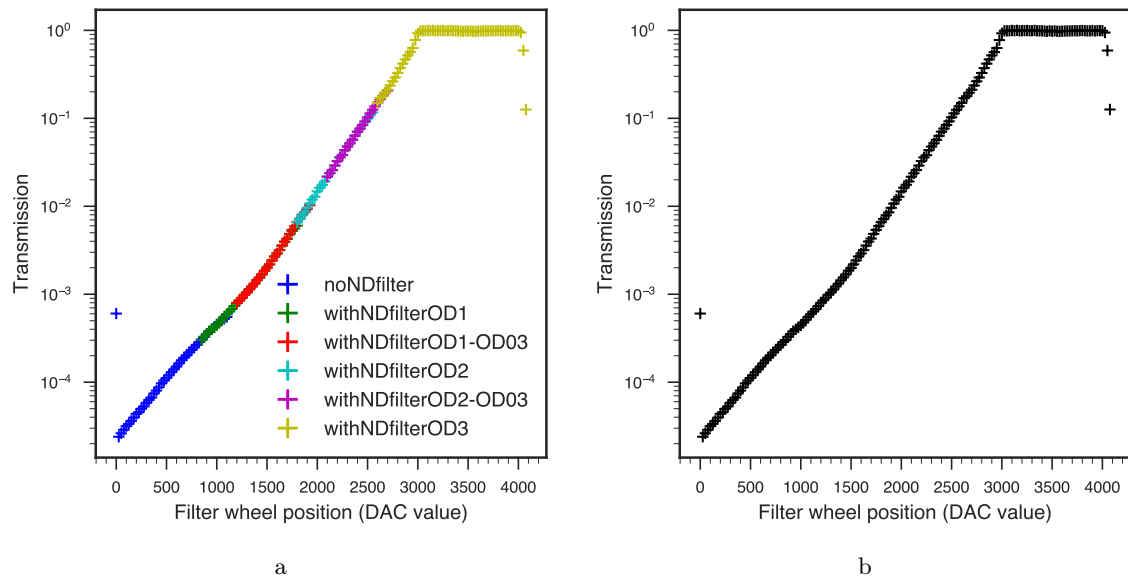
**Figure A.10** Filter wheel calibration measurement results showing (a) individual measurements after scaling using the overlapping parts and (b) the extracted overall transmission as function of the value set to the DAC.

## A.2.5  DC UV LED

The DC UV LED was calibrated in the temperature chamber. Four characteristics were investigated:

1. Warm-up & stabilisation,

2. temperature dependence,

3. dynamic range & linearity, and

4. absolute brightness.

While the absolute brightness was measured with a National Institute of Standards and Technology (NIST)-absolute-calibrated photodiode, all other characteristics were determined using one of the SensL SiPMs. The temperature chamber was set to 20°C for all measurements but for the temperature dependence investigation. In the latter case the temperature was varied over 30°C in steps of 2°C and the recorded SSs and FSs were corrected for the SiPM temperature dependence according to Eq. A.5.

### A.2.5.1  Warm-up and stabilisation

As shown by Fig. A.13a, the typical warm-up time of the LED is of the order of 10 min in which the LED light output suffers a drop of the order of ~5% (SS) to ~9% (FS). After this time, the LED amplitude fluctuates on a <1% level.
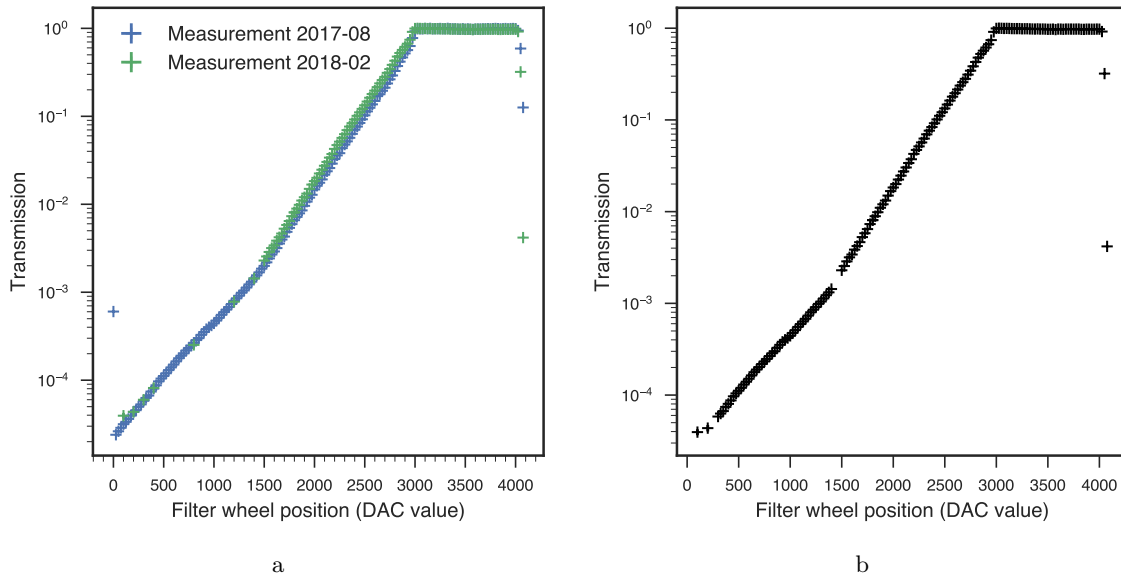
a
b

**Figure A.11** Filter wheel calibration measurement results showing (a) a comparison between two calibration measurements before and after optimisation of the light path in the laser box and (b) a combination of both measurements used as the final calibration measurement and look-up table after the light path optimisation.

### A.2.5.2 Temperature dependence

The LED shows a linear temperature dependence (residuals[4] ≤1%) as shown by Fig. A.13b. The light output decreases with increasing temperature by ∼0.58%/°C (SS) – ∼0.65%/°C (FS). A hysteresis effect (light output depending on temperature increase or decrease) is observed on a ∼1% level.

### A.2.5.3 Dynamic range and linearity

Measuring the SiPM signal as function of the LED DAC amplitude setting results in a dynamic range of more than one order of magnitude – factor of ∼149 (SS mean) / ∼160 (FS variance) between lowest and highest amplitude DAC setting (cf. Fig. A.13c). The dependence of the brightness on the DAC setting is roughly linear justifying a linear interpolation between two measurements to be used to resolve DAC settings for brightness levels between two measurements.

### A.2.5.4 Absolute brightness

Measuring the absolute brightness with the absolute-calibrated photodiode at a distance of 29 cm results in (1) the same dynamic range as measured with the SensL SiPM (used as a cross-check) and (2) an absolute brightness (photon rate per SiPM pixel) of ∼21 GHz at the highest DAC amplitude setting (cf. Fig. A.13d). Extrapolated to a distance of 1 m and 2 m, the maximum LED brightness is ∼1.7 GHz at 1 m and ∼400 MHz at 2 m, respectively.

---

[4]defined as $(\text{data}_i - f_i)/\text{data}_i$, where $\text{data}_i$ is the measured quantity at index $i$ and $f_i$ the resulting fit value at the same index
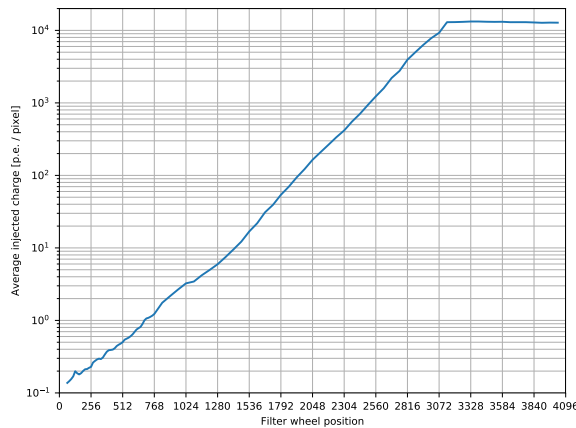
*J. Zorn*

**Figure A.12** Filter wheel calibration measurement results of FlashCam filter wheel (plot provided by F. Werner).

## A.3 Conclusion and impacts on camera characterisation and calibration measurements

The calibration results of all devices described in the previous sections satisfy them to be used for characterisation and calibration measurements of both CHEC cameras. Detailed conclusions and impacts are presented in the following subsections.

### A.3.1 Laser

The following conclusions can be drawn from the laser calibration measurements:

- Neither the laser power supply nor the laser have to be temperature-stabilised by the user since the laser itself is equipped with an internal temperature stabilisation.

- In general, the laser is stable over a time scale of ∼2 h (drift of less than 0.5%). Since typical CHEC performance and calibration measurements, in which the laser must be considered as stable, last between tens of seconds and ∼2 h, the resulting accuracy in laser brightness is ≤1%.

- A warm-up time of ∼10 minutes should be considered.

- Laser pulse-to-pulse fluctuations are less than 1.7%.

- For all CHEC-related laser illumination measurements, the deliberate shaping of electrical pulses by the camera preamplifier circuit dominates the intrinsic width of the laser pulse so that the FWHM of the pulses measured by the camera is quite stable as long as no saturation effects occur.

### A.3.2 Laser beam uniformity

The maximum spread in laser beam uniformity is ∼9%. While this can easily be corrected for in the analysis of e.g. charge and time resolution measurements by using the beam profile model in the offline flat-fielding procedure, it challenges trigger performance measurements.

a



b



c



d
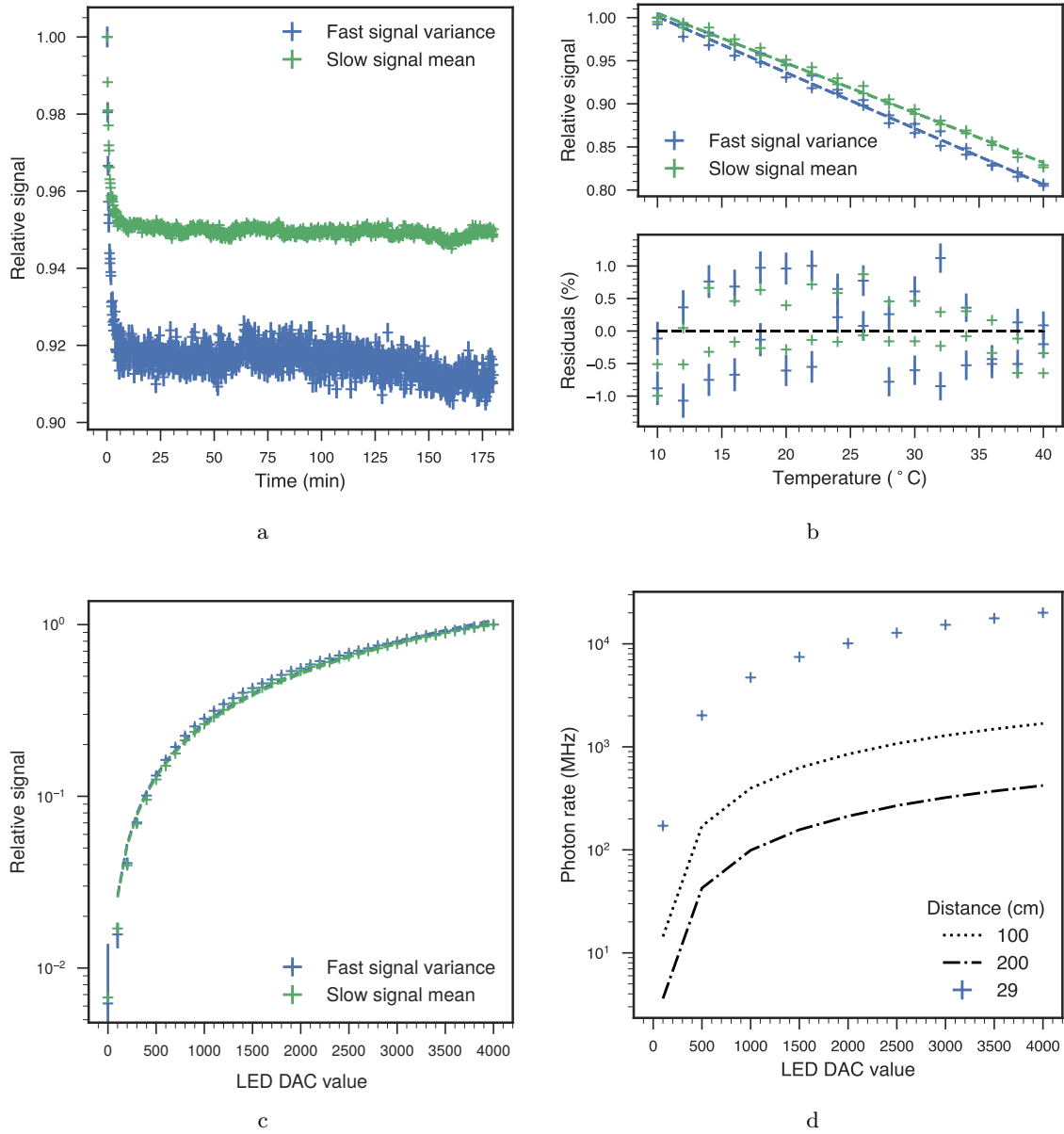
**Figure A.13** (a) Relative FS-/SS-SiPM signal (normalised to starting point) as function of time after the LED was switched on and set to a DAC value of 1000. (b) The top panel shows the relative FS-/SS-SiPM signal (normalised to measurement at 10°C, corrected for SiPM-temperature dependence) as function of ambient temperature in the temperature chamber while the bottom panel shows the residuals of the linear fit to the data points. The measurement was done in a temperature loop, first decreasing from 40°C down to 10°C and then increasing back to 40°C. This is why two data points exist for each temperature. (c) Relative FS-/SS-SiPM signal (normalised to signal at DAC setting 4000) as function of LED DAC setting and linear fits to both datasets. (d) Absolute brightness as function of LED DAC setting measured at a distance of 29 cm and extrapolated to distances of 1 m and 2 m, respectively.

Translating the threshold setting unit from mV to number of photons is one possible work-around. Hence, the given spread in laser beam uniformity does not cause any limitations in the ability of performance and calibration measurements with the given laboratory set-up.

### A.3.3 Filter wheel

CHEC is required to detect very faint (a few photons pixel) and very bright (a few thousand of photons per pixel) Cherenkov signals. Thus, a high dynamic range in laser amplitudes of 3–4 orders of magnitude is required for calibration and performance measurements. The filter wheel used in the laboratory set-up fulfils this requirement. Furthermore, the determined transmission for each filter wheel position including linear interpolation between different measurements and thus the number of photons is accurate on a ≤5% level.

### A.3.4 DC UV LED

The following conclusions can be drawn from the DC UV LED calibration measurements:

- A warm-up time of ∼10 minutes should be considered.

- A temperature stabilisation on a 1–2°C-level is desired to keep the LED brightness constant on a 1%-level. This is achieved by the use of air conditioning in the laser room.

- Some camera performance measurement are required to be performed at emulated NSB levels between ∼20 MHz and ∼700 MHz. The LED covers a dynamic range in brightness of two orders of magnitude and gives a sufficient minimum and maximum absolute brightness if the camera is positioned at a distance of ∼1.5 m from the LED.

- Since the LED is not aligned with the optical axis (diffuser–camera centre) but slightly offset, a non-uniform emulated NSB level is expected to be measured at different locations of the camera focal plane.

CHEC-S HV stability issue

"True stability results when presumed order and presumed disorder are balanced."

Tom Robbins

During the verification of the L2 trigger algorithm (cf. Sec. 6.4.3), it was observed that many valid NN combinations did not fire an L2 trigger. The cause could be identified being due to disappearing L1 trigger signals over time. To identify the source of the issue – the T5TEA ASIC (generating the L1 trigger signals) itself or the input signal to the TM – the waveforms that were recorded in the NN logic test were analysed. It was observed that the same SPs that showed disappearing L1 trigger signals also showed decreasing peak amplitudes over time. Further analyses, testing correlations with other parameters, revealed a positive correlation between SiPM bias voltage and peak amplitude for many SPs. Fig. B.1 shows the SP peak amplitude-SP bias voltage dependence of TM 9 for nine SPs that show a significant decrease in SP peak amplitude in a 10-hour laser measurement. The behaviour was observed to be different for different SPs. For some SPs, a decrease in SP peak amplitude was observed even though the SP voltage stayed constant. However, in all cases of a strong drop in SP peak amplitude, there also was a strong drop in SP bias voltage.
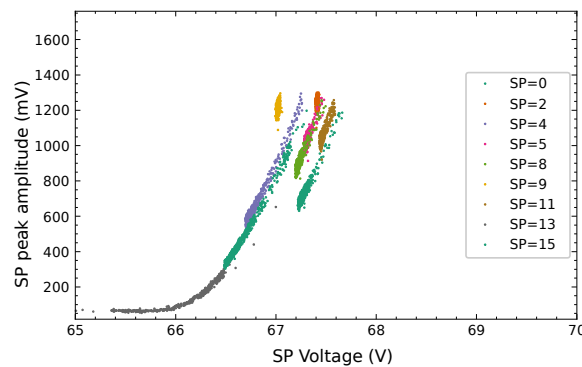


**Figure B.1** Scatter plot showing SP peak amplitudes and SP (bias) voltages for nine SPs of TM 9 measured in a 10 h laser measurement. Plot produced by J. J. Watson.
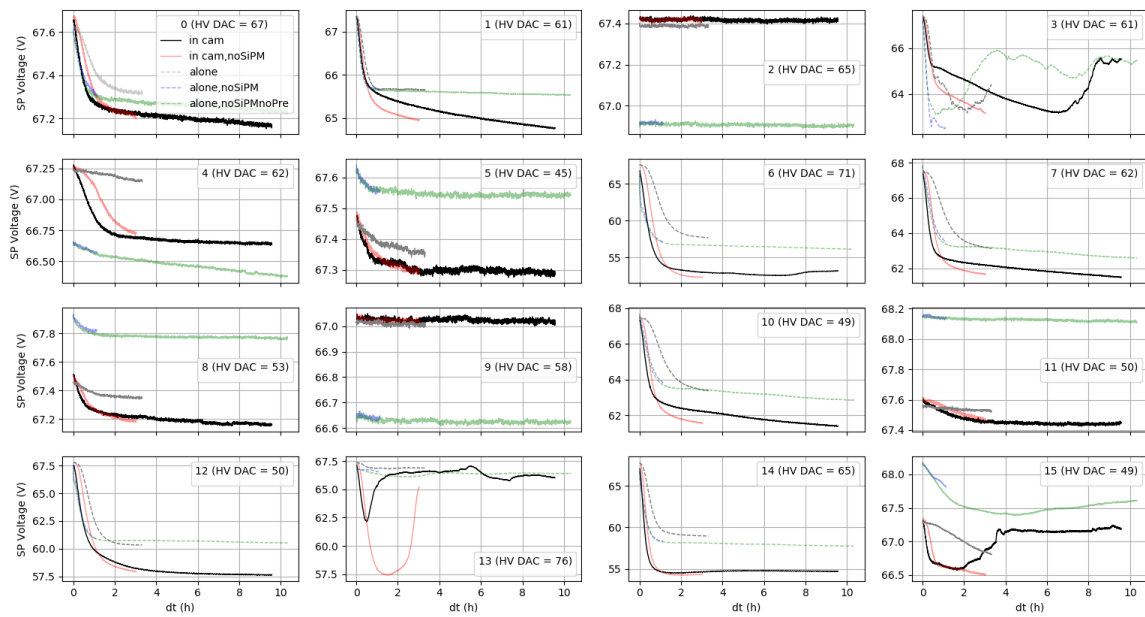
**Figure B.2** SP (bias) voltage-time dependence for all SPs on TM 9 for different measurement set-ups. For details refer to text.

As a next step, the cause of the bias voltage decrease was investigated. For this purpose, TM 9 was taken out of the camera and further tested in a stand-alone set-up in the temperature chamber. To examine the possible influence of different hardware components like SiPM and preamplifier, different measurements were performed: (1) "TM alone", i.e. TM with SiPM and preamplifier attached, (2) "TM alone,noSiPM", i.e. TM with preamplifier attached only, and (3) "TM alone,noSiPMnoPre", i.e. TM with neither preamplifier nor SiPM attached. The results were compared to the in-camera measurements with and without SiPM attached (cf. Fig. B.2). Apart from the differences between SPs (some showing a continuous drop of SP bias voltage over time, others showing a rather irregular SP bias voltage-time dependence), no significant difference between the individual measurement set-ups were observed. Hence, it was concluded the cause of the problem being on the TM itself.

Further measurements (performed by M. Barcelo) of the electrical components on the TM power board, where the HV generators are located, revealed that a wrong capacitor had been used in the production not fulfilling the specification. Replacing those capacitors by new ones with the correct specifications solved the HV stability issue. Consequently, a new NN logic test after the capacitor replacement in all TMs showed the expected results (cf. Fig. 6.11b).

# Bibliography

[1] R. Engel, D. Heck, and T. Pierog. Extensive air showers and hadronic interactions at high energy. *Annual Review of Nuclear and Particle Science*, 61:467–489, 2011.

[2] T. Antoni et al. KASCADE measurements of energy spectra for elemental groups of cosmic rays: Results and open problems. *Astroparticle Physics*, 24(1):1 – 25, 2005.

[3] B. S. Acharya et al. *Science with the Cherenkov Telescope Array.* WSP, 2018.

[4] M. S. Longair. *High Energy Astrophysics.* February 2011.

[5] W.I. Axford, E. Leer, and G. Skadron. The acceleration of cosmic rays by shock waves. *International Cosmic Ray Conference*, 11:132–137, 1977.

[6] F. A. Aharonian, A. M. Atoyan, and T. Kifune. Inverse Compton gamma radiation of faint synchrotron X-ray nebulae around pulsars. *Monthly Notices of the Royal Astronomical Society*, 291:162–176, October 1997.

[7] F. A. Aharonian. *Very High Energy Cosmic Gamma Radiation - A crucial window on the Extreme Universe.* World Scientific Publishing Co. Pte. Ltd., 2004.

[8] V. S. Berezinskii et al. *Astrophysics of cosmic rays.* 1990.

[9] T. C. Weekes. *Very high energy gamma-ray astronomy.* CRC Press, 2003.

[10] H. Bethe. Zur Theorie des Durchgangs schneller Korpuskularstrahlen durch Materie. *Annalen der Physik*, 397(3):325–400, 1930.

[11] F. Bloch. Zur Bremsung rasch bewegter Teilchen beim Durchgang durch Materie. *Annalen der Physik*, 408(3):285–320, 1933.

[12] H. Bethe and W. Heitler. On the Stopping of Fast Particles and on the Creation of Positive Electrons. *Proceedings of the Royal Society of London Series A*, 146:83–112, August 1934.

[13] M. Bartelmann. *Theoretical Astrophysics - An introduction.* ISBN-10: 9783527410040. Wiley-VCH, 1 edition, 2012.

[14] J. D. Jackson. *Classical Electrodynamics.* ISBN 0-471-30932-X. John Wiley & Sons, 3 edition, 1999.

[15] B. W. Caroll and D. A. Ostlie. *An Introduction to Modern Astrophysics.* ISBN 978-1-108-42216-1. Cambridge University Press, 2 edition, 2017.

[16] G. R. Blumenthal and R. J. Gould. Bremsstrahlung, Synchrotron Radiation, and Compton Scattering of High-Energy Electrons Traversing Dilute Gases. *Rev. Mod. Phys.*, 42:237–270, Apr 1970.

[17] S. Hoppe. *Emitters of VHE γ-radiation as revealed by the H.E.S.S. Galactic plane survey.* PhD thesis, Ruperto-Carola University of Heidelberg, 2008.

[18] J. A. Hinton and W. Hofmann. Teraelectronvolt Astronomy. *Annual Review of Astronomy and Astrophysics*, 47(1):523–565, Sep 2009.

[19] V. Zabalza. naima: a Python package for inference of relativistic particle energy distributions from observed nonthermal spectra. *Proceedings of International Cosmic Ray Conference 2015*, page 922, 2015.

[20] R. J. Murphy, C. D. Dermer, and R. Ramaty. High-energy processes in solar flares. *The Astrophysical Journal Supplement Series*, 63:721–748, March 1987.

[21] F. W. Stecker. Cosmic gamma ray production processes, galactic and extragalactic gamma rays, and cosmology. Technical report, NASA Goddard Space Flight Center; Greenbelt, MD, United States, 1971.

[22] A. M. Hillas. The origin of ultrahigh-energy cosmic rays. *Annual Review of Astronomy and Astrophysics*, 22:425–444, 1984.

[23] J. Blümer and K. H. Kampert. Search for the sources of cosmic radiation. *Physikalische Blätter*, 56N3:39–45, 2000.

[24] P. S. Coppi and F. A. Aharonian. Constraints on the Very High Energy Emissivity of the Universe from the Diffuse GeV Gamma-Ray Background. *Astrophysical Journal*, 487:L9–L12, September 1997.

[25] J. Blümer, R. Engel, and J. R. Hörandel. Cosmic rays from the knee to the highest energies. *Progress in Particle and Nuclear Physics*, 63(2):293–338, Oct 2009.

[26] V. S. Ptuskin et al. Diffusion and drift of very high energy cosmic rays in galactic magnetic fields. *Astronomy and Astrophysics*, 268(2):726–735, Feb 1993.

[27] J. R. Hörandel. Models of the knee in the energy spectrum of cosmic rays. *Astroparticle Physics*, 21(3):241–265, Jun 2004.

[28] P. Homola. Search for Ultra-High Energy Photons with the Pierre Auger Observatory. *CERN Proceedings*, 1(0):283, 2018.

[29] F. A. Aharonian. Gamma rays from supernova remnants. *Astroparticle Physics*, 43:71–80, March 2013.

[30] A. U. Abeysekara et al. Extended gamma-ray sources around pulsars constrain the origin of the positron flux at Earth. *Science*, 358(6365):911–914, Nov 2017.

[31] T. K. Gaisser, R. Engel, and E. Resconi. *Cosmic Rays and Particle Physics.* Cambridge University Press, June 2016.

[32] S. Rosswog and M. S Brüggen. *Introduction to High-Energy Astrophysics.* Cambridge University Press, 2007.

[33] R. Mushotzky. Supernova remnants lecture 3, 2016. Lecture notes, `https://www.astro.umd.edu/~richard/ASTR480/A480_supernova_remnants_2016_lec3.pdf`.

[34] J. R. Oppenheimer and G. M. Volkoff. On massive neutron cores. *Physical Review*, 55:374–381, Feb 1939.

[35] H. C. Spruit. The source of magnetic fields in (neutron-) stars. In Klaus G. Strassmeier, Alexander G. Kosovichev, and John E. Beckman, editors, *Cosmic Magnetic Fields: From Planets, to Stars and Galaxies*, volume 259 of *IAU Symposium*, pages 61–74, Apr 2009.

[36] A. R. Hewish et al. Observation of a rapidly pulsating radio source. *Nature*, 217, 02 1968.

[37] V. M. Kaspi and A. M. Beloborodov. Magnetars. *Annual Review of Astronomy and Astrophysics*, 55(1):261–301, Aug 2017.

[38] R. C. Duncan and C. Thompson. Formation of very strongly magnetized neutron stars - Implications for gamma-ray bursts. *Astrophysical Journal*, 392:L9–L13, June 1992.

[39] Lilia Ferrario and Dayal Wickramasinghe. Modelling of isolated radio pulsars and magnetars on the fossil field hypothesis. *Monthly Notices of the Royal Astronomical Society*, 367(3):1323–1328, Apr 2006.

[40] J. P. Williams, L. Blitz, and C. F. McKee. The Structure and Evolution of Molecular Clouds: from Clumps to Cores to the IMF. *Protostars and Planets IV*, page 97, May 2000.

[41] S. E. de Mink et al. The Incidence of Stellar Mergers and Mass Gainers among Massive Stars. *The Astrophysical Journal*, 782:7, February 2014.

[42] E. Parizot et al. Superbubbles and energetic particles in the Galaxy. I. Collective effects of particle acceleration. *Astronomy and Astrophysics*, 424:747–760, Sep 2004.

[43] J. Seo, H. Kang, and D. Ryu. The Contribution of Stellar Winds to Cosmic Ray Production. *Journal of Korean Astronomical Society*, 51(2):37–48, Apr 2018.

[44] R. Weaver et al. Interstellar bubbles. II - Structure and evolution. *Astrophysical Journal*, 218:377–395, December 1977.

[45] M.-M. Mac Low and R. McCray. Superbubbles in disk galaxies. *Astrophysical Journal*, 324:776–785, January 1988.

[46] F. Combes. Distribution of CO in the Milky Way. *Annual Review of Astronomy and Astrophysics*, 29(1):195–237, 1991.

[47] F. Aharonian, R. Yang, and E. de Oña Wilhelmi. Massive Stars as Major Factories of Galactic Cosmic Rays. *Nature Astronomy*, 3(6):561–567, 2019.

[48] F. A. Aharonian. Very high and ultra-high-energy gamma-rays from giant molecular clouds. *Astrophysics and Space Science*, 180:305–320, June 1991.

[49] T. Wilson, K. Rohlfs, and S. Huettemeister. *Tools of Radio Astronomy*. Springer, 5 edition, 2013.

[50] A. W. Strong et al. The distribution of cosmic-ray sources in the galaxy, gamma-rays, and the gradient in the CO-to-H2 relation. *Astronomy and Astrophysics*, 422:L47–L50, 2004.

[51] FITS working group. *Definition of the Flexible Image Transport System (FITS)*. International Astronomical Union, 4.0 edition, 2016.

[52] Z. Deretsky. Windows in our atmosphere for different wavelengths of the electromagnetic spectrum, July 2019. National Science Foundation, `http://www.zina-studio.com/p489212137/hF1B5103#hf1b5103`.

[53] S. Singer. The Vela satellite program for detection of high-altitude nuclear detonations. *Proceedings of the IEEE*, 53(12):1935–1948, Dec 1965.

[54] A. B. Atwood et al. The Large Area Telescope on the Fermi Gamma-Ray Space Telescope Mission. *The Astrophysical Journal*, 697(2):1071–1102, May 2009.

[55] R. Ulrich. *Measurement of the proton-air cross section using hybrid data of the Pierre Auger Observatory*. PhD thesis, Universität Karlsruhe (TH), December 2007.

[56] J. Matthews. A Heitler model of extensive air showers. *Astroparticle Physics*, 22:387–397, 2005.

[57] J. V. Jelley. *Cherenkov radiation and its applications*. Pergamon Press, 1958.

[58] I. M. Frank and I. E. Tamm. Coherent visible radiation of fast electrons passing through matter. *Proceedings of the USSR Academy of Sciences*, 14(3):109–114, 1937.

[59] A. Bouvier et al. Photosensor Characterization for the Cherenkov Telescope Array: Silicon Photomultiplier versus Multi-Anode Photomultiplier Tube. *Proceedings of the SPIE*, 8852, 08 2013.

[60] H. J. Völk and K. Bernlöhr. Imaging Very High Energy Gamma-Ray Telescopes. *Experimental Astronomy*, 25:173–191, 2009.

[61] K. Bernlöhr, August 2018. `https://www.mpi-hd.mpg.de/hfm/~bernlohr/HESS/MC_images/showers/`.

[62] A. U. Abeysekara et al. Observation of the Crab Nebula with the HAWC Gamma-Ray Observatory. *The Astrophysical Journal*, 843(1):39, 2017.

[63] J. A. Hinton and the HESS Collaboration. The status of the HESS project. *New Astronomy Reviews*, 48:331–337, April 2004.

[64] T. C. Weekes et al. VERITAS: the Very Energetic Radiation Imaging Telescope Array System. *Astroparticle Physics*, 17:221–243, May 2002.

[65] C. Bigongiari. The MAGIC Telescope. *Proceedings of Science*, HEP2005:020, 2006.

[66] M. Actis et al. Design concepts for the Cherenkov Telescope Array CTA: an advanced facility for ground-based high-energy gamma-ray astronomy. *Experimental Astronomy*, 32:193–316, December 2011.

[67] H. J. Rose. Cherenkov Telescope Calibration using Muon Ring Images. *24th International Cosmic Ray Conference*, 3, 1995.

[68] R. Chalme-Calvet, M. de Naurois, and J.-P. Tavernet. Muon efficiency of the H.E.S.S. telescope. In *Atmospheric Monitoring for High-Energy Astroparticle Detectors (Atmo-HEAD) Conference, Saclay (France)*, 2014. ArXiv:1403.4550.

[69] J. Zorn. Sensitivity Improvements of Very-High-Energy Gamma-Ray Detection with the Upgraded H.E.S.S. I Cameras using Full Waveform Processing. *International Cosmic Ray Conference*, 36:834, Jul 2019.

[70] A. M. Hillas. Cerenkov light images of EAS produced by primary gamma. *International Cosmic Ray Conference*, 3, August 1985.

[71] R. D. Parsons and J. A. Hinton. A Monte Carlo Template based analysis for Air-Cherenkov Arrays. *Astroparticle Physics*, 56:26–34, 2014.

[72] V. F. Hess. Über Beobachtungen der durchdringenden Strahlung bei sieben Freiballon-fahrten. *Physikalische Zeitschrift*, 13:1084–1091, November 1912.

[73] September 2018. `https://en.wikipedia.org/wiki/High_Energy_Stereoscopic_System`.

[74] August 2018. `http://www.magnetic-declination.com/`.

[75] A. Chulliat et al. The US/UK World Magnetic Model for 2015-2020. Technical report, National Geophysical Data Center, NOAA, 2015.

[76] J. M. Davies and E. S. Cotton. Design of the quartermaster solar furnace. *Solar Energy*, 1:16–22, April 1957.

[77] K. Bernlöhr et al. The optical system of the HESS imaging atmospheric Cherenkov telescopes, Part 1: Layout and components of the system. *Astroparticle Physics*, 20:111–128, 2003.

[78] S. Bonnefoy et al. Performance of the upgraded H.E.S.S. cameras. *International Cosmic Ray Conference*, 301:805, Jan 2017.

[79] G. Giavitto et al. A major electronics upgrade for the H.E.S.S. Cherenkov telescopes 1-4. *International Cosmic Ray Conference*, 34:996, Jul 2015.

[80] G. Giavitto. A NECTAr-based upgrade for the Cherenkov cameras of the H.E.S.S. 12-meter telescopes. *in prep.*, 2019.

[81] R. Wischnewski et al. Performance study of a digital camera trigger for CTA. 9:63–66, 01 2011.

[82] N. Bulian et al. Characteristics of the multi-telescope coincidence trigger of the HEGRA IACT system. *Astroparticle Physics*, 8(4):223 – 233, 1998.

[83] M. Rissi et al. A New Sum Trigger to Provide a Lower Energy Threshold for the MAGIC Telescope. *IEEE Transactions on Nuclear Science*, 56(6):3840–3843, Dec 2009.

[84] J. A. Hinton et al. A New Era in Gamma-Ray Astronomy with the Cherenkov Telescope Array. *Astroparticle Physics*, 43:1–2, March 2013.

[85] March 2019. `https://www.cta-observatory.org/`.

[86] K. Bernlöhr et al. Monte Carlo design studies for the Cherenkov Telescope Array. *Astroparticle Physics*, 43:171–188, March 2013.

[87] K. Schwarzschild. Untersuchungen zur geometrischen Optik I. *Astronomische Mitteilungen der Universitaets-Sternwarte zu Goettingen*, 9:1, June 1905.

[88] A. Couder. 183 (II), 1276. Technical report, Comptes rendus de l'Académie des sciences Paris, 1926.

[89] V. Vassiliev, S. Fegan, and P. Brousseau. Wide field aplanatic two-mirror telescopes for ground-based $\gamma$-ray astronomy. *Astroparticle Physics*, 28:10–27, September 2007.

[90] R. White. CHEC: a Compact High Energy Camera for the Cherenkov Telescope Array. *Journal of Instrumentation*, 12:C12059, Dec 2017.

[91] K. Bechtol et al. TARGET: A multi-channel digitizer chip for very-high-energy gamma-ray telescopes. *Astroparticle Physics*, 36:156–165, August 2012.

[92] P. Laporte et al. SST-GATE: an innovative telescope for very high energy astronomy. In *Ground-based and Airborne Telescopes IV*, volume 8444 of *Proceedings of the SPIE*, page 84443A, September 2012.

[93] J. L. Dournaux et al. Operating performance of the gamma-ray Cherenkov telescope: An end-to-end Schwarzschild-Couder telescope prototype for the Cherenkov Telescope Array. *Nuclear Instruments and Methods in Physics Research A*, A845:355–358, 2017.

[94] S. Vercellone et al. The ASTRI Project: An Innovative Prototype for a Cherenkov Dual-mirror Small-telescope. In *AAS/High Energy Astrophysics Division*, volume 13 of *AAS/High Energy Astrophysics Division*, page 123.31, April 2013.

[95] F. Aharonian et al. Observations of the Crab Nebula with H.E.S.S. *Astron. Astrophys.*, 457:899–915, 2006.

[96] D. Heck, J. Knapp, J. N. Capdevielle, G. Schatz, and T. Thouw. *CORSIKA: a Monte Carlo code to simulate extensive air showers.* February 1998.

[97] K. Bernlöhr. Simulation of Imaging Atmospheric Cherenkov Telescopes with CORSIKA and sim_telarray. *Astroparticle Physics*, 30:149–158, 2008.

[98] S. Ohm, C. van Eldik, and K. Egberts. $\gamma$/hadron separation in very-high-energy $\gamma$-ray astronomy using a multivariate analysis method. *Astroparticle Physics*, 31(5):383–391, Jun 2009.

[99] A. Hoecker et al. TMVA - Toolkit for Multivariate Data Analysis. *arXiv e-prints*, page physics/0703039, Mar 2007.

[100] D. Berge, S. Funk, and J. Hinton. Background modelling in very-high-energy $\gamma$-ray astronomy. *Astronomy and Astrophysics*, 466(3):1219–1229, May 2007.

[101] A. Jardin-Blicq. *The TeV $\gamma$-ray emission of the Galactic Plane.* PhD thesis, Ruperto-Carola University of Heidelberg, 2019.

[102] T. P. Li and Y. Q. Ma. Analysis methods for results in gamma-ray astronomy. *Astrophysical Journal*, 272:317–324, Sep 1983.

[103] A. Donath. Towards the H.E.S.S. Galactic Plane Survey Gamma-Ray Source Catalog. Master's thesis, Ruperto-Carola University of Heidelberg, 2014.

[104] A. De Franco et al. The first GCT camera for the Cherenkov Telescope Array. *Proceedings of Science*, ICRC2015:1015, 2016.

[105] J. Zorn. CHEC – A compact high energy camera for the Cherenkov Telescope Array. *Nuclear Instruments and Methods in Physics Research A*, 10 2018.

[106] J. Zorn et al. Characterisation and testing of CHEC-M – A camera prototype for the small-sized telescopes of the Cherenkov Telescope Array. *Nuclear Instruments and Methods in Physics Research A*, A904:44–63, 2018.

[107] J. J. Watson. *Calibration and analysis of the GCT camera for the Cherenkov Telescope Array.* PhD thesis, University of Oxford, 2018. `https://ora.ox.ac.uk/objects/uuid:1794e10a-12b1-4f48-84df-582f48b0e702`.

[108] Hamamatsu Photonics K.K. Editorial Commitee. *Photomultiplier tubes, basics and applications.* Hamamatsu, 3a edition, 2007. Editing: World Technical Writing, Inc.

[109] Introduction to SiPM, 2011. SensL technical note, `https://www.sensl.com/downloads/ds/TN%20-%20Intro%20to%20SPM%20Tech.pdf`.

[110] Hamamatsu. *Hamamatsu S12642-1616PA-50 SiPM.* data sheet.

[111] S. Vinogradov. Analytical models of probability distribution and excess noise factor of solid state photomultiplier signals with crosstalk. *Nuclear Instruments and Methods in Physics Research A*, 695:247–251, Dec 2012.

[112] A. Albert et al. TARGET 5: A new multi-channel digitizer with triggering capabilities for gamma-ray atmospheric Cherenkov telescopes. *Astroparticle Physics*, 92:49–61, June 2017.

[113] S. Funk et al. TARGET: A digitizing and trigger ASIC for the Cherenkov telescope array. In *6th International Symposium on High Energy Gamma-Ray Astronomy*, volume 1792 of *American Institute of Physics Conference Series*, page 080012, January 2017.

[114] J. Catalano. Characterization of a custom designed trigger ASIC (T5TEA) for the Cherenkov Telescope Array, 2016. Bachelor's thesis, `https://ecap.nat.fau.de/wp-content/uploads/2017/04/2016_Catalano_Bachelor.pdf`.

[115] J. Serrano et al. The white rabbit project. In *Proceedings of ICALEPCS TUC004, Kobe, Japan*, 2009.

[116] August 2019. `https://en.wikipedia.org/wiki/Jumbo_frame`.

[117] August 2019. `https://sevensols.com`.

[118] A. Brown et al. Flasher and muon-based calibration of the GCT telescopes proposed for the Cherenkov Telescope Array. *Proceedings of Science*, ICRC2015:934, 2016.

[119] W. Pence. CFITSIO, v2.0: A New Full-Featured Data Interface. In D. M. Mehringer, R. L. Plante, and D. A. Roberts, editors, *Astronomical Data Analysis Software and Systems VIII*, volume 172 of *Astronomical Society of the Pacific Conference Series*, page 487, 1999.

[120] J. D. Case et al. Simple network management protocol (snmp). *RFC*, 1157, May 1990.

[121] CTA High-Level Data Model Definitions, August 2016. Internal CTA Document (Draft V0.3).

[122] hipeCTA - a high performance library for the Cherenkov Telescope Array, 2018. `https://indico.cern.ch/event/587955/contributions/2937598/attachments/1679302/2697277/hipeCTA_CHEP2018_Vuillaume.pdf`.

[123] CTA. *CTA Experimental Pipeline Framework (ctapipe)*, 2018. `https://cta-observatory.github.io/ctapipe/index.html`.

[124] D. Hanna. Calibration Techniques for VERITAS. *International Cosmic Ray Conference*, 3:1417–1420, 2008.

[125] J. J. Watson et al. Inauguration and First Light of the GCT-M Prototype for the Cherenkov Telescope Array. *AIP Conference Proceedings*, 1792(1):080006, 2017.

[126] S. Gentile, E. Kuznetsova, and F. Meddi. Photon detection efficiency of Geiger-mode avalanche photodiodes. In *International Linear Collider Workshop (LCWS10 and ILC10) Beijing, China, March 26-30, 2010*, 2010.

[127] T. Bretz. Zenith angle dependence of the cosmic ray rate as measured with imaging air-Cherenkov telescopes. *Astroparticle Physics*, 111:72–86, Sep 2019.

[128] July 2019. `https://en.wikipedia.org/wiki/Flash_ADC`.

[129] A. Mitchell. *Optical Efficiency Calibration for Inhomogeneous IACT Arrays and a Detailed Study of the Highly Extended Pulsar Wind Nebula HESS J1825-137*. PhD thesis, Ruperto-Carola-University of Heidelberg, 2016.

[130] August 2019. `https://tycho.usno.navy.mil/mjd.html`.

[131] Private communication with K. Bernlöhr.

[132] M. Meyer, D. Horns, and H. S. Zechlin. The Crab Nebula as a standard candle in very high-energy astrophysics. *Astronomy and Astrophysics*, 523:A2, Nov 2010.

[133] J-F. Glicenstein et al. The NectarCAM camera project. In *Proceedings, 33rd International Cosmic Ray Conference (ICRC2013): Rio de Janeiro, Brazil, July 2-9, 2013*, page 0767, 2013.

[134] A. Abramowski et al. Discovery of extended VHE $\gamma$-ray emission from the vicinity of the young massive stellar cluster Westerlund 1. *Astronomy and Astrophysics*, 537:A114, Jan 2012.

[135] October 2019. ESO at a glance, `https://www.eso.org/public/about-eso/esoglance/`.

[136] M. C. Weisskopf et al. Chandra X-ray Observatory (CXO): overview. In J. E. Truemper and B. Aschenbach, editors, *Proc. SPIE*, volume 4012 of *Society of Photo-Optical Instrumentation Engineers (SPIE) Conference Series*, pages 2–16, Jul 2000.

[137] October 2019. Westerlund 1: Neutron Star Discovered Where a Black Hole Was Expected, `https://chandra.harvard.edu/photo/2005/wd1/`.

[138] B. Westerlund. A heavily reddened cluster in ARA. *Publications of the Astronomical Society of the Pacific*, 73:51, Feb 1961.

[139] August 2019. SIMBAD Astronomical Database - CDS (Strasbourg), `http://simbad.u-strasbg.fr/simbad/sim-id?Ident=Westerlund+1`.

[140] J. S. Clark et al. On the massive stellar population of the super star cluster Westerlund 1. *Astronomy and Astrophysics*, 434(3):949–969, May 2005.

[141] M. Aghakhanloo et al. Inferring the distance to Westerlund 1 from Gaia DR2. *arXiv e-prints*, page arXiv:1901.06582, Jan 2019.

[142] R. Kothes and S. M. Dougherty. The distance and neutral environment of the massive stellar cluster Westerlund 1. *Astronomy and Astrophysics*, 468(3):993–1000, Jun 2007.

[143] J. H. Groh et al. Detection of additional Wolf-Rayet stars in the starburst cluster Westerlund 1 with SOAR. *Astronomy and Astrophysics*, 457(2):591–594, Oct 2006.

[144] M. P. Muno et al. Diffuse, Nonthermal X-Ray Emission from the Galactic Star Cluster Westerlund 1. *The Astrophysical Journal*, 650(1):203–211, Oct 2006.

[145] N. J. Wright et al. The ionized nebula surrounding the red supergiant W26 in Westerlund 1. *Monthly Notices of the Royal Astronomical Society*, 437(1):L1–L5, Jan 2014.

[146] T. K. T. Fok et al. Maser Observations of Westerlund 1 and Comprehensive Considerations on Maser Properties of Red Supergiants Associated with Massive Clusters. *The Astrophysical Journal*, 760(1):65, Nov 2012.

[147] J. S. Clark et al. Unveiling the X-ray point source population of the Young Massive Cluster Westerlund 1. *Astronomy and Astrophysics*, 477:147–163, January 2008.

[148] Scott J. W. et al. Discovery of Nonthermal X-Ray Emission from the Embedded Massive Star-forming Region RCW 38. *The Astrophysical Journal*, 580(2):L161–L165, dec 2002.

[149] A. Bamba et al. Thermal and Nonthermal X-Rays from the Large Magellanic Cloud Superbubble 30 Doradus C. *The Astrophysical Journal*, 602(1):257–263, feb 2004.

[150] M. P. Muno et al. A Neutron Star with a Massive Progenitor in Westerlund 1. *The Astrophysical Journal*, 636(1):L41–L44, Jan 2006.

[151] D. M. Fenech et al. An ALMA 3 mm continuum census of Westerlund 1. *Astronomy and Astrophysics*, 617:A137, Oct 2018.

[152] J. van Paradijs and N. White. The Galactic Distribution of Low-Mass X-Ray Binaries. *Astrophysical Journal Letters*, 447:L33, July 1995.

[153] H. J. Grimm, M. Gilfanov, and R. Sunyaev. The Milky Way in X-rays for an outside observer. Log(N)-Log(S) and luminosity function of X-ray binaries from RXTE/ASM data. *Astronomy and Astrophysics*, 391:923–944, Sep 2002.

[154] M. Gilfanov, M. Revnivtsev, and S. Molkov. Boundary layer, accretion disk and X-ray variability in the luminous LMXBs. *Astronomy and Astrophysics*, 410:217–230, October 2003.

[155] H. Abdalla et al. The population of TeV pulsar wind nebulae in the H.E.S.S. Galactic Plane Survey. *Astronomy and Astrophysics*, 612:A2, Apr 2018.

[156] J. Majumdar, F. Calore, and D. Horns. Search for gamma-ray spectral modulations in Galactic pulsars. *Journal of Cosmology and Astroparticle Physics*, 2018(4):048, Apr 2018.

[157] R. N. Manchester et al. The Australia Telescope National Facility Pulsar Catalogue. *The Astronomical Journal*, 129:1993–2006, April 2005.

[158] M. Sakai et al. Discovery of Diffuse Hard X-Ray Emission from the Vicinity of PSR J1648-4611 with Suzaku. *Publications of the Astronomical Society of Japan*, 65, 01 2013.

[159] C. J. Clark et al. The Einstein@Home Gamma-ray Pulsar Survey. I. Search Methods, Sensitivity, and Discovery of New Young Gamma-Ray Pulsars. *The Astrophysical Journal*, 834(2):106, Jan 2017.

[160] N. Ladd et al. Beam Size, Shape and Efficiencies for the ATNF Mopra Radio Telescope at 86-115 GHz. *Publications of The Astronomical Society of Australia*, 22:62–72, 01 2005.

[161] HI4PI Collaboration. HI4PI: A full-sky H I survey based on EBHIS and GASS. *Astronomy and Astrophysics*, 594:A116, Oct 2016.

[162] F. Aharonian et al. The H.E.S.S. Survey of the Inner Galaxy in Very High Energy Gamma Rays. *The Astrophysical Journal*, 636(2):777–797, Jan 2006.

[163] R. C. G. Chaves, E. de Oña Wilhemi, and S. Hoppe. The H.E.S.S. Galactic Plane Survey. In F. A. Aharonian, W. Hofmann, and F. Rieger, editors, *American Institute of Physics Conference Series*, volume 1085 of *American Institute of Physics Conference Series*, pages 219–222, December 2008.

[164] F. Aharonian et al. Observations of the Crab nebula with HESS. *Astronomy and Astrophysics*, 457(3):899–915, Oct 2006.

[165] J. Kerp et al. The Effelsberg Bonn H I Survey (EBHIS). *Astronomische Nachrichten*, 332:637, July 2011.

[166] N. M. McClure-Griffiths et al. Gass: The Parkes Galactic All-Sky Survey. I. Survey Description, Goals, and Initial Data Release. *The Astrophysical Journal Supplement*, 181(2):398–412, Apr 2009.

[167] T. M. Dame, D. Hartmann, and P. Thaddeus. The Milky Way in Molecular Clouds: A New Complete CO Survey. *The Astrophysical Journal*, 547(2):792–813, Feb 2001.

[168] H Abdalla et al. The H.E.S.S. Galactic Plane Survey. *Astronomy and Astrophysics*, 612:A1, Apr 2018.

[169] H. Abdalla et al. Particle transport within the pulsar wind nebula HESS J1825-137. *Astronomy and Astrophysics*, 621:A116, Jan 2019.

[170] M. Heyer and T. M. Dame. Molecular clouds in the milky way. *Annual Review of Astronomy and Astrophysics*, 53(1):583–629, 2015.

[171] C. Leitherer et al. Starburst99: Synthesis models for galaxies with active star formation. *The Astrophysical Journal Supplement Series*, 123(1):3–40, jul 1999.

[172] L. Ciotti and A. D'Ercole. SNR expansion in a pre-existent cavity. *Astronomy and Astrophysics*, 215:347–359, May 1989.

[173] R. Wünsch et al. Two-dimensional Hydrodynamic Models of Super Star Clusters with a Positive Star Formation Feedback. *Astrophysical Journal*, 683:683–692, August 2008.

[174] March 2019. `https://www.berkeleynucleonics.com/model-577`.

[175] April 2019. `https://teledynelecroy.com/oscilloscope/wavepro-hd-oscilloscope/resources/product-manuals`.

[176] Pdl 800-b manual, July 2017. `https://www.picoquant.com/products/category/picosecond-pulsed-driver/pdl-800-b-picosecond-pulsed-diode-laser-driver`.

[177] F. Werner et al. Performance Verification of the FlashCam Prototype Camera for the Cherenkov Telescope Array. *Nuclear Instruments and Methods in Physics Research A*, A876:31–34, 2017.

[178] April 2019. `https://www.universal-robots.com/products/ur5-robot/`.

[179] March 2019. `https://sensl.com/downloads/ds/DS-MicroJseries.pdf`.

[180] March 2019. `https://ww2.minicircuits.com/pdfs/ZFL-1000LN+.pdf`.

# Acknowledgements

> "No one who achieves success does so without acknowledging the help of others. The wise and confident acknowledge this help with gratitude."

<div align="right">Alfred North Whitehead</div>

This thesis and the work related to it would not have been possible without the support of a number of people.

First and foremost, I want to thank my supervisor Prof. Dr. Jim Hinton. About 4.5 years ago, even one year before the designated starting date of my PhD, I came to him with the wish to work on CTA as part of my PhD project. With satisfying this wish, Jim gave me the opportunity to do exactly want I wanted to: working on hardware, testing and developing Cherenkov cameras, going on observing campaigns, and at the same time also doing some science. Each discussion with him was very fruitful and inspirational. Quite some times I came to his office with just one question and left it with a few more. Moreover, I want to thank him for his support with my other passion beside physics: the refereeing. Without his understanding and the opportunity of flexible working hours, combing my PhD with refereeing and my family would absolutely not have been possible.

I want to thank Dr. Stefan Hippler for being part of my thesis committee and the other members of my jury Prof. Dr. Stefan Wagner, Prof. Dr. Stephanie Hansmann-Menzemer, and Prof. Dr. Tilman Plehn.

Furthermore, I want to thank Dr. Richard White. It was amazing to work with him as he has a tremendous knowledge especially in hardware. Maybe most of the time in the past three years I was working with him and I do not regret any minute of it. I love to remember the observation campaigns with CHEC-M in Meudon with a few hours of sleep and the quite hard time we had to get some nice results out of CHEC-M.

I am very grateful to Dr. Dan Parsons and Dr. Vincent Marandon for their great help especially in the H.E.S.S. part of the thesis. I could count on them and bother them not only once regarding any questions, being them physics related or just how to extract a plot from a `ROOT` file. I also appreciate the time they spent for proofreading my thesis, and that they gave several talks on my behalf at the H.E.S.S. collaboration meetings. Merci beaucoup!

Many thanks go to Dr. Jason Watson who I could always ask in any software-related question, to Dr. Axel Donath for his support with `gammapy`, as well as to Dr. Konrad Bernlöhr for his help with H.E.S.S. simulations. Furthermore, I don't want to forget to thank Miquel Barcelo (for his support in several technical-related aspects with CHEC), Dr. Harm Schoorlemmer and Dr. Luigi Tibaldo (who both stopped working on CHEC but spent quite some

time to introduce me to concepts of CHEC at the start of my PhD), and Francesco Conte (especially for his awesome cooking capabilities during the CHEC-S campaign in Sicily).

Another big thanks goes to Simon Sailer. I had a really great time with him, not only every day in our office but also during four weeks in Namibia. I love to remember the discussions, especially about muon rings and their geometry, our 2-hour drive on the best-quality roads to a shopping mall (and standing in front of closed doors in the end.. ), and our numberless ping-pong matches. It was very nice to work with you!

In addition to that, I thank all my other colleagues and the technicians for creating a pleasant and productive working environment without forgetting about fun. I am very happy that I could be part of such a nice group!

A further thanks goes to Prof. Dr. Gavin Rowell and Cameron Snoswell, both from University of Adelaide, for providing me with the latest Mopra data of the Westerlund 1 region.

I don't want to forget about my time at KIT in Karlsruhe where I studied. Without the support of Dr. Joel Cramer, Dr. Johannes King, Dr. Markus Neuwirth, Dr. Daniel Schell, and (future Dr.) Johannes Fischer and the numberless afternoons we spent together in doing exercises, I probably would have not managed to achieve the current status. Talking about my time at KIT, Prof. Dr. Ralph Engel who was my Master thesis' supervisor played a major role concerning my career. He not only gave me the taste for particle astrophysics but also the advice to choose a PhD where I could develop hardware instead of only doing analysis. It was also because of this advice why I chose MPIK for my PhD in the end.

Of course, such an intensive time is not possible without friends and family. I want to thank my friends for their support and the time they spent with me since I know them and especially during the past three years. The feeling of having them in my life is invaluable! I further want to express my deep gratitude to my parents, Susanne and Wolfgang, and to my stepfather, Thomas. They educated me to be open-minded, self-confident and curious about nature, and they taught me to take decisions and sometimes to choose a way which may not be the typical and most convenient one in the beginning.

Finally, I want to mention my wife Nadjma and my five-month-old son Younes who show me everyday what life means. I thank Nadjma for her great support in all parts of my life, for her deep understanding, for her power and the way how she is. We moved to Mannheim because of my PhD and I really appreciate that she agreed on that. I further appreciate that she tolerated my repeating absence due to traveling, either for the physics or for the refereeing. Without her and her love, any of what I managed to do in the past three years would not have been possible. What a fortune that we met. I love you more than anything else in my life!